

**Semiconductor Contacts for Nanoelectronics: SnS Nanoribbons, SnS Thin Films,
and Silver Nanowire-Based Transparent Conductors**

Submitted in partial fulfillment of the requirements for

the degree of

Doctor of Philosophy

in

Materials Science and Engineering

Jenifer R. Hajzus

B.S., Physics, Rensselaer Polytechnic Institute

M.S., Materials Science and Engineering, Carnegie Mellon University

Carnegie Mellon University
Pittsburgh, PA

April, 2018

Acknowledgements

I would like to thank Professor Lisa Porter for giving me the opportunity to work in her group and for devoting the time to serve as my advisor. Her guidance, insight, and support during my graduate studies are truly appreciated. I would also like to sincerely thank my committee members, Professor Michael Bockstaller, Professor Tomasz Kowalewski, and Professor Randall Feenstra for their constructive feedback and discussion.

I gratefully acknowledge support from the US Civilian Research & Development Foundation (Award Number OISE-14-60114-0), a Bertucci Graduate Fellowship, and a CNST-UMD Collaboration Travel Grant.

I am thankful to have worked with the past and present members of the Porter research group. In particular, thank you to Sudarshan Narayanan, Yao Yao, and Jacob Melby for instruction on lab techniques, helpful discussions, and time spent on equipment maintenance, which were essential to completing this research. I'd additionally like to thank the undergraduate students I have worked with: Rekha Schnepf, Javier Flores, and Ryan Aguirre.

Thank you to Kumar Das and Yi Luo for useful discussions concerning device physics and fabrication. Many thanks to collaborators from NIST on the contacts to SnS nanoribbons work: thank you to Adam Biacchi for synthesizing the SnS nanoribbons, Son Le for assistance with device fabrication and e-beam lithography, and Angela Hight Walker and Curt Richter for valuable insight. Thank you to the staff in the CMU MSE department including Adam Wise, Tom Nuhfer, and Betsy Clark for training and assistance with materials characterization techniques. Additionally, I'd like to thank Bill Pingitore for advice on experimental setups, and Brett Riale for equipment support.

I am grateful for the friends who made my time in graduate school more enjoyable. Lastly, thank you to my parents for their encouragement and continuous support.

Abstract

Metal-semiconductor contacts are ubiquitous in electronic and optoelectronic devices. However, control over the properties and performance of metal-semiconductor contacts is often difficult to achieve. Reductions in dimensions and the need for low-cost materials for optoelectronic applications have introduced new semiconductors to which contact behavior must be understood. The bulk of this thesis concerns the behavior of contacts to tin(II) sulfide (SnS), a layered semiconductor that is of interest for two-dimensional electronics and as an earth-abundant, low-toxic absorber material for thin film solar cells. Contact metals with a range of work functions were characterized on two forms of SnS: (1) individual, solution-synthesized, p-type SnS nanoribbons and (2) electron-beam evaporated, polycrystalline SnS thin films.

Lower work function metals (Cr/Au and Ti/Au) formed Schottky contacts on SnS nanoribbons, whereas higher work function metals (Ni/Au and Pd/Au) formed ohmic or semi-ohmic contacts. Schottky barrier heights and ideality factors of Cr/Au and Ti/Au contacts were calculated by fitting current-voltage measurements to a back-to-back Schottky diode model. Specific contact resistance values for Ni/Au ($\leq 10^{-4} \Omega \text{ cm}^2$) and Pd/Au ($\leq 10^{-3} \Omega \text{ cm}^2$) were calculated from TLM and contact end resistance measurements on individual nanoribbons. The calculated Schottky barriers for Cr/Au ($\sim 0.39 \text{ eV}$) and Ti/Au ($\sim 0.50 \text{ eV}$) and the ohmic behavior of Ni/Au and Pd/Au correspond well with behavior predicted by Schottky–Mott theory.

Nanocrystalline SnS thin films were deposited by electron-beam evaporation. A substrate temperature of 300°C followed by a 300°C anneal produced the α -SnS phase, whereas Raman spectroscopy and x-ray diffraction indicated a mixture of π -SnS and α -SnS phases in films deposited at 100°C and 200°C . Ti/Au, Ru/Au, Ni/Au, and Au as-deposited metallizations formed ohmic contacts to α -SnS thin films. Average specific contact resistances measured with

circular transfer length method (CTLTM) structures were found to decrease with increasing metal work function from Ti/Au, Ru/Au, Ni/Au, to Au. After annealing the contacts at 350°C in argon, Ru/Au had the lowest average specific contact resistance of $1.9 \times 10^{-3} \Omega\text{-cm}^2$. Ni/Au and Ti/Au contacts were found to be unstable after annealing.

Solution-processed, silver nanowire (Ag NW)-polymer composites were also investigated as alternatives to contacts based on transparent conducting oxides. Solution-processed Ag NWs dispersed in polymers such as poly(ethylene dioxythiophene):poly(styrene sulfonate) (PEDOT:PSS) demonstrated improved film uniformity relative to those dispersed in isopropanol. Whereas PEDOT:PSS reduced the transmittance of the films, two non-conductive, transparent polymers (polystyrene sulfonate (PSS) and polyvinyl alcohol (PVA)) resulted in NW films with improved figures of merit for transmittance and conductance. The Ag NWs formed rectifying contacts to Si prior to annealing. The lowest interfacial resistance of 90 nm-diameter Ag NWs on Si was observed after annealing at 650°C for 15 sec. Fragmentation at Ag NW junctions occurred at temperatures as low as 200°C for 35-nm diameter Ag NWs and precluded the formation of ohmic contacts.

Table of Contents

Acknowledgements	iii
Abstract.....	iv
Table of Contents	vi
List of Tables	x
List of Figures.....	xii
Chapter 1: Introduction	1
1.1 References.....	3
Chapter 2: Background.....	4
2.1 Metal/Semiconductor Interfaces and Contact Resistance.....	4
2.1.1 The Schottky-Mott Model.....	4
2.1.2 The Bardeen Model and Interface States	6
2.1.3 Metal Induced Gap States	8
2.1.4 Image Force Lowering.....	9
2.1.6 Current Transport Mechanisms.....	10
2.1.7 Specific Contact Resistance	11
2.2 References.....	14
Chapter 3: Experimental Methods.....	15
3.1 Thin Film Deposition	15
3.1.1 Electron Beam Evaporation	15
3.1.2 Polymer and Nanomaterial Deposition	15
3.2 Heat Treatment	16
3.2.1 Rapid Thermal Annealing (RTA)	16

3.2.2 Tube Furnace Annealing.....	17
3.3 Electrical Characterization	17
3.3.1 Van der Pauw Sheet Resistance and Hall Measurements	17
3.3.2 CTLM Pattern Fabrication and Measurements.....	19
3.3.3 Contact Fabrication on SnS Nanoribbons.....	22
3.4 Optical Characterization.....	25
3.5 Scanning Electron Microscopy (SEM).....	25
3.5.1 Secondary Electron Images.....	26
3.5.2 Energy Dispersive X-ray Spectroscopy (EDX or EDS)	26
3.6 Atomic Force Microscopy (AFM).....	26
3.7 Raman Spectroscopy	27
3.8 X-ray Diffraction (XRD)	27
3.9 References.....	28
Chapter 4: Schottky Barrier Heights and Specific Contact Resistances on SnS Nanoribbons	29
4.1 Introduction.....	29
4.1.1 Two-Dimensional (2D) Materials.....	29
4.1.2 Two-Dimensional SnS	31
4.1.3 Contacts to 2D Semiconductors.....	32
4.1.4 Contribution of This Work.....	36
4.2 Experimental Methods	38
4.2.1 Device Fabrication.....	38
4.2.2 Characterization	39

4.3 Results and Discussion.....	41
4.3.1 Current-Voltage Characteristics.....	41
4.3.2 Schottky Barrier Height I - V Measurement	41
4.3.3 Specific Contact Resistance Measurement	46
4.4 Conclusion	54
4.5 References.....	54
Chapter 5: Deposition and Characterization of Electron-Beam Evaporated SnS Thin Films and Comparison of Ohmic Contacts.....	60
5.1 Introduction.....	60
5.1.1 Motivation.....	60
5.1.2 Contribution of This Work.....	65
5.1.3 Sn-S System.....	65
5.1.4 SnS Polymorphs.....	70
5.1.5 SnS Thin Film Deposition Methods and Processing	73
5.1.6 Review of Electron-Beam Evaporated SnS Films	73
5.1.7 Review of Contacts to SnS	75
5.2 Deposition and Characterization of Electron-Beam Evaporated SnS Thin Films	78
5.2.1 Experimental Methods: Deposition of SnS Thin Films.....	78
5.2.2 Results: Characterization of SnS Source	79
5.2.3 Results: Deposition and Characterization of 50 nm and 515 nm Thick SnS Films.....	81
5.2.4 Results: Impact of Substrate Temperature on Properties of SnS Films.....	90
5.3 Contacts to Electron-Beam Evaporated SnS Thin Films.....	120

5.3.1 Experimental Methods: Specific Contact Resistance Test Structure Fabrication and Measurement.....	120
5.3.2 Results: Initial Study of Contacts on 50 nm Thick Films.....	121
5.3.3 Results: Contacts on $T_{\text{sub}} = 300^{\circ}\text{C}$, Post Annealed Films.....	124
5.4 Conclusion	130
5.5 References.....	130
Chapter 6: Transparent Conducting Electrodes Based on Ag NWs and Ag NW/Polymer composites.....	137
6.1 Introduction.....	137
6.1.1 Transparent Electrodes.....	137
6.1.2 Silver Nanowire-Based Transparent Conducting Electrodes	138
6.1.3 Silver Nanowire Contacts to Silicon.....	141
6.1.4 Contribution of This Work.....	143
6.2 Ag NW and Ag NW/Polymer Composite Films	145
6.2.1 Experimental Methods	145
6.2.2 Results.....	146
6.3 The Ag NW/Si Interface	154
6.3.1 Introduction.....	154
6.3.2 Experimental Methods.....	156
6.3.3 Results.....	157
6.4 Conclusions.....	168
6.5 References.....	170
Chapter 7: Summary and Future Directions	173

List of Tables

Table 4.1: Average fit parameters for Cr/Au and Ti/Au Schottky contacts.	45
Table 4.2: Specific contact resistances and related parameters, calculated using the contact end resistance method.	49
Table 4.3: Specific contact resistance parameters extracted by the transfer length method (TLM) for Ni/Au and Pd/Au contacts.	49
Table 5.1: Summary of contacts to SnS thin films in literature. R refers to resistance measured between two contacts.	76
Table 5.2: Van der Pauw resistivity and Hall measurement results for as-deposited and annealed (300 °C / 1 hr) 50 nm thick SnS films on borosilicate glass.	83
Table 5.3: Comparison of Hall measurement results of 50 nm thick SnS films deposited at $T_{\text{sub}} = \text{RT}$ and post annealed at 300°C for 1 hr on borosilicate glass and soda lime glass substrates.	89
Table 5.4: Characteristics of the XRD peak between the α -SnS (111) and (040) Bragg reflections for different deposition conditions.	89
Table 5.5. Thicknesses of as-deposited and annealed SnS films deposited at different substrate temperatures. The post treatment “anneal” refers to an anneal at 300°C for 1 hr in vacuum ($\sim 10^{-7}$ Torr). Target thicknesses monitored by the QCM in the deposition chamber are listed in addition to film thicknesses measured with AFM.	90
Table 5.6 Summary of phases present determined by XRD and Raman spectroscopy.	117
Table 5.7: Hall measurement results of a mixed π -SnS and α -SnS film, which was deposited at 200 °C, and of an α -SnS film, which was deposited at 300 °C then post annealed at 300 °C.	117
Table 5.8: Indirect band gaps extracted from 1.75 eV -2 eV region of Tauc plot in Figure 5.28 (e) for SnS films deposited at different substrate temperatures and with different post-deposition treatments. Composition was determined from XRD and Raman spectroscopy.	118
Table 5.9: Extracted contact resistance parameters for Ni/Au contacts after annealing: with smallest contact spacing included in fit, and without.	127
Table 6.1: Properties of transparent conductive materials from literature.	138
Table 6.2: Bulk-like and percolative-like figure of merit parameters extracted from the sheet resistance versus transmittance plot in Figure 6.3 b, from Narayanan, Hajzus, et. al. ¹⁶	

Reproduced with permission from ECS Journal of Solid State Science and Technology, 3
(11) P363-P369 (2014). Copyright 2014, The Electrochemical Society. 150

Table 6.3: Summary of I-V characteristics of 90nm diameter Ag NW films after heat treatments.
“R” refers to a rectifying contact. “S-O” refers to a semi-ohmic contact. 160

List of Figures

- Figure 2.1: Band diagrams illustrating the Schottky-Mott model for a metal/(n-type) semiconductor interface. 5
- Figure 2.2: Band diagram illustrating a metal / (n-type) semiconductor interface with interface states. The Fermi level is pinned near E_o . 7
- Figure 2.3: Band diagrams of an n-type semiconductor showing current transport mechanisms. The doping concentration increases from left to right and the transport of electrons is indicated by the arrows. The dotted line indicates the Fermi level position. After Ref [3]. 10
- Figure 2.4: Depiction of transfer length and TLM structure. (a) Illustration (not to scale) of transfer length with current crowding represented by yellow arrows. (b) Illustration of TLM structure. (c) Plot used to extract contact resistance and related parameters from TLM structures. 13
- Figure 3.1: Schematic of contact configuration for van der Pauw Hall measurements. 19
- Figure 3.2: (a) Schematic of circular transfer length method (CTLTM). The grey area represents the metal and the brown area represents the semiconductor. (b) Illustration depicting inner radius, r_o , outer radius, r_l , and spacing, s . 20
- Figure 3.3: Schematic of photolithography process used to fabricate CTLTM structures. 21
- Figure 3.4: Deposition of SnS nanoribbons and identification of areas of interest for contact fabrication. 23
- Figure 3.5: Fabrication of contact structures on SnS nanoribbons. 24
- Figure 4.1: Orthorhombic $Pnma$ crystal structure of α -SnS viewing from the (a) (100) plane, and slightly tilted from the (b) (010), and (c) (001) planes. SEM images of (d) a solution-synthesized nanoribbon on a SiO_2/Si substrate and (e) a high concentration of nanoribbons drop cast onto a substrate. *Nanoscale*, 2018, 10, 319-327- Reproduced by permission of the Royal Society of Chemistry. 37
- Figure 4.2: (a) Cross sectional schematic of device structure. Two nanoribbons with different contact configurations are shown. (b) Optical microscope image of a sample with many contact test structures patterned in one area and (c) a higher magnification image of a nanoribbon with four contacts. Average I-V sweeps for each contact metallization with 1 μm channel spacing on a (d) log and (e) linear scale, showing ohmic and semi-ohmic behavior for Pd/Au and Ni/Au contacts, and Schottky behavior for Cr/Au and Ti/Au contacts. Inset in (d) is an SEM image of a two contact Ni/Au device. *Nanoscale*, 2018, 10, 319-327- Reproduced by permission of the Royal Society of Chemistry. 40
- Figure 4.3: Example fits of I-V sweeps to the back-to-back Schottky diode equation for (a) Cr/Au contacts on SnS and (b) Ti/Au contacts on SnS. I-V sweeps were measured between

adjacent contacts. (c) Schottky-Mott band alignment of metals and SnS. χ is the electron affinity of SnS, E_g is the band gap, E_{vac} is the vacuum level, E_C is the conduction band minimum, and E_V is the valence band maximum. (d) Band alignment determined from experiments. *Nanoscale*, 2018, 10, 319-327- Reproduced by permission of the Royal Society of Chemistry.

44

Figure 4.4: (a) Transmission line model for metal-semiconductor contact. (b) Schematic of contact end resistance measurement. (c) SEM image of a CER structure for Ni/Au contacts on a SnS nanoribbon. (d) Example measurement of V_{23} for contact end resistance measurement of a set of Pd/Au contacts. (e) Schematic of contact front resistance measurement. *Nanoscale*, 2018, 10, 319-327- Reproduced by permission of the Royal Society of Chemistry.

48

Figure 4.5: Transfer length method (TLM) plots for extracting sheet resistance, specific contact resistance, and transfer lengths of contacts on an individual SnS nanoribbon for (a) Ni/Au contacts and (b) Pd/Au contacts. Inset in (a) is an SEM image of a representative TLM device. *Nanoscale*, 2018, 10, 319-327- Reproduced by permission of the Royal Society of Chemistry.

52

Figure 5.1: Absorption coefficients of different photovoltaic materials from literature.

63

Figure 5.2: Phase diagram of S-Sn system based on Sharma R.C., and Chang Y.A. from ASM Alloy Phase Diagram Database.⁵³ Reprinted with permission of ASM International. All rights reserved. www.asminternational.org

66

Figure 5.3: Vapor pressure of SnS (g) over SnS (s) as a function of temperature.

69

Figure 5.4: Crystal structures of tin sulfide phases and SnS polymorphs.

70

Figure 5.5: (a) SEM image of SnS granular source. (b) XRD scan of SnS source as received and after performing e-beam evaporations.

80

Figure 5.6: SEM (a,b) and AFM topography (c,d) images of (a,c) 50 nm and (b,d) 515 nm thick SnS films deposited on borosilicate glass at room temperature.

81

Figure 5.7: XRD spectra of 50 nm and 515 nm thick as deposited films and an annealed 50 nm thick film from $2\theta = 20^\circ$ to 70° .

85

Figure 5.8: XRD spectra of 50 nm and 515 nm thick as deposited films and an annealed 50 nm thick film from $2\theta = 30^\circ$ to 34° showing locations of α -SnS, π -SnS and secondary phase peaks.

86

Figure 5.9: Optical properties of 50 nm and 515 nm thick, as-deposited films and 50 nm thick annealed films. (a) Transmittance spectra, (b) Reflectance spectra, (c) absorbance spectra, (d) absorption coefficient.

88

Figure 5.10: SEM images of SnS films on Si substrates deposited at $T_{sub} = RT, 100^\circ C, 200^\circ C$, and $300^\circ C$, as indicated by the temperatures listed in the center of the image. Films in the

left column are as-deposited. Films in the right column were post-annealed at 300°C for 1 hr in vacuum. 92

Figure 5.11: SEM images of SnS thin films deposited at 300°C and annealed in vacuum at 300°C for 1 hr. (a) Film deposited onto Si. (b) Film deposited onto soda lime glass during the same deposition batch as the film in (a). (c) Film deposited onto Si with glass slide underneath Si substrate. (d) Film deposited onto soda lime glass during deposition in which there was no film adherence to Si. (e) Film deposited onto borosilicate glass during the same deposition batch as (d). 94

Figure 5.12: XRD spectra of SnS thin films deposited on soda lime glass at different substrate temperatures in the as-deposited condition. 95

Figure 5.13: XRD spectra of SnS thin films deposited on soda lime glass at different substrate temperatures that were annealed at 300 °C for 1 hr. 96

Figure 5.14: XRD spectra in 30°-34° range for SnS thin films deposited at different substrate temperatures: (a) as deposited and (b) post-annealed films. The temperature labels indicate substrate temperature during depositions. All films represented in (b) were annealed at 300 °C for 1 hr in vacuum. 97

Figure 5.15: Fit of the XRD spectra of an annealed SnS film deposited at 300 °C. Peak positions were constrained to reported positions. (a) Fit containing a mixture of α -SnS and π -SnS peaks. (b) Fit containing a mixture of α -SnS, π -SnS, and Sn₂S₃ peaks. 98

Figure 5.16: Fit of the XRD spectra of an annealed SnS film deposited at 300 °C. Peak positions were allowed to shift from reported values. 99

Figure 4.17: Fit of the XRD spectra of an as-deposited SnS film deposited at 300 °C. Peak positions were allowed to shift from reported values. 101

Figure 5.18: Fit of the XRD spectra of an annealed SnS film deposited at 200 °C. Peak positions were allowed to shift from reported values. 103

Figure 5.19: Fit of the XRD spectra of an as-deposited SnS film deposited at 200 °C. Peak positions were allowed to shift from reported values. 104

Figure 5.20: Fit of the XRD spectra of an (a) annealed and (b) unannealed SnS film deposited at 100 °C. Peak positions were allowed to shift from reported values. 105

Figure 5.21: Fit of the XRD spectra of an (a) annealed and (b) unannealed SnS film deposited at RT. Peak positions were allowed to shift from reported values. 106

Figure 5.22: (a) Position of XRD peak between 31.5°-32° (b) Scherrer crystallite size determined from 31.5°-32° XRD peak (c) SEM measurement of the short dimension of grain size (d) Ratio of long dimension grain size to short dimension determined from SEM images. All anneals were conducted at 300 °C for 1 hr in vacuum. (e) Ratio of atomic % Sn:S for

- different film conditions, as determined by EDS analysis. (f) Resistivities of SnS films deposited at different conditions, as calculated from van der Pauw measurements. 108
- Figure 5.23: Raman spectra of as-deposited (a) and annealed (b) SnS films deposited at different substrate temperatures, as indicated. Incident laser wavelength was 532 nm. The anneals were conducted at 300 °C for 1 hr in vacuum. 110
- Figure 5.24: Raman spectra of as-deposited (a) and annealed (b) SnS films deposited at different substrate temperatures, as indicated. Incident laser wavelength was 633 nm. The anneals were conducted at 300 °C for 1 hr in vacuum. 111
- Figure 5.25: Example background subtraction of Raman spectrum of $T_{\text{sub}}=200$ °C, annealed film. 113
- Figure 5.26: Deconvolution of Raman spectra of as-deposited films with 633 nm excitation wavelength after background subtraction. 114
- Figure 5.27: Deconvolution of Raman spectra of annealed films with 633 nm excitation wavelength. Films were annealed at 300 °C for 1 hr. 116
- Figure 5.28 Optical spectra of SnS films. (a) Transmittance, (b) reflectance, (c) absorbance (d) absorption coefficient (e) Tauc plot for determining indirect band gap (f) Tauc plot for determining direct band gap. 119
- Figure 5.29: (a) Schematic of CTLM pattern indicating spacings. (b) Secondary electron SEM image of CTLM pattern. 121
- Figure 5.30: Results of CTLM measurements on 50 nm thick SnS films deposited at $T_{\text{sub}} = \text{RT}$. (a) I-V characteristics of metals deposited with a 5 μm CTLM spacing (b) Example least squares fit of total resistance versus outer radius to Equation 3.5 for Ni/Au contacts. (c) Extracted specific contact resistances for contacts on 50 nm thick SnS films: both as-deposited films with no surface treatment (red circles) and SnS films annealed at 300°C for 1 hr followed by a surface treatment of O_2 plasma followed by a 30s dip in 1% HF (green diamond). Annealing was performed prior to contact deposition. 122
- Figure 5.31: Results of CTLM measurements on 226 nm thick SnS films deposited at $T_{\text{sub}} = 300^\circ\text{C}$, then post annealed in vacuum at 300°C for 1hr. A surface treatment of O_2 plasma followed by a 1% HF dip was performed. (a) I-V characteristics of metals deposited with a 5 μm CTLM spacing (b) Example least squares fit of total resistance versus outer radius to Equation 3.5 for Ni/Au contacts. Extracted specific contact resistances (c) and sheet resistances (d) of metals deposited on SnS. Blue squares correspond to as-deposited contacts, whereas the magenta triangles correspond to contacts that were annealed at 350°C in Ar for 5 min. 124
- Figure 5.32: (a) Plot of outer radius versus total resistance of Ni/Au contacts on SnS after annealing the contacts, showing a deviation from the expected trend of decreasing total resistance with contact spacing. (b) Fit performed to Ni/Au contact data after annealing without small spacing included. (c) Current-voltage characteristics of Ti/Au contacts after

annealing. (d) Inconsistent electrical behavior after annealing Ti/Au contacts. The SnS film in (a-d) was deposited at the same conditions as in Figure 5.31. 126

Figure 5.33: Comparison of specific contact resistances and sheet resistances determined in this study to those in Gurunathan, *et. al.* and Yang, *et. al.*⁵¹ 128

Figure 5.34: (a) Topology of an SnS film obtained with AFM. The SnS film was deposited onto a soda lime glass substrate at $T_{\text{sub}} = 300^{\circ}\text{C}$ and post annealed at 300°C for 1 hr. RMS roughness = 12 nm. (b) Plan view secondary electron SEM image of an as-deposited Ni/Au contact on an SnS film on borosilicate glass showing conformation of the contact to the morphology of the SnS film. 129

Figure 6.1: (a) Five-fold twinned structure of Ag NW illustrating the location of $\{100\}$ and $\{111\}$ planes. (b) Depiction of NW growth mechanism involving PVP adsorption to $\{100\}$ planes and diffusion of Ag atoms towards $\{111\}$ planes. After Ref [11]. 139

Figure 6.2: (a) TEM image of Ag NWs (purchased from Blue Nano, Inc.) drop cast onto a copper grid (SPI supplies) obtained with a JEM 2000EX II microscope. The average NW diameter in suspension was 90 nm. (b) Selected area electron diffraction (SAED) pattern of a 90 nm NW along the $[111]$ zone axis showing crystalline material. 140

Figure 6.3: Plots of sheet resistance versus transmittance for Ag NW and Ag NW-polymer films. (a) Data collected by the author. (b) More complete dataset from paper by Narayanan, Hajzus, *et al.*¹⁶ Reproduced with permission from ECS Journal of Solid State Science and Technology, 3 (11) P363-P369 (2014). Copyright 2014, The Electrochemical Society. 147

Figure 6.4: SEM micrographs of (a) pristine Ag NW, (b) Ag NW-PEDOT:PSS, and (c) Ag NW-PSS films. 151

Figure 6.5: Plots of sheet conductance vs nanowire areal fraction for Ag NW and Ag NW-polymer films. (a) Data collected by the author. (b) More complete set of data from the author's co-authored publication.¹⁶ Reproduced with permission from ECS Journal of Solid State Science and Technology, 3 (11) P363-P369 (2014). Copyright 2014, The Electrochemical Society. 153

Figure 6.6: (a) Binarized SEM image of pristine Ag NW film. (b) Pristine Ag NW film after performing image dilation of $r = 15$ pixels. (c) Areal fraction of Ag NW-based films as a function of disc radii. (d) Variation of fit parameters as a function of initial areal fractions. (a-c) Are from Narayanan *et. al.*¹⁶ Reproduced with permission from ECS Journal of Solid State Science and Technology, 3 (11) P363-P369 (2014). Copyright 2014, The Electrochemical Society. 155

Figure 6.7: (a) Schematic of samples fabricated to measure electrical properties of the Ag NW/n-Si interface. (b) Similar structure fabricated with circular Ag thin film contacts evaporated through a shadow mask. 156

Figure 6.8: Current-voltage characteristics for Ag thin films on n-Si after annealing sequence for (a) $814\text{ }\mu\text{m}$ -diameter circular contact and (b) $2580\text{ }\mu\text{m}$ -diameter circular contact. Specific

contact resistances were estimated from a plot of inverse contact diameter versus contact resistance (c). 158

Figure 6.9: SEM micrographs of thin Ag film after annealing at (a) 600°C for 60 s in N₂ and (b) 900°C for 5 min in N₂. Colored circles show locations where EDX was performed. Oxygen is present. 159

Figure 6.10: Current-voltage characteristics measured as indicated in Fig. 6.7 a for 90 nm-diameter Ag NW films on n-Si after annealing sequence. 161

Figure 6.11: SEM micrographs of 90 nm-diameter Ag NW films after annealing at the indicated temperatures for the specified times. Circled areas show separation of NWs at the junctions after heat treatment. 162

Figure 6.12: Current-voltage characteristics of 35 nm-diameter NWs after annealing at indicated temperatures. (a, c, e, g) Vertical measurement. (b, d, f, h) Lateral measurement of Ag NW film. 165

Figure 6.13: SEM micrographs of 35 nm-diameter Ag NW films on n-Si after annealing at various temperatures for 5 s in an RTA. 166

Figure 6.14: SEM micrographs of 35 nm-diameter Ag NW films on glass substrates after annealing for 20 min at the specified temperatures in low vacuum. Changes in sheet resistance, ΔR_s , are indicated. 167

Figure 6.15: Sheet resistance versus transmittance for pristine Ag NW films with 90 nm-diameters and 35 nm diameters. Films were annealed at 180°C. 168

Chapter 1: Introduction

Interest in two-dimensional (2D) materials has increased dramatically since the isolation of graphene by Novoselov, *et al.*¹ in 2004. As new crystals are investigated, the diversity of properties in the family of 2D materials has expanded. For example, tin(II) sulfide (SnS) is a layered semiconductor with an orthorhombic structure leading to intralayer anisotropy in its optical, electronic, mechanical and thermal properties. Monolayers of SnS are proposed to possess high piezoelectric coefficients² and thermoelectric figures of merit,^{3, 4} ferroelectricity,^{5, 6} ferroelasticity,^{5, 7} and valley pairs selectable by linearly polarized light.^{6, 8} SnS is of interest for opto-electronic, thermoelectric, and piezoelectric applications. SnS shows promise as a low-toxic, earth-abundant, low-cost, thin film solar cell material due to its favorable band gap and an absorption coefficient greater than 10^5 cm^{-1} in the visible range. An additional practical advantage for this application is that SnS doesn't contain toxic or scarce elements such as Cd, In or Te.

In order to realize devices based on SnS, one must be able to fabricate ohmic and rectifying (Schottky) metal contacts to this material. Low resistance ohmic contacts are essential to enable current flow into and out of a device (e.g., solar cell) without limiting its performance and to facilitate measurement of certain intrinsic properties, such as charge carrier mobility.^{9, 10} Schottky contacts, in contrast, are employed in a subset of devices to turn current flow on or off by an applied voltage and therefore rely on the presence of an energy barrier to charge carriers (a.k.a., Schottky barrier) at the metal-semiconductor interface.

The first portion of this thesis presents an investigation of ohmic and Schottky contacts to solution-synthesized SnS nanoribbons. The electrical behavior of four different metal contacts to

individual SnS nanoribbons is investigated with the intent of determining the extent to which the electrical behavior and properties (i.e., Schottky barrier height or contact resistance) are determined by the choice of metal. As such, metals with a range of work functions were selected: Ti ($\phi_M = 4.33$ eV), Cr ($\phi_M = 4.50$ eV), Ni ($\phi_M = 5.15$ eV), and Pd ($\phi_M = 5.22$ eV). Contact resistances and Schottky barrier heights were calculated and a model for the energy band alignments between the metals and SnS is proposed.

The second portion of this thesis concerns the characterization of SnS thin films deposited by electron-beam evaporation and an investigation of various ohmic metal contacts to this material. The effects of deposition and processing conditions on the SnS phase composition, morphology, and electrical properties are discussed based on the results from several characterization techniques. Conditions are reported for which only α -SnS was detected, and when a mixture of π -SnS and α -SnS phases was observed. Metals with a range of work functions (Ti/Au, Ru/Au, Ni/Au, and Au) were investigated and found to form ohmic contacts to α -SnS thin films. A correlation between the specific contact resistance and the metal workfunction is reported, as is the effect of annealing (at 350°C in Ar), which was found to be specific to each metal. The results suggest alternative metallization to Mo, which has been the standard ohmic contact in SnS thin-film solar cells.¹¹

The third portion of this thesis concerns the use of silver nanowire (Ag NW) network films for transparent contacts, as a potential low-cost, flexible, alternative to indium tin oxide (ITO). Incorporating a transparent conductive polymer such as poly(ethylene dioxythiophene):poly(styrene sulfonate) (PEDOT:PSS) into the Ag NW network is known to enhance film uniformity; however, PEDOT:PSS reduces the transmittance and results in a lower figure of merit. Poly(styrene sulfonate) (PSS) and poly(vinyl alcohol) (PVA) are non-conductive

but have higher transparency than PEDOT:PSS. In this study we incorporated PSS and PVA into Ag NW networks and compared the film morphology, transmittance, and sheet resistance properties of these composites with those of pristine Ag NW networks and Ag NW/PEDOT:PSS composite networks. Incorporating a non-conductive transparent polymer was found to provide many of the same benefits (improved morphology and lower percolation threshold for conductivity) as incorporating PEDOT:PSS but yielded Ag NW networks with higher transparency. Pristine Ag NWs formed rectifying contacts to Si prior to annealing. Diameter-dependent thermal instability, evidenced by fragmentation at NW junctions, was found to limit the annealing temperature of Ag NWs, and precluded the formation of ohmic contacts.

1.1 References

1. K. S. Novoselov, A. K. Geim, S. V. Morozov, D. Jiang, Y. Zhang, S. V. Dubonos, I. V. Grigorieva and A. A. Firsov, *Science*, 2004, **306**, 666-669.
2. R. Fei, W. Li, J. Li and L. Yang, *Appl. Phys. Lett.*, 2015, **107**, 173104.
3. L. M. Sandonas, D. Teich, R. Gutierrez, T. Lorenz, A. Pecchia, G. Seifert and G. Cuniberti, *J. Phys. Chem. C*, 2016, **120**, 18841-18849.
4. S. D. Guo and Y. H. Wang, *Journal of Applied Physics*, 2017, **121**, 034302.
5. M. H. Wu and X. C. Zeng, *Nano Lett.*, 2016, **16**, 3236-3241.
6. P. Z. Hanakata, A. Carvalho, D. K. Campbell and H. S. Park, *Physical Review B*, 2016, **94**, 035304.
7. H. Wang and X. F. Qian, *2d Materials*, 2017, **4**, 015042.
8. A. S. Rodin, L. C. Gomes, A. Carvalho and A. H. C. Neto, *Physical Review B*, 2016, **93**, 045431.
9. S. Das, H. Y. Chen, A. V. Penumatcha and J. Appenzeller, *Nano Lett.*, 2013, **13**, 100-105.
10. B. Radisavljevic, A. Radenovic, J. Brivio, V. Giacometti and A. Kis, *Nat. Nanotechnol.*, 2011, **6**, 147-150.
11. J. A. Andrade-Arvizu, M. Courel-Piedrahita and O. Vigil-Galan, *J. Mater. Sci.: Mater. Electron.*, 2015, **26**, 4541-4556.

Chapter 2: Background

2.1 Metal/Semiconductor Interfaces and Contact Resistance

2.1.1 The Schottky-Mott Model

Many models have been developed to describe the behavior of metal-semiconductor interfaces. The most simple of these is the Schottky-Mott model. According to this model, when two materials are brought into contact, their Fermi levels, or electron chemical potentials, align. In a non-degenerate semiconductor, the Fermi level lies within the band gap at the energy in which the probability of occupancy by electrons is 50%, in accordance with Fermi-Dirac statistics.

When a metal and n-type semiconductor with a work function less than the metal are brought into electrical contact (Figure 2.1 a), electrons flow from the semiconductor to the metal until the Fermi levels are aligned. This charge transfer results in a depletion region in the semiconductor containing positive charge from ionized donors. The positive charge in the semiconductor depletion region is balanced by a negative charge at the surface of the metal, creating an electric field.¹ Due to differences in work function, which is the amount of energy required to remove an electron from the Fermi level to rest outside of the material (*i.e.* to the vacuum level) and the required continuity of the vacuum level, the semiconductor conduction and valence bands bend within the depletion region.¹

The Schottky-Mott model predicts the energy barrier that is formed at the metal-semiconductor interface. According to the model, the “Schottky” barrier height, ϕ_B , between a metal and an n-type semiconductor is given as

$$\phi_B = \phi_M - \chi_s, \quad (2.1)$$

where ϕ_M is the metal work function, and χ_s is the electron affinity of the semiconductor. The barrier height between a metal and a p-type semiconductor is modified as follows:

$$\phi_B = \chi_s + E_g - \phi_M, \quad (2.2)$$

where E_g is the semiconductor band gap.²

Figure 2.1 shows electron energy band diagrams at metal / (n-type) semiconductor interfaces for two different scenarios. When $\phi_M > \chi_s$ (Figure 2.1 a), a finite Schottky barrier forms. This barrier prevents electron flow from the metal to the semiconductor but allows electron flow from semiconductor to metal once a threshold voltage is reached. This scenario produces a rectifying contact. When $\phi_M < \chi_s$ (Figure 2.1 b), the conduction and valence bands

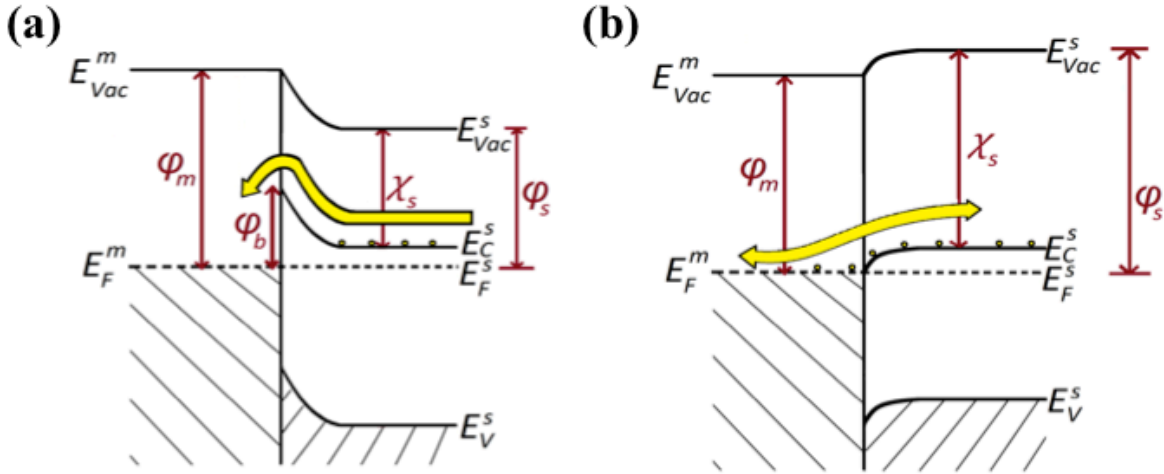


Figure 2.1: Band diagrams illustrating the Schottky-Mott model for a metal/(n-type) semiconductor interface. In (a), the metal work function is greater than the semiconductor work function ($\phi_M > \phi_S$) and a Schottky barrier, ϕ_B forms at the interface. In (b), $\phi_M < \phi_S$, resulting in a negligible Schottky barrier.

bend downward at the interface, resulting in a negligible Schottky barrier and an ohmic contact: i.e., linear and symmetric I - V characteristics for either sign of voltage bias.³

2.1.2 The Bardeen Model and Interface States

Contrary to the Schottky Mott model, many semiconductors, including silicon, exhibit a weak dependence of barrier height on metal work function. To explain this deviation from the Schottky Mott theory, Bardeen introduced the concept of Fermi level pinning due to states within the bandgap. The index of interface behavior:

$$S \equiv \frac{d\phi_B}{d\chi_m} \quad (2.3)$$

quantifies the extent to which the metal work function affects the barrier height and is the slope of barrier height versus metal electronegativity.⁴ $S = 1$ in the Schottky-Mott limit, whereas $S = 0$ in the Bardeen limit.⁵

Electrons in a crystalline material are influenced by a periodic potential arising from the repeating arrangement of atoms in its crystalline lattice, giving rise to its band structure. At a surface, this periodicity is terminated, leading to surface states that differ from the bulk material. If a surface is created outside of an ultra high vacuum chamber, these states can be altered by the adsorption of a layer of contaminants from the environment. Therefore, the properties of metal-semiconductor contacts are sensitive to the surface preparation and cleaning method of the semiconductor. Additionally, the equilibrium position of atoms at the surface may differ than in bulk, leading to surface relaxation or reconstruction.

In Bardeen's model, interface states exist within the bandgap,¹ which can be comprised of surface states, states arising from extended and point defects, and metal induced gap states.^{6,7}

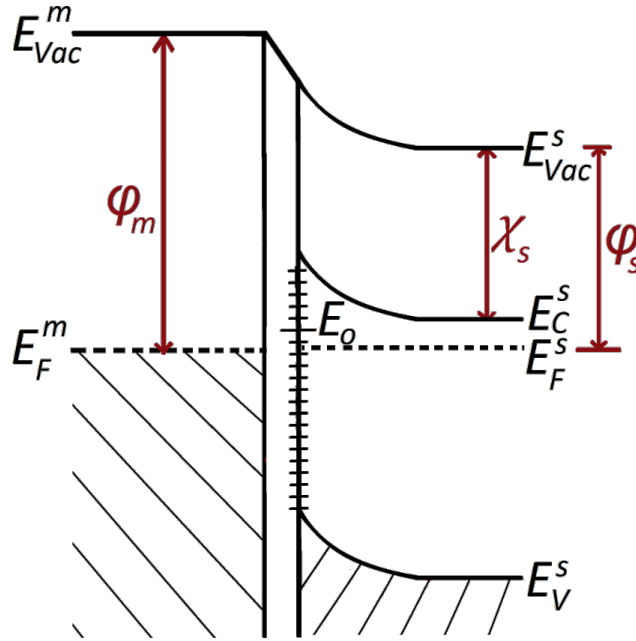


Figure 2.2: Band diagram illustrating a metal / (n-type) semiconductor interface with interface states. The Fermi level is pinned near E_o .

In this model (Figure 2.2), the metal and semiconductor are separated by a thin insulator with a continuous distribution of interface states at the semiconductor/insulator interface. This model assumes that the insulator layer does not impact the surface states of the semiconductor or metal and is thin enough for electron tunneling.

A charge neutrality energy level, E_o , exists such that if the states up to that level are occupied, the semiconductor surface is electrically neutral. There are three sources of charges: Q_m on the surface of the metal, Q_d due to uncompensated donors in the depletion region (assuming an n-type semiconductor), and Q_{ss} , due to surface or interface states. Since there is no electric field in the metal or semiconductor at a distance from the junction, the net charge must equal zero, *i.e.* ¹

$$Q_m + Q_d + Q_{ss} = 0 . \quad (2.4)$$

If the Fermi level is below E_o , the semiconductor surface has a positive charge. This positive charge is balanced by a reduction in Q_d . Q_d is proportional to the product of the donor density and the depletion width. Therefore the depletion width is reduced, which in turn decreases the amount of band bending and the barrier height. E_o shifts closer to the Fermi level, reducing the positive charge contribution from the interface states. If the Fermi level is above E_o , the opposite will occur.

Q_{ss} is proportional to the product of the density of interface states, D_{ss} , and the distance of the Fermi level from E_o . If the density of interface states is high, as it often is for covalent materials such as silicon, the distance between the Fermi level and the neutral level will be small and the Fermi level will be “pinned” near E_o .²

Bardeen considered surface states arising from a semiconductor/vacuum interface, but conditions become different when a semiconductor is in direct contact with a metal. The lattice mismatch of the materials can impact the atomic positions at the interface, reactions can occur, and chemical bonds can form.

2.1.3 Metal Induced Gap States

It has been found experimentally that the deposition of a metal layer, even less than one monolayer in thickness, can pin the Fermi level. A theory to describe this was put forth by Heine.⁸ By considering the continuity of the wavefunctions at the metal - semiconductor interface, he hypothesized that Bloch wave functions from the metal decay exponentially into the band gap of the semiconductor, resulting in metal-induced gap states (MIGS). MIGS have an effective neutral energy level near the middle of the gap, similar to the surface states in Bardeen’s model. The amount of Fermi level pinning due to MIGS was found to be a function

of the dielectric constant of the transition region, the width of the interfacial region, and the MIGS density of states at the neutrality level.⁹

2.1.4 Image Force Lowering

An electron at a distance x from a metal will induce a positive charge on the metal's surface. The attractive force between the electron and the induced charge is equal to the Coulomb force that would exist between the electron and an equal positive charge at $-x$ (*i.e.* an image charge). The total potential energy of the electron is equal to the sum of the potential energy due to the image charge (which is negative relative to an electron at infinity) and the potential energy due to the Schottky barrier. As a result, the barrier height is reduced by

$$\Delta\phi = \sqrt{\frac{q\mathcal{E}_{max}}{4\pi\epsilon_s}} = \left[\frac{q^3 N |\psi_s|}{8\pi^2 \epsilon_s^3}\right]^{1/4}, \quad (2.5)$$

where \mathcal{E}_{max} is the maximum electric field in the depletion region (at the interface), N is the donor density, ϵ_s is the permittivity in the semiconductor, and ψ_s is the surface potential. For n-type substrates,

$$\psi_s = \phi_{b0} - \phi_s + V_R \quad (2.6)$$

where V_R is the reverse bias and ϕ_{b0} is the barrier height neglecting image force lowering. As apparent from Equations 2.5 and 2.6, $\Delta\phi$ increases with increasing doping concentration and reverse bias. Therefore, reverse-bias currents in metal-semiconductor Schottky diodes are voltage-dependent.² At low applied voltages and low-to-moderate doping concentrations, $\Delta\phi$ is generally very small (\sim few mV) and can often be neglected.

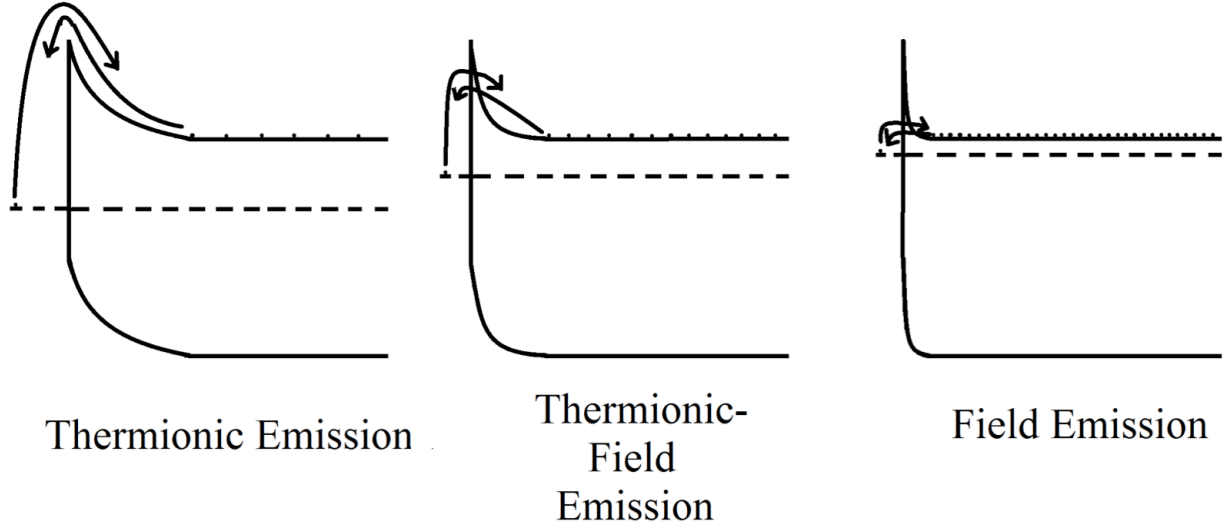


Figure 2.3: Band diagrams of an n-type semiconductor showing current transport mechanisms. The doping concentration increases from left to right and the transport of electrons is indicated by the arrows. The dotted line indicates the Fermi level position. After Ref [3].

2.1.6 Current Transport Mechanisms

Current transport mechanisms for a metal-semiconductor contact are illustrated in Figure 2.2. The doping density is inversely related to the depletion width ($W_D \propto N_D^{-1/2}$).² For high doping concentrations, the barrier is sufficiently narrow for electrons to tunnel through it, resulting in transport by field emission. If no tunneling occurs, the electrons must be excited by thermal energy over the barrier resulting in thermionic emission.

To determine which type of emission occurs, a characteristic energy, defined as

$$E_{00} = \frac{qh}{4\pi} \sqrt{\frac{N}{\epsilon_s \epsilon_0 m_{tun}^*}} \quad (2.7)$$

can be calculated.³ For $kT \gg E_{00}$, thermionic emission dominates, for $kT \ll E_{00}$, field emission dominates, and if $kT \approx E_{00}$, thermionic-field emission occurs.³ For silicon, thermionic emission

tends to occur at doping concentrations of $N \leq 3 \times 10^{17} \text{ cm}^{-3}$, whereas thermionic field emission and field emission tend to occur at $3 \times 10^{17} \text{ cm}^{-3} < N < 2 \times 10^{20} \text{ cm}^{-3}$ and $N \geq 2 \times 10^{20} \text{ cm}^{-3}$, respectively.³ In the case of thermionic emission, current density is dependent upon barrier height and temperature and is independent of doping density, but for field emission, it is dependent upon doping density.^{1,2}

2.1.7 Specific Contact Resistance

Definition

A property called the specific interfacial resistivity describes the metal-semiconductor interface quantitatively. It is given by:

$$\rho_i = \left. \frac{\partial V}{\partial J} \right|_{V=0, A \rightarrow 0} \quad (2.8)$$

and has units of $\Omega\text{-cm}^2$.³ V , J , and A are voltage, current density, and area, respectively. In practice, the specific interfacial resistivity cannot be measured because a real contact includes a part of the metal and semiconductor next to the junction, current crowding at the entrance to the contact, spreading resistance, and any oxide or other interfacial layers.^{3,10} There may also be diffusion of one material into the other, resulting in an unknown contact area. Defects, dislocations, and surface damage may result in non-ideal measurements as well.³ For this reason, a second quantity, the specific contact resistivity ρ_c , is defined. This is an experimental quantity with units of $\Omega\text{-cm}^2$, and it includes the interface as well as the regions immediately above and below it.³

Measurement

Various structures have been developed to measure specific contact resistivity, each with their own merits and limitations. One of the earliest structures, developed by Cox and Strack, consists of circular metal contacts of varying diameters on the front of the substrate and a large back contact. While this structure is applicable to measuring the specific contact resistance of devices with vertical structures, it is not very accurate when measuring small ρ_c .¹¹ Spreading resistance can lead to large errors, but can be reduced by using small area contacts.³

A lateral structure can be used to avoid the requirement of a back contact. To account for current crowding at edges of lateral contacts, Murrmann and Widmann developed the transmission line model (discussed further in Section 4.3.3). In this model, a transfer length (Figure 2.4 a) is defined as:

$$L_T = \sqrt{\rho_c / R_{sh}} . \quad (2.9)$$

For long contacts, L_T is the distance under the metal electrode that $1/e$ of the current will travel before entering the metal.³

The transfer length method (TLM) is a measurement technique involving many contacts of the same length, L , separated by varying semiconductor channel spacings, d . A linear TLM structure is depicted in Figure 2.4 b. In this method, the total resistance, R_T , between adjacent contacts is measured and is plotted as a function of d (Figure 2.4 c). The total resistance between adjacent contacts in a linear TLM structure with $L \geq 3L_T$ is given by

$$R_T = \frac{R_{sh}}{Z} (d + 2L_T) , \quad (2.10)$$

where R_{sh} is the semiconductor sheet resistance.

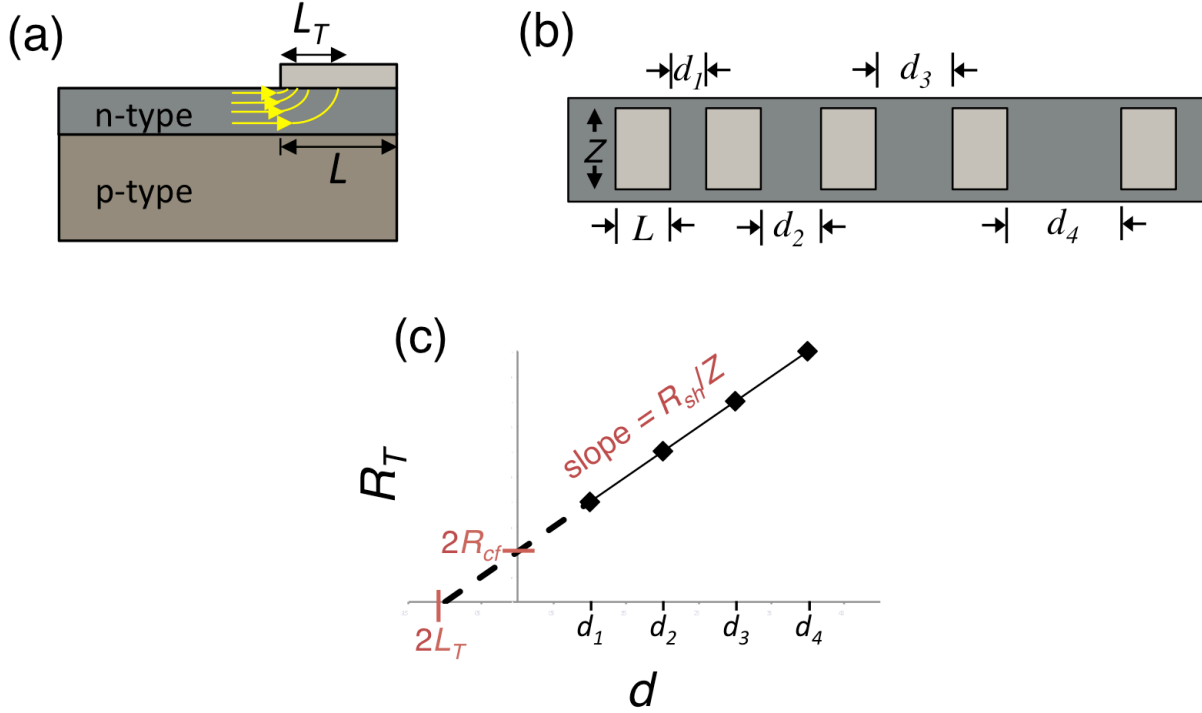


Figure 2.4: Depiction of transfer length and TLM structure. (a) Illustration (not to scale) of transfer length with current crowding represented by yellow arrows. (b) Illustration of TLM structure. (c) Plot used to extract contact resistance and related parameters from TLM structures.

For long contacts (*i.e.* $L \geq 3L_T$), the contact resistance at the front of the contact, R_{cf} , can be approximated as

$$R_{cf} \approx \frac{\rho_c}{L_T Z}. \quad (2.11)$$

The x -intercept of the plot in Figure 2.4 c is equal to $2R_{cf}$, R_{sh} can be determined from the slope, and the transfer length is determined by extrapolating the x -intercept. Equation 2.9 can then be used to solve for ρ_c .³

Lateral structures are designed with doped channels underneath and between the contacts to confine current flow. Error can occur if the width of the contact is less than the width of isolated channel. Circular transfer length method (CTLTM) structures can be made to avoid the

requirement of channel isolation. In these structures, current cannot flow around the contact because the semiconductor channel is enclosed by the metal. They do not require a mesa structure etched into the semiconductor.³

The linear TLM method can be integrated into a CTLM pattern by using circles of different radii to form varying semiconductor channel lengths.³ Equation 2.10 is modified to take into account the circular geometry of the test structure. Further details on CTLM measurements are discussed in Section 3.3.2.

2.2 References

1. E. H. Rhoderik and R. H. Williams, *Metal-Semiconductor Contacts*, Oxford University Press, New York City, 2nd edn., 1988.
2. S. M. Sze and K. K. Ng, in *Physics of Semiconductor Devices*, J. Wiley & Sons, Hoboken, NJ, 3rd edn., 2007, ch. 3, pp. 134-196.
3. D. K. Schroder, J. Wiley & Sons, Hoboken, NJ, 3rd edn., 2006, ch. 3, pp. 127-184.
4. S. Kurtin, T. C. McGill and C. A. Mead, *Phys. Rev. Lett.*, 1969, **22**, 1433-1436.
5. L. M. Porter and R. F. Davis, *Materials Science and Engineering B-Solid State Materials for Advanced Technology*, 1995, **34**, 83-105.
6. D. K. Schroder and D. L. Meier, *IEEE Trans. Electron Devices*, 1984, **31**, 637-647.
7. H. Lüth, *Solid Surfaces, Interfaces and Thin Films*, Springer- Verlag Berlin Heidelberg, New York City, 5th edn., 2010.
8. V. Heine, *Physical Review*, 1965, **138**, 1689-1696.
9. W. Monch, *Electronic Structure of Metal-Semiconductor Contacts*, Kluwer Academic Publishers, Boston, 1990.
10. S. S. Cohen, *Thin Solid Films*, 1983, **104**, 361-379.
11. J. Crofton, L. M. Porter and J. R. Williams, *Physica Status Solidi B-Basic Research*, 1997, **202**, 581-603.

Chapter 3: Experimental Methods

3.1 Thin Film Deposition

3.1.1 Electron Beam Evaporation

Electron beam (e-beam) evaporation is used throughout this study to deposit thin metal or semiconductor films. E-beam evaporation is a form of physical vapor deposition that is conducted in a high (or ultra-high) vacuum chamber.

The electron beam is focused, by use of electromagnets, onto a pure source material that is contained in a water-cooled crucible. The electron beam heats the source material, raising its vapor pressure such that it exceeds the pressure of the surrounding chamber, resulting in evaporation (or sublimation). A substrate is placed upside down above the source, and the vapor is deposited within line of site onto the substrate. The source material, typically in the form of pellets or sometimes powders, is often held in a crucible liner made from a compatible material, which allows for more even heat distribution.

Electron beam evaporation in this work was performed inside of an ultra high vacuum (UHV) chamber with load lock located in Prof. Porter's lab. The system is comprised of a 3kW Thermionics e-gun with 5 crucible positions. A base pressure of 10^{-9} – high 10^{-10} Torr was attained in the chamber through the use of a turbomolecular pump and a cryogenic pump. Film thickness and deposition rate were monitored with a quartz crystal microbalance (QCM).

3.1.2 Polymer and Nanomaterial Deposition

Polymers and nanomaterial dispersions can be deposited by inexpensive methods such as spin coating, drop casting, inkjet printing, and roll-to-roll processing. In this work, spin- and

drop casting were used. During spin casting, the substrate is placed on a chuck and held in place by a vacuum. A small amount of polymer or nanomaterial is pipetted onto the substrate, and the chuck is spun at high speeds, resulting in films that can be less than 100 nm thick.

Thickness is controlled by the spin speed and number of coats, and depends upon the viscosity of the polymer, its molecular weight, solvent and concentration. Spin recipes may include a short, low speed step to spread the polymer across the substrate, followed by the main spin speed during which the thickness of the film is controlled and solvents are evaporated, and then a quick, high-speed step to remove residual solution from the corners of the substrate. Samples are subsequently heated in an oven or hot plate to evaporate remaining solvent in the film. In this work, thickness versus spin speed was calibrated by measuring film thickness with a Filmetrics spectroscopic reflectometer.

The areal density of nanomaterials on substrates was controlled by the nanomaterial dispersion concentration as well as spin speed and number of coats. For denser nanomaterial coverage, drop casting was used, in which a drop of nanomaterial suspension was placed on the substrate and solvents were evaporated.

3.2 Heat Treatment

3.2.1 Rapid Thermal Annealing (RTA)

An AG Associates (now Allwin21 Corp.) MiniPulse rapid thermal annealer was used to anneal Ag nanowires (NWs) on silicon. The RTA consists a quartz chamber surrounded on top and bottom by an array of tungsten halogen lamps inside of a water- and air-cooled chamber. The sample is set on a silicon wafer on a quartz tray that is inserted into the sealed quartz chamber and a gas such as N₂ or Ar is introduced into the chamber. The sample is heated at very

high ramp rates through radiative heating by the tungsten halogen lamps. The temperature is monitored by a thermocouple attached to the silicon wafer on the tray. The RTA allows for heating recipes with ramp and holding times of less than a minute.

3.2.2 Tube Furnace Annealing

Thermocraft Inc. and Lindburg resistive tube furnaces were used to anneal contacts and semiconductor samples. Samples were loaded into a quartz tube on a quartz boat, and N₂ or Ar, or forming gas was introduced into the tube, with flow rate controlled by a flow meter. The tube was purged with inert gas prior to heating.

3.3 Electrical Characterization

3.3.1 Van der Pauw Sheet Resistance and Hall Measurements

Sheet resistance measurements of Ag NW, polymer and composite films were performed by the four-point probe van der Pauw method using a Singatone probe station connected to an Agilent HP 4155C semiconductor parameter analyzer. Four Ag paste contacts were applied to the corners of the films (Figure 3.1) to ensure contact between the probe and NW network and/or polymer. Samples were heated at 100°C for 1 hour to evaporate solvents from the Ag paste.

Additionally, van der Pauw Hall and sheet resistance measurements were performed on SnS thin films with an MMR Technologies Hall Measurement System. The measurements were facilitated by MMR Technologies Hall software.

First, a van der Pauw resistivity measurement was performed with no magnetic field applied to the sample. Current was applied between two adjacent contacts and voltage measured between the opposite two contacts. This process was repeated for all contacts pairs and for opposite polarity. A resistance was calculated for the each contact configuration. The ratio of

resistance for different configurations was used to calculate a form factor, F , to account for arbitrarily shaped samples. The resistivity was then calculated from the equation:

$$\rho = \frac{\pi d F (R_{12,34} + R_{23,41})}{2 \ln (2)} \quad (3.1)$$

where d is the thickness of the sample, and $R_{12,34}$ refers to the resistance measured with current applied between probes 1 and 2 and voltage measured between probes 3 and 4, indicated in Figure 3.1.

Subsequently, a magnetic field of ~ 3500 G was applied perpendicular to the plane of the sample. Resistance was then calculated by applying current diagonally between contacts 1 and 3 and measuring voltage between contacts 2 and 4, which is normal to the applied current and applied magnetic field. This measurement was repeated for the opposite contact configuration. Next, the direction of the magnetic field was reversed and the measurements were repeated. The mobility in $\text{cm}^2/\text{V-s}$ was calculated from

$$\mu = \frac{10^8 (\Delta R_{13,24} + \Delta R_{24,13}) d}{2 \rho \Delta B} \quad (3.2)$$

where $\Delta R_{13,24}$ is the change in resistance measured under positive and negative magnetic field directions, and ΔB is the change in magnetic field. A negative mobility value indicates that the majority carriers are electrons; a positive value indicates that holes are the majority carriers. The carrier density in cm^{-3} was calculated from

$$\eta = \frac{6.24 \times 10^{18}}{\rho \mu} \quad (3.3)$$

where 6.24×10^{18} is the number of elementary charges in 1 Coulomb. The Hall coefficient (in cm^3/C) was calculated from Equation 3.4.¹

$$R_{Hall} = \rho \mu \quad (3.4)$$

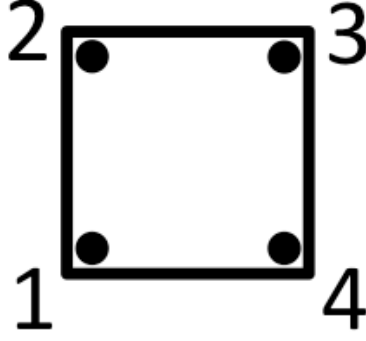


Figure 3.1: Schematic of contact configuration for van der Pauw Hall measurements.

3.3.2 CTLM Pattern Fabrication and Measurements

Various structures for measuring contact resistance were discussed in Chapter 2. This section will provide detail on the circular transfer length (CTLM) method, which was used in this study to calculate the specific contact resistivity for ohmic contacts on SnS e-beam deposited films. The CTLM pattern, which contains a pattern of rings with various spacings, is illustrated in Figure 3.2. A photolithography process, depicted in Figure 3.3, was used to create the CTLM patterns. A Karl Süss MJB3 contact aligner was used.

The total resistances between contacts of each ring were measured. The measurements consisted of a current-voltage sweep from -1 V to 1 V applied between two probes: one on the inner metal circle and the other on the metal outside of the semiconducting channel. The resistance, R_T , for each channel length was calculated and plotted versus outer contact radius, r_l . A non-linear least squares fit to the data was then performed in MATLAB to the equation²

$$R_T = \frac{R_{sh}}{2\pi} \left[\ln \left(\frac{r_1}{r_o} \right) + \frac{L_T}{r_o} \frac{I_o(r_o/L_T)}{I_1(r_o/L_T)} + \frac{L_T}{r_1} \frac{K_o(r_1/L_T)}{K_1(r_1/L_T)} \right] \quad (3.5)$$

where R_{sh} , and L_T , are the semiconductor sheet resistance and transfer length, respectively. I_o , I_l , K_o , and K_l are the modified Bessel Functions. r_o and r_l are defined in Figure 3.2 (b), such that $r_l - r_o = s$, where s is the semiconductor channel spacing. An initial guess of the R_{sh} value was taken from the Hall measurement. After R_{sh} and L_T were determined, specific contact resistance was calculated from Equation 2.9.

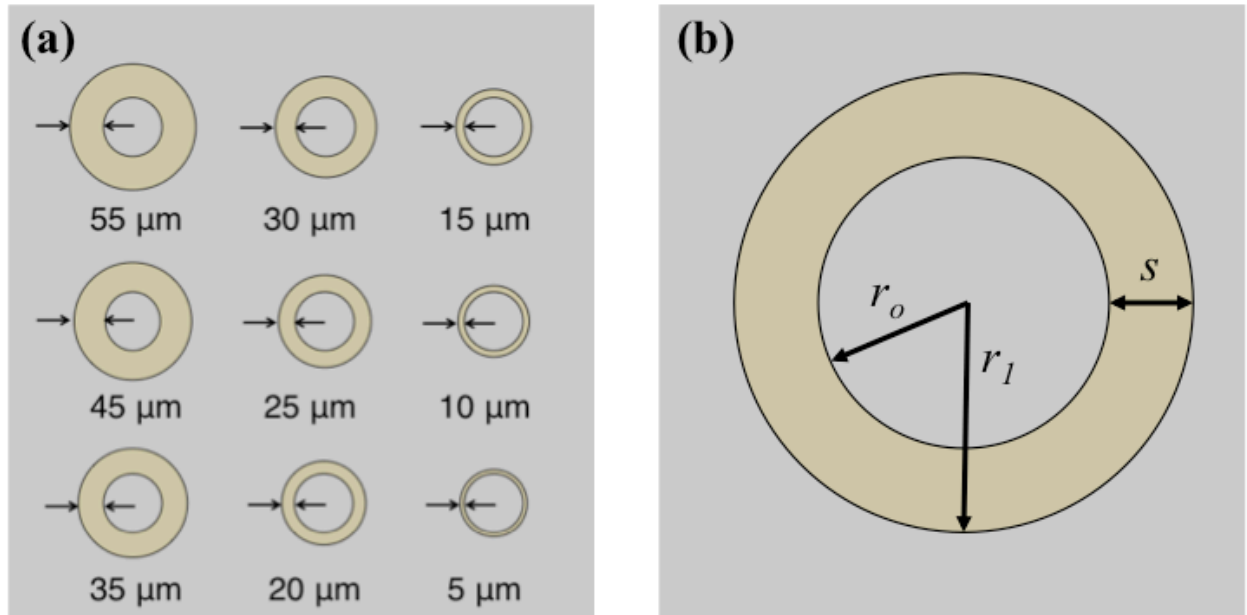


Figure 3.2: (a) Schematic of circular transfer length method (CTLTM). The grey area represents the metal and the brown area represents the semiconductor. (b) Illustration depicting inner radius, r_o , outer radius, r_l , and spacing, s .

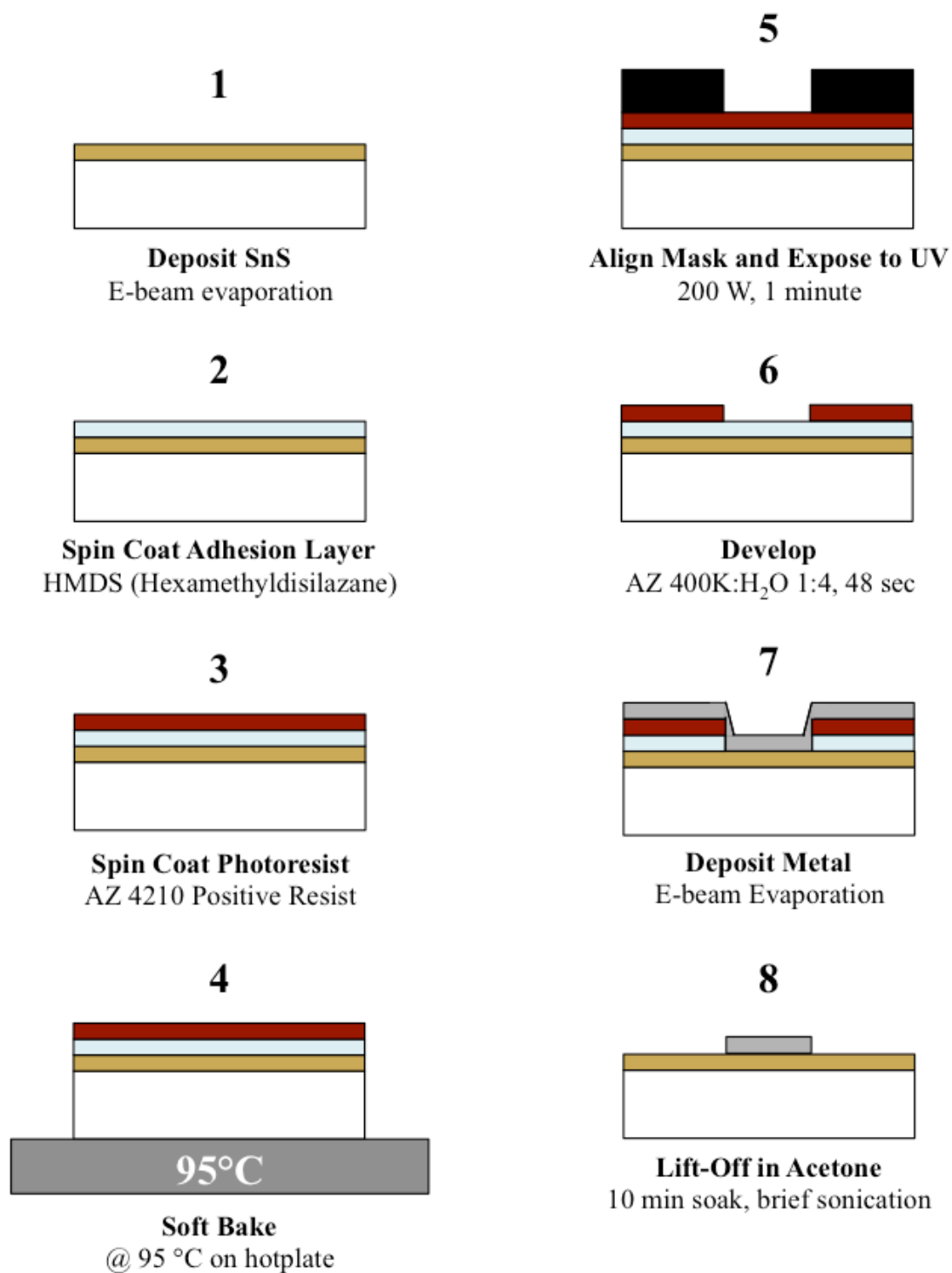


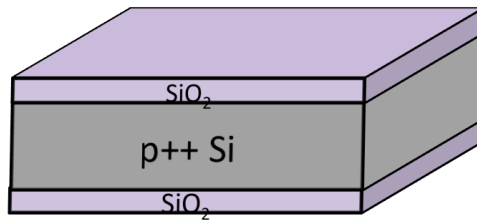
Figure 3.3: Schematic of photolithography process used to fabricate CTLM structures.

3.3.3 Contact Fabrication on SnS Nanoribbons

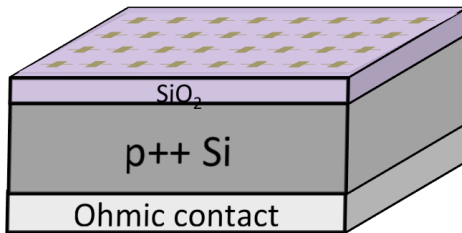
Contact test structures on SnS nanoribbons were fabricated using electron-beam (e-beam) lithography. Figures 3.4 and 3.5 illustrate the process. Further details are provided in Section 4.2.

First, the back oxide of a thermally oxidized Si substrate was removed using buffered oxide etch (BOE), and a Ni/Au ohmic back contact was deposited using e-beam evaporation (Figure 3.4). Fiduciary marks were patterned using a Karl Süss MA6 contact aligner and a mask provided by Son Le from NIST. Ti/Au was e-beam evaporated and liftoff was performed to fabricate the fiduciary marks. SnS nanoribbons dispersed in toluene, which were synthesized by Adam Biacchi at NIST, were spin coated onto the fiduciary substrates. Samples were then annealed to remove organics from the surface of the SnS nanoribbons. Areas containing many individual nanoribbons were identified using an optical microscope. These areas are of interest for contact fabrication.

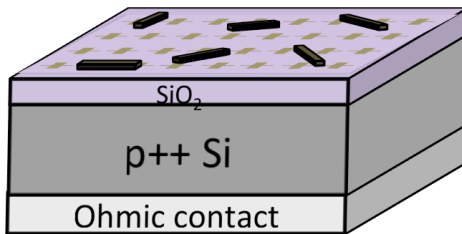
Optical microscope images of the areas of interest were overlaid onto a layout of the fiduciary mask in AutoCAD software. Contact structures were custom designed in AutoCAD based on nanoribbon locations (Figure 3.5). Two layers of e-beam resist were spin coated onto the samples. The first layer (PMMA A4 495) was ~180 nm thick, and the second layer (PMMA A4 950) was ~200 nm thick. The resist was baked at 180 °C for 2 min after each coat. E-beam lithography was performed using a Zeiss NVision 40 FESEM with Raith ELPHY Quantum software. During e-beam lithography, the focused e-beam in the SEM exposed areas of the PMMA resist. The Raith software used the pattern designed in AutoCAD to selectively expose certain regions of the PMMA to the e-beam, and a beam blanker prevented exposure in undesired regions. The samples were then developed with MIBK:IPA 1:3 developer. Immediately prior to contact evaporation, samples were dipped in 1% hydrofluoric acid (HF) then DI water for 30s.



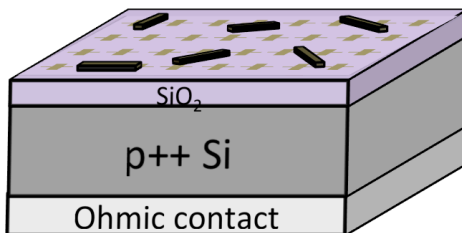
1. Begin with thermally oxidized Si (100 nm SiO_2)



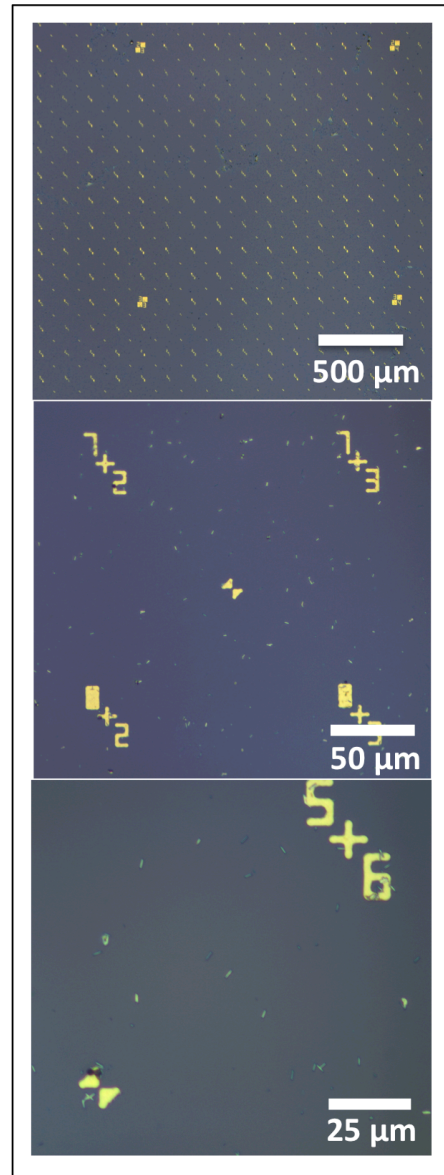
2. Pattern fiduciary marks and deposit ohmic back contact



3. Spin coat SnS nanoribbons onto substrate



4. Anneal at 375°C in forming gas to remove organics



5. Identify areas of interest using optical microscope

Figure 3.4: Deposition of SnS nanoribbons and identification of areas of interest for contact fabrication. Device structure schematics are not to scale.

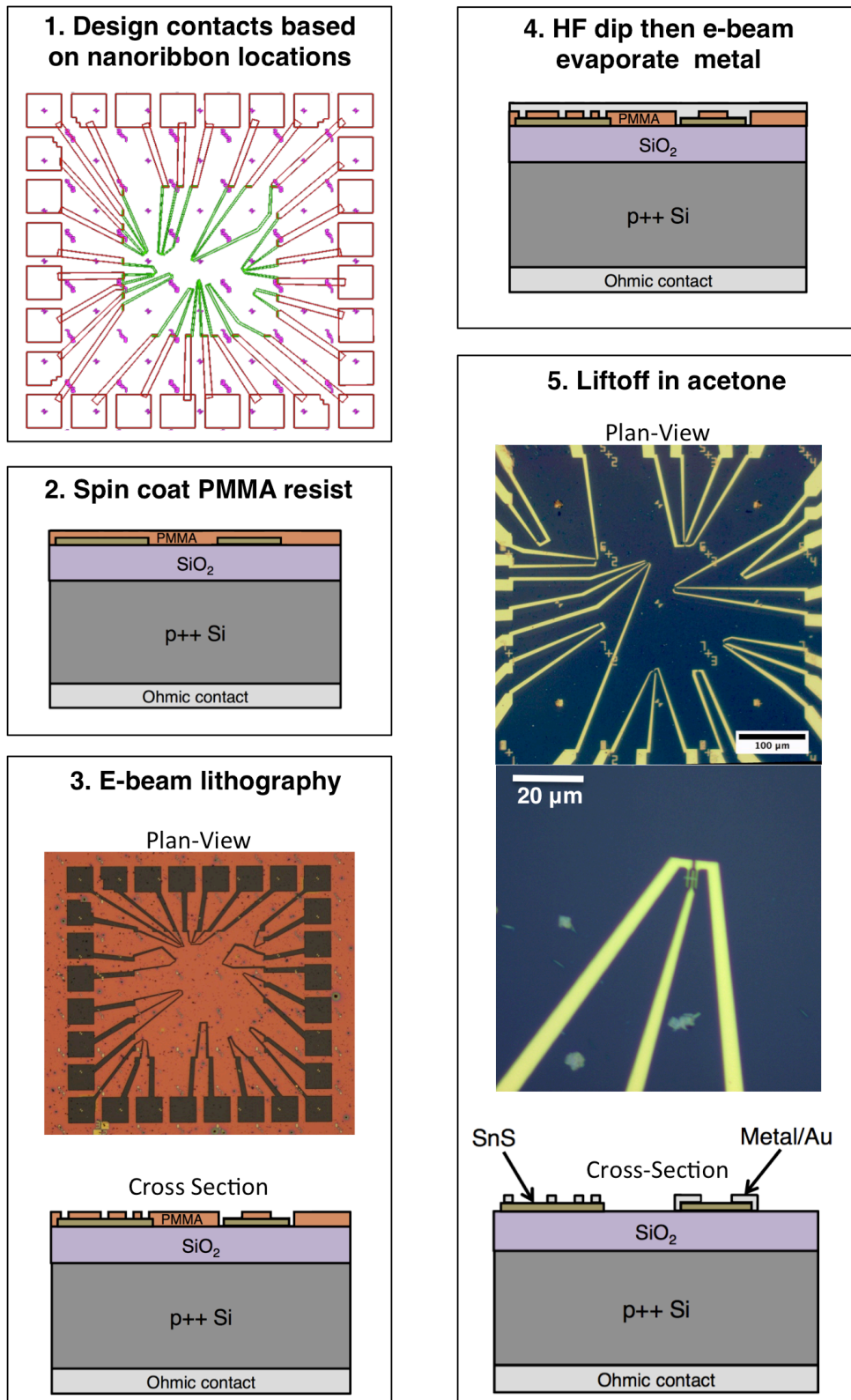


Figure 3.5: Fabrication of contact structures on SnS nanoribbons.

Metal/Au contacts were evaporated using the e-beam evaporation system in Prof. Porter's lab (Section 3.1.1). Liftoff was performed by soaking in acetone. Details on the contact test structures that were used on SnS nanoribbons and their measurements are discussed in Chapter 4.

3.4 Optical Characterization

Reflectance and transmittance spectra were measured using an Optronics OL770 spectrometer with an OL700-71 6 inch diameter integrating sphere attachment. Light was produced from a xenon flash source with wavelength range of 220-788 nm and directed towards the sample in a reflectance or transmittance configuration. The resulting light intensity was collected by a photodetector.

3.5 Scanning Electron Microscopy (SEM)

Scanning electron microscopy is an analysis technique that allows observation of materials on the nanometer and micrometer scale. A scanning electron microscope consists of an electron gun, condenser lenses, scan unit, objective and stigmation lenses, and detector(s). The beam is emitted from a filament, thermionically or through field emission, and focused with the condenser lenses and raster-scanned over a rectangular area of the sample. The interaction of the beam with the sample produces secondary electrons, backscattered electrons, and characteristic x-rays, which are most commonly used for characterization, as well as Auger electrons, Bremsstrahlung x-rays, and cathodoluminescence.³

3.5.1 Secondary Electron Images

Secondary electrons are low energy electrons emitted from the top several Ångstroms of the sample and are detected to provide topological information.³ Phillips XL-30 Field Emission SEM, PHENOM-Pro SEM, and FEI Quanta 600 Field Emission SEMs were used in this study to obtain secondary electron images. Samples were mounted onto a sample holder with conductive carbon tape. In some cases, 2 nm of platinum was sputter coated onto non-conductive samples to reduce charging effects.

3.5.2 Energy Dispersive X-ray Spectroscopy (EDX or EDS)

EDX is an elemental analysis technique involving the detection of the spectrum of characteristic x-rays emitted from the sample. The depth of x-ray generation is on the order of hundreds of nanometers to a few microns and depends upon the accelerating voltage used, the angle of electron beam incidence, and the elemental makeup of the sample (the atomic weight, atomic number, and density). A Phillips XL-30 Field Emission SEM was used for EDX analysis and INCA software was used for quantification of results.³

3.6 Atomic Force Microscopy (AFM)

AFM is a technique used to obtain topographic maps with nanometer resolution. The AFM consists of a cantilever with a tip radius of less than 10 nm that is rastered across a surface with a piezoelectric scanner. A laser is used to detect changes in tip deflection or oscillation amplitude of the cantilever, and a feedback loop works to maintain these at a defined set point, thereby constructing a topographic map. An NT-MDT Solver, NT-MDT NTegra AFM, NT-MDT Spectra AFM/Raman, and a Veeco Dimension 3100 were used in this study.

3.7 Raman Spectroscopy

Raman spectroscopy is a vibrational spectroscopy technique used for applications such as identifying materials, determining bonding types, and investigating strain in films. A monochromatic light source illuminates the sample, producing Rayleigh (elastic) and Raman (inelastic) scattered light. The elastically scattered light is filtered and the Raman light passes through a diffraction grating to a detector. Different materials have unique Raman active vibration modes, allowing materials to be identified by their Raman spectra. An NT-MDT Spectra AFM/Raman instrument was used in this study.

3.8 X-ray Diffraction (XRD)

X-ray diffraction is a technique that provides crystallographic information about a material. In this work, a Rigaku Miniflex 600 XRD with CuK_α ($\lambda = 1.541 \text{ \AA}$) radiation was used. X-rays are generated by accelerating electrons towards a target material, in this case Cu. The high-energy electrons cause electrons in the target material to be excited to higher energy levels, which then return to their original levels, producing x-rays. A filter is used to obtain monochromatic X-rays, which are collimated and directed towards the sample. The sample and x-ray detector are continuously rotated; when Bragg's condition is satisfied, constructive interference occurs and an intensity peak is recorded.⁴

3.9 References

1. MMR Technologies Inc., *Hall and Van der Pauw Measurement System Software Package Version 2.0 User's Manual*, Mountain View, CA, 1995.
2. G. S. Marlow and M. B. Das, *Solid-State Electron.*, 1982, **25**, 91-94.
3. J. Goldstein, D. Newbury, P. Echlin, D. Joy, A. D. Romig, C. Lyman, C. Fiori and E. Lifshin, *Scanning Electron Microscopy and X-ray Microanalysis: A Text for Biologists, Materials Scientists, and Geologists*, Plenum Press, New York, 2 edn., 1992.
4. M. De Graef and M. E. McHenry, *Structure of Materials: An Introduction to Crystallography, Diffraction, and Symmetry*, Cambridge University Press, New York, 2007.

Chapter 4: Schottky Barrier Heights and Specific Contact Resistances on SnS Nanoribbons

The contents of this chapter are adapted from J. R. Hajzus, A. J. Biacchi, S. T. Le, C. A. Richter, A. R. H. Walker and L.M. Porter, “Contacts to solution-synthesized SnS nanoribbons: Dependence of barrier height on metal work function,” *Nanoscale*, vol. 10, issue 1, pp. 319-327 (2018), doi:10.1039/C7NR07403D- Reproduced by permission of The Royal Society of Chemistry. <http://pubs.rsc.org/en/content/articlelanding/2018/nr/c7nr07403d>

4.1 Introduction

4.1.1 Two-Dimensional (2D) Materials

The discussion of two-dimensional (2D) materials often begins with graphene. Graphene, a 2D hexagonal lattice of carbon atoms, was experimentally isolated in 2004 by Novoselov, *et al.*¹ by the mechanical exfoliation of graphite. Single layer graphene is a semimetal with an energy dispersion relation containing conical Dirac points which gives rise to novel electrical behavior. It has interesting properties such as electron mobilities greater than 200,000 cm²/V-s, ability to withstand high current densities, thermal conductivities of 5 x 10³ W/m-K, and strength that is five times greater than steel.² However, graphene lacks a bandgap, making it inapplicable for traditional CMOS technologies.³

The isolation of graphene lead to renewed interest in other layered materials with covalent in-plane bonds and van der Waals forces between layers. These materials can similarly be exfoliated to monolayer thickness with simple scotch tape methods. Shortly after the experimental discovery of graphene, Novoselov, *et al.*⁴ reported isolation and electrical properties of 2D BN, MoS₂, NbSe₂, and Bi₂Sr₂CaCu₂O_x. The 2D crystals could be identified with an optical microscope when placed onto an SiO₂/Si wafer.⁴

The diversity of properties of 2D materials has since vastly expanded with the investigation of new 2D crystals. For example, the 2D transition metal dichalcogenides (TMDs)^{2, 5} (e.g. MoS₂^{4, 6, 7}, WS₂⁸⁻¹⁰, MoSe₂^{11, 12}, WSe₂^{13, 14}) possess properties ranging from semiconducting to metallic, superconducting or ferromagnetic. III-VI layered semiconductors (e.g. GaSe,^{15, 16} InSe^{17, 18}), the topological insulators Bi₂Te₃^{19, 20} and Bi₂Se₃,²¹ and elemental materials such as phosphorene, silicene, germanene, and stanene^{2,22} have also been investigated. Phosphorene, exfoliated from bulk black phosphorous (BP),²³⁻²⁸ is a p-type semiconductor with a thickness-tunable band gap spanning the energy range between graphene and TMDs²⁹ (~ 0.3 eV in bulk BP³⁰⁻³² to ~ 2 eV, direct, in phosphorene monolayers^{24, 29, 33}). It has a higher carrier mobility than MoS₂ and other TMDs with a hole field-effect mobility of 984 cm²/V-s for multilayer²³ and a predicted hole mobility of 10,000 to 26,000 cm²/V-s for a monolayer²⁷. Contrary to the hexagonal crystal structure of graphene and most TMDs, phosphorene has an orthorhombic, puckered honeycomb structure leading to intralayer anisotropy in its effective carrier mass and in its optical, electronic, mechanical and thermal properties.³⁴ Its structure results in unique properties, such as anisotropic thermoelectric behavior, in which the directions of high thermal and electrical conductivity are perpendicular to each other, leading to a high thermoelectric figure of merit in the armchair direction.³⁵ However, phosphorene degrades over the course of hours when exposed to air, causing complete device failure after a week.³⁶ Encapsulation is therefore required.^{36, 37}

A related family of 2D materials is the group-IV monochalcogenides (MX; e.g. M = Sn, Ge; X = S, Se), which are isoelectronic with BP. Similar to BP, their layered structure is buckled and orthorhombic, but with lower symmetry due to two atomic species. Due to a break in inversion symmetry, IV-VI monolayers are calculated to exhibit significant spin-orbit splitting

relevant for spintronics applications³⁸⁻⁴¹ and very large piezoelectricity.^{42, 43} They are predicted to be stable in monolayer form, with micromechanical exfoliation being a viable method for producing single-layered material.⁴⁴ Additionally, they are expected to be more stable in oxygen-containing environments than phosphorene.^{45, 46} Monolayer SnSe, synthesized by colloidal synthesis⁴⁷ or by vapor transport followed by N₂ etching,⁴⁸ has been reported.

4.1.2 Two-Dimensional SnS

The experimental research in this chapter focuses on the semiconductor tin sulfide (SnS), a group IV monochalcogenide. Its thickness-dependent, indirect band gap increases non-monotonically⁴⁹ from 1.1 eV in bulk^{50, 51} to ~ 2 eV in monolayer form.^{39, 44, 49, 51-53} It is natively p-type due to the favorable formation of Sn vacancies, which act as shallow acceptors.⁵⁴ Bulk SnS can form in a few polytypes (discussed further in Chapter 5); however orthorhombic α -SnS (space group *Pnma*, lattice constants $a = 1.1180$ nm, $b = 0.3982$ nm, and $c = 0.4329$ nm⁵⁵) is most stable at standard conditions⁵⁶ and can be thought of as a distorted rocksalt structure (Figure 4.1a-c). Sn(5s) electron lone pairs stereochemically repel each other leading to its buckled, layered structure.⁵⁷ Intralayer bonding is strong and covalent, whereas interactions between layers are weak.

Singh *et al.*⁴⁴ investigated the structural stability of α -SnS monolayers by performing DFT-based calculations. By calculating formation energies of single-layer SnS in various structures and comparing their energies to those in bulk crystals, the authors found that monolayer SnS is most stable in the distorted rocksalt structure. Conversely, Mehboudi *et al.*⁵⁸ calculated that the crystal structure of monolayer SnS, becomes disordered at temperatures as low as room temperature, altering its predicted properties.

Interesting properties of SnS monolayers have been proposed such as a high piezoelectric coefficient,⁴³ high thermoelectric figure of merit (ZT),^{59, 60} ferroelectricity,^{41, 61} ferroelasticity,^{41, 62} and valley pairs selectable by linearly polarized light.^{40, 61} SnS monolayer- and thin film-based van der Waals heterojunctions have been computationally and experimentally investigated,^{44, 63-67} and SnS multilayers have been experimentally demonstrated in transistors^{68, 69} and photodetectors.^{67, 70} While monolayer SnS has yet to be isolated, bilayer SnS has been synthesized by liquid-phase exfoliation^{67, 71}, and multilayers have been synthesized by physical vapor transport,^{69, 72} mechanical exfoliation,⁶⁸ and solution methods.⁷⁰

4.1.3 Contacts to 2D Semiconductors

Metal-semiconductor contacts are essential components of electronic and optoelectronic devices. The contact resistance of ohmic contacts becomes increasingly dominant at reduced channel dimensions. Additionally, highly resistive ohmic contacts can obscure the measurement of intrinsic properties, e.g., carrier mobilities, of emerging 2D materials.^{6, 73} As such, it is important to be able to measure and understand the factors that control the contact resistance.

In principle the contact resistance is at least partly determined by the Schottky barrier height, ϕ_B , at the metal-semiconductor interface. As discussed in Section 2.1.1, Schottky-Mott theory states that for a p-type semiconductor, ϕ_B is equal to the sum of the semiconductor band gap (E_g) and electron affinity (χ) minus the work function of the metal (ϕ_M). However, this model is considered to be an oversimplification and deviations from it are often observed due to interface states and/or other factors.

Early studies on bulk, layered semiconductors suggested that there should be less Fermi level pinning for layered semiconductors because there are no surface states introduced from

dangling bonds or reconstruction of the surface. Lince *et al.*⁷⁴ examined XPS binding energy shifts after *in situ* metal evaporation of Ag, Al, Au, Co, Fe, In, Mn, Pd, Rh, Ti, and V on bulk MoS₂ and found no Fermi level pinning ($S = d\Phi_B/d\Phi_M = 1.28 \pm 0.2$). While the data interpretation in this particular study has been questioned by some,⁷⁵ additional studies on metal/MoS₂ interfaces by McGovern *et al.*⁷⁶ as well as studies on other bulk layered materials such as GaSe,^{77,78,79} WS₂,⁸⁰ SnS₂,⁸⁰ and WSe₂⁸¹ report Schottky-Mott behavior for non-reactive contacts and Fermi-level pinning for reactive contacts.

In contrast, Das *et al.* extracted Schottky barrier heights for Ti, Ni, Pt, and Sc contacts on multilayer MoS₂ and found only a weak dependence of Schottky barrier height on metal work function ($S = 0.1$).⁷³ The Fermi level was pinned near the conduction band.

Different mechanisms for Fermi level pinning of 2D semiconductors have been suggested. McDonnell *et al.*⁸² suggested current transport at metal-MoS₂ interfaces occurs by parallel conduction through defects with effectively low work functions. This phenomenon was used to explain their experimental observations of Fermi level pinning in contacts on bulk MoS₂.⁸² Another report calculated that S vacancies, which have low formation energy relative to Mo vacancies, form energy states near the conduction band in monolayer MoS₂, pinning the Fermi level.⁸³ Bampoulis *et al.* measured Schottky barrier heights using conductive AFM tips with different workfunctions and found that the S parameter was lower in regions of metal-like defects than in defect-free regions of MoS₂.⁸⁴

First principles studies on metal-2D MoS₂ interfaces assume a perfect, defect-free crystal, yet also predict Fermi level pinning. These studies therefore suggest that Fermi level pinning is not solely due to defect states. Gong *et al.*⁸⁵ proposed that Fermi level pinning in MoS₂ is due to a modification of the metal work function and the creation of gap states due to weakened

intralayer bonding between Mo and S. The work function of a metal consists of a volume contribution and a contribution from a dipole layer at the surface. Gong *et al.*⁸⁵ proposed that when MoS₂ is adsorbed onto the surface of a metal, interface dipoles form due to charge redistribution at the metal-semiconductor interface and modify the metal workfunction. The change in the dipole moment is dependent upon the intrinsic metal workfunction and is related to the metal's adsorption strength and distance from MoS₂. In addition to a work function change, an interaction between the metal contact and S atoms weakens the intralayer Mo-S bond, causing the formation of gap states. This Fermi level pinning mechanism differs from that of metal induced gap states (MIGS) because the states introduced are metal-dependent.

It has also been suggested that the Fermi level pinning at metal-2D semiconductor interfaces is independent of choice of metal and is due to MIGS, similar to metal contacts to bulk semiconductors.⁸⁶ If the separation between the metal and 2D semiconductor is large, Fermi level pinning due to MIGS will be reduced. A reduction in Fermi level pinning due to increased separation is also consistent with the mechanism proposed by Gong, *et al.*.

Insertion of an ultrathin insulating layer has been employed to unpin the Fermi level of metal-Ge contacts for CMOS MOSFETS.⁸⁷ The electron wave function of the metal is attenuated in the insulating layer, reducing the density of interface states from MIGS, and the Schottky barrier height may be further reduced by dipole formation at the semiconductor-insulator interface. The thickness of this layer is optimized to unpin the Fermi level while allowing current injection through the tunnel barrier. Similarly, interfacial layers have been employed to reduce contact resistance to 2D materials. For example, interfacial layers (MgO,⁸⁸ TiO₂,^{89, 90}, BN^{91, 92}) between metal and MoS₂ have been shown to reduce contact resistance and Schottky barrier heights.

If a reaction occurs at the metal-semiconductor interface, the work function can change to that of the newly formed material. XPS studies by McDonnell *et al.*⁹³ found that in ultra high vacuum (UHV) deposition conditions ($<3 \times 10^{-9}$ mbar), Ti reacts with MoS₂ to form a titanium sulfide (Ti_xS_y), metallic Mo, and a molybdenum sulfide (Mo_xS_y) at the interface. A different reaction occurred for Ti depositions in high vacuum (HV) conditions ($\sim 1 \times 10^{-6}$ mbar), such that no reaction between Ti and MoS₂ was detected, but the formation of TiO₂ at the interface was evident. XPS studies by Smyth *et al.*⁹⁴ found that Sc is completely oxidized when deposited in HV conditions and a molybdenum oxysulfide forms at the interface. In UHV conditions, Sc reacts to form a sulfide at the MoS₂ interface and a scandium oxide is present at the surface of the metal. HV conditions are typical of many e-beam evaporation chambers. These results suggest that in the study by Das *et al.*,⁷³ TiO₂ and a scandium oxide or a molybdenum oxysulfide were likely present at the interface instead of Ti and Sc.

It is noted that the contact depositions in the present work were performed in a vacuum chamber with base pressure in the 10^{-9} Torr range ($\sim 1.3 \times 10^{-9}$ mbar to 1.3×10^{-8} mbar, i.e. the UHV to very high vacuum range); therefore, based on these studies, significant oxidation of Ti and Cr⁹⁴ during depositions is unlikely to occur. A 40 nm thick Au capping layer was deposited onto the contacts with the intent of reducing oxidation of the contacts upon exposure to air.

The effect of oxygen on surface states of SnS was investigated using first principles calculations by Tritsarlis *et al.*⁹⁵ by replacing S atoms at different SnS surface orientations with O atoms and calculating the density of states. There were no surface states for the pristine SnS(100) surface. However, other surface orientations exhibited states below the conduction band and above the valence band associated with dangling bonds. The substitution of O atoms removed these states in the band gap.

4.1.4 Contribution of This Work

In this work, the electrical behavior of four different metal contacts to individual SnS nanoribbons was investigated to determine the effect of metal workfunction on the electrical behavior of contacts to this material (i.e., the extent to which the Schottky-Mott theory is followed). As such, metals with a range of work functions were selected: Ti ($\phi_M = 4.33$ eV),⁹⁶ Cr ($\phi_M = 4.50$ eV),⁹⁶ Ni ($\phi_M = 5.15$ eV),⁹⁷ and Pd ($\phi_M = 5.22$ eV).⁹⁶ Current-voltage measurements of device structures fabricated using e-beam lithography were used to establish whether the contacts were ohmic or rectifying. Contact resistances and Schottky barrier heights were calculated from the measurements. From the results, a model for band alignments between the metals and SnS is proposed; this model is close to that predicted based on the Schottky-Mott model and reported properties in the published literature. This work provides a reference point for selecting contact metals for devices fabricated on colloidal-synthesized SnS nanocrystals.

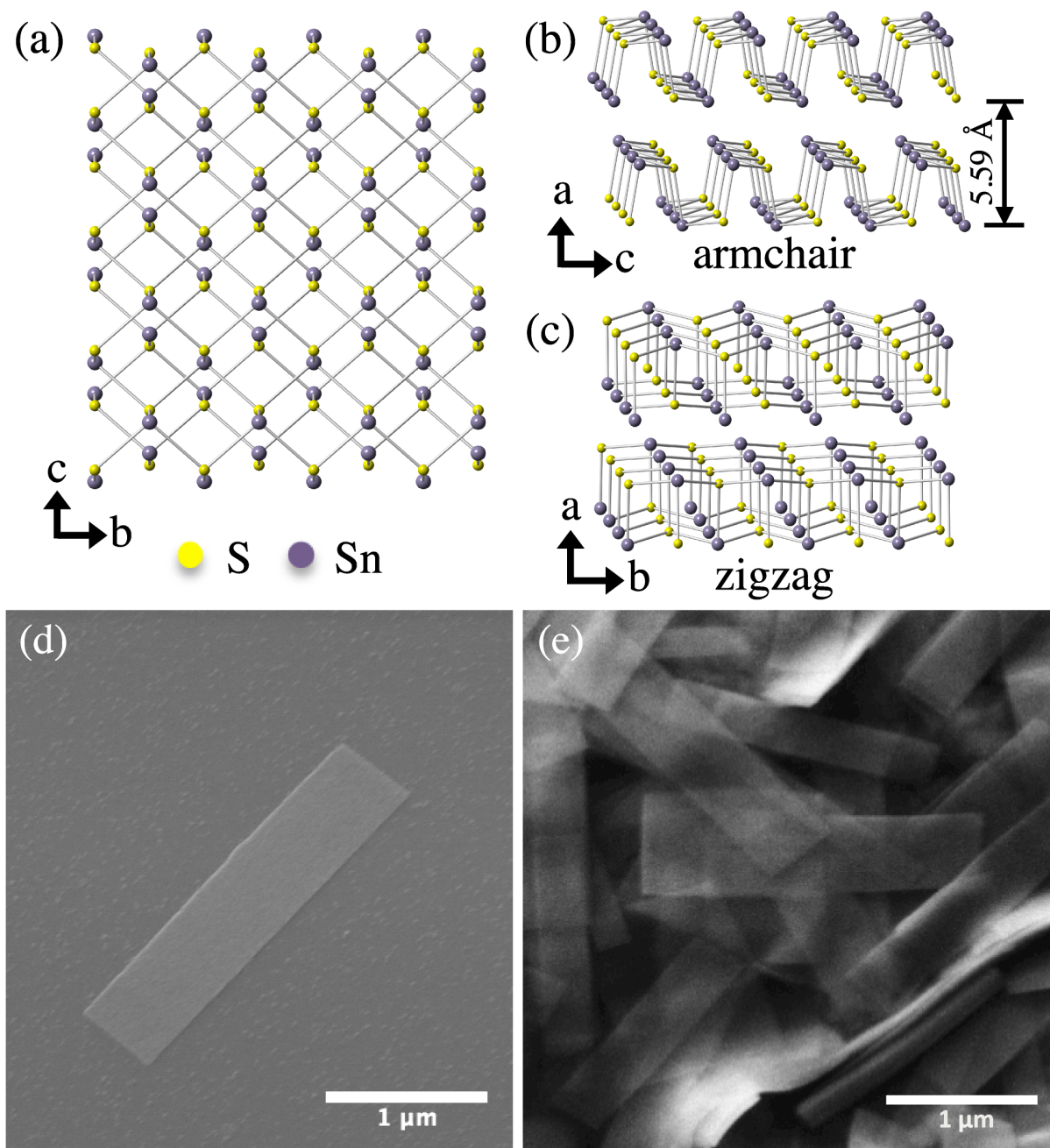


Figure 4.1: Orthorhombic $Pnma$ crystal structure of α -SnS viewing from the (a) (100) plane, and slightly tilted from the (b) (010), and (c) (001) planes. SEM images of (d) a solution-synthesized nanoribbon on a SiO_2/Si substrate and (e) a high concentration of nanoribbons drop cast onto a substrate. *Nanoscale*, 2018, **10**, 319-327- Reproduced by permission of the Royal Society of Chemistry.

4.2 Experimental Methods

4.2.1 Device Fabrication

Colloidal SnS nanoribbons were synthesized in solution by collaborators at NIST.⁹⁸⁻¹⁰⁰ Briefly, elemental sulfur powder was dissolved in oleylamine, to which tin(II) chloride was added in a reaction flask. The solution was heated under vacuum to remove residual water, then heated to 180 °C under argon for 1 hr, then quenched. The resulting nanocrystals were separated from the reaction solution by a series of centrifugations then redispersed in toluene. The semiconductor nanocrystals are several μm in length (average lengths and widths are 2.8 μm and 500 nm, respectively), but only ~17-20 nm or less in thickness. Previous studies by collaborators at NIST indicate the nanoribbons are phase-pure orthorhombic SnS, with p-type conductivity and a hole concentration estimated to be on the order of 10^{16} cm^{-3} .⁹⁸ The ratio of Sn to S is near stoichiometric, and the nanoribbons are single crystalline with preferred (100) orientation when dropcast onto a substrate. The length and widths of the nanoribbons correspond to the zigzag and armchair directions, respectively.

Diluted SnS nanoribbon dispersions in toluene were spin coated at 3,000 rpm for 30 seconds onto a $\text{SiO}_2/\text{p++Si}$ substrate with Ti/Au fiduciary marks and a Ni/Au ohmic back contact (Figure 4.2 a). The SiO_2 thermal oxide thickness was 100 nm. Following deposition, excess toluene was evaporated in an oven at 80 °C for 1 minute. Samples were then placed in a 2" quartz tube furnace and annealed at 375 °C for 15 minutes in forming gas (5 % H_2 /95 % Ar, flow rate 800 sccm). Spectroscopic analysis by collaborators at NIST has indicated that annealing under these reducing conditions fully removes residual organics from the surface.^{98, 100}

Contacts were patterned to individual nanoribbons using electron-beam lithography (Zeiss NVision 40 FESEM with Raith Elphy Quantum). Three different contact configurations

were used: (1) two large contacts spaced 1 μm apart; (2) three contacts of equivalent length with spacings of 500 nm and 1 μm ; and (3) four contacts of equivalent length with spacings of 250 nm, 500 nm, and 1 μm (Figure 4.2 c). Contact lengths were designed to be either 250 nm or 500 nm.

Prior to metal deposition, samples were dipped in 1% hydrofluoric acid (HF) for 30 s, dipped in deionized water for 30 s, and then blown dry with N_2 . Samples were immediately (within 5 to 10 min) loaded into an e-beam evaporation system (Thermionics) with a base pressure in the 10^{-9} Torr range. All metals were evaporated at a rate of 0.1 nm/s, as monitored by a quartz crystal microbalance (QCM). For each contact scheme, 40 nm of the selected metal was deposited, followed by 40 nm of Au. The purities of the commercial metal sources were: 99.995 % Ni, 99.95 % Pd, 99.996 % Cr, 99.995 % Ti and 99.999 % Au. Following evaporation, liftoff was performed in acetone.

4.2.2 Characterization

Electrical measurements were performed in the dark with a Signatone S-1060H-4QR probe station connected to an Agilent HP 4155C semiconductor parameter analyzer with voltage measurement input resistance $> 10^{13} \Omega$. Scanning electron microscope (SEM) micrographs were acquired with either a Phillips XL30 FESEM or Zeiss InVision 40 FESEM and were used to determine contact dimensions and channel lengths. A minimum of 15 pairs of contacts were analyzed for each deposited metal.

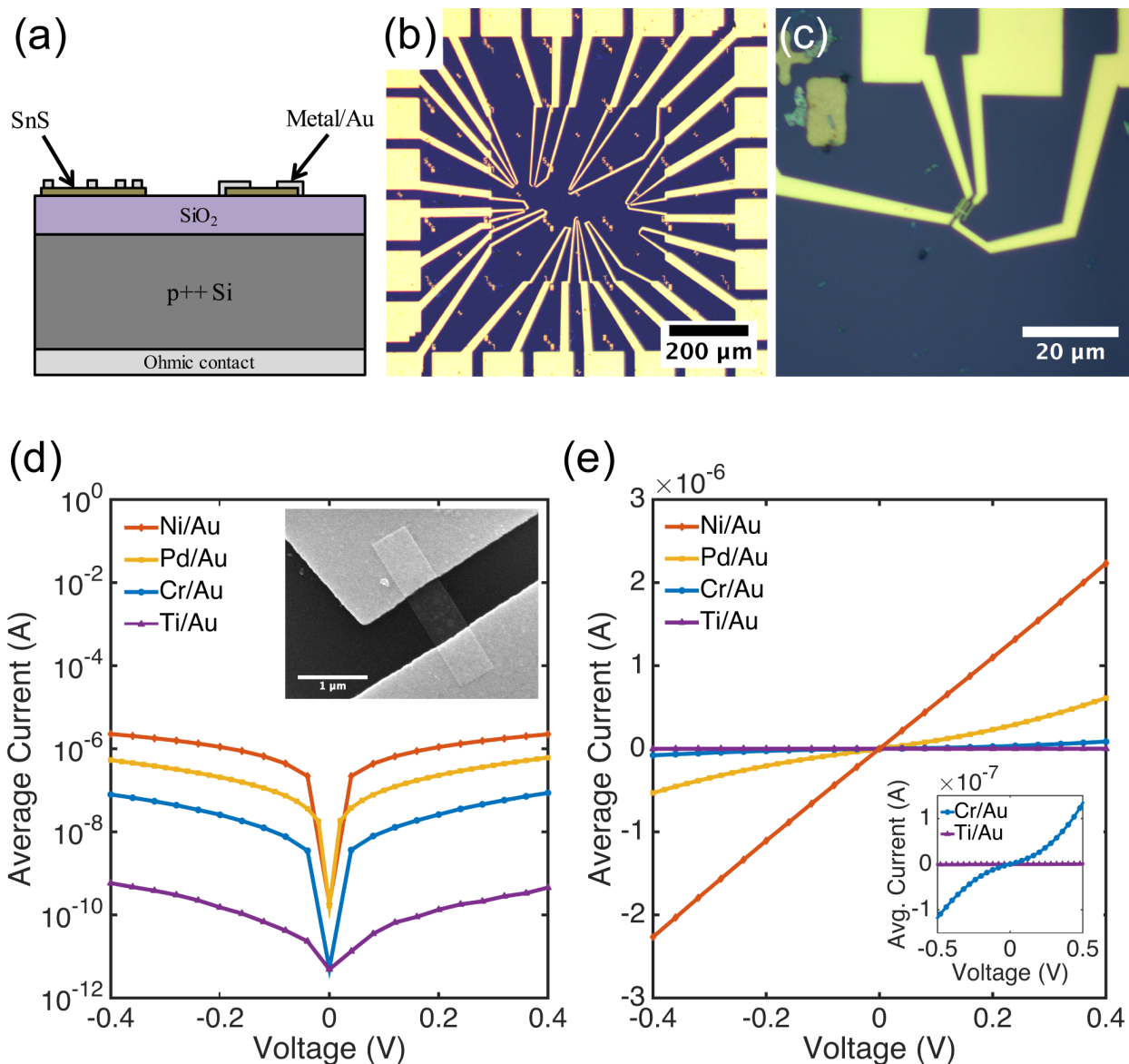


Figure 4.2: (a) Cross sectional schematic of device structure. Two nanoribbons with different contact configurations are shown. (b) Optical microscope image of a sample with many contact test structures patterned in one area and (c) a higher magnification image of a nanoribbon with four contacts. Average I-V sweeps for each contact metallization with 1 μm channel spacing on a (d) log and (e) linear scale, showing ohmic and semi-ohmic behavior for Pd/Au and Ni/Au contacts, and Schottky behavior for Cr/Au and Ti/Au contacts. Inset in (d) is an SEM image of a two contact Ni/Au device. *Nanoscale*, 2018, **10**, 319-327- Reproduced by permission of the Royal Society of Chemistry.

4.3 Results and Discussion

4.3.1 Current-Voltage Characteristics

Current-voltage sweeps were performed between adjacent contact pairs, and results are presented in Figure 4.2 d, e. The total resistance between contacts decreases from Ti/Au, Cr/Au, Pd/Au, to Ni/Au. Additionally, Schottky behavior was observed for the contact metals with low work functions (Cr and Ti), whereas ohmic or semi-ohmic behavior was exhibited for the contact metals with high work functions (Ni and Pd). These results were consistent for the 15 – 28 pairs of contacts that were analyzed for each metal. To quantify the electrical behavior of the contacts, measurements were conducted to calculate Schottky barrier heights and specific contact resistances of the Schottky and ohmic contacts, respectively.

4.3.2 Schottky Barrier Height I - V Measurement

The Cr and Ti Schottky contact pairs consist of two back-to-back Schottky diodes in series, separated by a SnS channel length. Different methods have been developed to analyze the room temperature I - V behavior of such a configuration.¹⁰¹⁻¹⁰³ Here, a method similar to those of Chiquito *et al.*¹⁰⁴ and Nouchi *et al.*¹⁰⁵ is used.

The current, I , through back-to back Schottky diodes 1 and 2 can be described by the thermionic emission equation¹⁰⁶

$$I_1 = I_{01} \left[1 - \exp \left(-\frac{qV_1}{kT} \right) \right] \quad (4.1a)$$

$$I_2 = I_{02} \left[\exp \left(\frac{qV_2}{kT} \right) - 1 \right] \quad (4.1b)$$

where q is the elementary charge, k is Boltzmann's constant, and $V_{1,2}$ is the voltage through each diode. The subscripts refer to diodes 1 and 2, respectively. $I_{01,02}$ is the saturation current given by

$$I_{01} = S_1 A^{**} T^2 \exp\left(\frac{q\phi_1}{kT}\right) \quad (4.2a)$$

$$I_{02} = S_2 A^{**} T^2 \exp\left(\frac{q\phi_2}{kT}\right) \quad (4.2b)$$

where A^{**} is the effective Richardson constant, $\phi_{1,2}$ are the effective Schottky barrier heights, and $S_{1,2}$ are the contact areas; the subscripts refer to diodes 1 and 2, respectively.

Current through each diode is equivalent ($I_1 = -I_2 = I$), and the voltage drop across each diode is given as

$$V_1 = -\frac{kT}{q} \ln\left(1 - \frac{I}{I_{01}}\right) \quad (4.3a)$$

$$V_2 = \frac{kT}{q} \ln\left(1 + \frac{I}{I_{02}}\right) \quad (4.3b)$$

By summing the voltages and solving for I , the total current through the device is

$$I = \frac{2I_{01}I_{02} \sinh\left(\frac{qV}{2kT}\right)}{I_{01} \exp\left(-\frac{qV}{2kT}\right) + I_{02} \exp\left(\frac{qV}{2kT}\right)} \quad (4.4)$$

where V is the applied voltage, q is the elementary charge, k is Boltzmann's constant, and T is temperature.

Ideality factors, $n_{1,2}$, can be introduced to account for a voltage dependence of the Schottky barrier height.¹⁰⁷ The voltage dependence of the barrier height is a consequence of image force lowering, and in some cases an interfacial layer and interface states.^{107, 108} The ideality factor can also increase due to tunneling through the barrier or carrier recombination in the depletion region. A characteristic energy, E_{00} , was calculated to determine the conduction

mechanism at the interface.¹⁰⁹ When E_{00} is much smaller than the thermal energy (kT), thermionic emission is expected.¹⁰⁶ Tunneling is not expected in forward bias at these doping concentrations at room temperature, as $E_{00} \approx 0.7$ meV (calculated using a dielectric constant of 32.8^{42, 110, 111} and hole effective mass of $0.23m_0$ ^{49, 51, 112}). However, tunneling and image force lowering may have a greater impact in reverse bias.^{107, 109} Additionally, there have been reports of larger tunneling contributions for very thin nanostructures.^{73, 113} Taking into account the ideality factor, the modified barrier height is written as^{104, 107,}

$$\Phi_{1,2} = \Phi_{01,02} + V \left(\frac{1}{n_{1,2}} - 1 \right) \quad (4.5)$$

where $\Phi_{01,02}$ are the true Schottky barrier heights for diodes 1 and 2, respectively.

The I - V curves were fit to Equations 1-3 using a nonlinear least squares method. The Richardson's constant used was $27.6 \text{ A}/(\text{cm}^2\text{-K}^2)$, which was calculated with literature values for the bulk SnS hole effective mass in the zigzag direction.^{49, 51, 112} It was found that the value used for Richardson's constant did not greatly impact the extracted fit parameters.

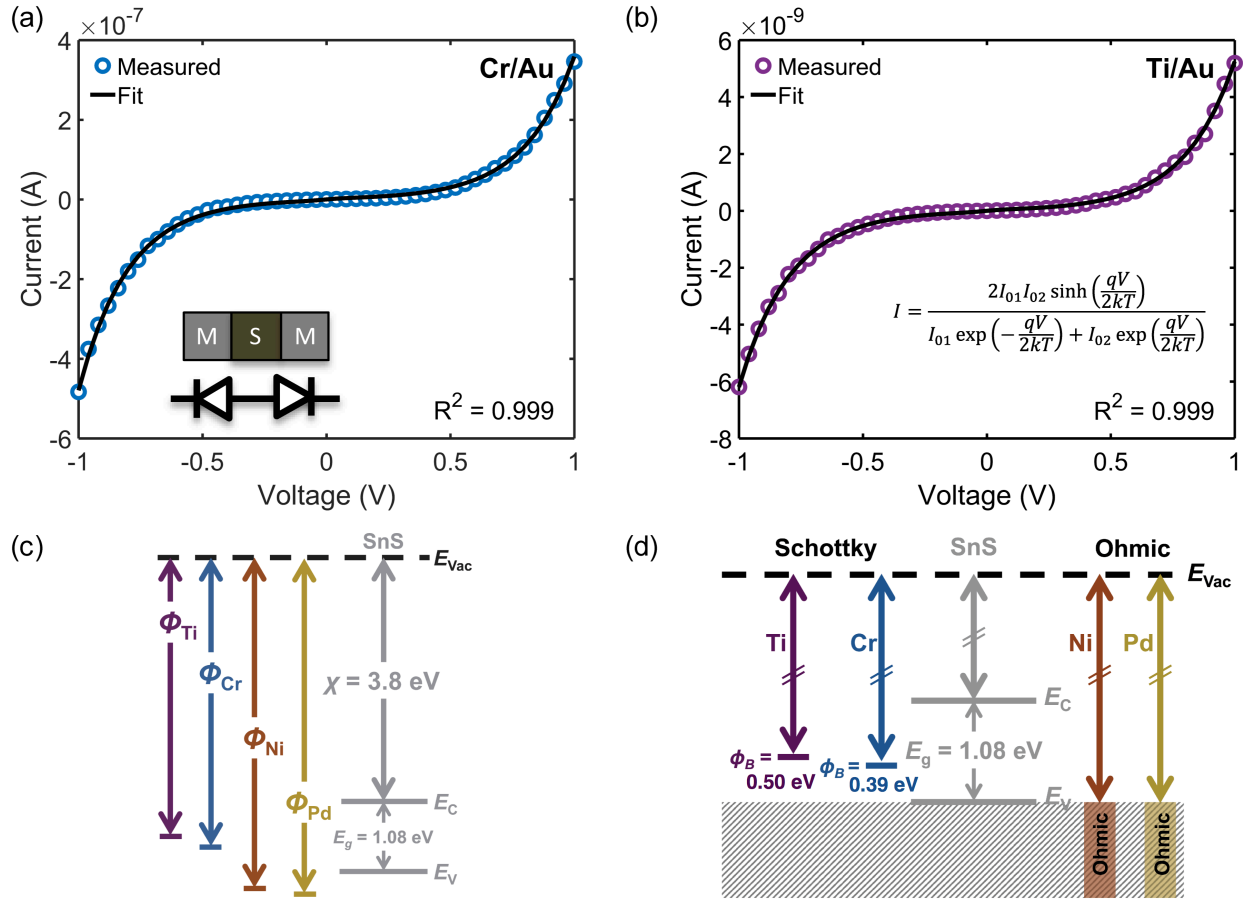


Figure 4.3: Example fits of I-V sweeps to the back-to-back Schottky diode equation for (a) Cr/Au contacts on SnS and (b) Ti/Au contacts on SnS. I-V sweeps were measured between adjacent contacts. (c) Schottky-Mott band alignment of metals and SnS. χ is the electron affinity of SnS, E_g is the band gap, E_{vac} is the vacuum level, E_c is the conduction band minimum, and E_v is the valence band maximum. (d) Band alignment determined from experiments. *Nanoscale*, 2018, **10**, 319-327- Reproduced by permission of the Royal Society of Chemistry.

Example fits using Equations 4.2-4.4 for Cr/Au and Ti/Au back-to-back Schottky contacts are shown in Figure 4.3 a,b. As indicated by the fit parameters listed in Table 4.1, the calculated average Schottky barrier heights at the interface with SnS nanoribbons were 0.39 eV and 0.50 eV for Cr/Au and Ti/Au, respectively. These values are in close agreement with the values ($\phi_{B,Cr} = 0.38$ eV and $\phi_{B,Ti} = 0.55$ eV) predicted by the Schottky-Mott metal-semiconductor band alignment model (Figure 4.3 c). The electron affinity listed is a reported value for the (100) surface of bulk SnS.¹¹⁴ The band gap of bulk SnS has been reported to be

Table 4.1: Average fit parameters for Cr/Au and Ti/Au Schottky contacts. ϕ_B is the average of ϕ_{01} and ϕ_{02} , and n the average of n_1 and n_2 .

Metal	Φ_B (eV)	n	R^2	No. Devices
Cr/Au	0.39 ± 0.05	1.12 ± 0.02	0.996 ± 0.002	20
Ti/Au	0.50 ± 0.06	1.13 ± 0.07	0.996 ± 0.003	15

1.08 eV¹¹⁵ and was confirmed experimentally by collaborators at NIST via diffuse reflectance spectra measurement on dropcast films of SnS nanoribbons and a Tauc plot.¹¹⁶

The experimentally determined alignment is depicted in Figure 4.3 d; the alignments of the ohmic contacts are assumed to be near or below the valence band maximum. The results indicate a lack of Fermi-level pinning and agree with a recent report of ohmic Ni contacts on 50 – 100 nm thick multilayer SnS.⁶⁸ Additionally, an older study reports Ag Schottky contacts to the (100) plane of bulk SnS with a barrier height of 0.649 eV.¹¹⁷ Although the work function of metals can vary depending on orientation and processing, this barrier height value is close to the 0.62 eV value predicted here for polycrystalline Ag ($\phi_M = 4.26$ eV).¹¹⁸

While ideality factors are low, they are higher than those expected for only image force lowering at this moderate doping concentration. This suggests an additional contribution to the ideality factor, such as from tunneling or an interfacial layer. SnS is known to form a thin native oxide at its surface,¹¹⁹ which was observed previously using X-ray photoelectron spectroscopy by collaborators at NIST.¹⁰⁰ The oxide can be removed under reducing conditions but regrows upon exposure to ambient air. While samples were dipped in HF prior to metal deposition, further study is needed to determine the extent to which the oxide layer was removed. There have been reports of oxide layers impacting Schottky barrier heights to MoS₂.^{88-90, 120}

4.3.3 Specific Contact Resistance Measurement

The specific contact resistance was measured for the ohmic Ni/Au and semi-ohmic Pd/Au contacts. For bulk semiconductors, the specific contact resistance can be measured by a transfer length method (TLM), involving four or more contacts with varying spacings. Due to the confined lengths of the nanoribbons, some were too small for a four contact TLM pattern. For those nanostructures, three contacts were patterned, and a contact end resistance (CER)¹²¹ measurement combined with a three-probe contact front resistance measurement were used.¹⁰⁶

The current in a metal-semiconductor contact encounters two competing resistances- the semiconductor sheet resistance, R_{sh} , and an interfacial resistance, which is experimentally quantified by the specific contact resistance, ρ_c . The interface is described by a transmission line model represented in Figure 4.4 a^{121, 122} The voltage distribution under the contact as a function of distance is given by¹²¹,

$$V(x) = \frac{i_l \sqrt{R_{sh} \rho_c}}{Z} \frac{\cosh\left(\frac{L-x}{L_T}\right)}{\sinh\left(\frac{L}{L_T}\right)} \quad (4.6)$$

where i_l is the current flowing into the contact, L is the length of the contact, Z is the width of the contact, x is the variable distance along the contact ($x = 0$ is the front of the contact and $x = L$ is the end of the contact), ρ_c is the specific contact resistance, and L_T is the transfer length. The transfer length is given by^{106, 121}

$$L_T = \sqrt{\rho_c / R_{sh}} \quad (4.7)$$

For long contacts ($L > 3L_T$), Equation 4.6 can be approximated as an exponential function and L_T is the distance under the contact in which $1 - (1/e)$ of the current has entered the metal.

Contact end resistance

The measurement configuration for the CER method is depicted in Figure 4.4 b. Here, three contacts with all L and unequal spacings between contacts, d , were fabricated on single nanoribbons (Figure 4.4 c). Current, I_{12} , was applied between contacts 1 and 2, and voltage, V_{23} , was measured between contacts 2 and 3 (Figure 4.4 d). The current flowing between contacts 2 and 3 is negligible when a high impedance voltage measurement unit is used. Therefore, this configuration provides a voltage sampling at the end of the contact (i.e., at $x = L$). From Equations 4.6 and 4.7, the contact end resistance, R_{ce} , is given as

$$R_{ce} = \frac{V_{23}}{I_{12}} = \frac{\rho_c}{L_T Z} \frac{1}{\sinh\left(\frac{L}{L_T}\right)} \quad (4.8)$$

Alternatively, when current, I_{12} , is measured between contacts 1 and 2, and voltage, V_{12} is applied between contacts 1 and 2, the voltage is sampled at the front of the contact (i.e., at $x = 0$). From Equations 4.6 and 4.7, the contact front resistance, R_{cf} , can be written as

$$R_{cf} = \frac{\rho_c}{L_T Z} \coth\left(\frac{L}{L_T}\right) \quad (4.9)$$

R_{cf} was determined as shown in Figure 4.4 e, where the total resistance between contacts 1 and 2 (R_{12}), and between 2 and 3 (R_{23}) were measured. The total resistance is¹⁰⁶

$$R_{12,23} = \frac{R_{sh} d_{12,23}}{Z} + 2R_{cf} \quad (4.10)$$

where $d_{12,23}$ are the spacings between contacts 1 and 2, or 2 and 3, respectively. Assuming the contact resistances for all three contacts are identical, R_{cf} can be solved for as¹²¹

$$R_{cf} = \frac{R_{23} d_{12} - R_{12} d_{23}}{2(d_{12} - d_{23})} \quad (4.11)$$

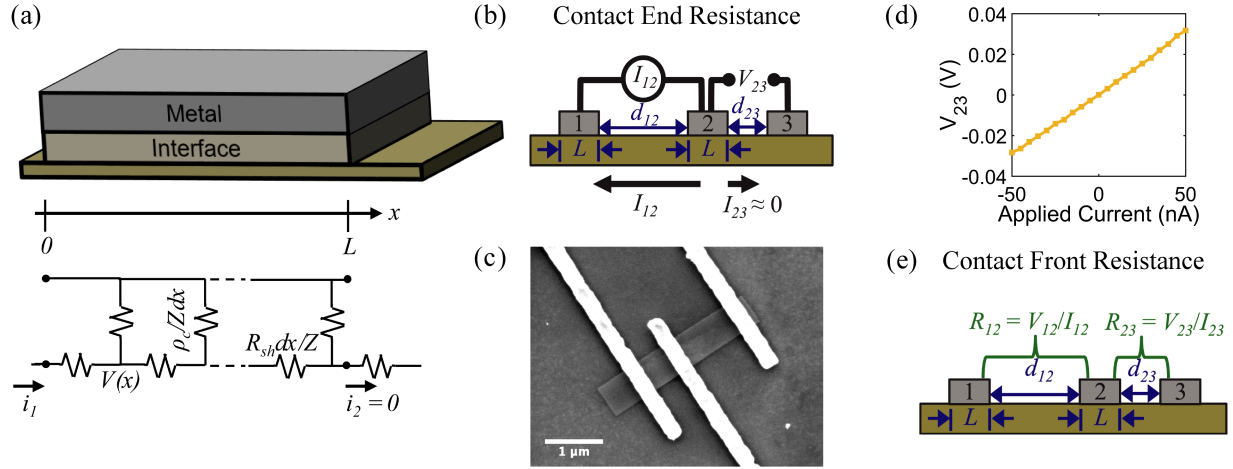


Figure 4.4: (a) Transmission line model for metal-semiconductor contact. (b) Schematic of contact end resistance measurement. (c) SEM image of a CER structure for Ni/Au contacts on a SnS nanoribbon. (d) Example measurement of V_{23} for contact end resistance measurement of a set of Pd/Au contacts. (e) Schematic of contact front resistance measurement. *Nanoscale*, 2018, **10**, 319-327- Reproduced by permission of the Royal Society of Chemistry.

The transfer length was determined by taking the ratio of the contact end and front resistances,

$$\frac{R_{ce}}{R_{cf}} = \frac{1}{\cosh\left(\frac{L}{L_T}\right)} \quad (4.12)$$

and the calculated L_T value was subsequently inserted into Equation 4.8 or 4.9 to solve for ρ_c . R_{sh} was then calculated from Equation 4.7.

The results of these measurements are displayed in Table 4.2. It can be seen that the calculated specific contact resistances of the Pd/Au contacts are higher than those of Ni/Au. The extracted transfer lengths were in most cases approximately equal to the length of the contacts or smaller, and in only a few cases, slightly longer. It was found that the calculated specific contact resistances of devices with transfer lengths longer than the contact were similar to those with shorter transfer lengths. The long transfer lengths will be discussed in terms of the transmission line model in the next section.

Table 4.2: Specific contact resistances and related parameters, calculated using the contact end resistance (CER) method.

Metal	$R_{cf}(\Omega)$	$R_{ce}(\Omega)$	L (nm)	L_T (nm)	$R_{sh}(\Omega/\square)$	$\rho_c(\Omega \cdot \text{cm}^2)$
Ni/Au	$4.3 (\pm 3.2) \times 10^4$	$2.8 (\pm 2.2) \times 10^4$	$3.7 (\pm 0.7) \times 10^2$	$3.5 (\pm 0.4) \times 10^2$	$6.1 (\pm 4.9) \times 10^4$	$5.4 (\pm 3.9) \times 10^{-5}$
Pd/Au	$2.5 (\pm 1.3) \times 10^6$	$7.3 (\pm 1.1) \times 10^5$	$2.8 (\pm 0.2) \times 10^2$	$2.2 (\pm 1.2) \times 10^2$	$7.9 (\pm 7.1) \times 10^6$	$1.3 (\pm 0.3) \times 10^{-3}$

Table 4.3: Specific contact resistances and related parameters extracted by the transfer length method (TLM).

Metal	R^2	$R_{cf}(\Omega)$	L (nm)	L_T (nm)	L_{eff} (nm)	$R_{sh}(\Omega/\square)$	$\rho_c(\Omega \cdot \text{cm}^2)$
Ni/Au	0.976	$7.2 (\pm 0.2) \times 10^4$	2.9×10^2	$6.4 (\pm 0.5) \times 10^2$	$2.7 (\pm 0.3) \times 10^2$	$2.7 (\pm 0.4) \times 10^4$	$1.1 (\pm 0.3) \times 10^{-4}$
Pd/Au	0.984	$6.9 (\pm 1.7) \times 10^5$	3.0×10^2	$1.6 (\pm 0.5) \times 10^2$	$1.5 (\pm 0.5) \times 10^2$	$2.3 (\pm 0.3) \times 10^6$	$5.9 (\pm 3.6) \times 10^{-4}$

The measured sheet resistance is lower for Ni/Au contacts than Pd/Au contacts. In this method, the extracted sheet resistance is the sheet resistance of the nanoribbon underneath the contact region. A few factors could alter the nanoribbon sheet resistance under the contact, such as a reaction at the interface (Pd and Ni are both thermodynamically predicted to react with SnS^{123, 124}), or a depletion width on the order of the thickness (the depletion width is on the order of a few hundred nanometers at this doping density). The variation in sheet resistance and contact resistance values may be a result of different amounts of reactions at the interface between devices.

Transfer length method (TLM)

For longer nanoribbons, a TLM design was patterned, consisting of four contacts on a single nanoribbon. The four contacts of equal length were separated by varying channel spacings, d . The total resistance, R_T , was measured between each set of adjacent contacts and is equal to the sum of the resistance contribution from the semiconductor, $(R_{sh} d)/Z$, and the two contact resistances, $2R_{cf}$. When R_T is plotted as a function of d , the y -intercept corresponds to the resistance contribution from the two contacts only and is equal to $2R_{cf}$. R_{sh} can be determined from the slope, and L_T can be determined by extrapolating the x -intercept.^{106, 125} Typically, this method makes use of the approximation that when $L \geq 3L_T$, the $\coth(L/L_T)$ term in Eq. 4.9 is approximately equal to 1, and therefore the x -intercept is equal to $-2L_T$ (Equation 2.10). However, Table 4.2 indicates that $L \geq 3L_T$ is not valid for the geometries here, so this approximation cannot be used. Therefore, the full Equation 4.9 was used, yielding a total resistance:

$$R_T = \frac{R_{sh}}{Z} \left(d + 2L_T \coth\left(\frac{L}{L_T}\right) \right) \quad (4.13)$$

In this case, the x -intercept is equal to $-2L_T \coth(L/L_T)$, and the y -intercept and slope remain equal to $2R_{cf}$ (following Equation 4.7 and Eq. 4.9) and R_{sh}/Z , respectively. A similar expression was derived for contacts to semiconductor nanowires with short contact lengths.¹²⁶

The specific contact resistance can also be written in terms of the contact resistance multiplied by the area of the contact. For long contacts ($L > 3L_T$), the transfer length is used for the length, and, from Equation 4.9, $R_{cf} \approx \rho_c/(L_T Z)$.¹⁰⁶ For very short contacts, $R_{cf} \approx \rho_c/(L Z)$.¹⁰⁶ For the intermediate contact lengths here, neither approximation is accurate, but an effective length can be defined, such that

$$L_{eff} = \frac{L_T}{\coth\left(\frac{L}{L_T}\right)}. \quad (4.14)$$

Then, $R_{cf} = \rho_c/(L_{eff} Z)$. Equation 4.6 is derived for a terminal contact, in which all current is collected between $x=0$ and $x=L$ such that i_2 in Figure 4.4 a is equal to zero.¹²¹ When the contact length becomes less than $3L_T$, R_{cf} begins to increase. $i_1 R_{cf}$ multiplied by L_{eff} is equal to the integral of the voltage along the entire contact, such that $\frac{1}{i_1} \int_0^L V(x) dx = R_{cf} \cdot L_{eff}$. The specific contact resistance can therefore be calculated by multiplying the measured R_{cf} by the contact width and effective length, or by solving for ρ_c in Equation 4.7 ($\rho_c = L_T^2 \cdot R_{sh}$). This approach assumes all current is collected within the length of the contact and does not take into account spreading resistance beyond the length of the contact.

Table 4.3 lists extracted parameters from plots of R_T vs d (Figure 4.5). Similar to the results extracted by the CER method, it is observed that the specific contact resistance of Ni is lower than that of Pd, and the extracted sheet resistance for Ni is lower than that of Pd.

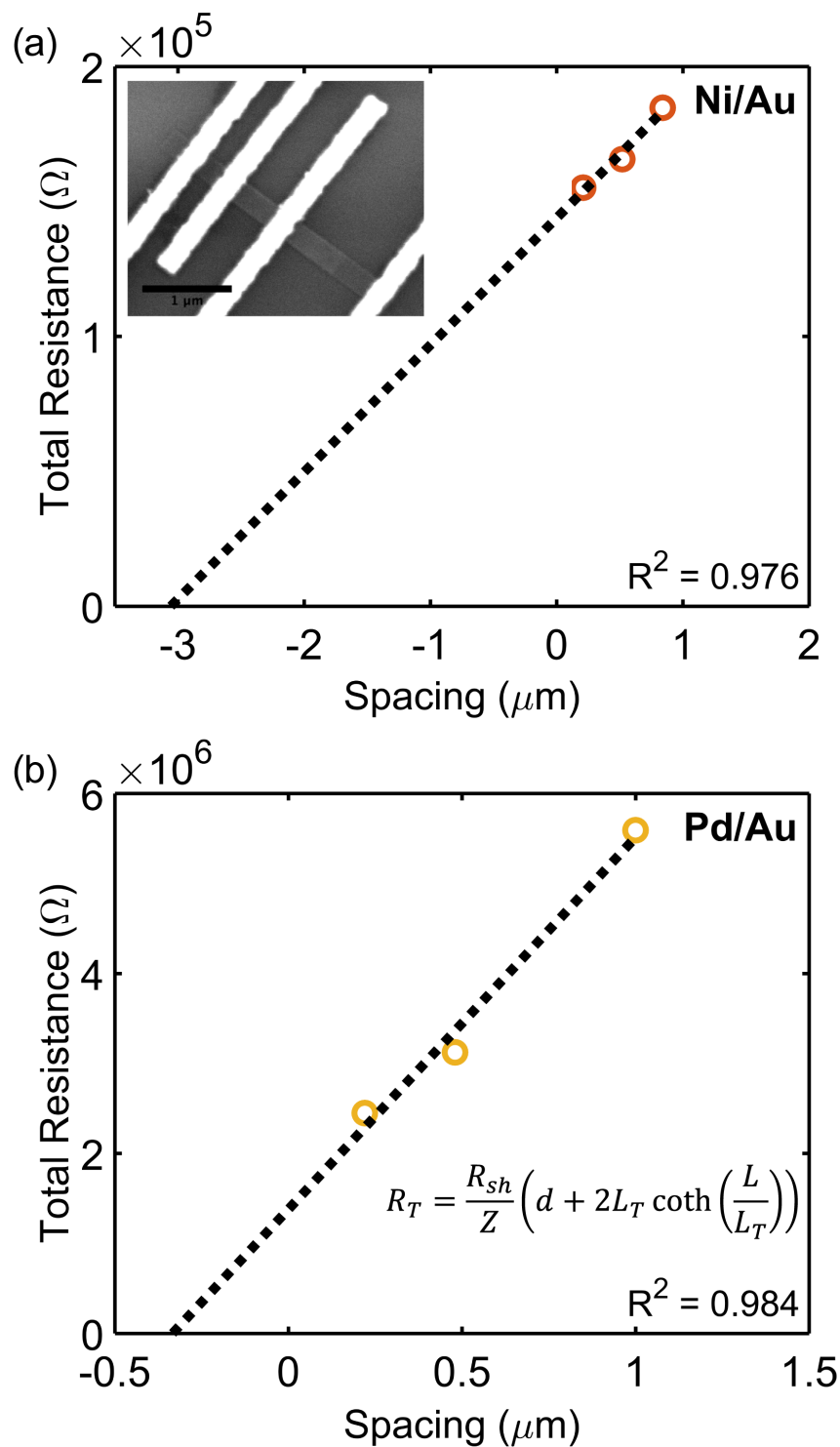


Figure 4.5: Transfer length method (TLM) plots for extracting sheet resistance, specific contact resistance, and transfer lengths of contacts on an individual SnS nanoribbon for (a) Ni/Au contacts and (b) Pd/Au contacts. Inset in (a) is an SEM image of a representative TLM device. *Nanoscale*, 2018, **10**, 319-327- Reproduced by permission of the Royal Society of Chemistry.

In this case, the transfer length for the Ni/Au contact is larger than the length of the contact, and the transfer length of Pd/Au was greater than $L/3$. As previously discussed, the specific contact resistances can be calculated using $R_{cf} = \rho_c / (L_{eff} Z)$, which are equivalent to the ρ_c calculated by Equations 4.7 and 4.13. Since R_{cf} will increase with decreasing contact length when the contact length is less than $3L_T$, this indicates that in devices, a contact length longer than those used here would be ideal to further reduce R_{cf} .

The TLM assumes the sheet resistance under the contact is equal to the nanoribbon sheet resistance in the channel. In reality, this may not be the case due to factors such as reactions at the interface or the depletion width being on the order of the thickness of the semiconductor.¹²⁷ An additional measurement of R_{ce} can take into account a change in underlying R_{sh} .^{127, 128} The contact end resistance measurement was performed on the Ni/Au TLM structure, and, in conjunction with R_{cf} determined by the TLM measurement, specific contact resistance parameters were extracted. The sheet resistance determined by incorporating this additional measurement was $3.3 \times 10^3 \Omega/\square$, which is lower than that measured by the TLM method alone ($2.7 \times 10^4 \Omega/\square$). This suggests the sheet resistance in the SnS region underneath the Ni/Au contact is lower than the sheet resistance of the pristine SnS channel and therefore may indicate a reaction occurred at the Ni/SnS interface. Further studies would be required to determine the exact nature of the Ni/SnS interface. Possible reaction products of bulk SnS and Ni calculated from FactSage®¹²³ include Ni_3Sn_2 and Ni_3S_2 . It is interesting to note that the work function of Ni_3S_2 has been reported to be ~ 5 eV,^{129, 130} which is similar to that of unreacted Ni; whereas the work function of Ni_3Sn_2 may be as low as 4.55 eV.¹³¹ Regardless of whether a reaction has occurred at this interface, Ni contacts to SnS nanoribbons appear to behave as predicted by the Schottky-Mott model for a high work function metal.

4.4 Conclusion

In this work, Ni, Pd, Cr, and Ti contact test structures were fabricated onto individual, solution-synthesized, p-type SnS nanoribbons. We conducted what we believe to be the first reported analysis of contact performance in devices fabricated from colloidal nanocrystals. The high work function metals (Ni and Pd) formed ohmic or semi-ohmic contacts to SnS nanoribbons, while the lower work function metals (Cr and Ti) formed Schottky contacts. The Schottky barrier heights calculated for Cr and Ti agree well with the band alignment predicted by Schottky-Mott theory, whereas the ohmic behavior of Ni and Pd also agree with the expectations from this model. Of the two ohmic metals, a lower specific contact resistance (on the order of $10^{-4} \Omega\text{-cm}^2$ or lower) was consistently calculated for Ni. The results of this study indicate a lack of Fermi level pinning in metal-SnS nanoribbon structures and can inform the selection of contact metals in the design of future SnS-based devices.

4.5 References

1. K. S. Novoselov, A. K. Geim, S. V. Morozov, D. Jiang, Y. Zhang, S. V. Dubonos, I. V. Grigorieva and A. A. Firsov, *Science*, 2004, **306**, 666-669.
2. A. B. Kaul, *Journal of Materials Research*, 2014, **29**, 348-361.
3. G. Fiori, F. Bonaccorso, G. Iannaccone, T. Palacios, D. Neumaier, A. Seabaugh, S. K. Banerjee and L. Colombo, *Nat. Nanotechnol.*, 2014, **9**, 768-779.
4. K. S. Novoselov, D. Jiang, F. Schedin, T. J. Booth, V. V. Khotkevich, S. V. Morozov and A. K. Geim, *Proc. Natl. Acad. Sci. U. S. A.*, 2005, **102**, 10451-10453.
5. Q. H. Wang, K. Kalantar-Zadeh, A. Kis, J. N. Coleman and M. S. Strano, *Nat. Nanotechnol.*, 2012, **7**, 699-712.
6. B. Radisavljevic, A. Radenovic, J. Brivio, V. Giacometti and A. Kis, *Nat. Nanotechnol.*, 2011, **6**, 147-150.
7. R. F. Frindt, *J. Appl. Phys.*, 1966, **37**, 1928-1929.
8. H. Matte, A. Gomathi, A. K. Manna, D. J. Late, R. Datta, S. K. Pati and C. N. R. Rao, *Angewandte Chemie-International Edition*, 2010, **49**, 4059-4062.
9. H. R. Gutierrez, N. Perea-Lopez, A. L. Elias, A. Berkdemir, B. Wang, R. Lv, F. Lopez-Urias, V. H. Crespi, H. Terrones and M. Terrones, *Nano Lett.*, 2013, **13**, 3447-3454.

10. J. N. Coleman, M. Lotya, A. O'Neill, S. D. Bergin, P. J. King, U. Khan, K. Young, A. Gaucher, S. De, R. J. Smith, I. V. Shvets, S. K. Arora, G. Stanton, H. Y. Kim, K. Lee, G. T. Kim, G. S. Duesberg, T. Hallam, J. J. Boland, J. J. Wang, J. F. Donegan, J. C. Grunlan, G. Moriarty, A. Shmeliov, R. J. Nicholls, J. M. Perkins, E. M. Grieveson, K. Theuwissen, D. W. McComb, P. D. Nellist and V. Nicolosi, *Science*, 2011, **331**, 568-571.
11. S. Tongay, J. Zhou, C. Ataca, K. Lo, T. S. Matthews, J. B. Li, J. C. Grossman and J. Q. Wu, *Nano Lett.*, 2012, **12**, 5576-5580.
12. S. Larentis, B. Fallahazad and E. Tutuc, *Appl. Phys. Lett.*, 2012, **101**, 223104.
13. H. Fang, S. Chuang, T. C. Chang, K. Takei, T. Takahashi and A. Javey, *Nano Lett.*, 2012, **12**, 3788-3792.
14. W. J. Zhao, Z. Ghorannevis, L. Q. Chu, M. L. Toh, C. Kloc, P. H. Tan and G. Eda, *ACS Nano*, 2013, **7**, 791-797.
15. P. A. Hu, Z. Z. Wen, L. F. Wang, P. H. Tan and K. Xiao, *ACS Nano*, 2012, **6**, 5988-5994.
16. D. J. Late, B. Liu, J. J. Luo, A. M. Yan, H. Matte, M. Grayson, C. N. R. Rao and V. P. Dravid, *Advanced Materials*, 2012, **24**, 3549-3554.
17. G. W. Mudd, S. A. Svatek, T. Ren, A. Patane, O. Makarovskiy, L. Eaves, P. H. Beton, Z. D. Kovalyuk, G. V. Lashkarev, Z. R. Kudrynskyi and A. I. Dmitriev, *Advanced Materials*, 2013, **25**, 5714-5718.
18. S. D. Lei, L. H. Ge, S. Najmaei, A. George, R. Kappera, J. Lou, M. Chhowalla, H. Yamaguchi, G. Gupta, R. Vajtai, A. D. Mohite and P. M. Ajayan, *ACS Nano*, 2014, **8**, 1263-1272.
19. H. J. Zhang, C. X. Liu, X. L. Qi, X. Dai, Z. Fang and S. C. Zhang, *Nature Physics*, 2009, **5**, 438-442.
20. Y. L. Chen, J. G. Analytis, J. H. Chu, Z. K. Liu, S. K. Mo, X. L. Qi, H. J. Zhang, D. H. Lu, X. Dai, Z. Fang, S. C. Zhang, I. R. Fisher, Z. Hussain and Z. X. Shen, *Science*, 2009, **325**, 178-181.
21. Y. Xia, D. Qian, D. Hsieh, L. Wray, A. Pal, H. Lin, A. Bansil, D. Grauer, Y. S. Hor, R. J. Cava and M. Z. Hasan, *Nature Physics*, 2009, **5**, 398-402.
22. M. S. Xu, T. Liang, M. M. Shi and H. Z. Chen, *Chemical Reviews*, 2013, **113**, 3766-3798.
23. L. K. Li, Y. J. Yu, G. J. Ye, Q. Q. Ge, X. D. Ou, H. Wu, D. L. Feng, X. H. Chen and Y. B. Zhang, *Nat. Nanotechnol.*, 2014, **9**, 372-377.
24. A. Castellanos-Gomez, L. Vicarelli, E. Prada, J. O. Island, K. L. Narasimha-Acharya, S. I. Blanter, D. J. Groenendijk, M. Buscema, G. A. Steele, J. V. Alvarez, H. W. Zandbergen, J. J. Palacios and H. S. J. van der Zant, *2D Materials*, 2014, **1**, 025001.
25. S. P. Koenig, R. A. Doganov, H. Schmidt, A. H. C. Neto and B. Ozyilmaz, *Applied Physics Letters*, 2014, **104**, 103106.
26. F. N. Xia, H. Wang and Y. C. Jia, *Nature Communications*, 2014, **5**, 4458.
27. J. S. Qiao, X. H. Kong, Z. X. Hu, F. Yang and W. Ji, *Nature Communications*, 2014, **5**, 4475.
28. H. Liu, A. T. Neal, Z. Zhu, Z. Luo, X. F. Xu, D. Tomanek and P. D. D. Ye, *ACS Nano*, 2014, **8**, 4033-4041.
29. A. H. Woomer, T. W. Farnsworth, J. Hu, R. A. Wells, C. L. Donley and S. C. Warren, *ACS Nano*, 2015, **9**, 8869-8884.
30. R. W. Keyes, *Physical Review*, 1953, **92**, 580-584.

31. Y. Maruyama, S. Suzuki, K. Kobayashi and S. Tanuma, *Physica B & C*, 1981, **105**, 99-102.
32. Y. Akahama and H. Kawamura, *Physica Status Solidi B-Basic Research*, 2001, **223**, 349-353.
33. L. B. Liang, J. Wang, W. Z. Lin, B. G. Sumpter, V. Meunier and M. H. Pan, *Nano Lett.*, 2014, **14**, 6400-6406.
34. X. Ling, H. Wang, S. X. Huang, F. N. Xia and M. S. Dresselhaus, *Proc. Natl. Acad. Sci. U. S. A.*, 2015, **112**, 4523-4530.
35. R. X. Fei, A. Faghaninia, R. Soklaski, J. A. Yan, C. Lo and L. Yang, *Nano Lett.*, 2014, **14**, 6393-6399.
36. J. S. Kim, Y. N. Liu, W. N. Zhu, S. Kim, D. Wu, L. Tao, A. Dodabalapur, K. Lai and D. Akinwande, *Scientific Reports*, 2015, **5**, 8989.
37. J. D. Wood, S. A. Wells, D. Jariwala, K. S. Chen, E. Cho, V. K. Sangwan, X. L. Liu, L. J. Lauhon, T. J. Marks and M. C. Hersam, *Nano Lett.*, 2014, **14**, 6964-6970.
38. K. S. Novoselov, A. Mishchenko, A. Carvalho and A. H. C. Neto, *Science*, 2016, **353**, aac9439.
39. L. C. Gomes and A. Carvalho, *Physical Review B*, 2015, **92**, 085406.
40. A. S. Rodin, L. C. Gomes, A. Carvalho and A. H. C. Neto, *Physical Review B*, 2016, **93**, 045431.
41. M. H. Wu and X. C. Zeng, *Nano Lett.*, 2016, **16**, 3236-3241.
42. L. C. Gomes, A. Carvalho and A. H. C. Neto, *Phys. Rev. B*, 2015, **92**, 214103.
43. R. Fei, W. Li, J. Li and L. Yang, *Appl. Phys. Lett.*, 2015, **107**, 173104.
44. A. K. Singh and R. G. Hennig, *Applied Physics Letters*, 2014, **105**, 042103.
45. L. C. Gomes, A. Carvalho and A. H. C. Neto, *Physical Review B*, 2016, **94**, 054103.
46. Y. Guo, S. Zhou, Y. Z. Bai and J. J. Zhao, *ACS Appl. Mater. Interfaces*, 2017, **9**, 12013-12020.
47. L. Li, Z. Chen, Y. Hu, X. W. Wang, T. Zhang, W. Chen and Q. B. Wang, *J. Am. Chem. Soc.*, 2013, **135**, 1213-1216.
48. J. Z. Jiang, C. P. Y. Wong, J. Zou, S. S. Li, Q. X. Wang, J. Y. Chen, D. Y. Qi, H. Y. Wang, G. Eda, D. H. C. Chua, Y. M. Shi, W. J. Zhang and A. T. S. Wee, *2d Materials*, 2017, **4**, 021026.
49. C. Xin, J. X. Zheng, Y. T. Su, S. K. Li, B. K. Zhang, Y. C. Feng and F. Pan, *J. Phys. Chem. C*, 2016, **120**, 22663-22669.
50. G. Valiukonis, D. A. Guseinova, G. Krivaite and A. Sileika, *Phys. Status Solidi B*, 1986, **135**, 299-307.
51. G. A. Tritsarlis, B. D. Malone and E. Kaxiras, *J. Appl. Phys.*, 2013, **113**, 233507.
52. L. Huang, F. G. Wu and J. B. Li, *Journal of Chemical Physics*, 2016, **144**, 114708.
53. C. Chowdhury, S. Karmakar and A. Datta, *J. Phys. Chem. C*, 2017, **121**, 7615-7624.
54. J. Vidal, S. Lany, M. d'Avezac, A. Zunger, A. Zakutayev, J. Francis and J. Tate, *Applied Physics Letters*, 2012, **100**, 032104.
55. P. Villars, *Pearson's Handbook Desk Edition: Crystallographic Data for Intermetallic Phases*, ASM International, Materials Park, OH, 1997.
56. L. A. Burton and A. Walsh, *J. Phys. Chem. C*, 2012, **116**, 24262-24267.
57. A. Walsh and G. W. Watson, *Journal of Physical Chemistry B*, 2005, **109**, 18868-18875.

58. M. Mehboudi, A. M. Dorio, W. Zhu, A. van der Zande, H. O. Churchill, A. A. Pacheco-Sanjuan, E. O. Harriss, P. Kumar and S. Barraza-Lopez, *Nano Lett.*, 2016, **16**, 1704-1712.
59. L. M. Sandomas, D. Teich, R. Gutierrez, T. Lorenz, A. Pecchia, G. Seifert and G. Cuniberti, *J. Phys. Chem. C*, 2016, **120**, 18841-18849.
60. S. D. Guo and Y. H. Wang, *Journal of Applied Physics*, 2017, **121**, 034302.
61. P. Z. Hanakata, A. Carvalho, D. K. Campbell and H. S. Park, *Physical Review B*, 2016, **94**, 035304.
62. H. Wang and X. F. Qian, *2d Materials*, 2017, **4**, 015042.
63. W. Q. Xiong, C. X. Xia, X. Zhao, T. X. Wang and Y. Jia, *Carbon*, 2016, **109**, 737-746.
64. K. Cheng, Y. Guo, N. N. Han, Y. Su, J. F. Zhang and J. J. Zhao, *J. Mater. Chem. C*, 2017, **5**, 3788-3795.
65. R. Browning, P. Plachinda, P. Padigi, R. Solanki and S. Rouvimov, *Nanoscale*, 2016, **8**, 2143-2148.
66. W. Wang, K. K. Leung, W. K. Fong, S. F. Wang, Y. Y. Hui, S. P. Lau and C. Surya, *Proc. SPIE 8470, Thin Film Solar Technology IV*, 15 October 2012, **8700E**.
67. Z. Y. Jia, S. L. Li, J. Y. Xiang, F. S. Wen, X. Bao, S. H. Feng, R. L. Yang and Z. Y. Liu, *Nanoscale*, 2017, **9**, 1916-1924.
68. S. Sucharitakul, U. R. Kumar, R. Sankar, F. C. Chou, Y. T. Chen, C. H. Wang, C. He, R. He and X. P. A. Gao, *Nanoscale*, 2016, **8**, 19050-19057.
69. Z. Tian, C. L. Guo, M. X. Zhao, R. R. Li and J. M. Xue, *ACS Nano*, 2017, **11**, 2219-2226.
70. Z. Deng, D. Cao, J. He, S. Lin, S. M. Lindsay and Y. Liu, *ACS Nano*, 2012, **6**, 6197-6207.
71. J. R. Brent, D. J. Lewis, T. Lorenz, E. A. Lewis, N. Savjani, S. J. Haigh, G. Seifert, B. Derby and P. O'Brien, *J. Am. Chem. Soc.*, 2015, **137**, 12689-12696.
72. J. Xia, X. Z. Li, X. Huang, N. N. Mao, D. D. Zhu, L. Wang, H. Xu and X. M. Meng, *Nanoscale*, 2016, **8**, 2063-2070.
73. S. Das, H. Y. Chen, A. V. Penumatcha and J. Appenzeller, *Nano Lett.*, 2013, **13**, 100-105.
74. J. R. Lince, D. J. Carre and P. D. Fleischauer, *Phys. Rev. B*, 1987, **36**, 1647-1656.
75. W. Jaegermann, in *Photoelectrochemistry and Photovoltaics of Layered Semiconductors*, ed. A. Aruchamy, Kluwer Academic Publishers, Netherlands, 1992, ch. 5, pp. 195-295.
76. I. T. McGovern, E. Dietz, H. H. Rotermund, A. M. Bradshaw, W. Braun, W. Radlik and J. McGilp, *Surface Science*, 1985, **152-153**, 1203-1212.
77. G. J. Hughes, A. McKinley, R. H. Williams and I. T. McGovern, *Journal of Physics C-Solid State Physics*, 1982, **15**, L159-L164.
78. R. H. Williams, A. McKinley, G. J. Hughes, V. Montgomery and I. T. McGovern, *Journal of Vacuum Science & Technology*, 1982, **21**, 594-598.
79. T. Tambo and C. Tatsuyama, *Surface Science*, 1989, **222**, 343-350.
80. W. Jaegermann, F. S. Ohuchi and B. A. Parkinson, *Surface Science*, 1990, **201**, 211-227.
81. W. Jaegermann, C. Pettenkofer and B. A. Parkinson, *Vacuum*, 1990, **41**, 800-803.
82. S. McDonnell, R. Addou, C. Buie, R. M. Wallace and C. L. Hinkle, *ACS Nano*, 2014, **8**, 2880-2888.
83. D. Liu, Y. Guo, L. Fang and J. Robertson, *Appl. Phys. Lett.*, 2013, **103**, 183113.
84. P. Bampoulis, R. van Bremen, Q. R. Yao, B. Poelsema, H. J. W. Zandvliet and K. Soththewes, *ACS Appl. Mater. Interfaces*, 2017, **9**, 19278-19286.

85. C. Gong, L. Colombo, R. M. Wallace and K. Cho, *Nano Lett.*, 2014, **14**, 1714-1720.
86. Y. Z. Guo, D. M. Liu and J. Robertson, *ACS Appl. Mater. Interfaces*, 2015, **7**, 25709-25715.
87. J. F. Wager and J. Robertson, *J. Appl. Phys.*, 2011, **109**, 094501.
88. J. R. Chen, P. M. Odenthal, A. G. Swartz, G. C. Floyd, H. Wen, K. Y. Luo and R. K. Kawakami, *Nano Lett.*, 2013, **13**, 3106-3110.
89. A. Dankert, L. Langouche, M. V. Kamalakar and S. P. Dash, *ACS Nano*, 2014, **8**, 476-482.
90. W. Park, Y. Kim, S. K. Lee, U. Jung, J. H. Yang, C. Cho, Y. J. Kim, S. K. Lim, I. S. Hwang, H. B. R. Lee and B. H. Lee, *IEEE Int. Electron Devices Meet.*, 2014, 5.5.1-5.1.4.
91. X. Cui, E. M. Shih, L. A. Jauregui, S. H. Chae, Y. D. Kim, B. C. Li, D. Seo, K. Pistunova, J. Yin, J. H. Park, H. J. Choi, Y. H. Lee, K. Watanabe, T. Taniguchi, P. Kim, C. R. Dean and J. C. Hone, *Nano Lett.*, 2017, **17**, 4781-4786.
92. M. Farmanbar and G. Brocks, *Phys. Rev. B*, 2015, **91**, 161304.
93. S. McDonnell, C. Smyth, C. L. Hinkle and R. M. Wallace, *ACS Appl. Mater. Interfaces*, 2016, **8**, 8289-8294.
94. C. M. Smyth, R. Addou, S. McDonnell, C. L. Hinkle and R. M. Wallace, *J. Phys. Chem. C*, 2016, **120**, 14719-14729.
95. G. A. Tritsarlis, B. D. Malone and E. Kaxiras, *J. Appl. Phys.*, 2014, **115**, 173702.
96. in *CRC Handbook of Chemistry and Physics*, ed. J. R. Rumble, CRC Press/Taylor & Francis, Boca Raton, FL, (Internet Version) 98th edn., 2018, pp. 12-119.
97. D. E. Eastman, *Phys. Rev. B*, 1970, **2**, 1-2.
98. A. J. Biacchi, S. T. Le, B. G. Alberding, J. A. Hagmann, S. J. Pookpanratana, E. J. Heilweil, C. A. Richter and A. R. Hight Walker, *submitted*.
99. J. R. Hajzus, A. J. Biacchi, S. T. Le, C. A. Richter, A. R. H. Walker and L. M. Porter, *Nanoscale*, 2018, **10**, 319-327.
100. B. G. Alberding, A. J. Biacchi, A. R. H. Walker and E. J. Heilweil, *J. Phys. Chem. C*, 2016, **120**, 15395-15406.
101. X. L. Tang, H. W. Zhang, H. Su and Z. Y. Zhong, *Phys. E*, 2006, **31**, 103-106.
102. Z. Y. Zhang, K. Yao, Y. Liu, C. H. Jin, X. L. Liang, Q. Chen and L. M. Peng, *Adv. Funct. Mater.*, 2007, **17**, 2478-2489.
103. J. Osvald, *Phys. Status Solidi A*, 2015, **212**, 2754-2758.
104. A. J. Chiquito, C. A. Amorim, O. M. Berengue, L. S. Araujo, E. P. Bernardo and E. R. Leite, *J. Phys.: Condens. Matter*, 2012, **24**, 225303.
105. R. Nouchi, *J. Appl. Phys.*, 2014, **116**, 184505.
106. D. K. Schroder, J. Wiley & Sons, Hoboken, NJ, 3rd edn., 2006, ch. 3, pp. 127-184.
107. E. H. Rhoderick and R. H. Williams, *Metal-Semiconductor Contacts*, Clarendon Press, New York City, 2nd edn., 1988.
108. S. M. Sze and K. K. Ng, in *Physics of Semiconductor Devices*, J. Wiley & Sons, Hoboken, NJ, 3rd edn., 2007, ch. 3, pp. 134-196.
109. F. A. Padovani and R. Stratton, *Solid-State Electron.*, 1966, **9**, 695-707.
110. H. R. Chandrasekhar, R. G. Humphreys, U. Zwick and M. Cardona, *Phys. Rev. B*, 1977, **15**, 2177-2183.
111. L. M. Yu, A. Degiovanni, P. A. Thiry, J. Ghijsen, R. Caudano and P. Lambin, *Phys. Rev. B*, 1993, **47**, 16222-16228.

112. R. E. Banai, L. A. Burton, S. G. Choi, F. Hofherr, T. Sorgenfrei, A. Walsh, B. To, A. Croll and J. R. S. Brownson, *J. Appl. Phys.*, 2014, **116**, 013511.
113. J. Appenzeller, M. Radosavljevic, J. Knoch and P. Avouris, *Phys. Rev. Lett.*, 2004, **92**, 048301.
114. V. Stevanovic, K. Hartman, R. Jaramillo, S. Ramanathan, T. Buonassisi and P. Graf, *Appl. Phys. Lett.*, 2014, **104**, 211603.
115. W. Albers, H. J. Vink, C. Haas and J. D. Wasscher, *J. Appl. Phys.*, 1961, **32**, 2220-2225.
116. A. J. Biacchi, D. D. Vaughn and R. E. Schaak, *J. Am. Chem. Soc.*, 2013, **135**, 11634-11644.
117. S. Karadeniz, M. Sahin, N. Tugluoglu and H. Safak, *Semiconductor Science and Technology*, 2004, **19**, 1098-1103.
118. A. W. Dweydari and C. H. B. Mee, *Phys. Status Solidi A*, 1975, **27**, 223-230.
119. A. de Kergommeaux, J. Faure-Vincent, A. Pron, R. de Bettignies, B. Malaman and P. Reiss, *J. Am. Chem. Soc.*, 2012, **134**, 11659-11666.
120. S. Lee, A. Tang, S. Aloni and H. S. P. Wong, *Nano Lett.*, 2016, **16**, 276-281.
121. H. H. Berger, *Solid-State Electron.*, 1972, **15**, 145-158.
122. H. Murrmann and D. Widmann, *IEEE Trans. Electron Devices*, 1969, **16**, 1022-1024.
123. C. W. Bale, E. Belisle, P. Chartrand, S. A. Decterov, G. Eriksson, A. E. Gheribi, K. Hack, I. H. Jung, Y. B. Kang, J. Melancon, A. D. Pelton, S. Petersen, C. Robelin, J. Sangster, P. Spencer and M. A. Van Ende, *CALPHAD: Comput. Coupling Phase Diagrams Thermochem.*, 2016, **54**, 35-53.
124. R. L. Gurunathan, J. Nasr, J. J. Cordell, R. A. Banai, M. Abraham, K. A. Cooley, M. Horn and S. E. Mohny, *J. Electron. Mater.*, 2016, **45**, 6300-6304.
125. G. S. Marlow and M. B. Das, *Solid-State Electron.*, 1982, **25**, 91-94.
126. S. E. Mohny, Y. Wang, M. A. Cabassi, K. K. Lew, S. Dey, J. M. Redwing and T. S. Mayer, *Solid-State Electron.*, 2005, **49**, 227-232.
127. H. Park, R. Beresford, R. Ha, H. J. Choi, H. Shin and J. Xu, *Nanotechnology*, 2012, **23**, 245201.
128. G. K. Reeves and H. B. Harrison, *IEEE Electron Device Lett.*, 1982, **3**, 111-113.
129. L. B. Hou, Q. J. Bu, S. Li, D. J. Wang and T. F. Xie, *RSC Adv.*, 2016, **6**, 99081-99087.
130. Y. P. Liao, K. Pan, Q. J. Pan, G. F. Wang, W. Zhou and H. G. Fu, *Nanoscale*, 2015, **7**, 1623-1626.
131. Y. B. Zhu, X. H. Zhang, J. L. Song, W. Wang, F. F. Yue and Q. Ma, *Appl. Catal., A*, 2015, **500**, 51-57.

Chapter 5: Deposition and Characterization of Electron-Beam Evaporated SnS Thin Films and Comparison of Ohmic Contacts

5.1 Introduction

5.1.1 Motivation

The photovoltaic market is currently dominated by first generation, Si-based technologies which comprised 94% of total global annual production (GWp) in 2016.¹ Silicon solar cells benefit from research advances of the silicon industry and the ability to produce Si with very high purity, contributing to relatively high efficiencies for monocrystalline cells. However, the band structure of Si, which consists of an indirect band gap of 1.12 eV and direct transition at ~ 3.3 eV^{2,3} is not optimal for solar energy conversion. According to the Shockley–Queisser limit, band gaps corresponding to the highest theoretical efficiencies are 1.15 eV and at 1.34 eV.⁴ While the band gap of silicon is close to the first maximum, it is indirect, which decreases light absorption. Second generation, inorganic thin film materials CdTe, $\text{CuIn}_{(1-x)}\text{Ga}_x\text{Se}_2$ (CIGS), and amorphous Si (a-Si) possess more favorable band structures for photovoltaics. For example, CIGS has a tunable direct bandgap from 1.035 eV to 1.68 eV,⁵ and CdTe has a direct band gap of ~ 1.5 eV.⁶ These semiconductors have higher absorption coefficients than Si, and therefore require only 1-3 μm of material to absorb sufficient light.⁷ In contrast, the record efficiency silicon-based cell, which is an amorphous Si (a-Si) and crystalline Si (c-Si) heterojunction, has a single crystalline Si wafer thickness of 165 μm .⁸ Thick layers require longer minority carrier diffusion lengths, which necessitate high purity material. Each of these requirements increases manufacturing costs of the cells. Furthermore, the highest efficiency cells utilize single

crystalline Si, which is more expensive to produce than polycrystalline Si. For example, the silicon-based cell with the record efficiency utilizes c-Si produced by the Czochralski process.⁸

Thin film solar cells possess attractive properties from a manufacturing standpoint. Due to their greater tolerance for grain boundaries and shorter requirements for minority carrier diffusion lengths, the demand for high purity and crystalline material is reduced. For example, the grain boundaries of CIGS are inherently passive,⁵ and grain boundaries in CdTe can be passivated by a chlorine treatment, which improves device performance.⁹ Thin film solar cells can be manufactured by additive deposition processes such as being deposited sequentially onto a moving substrate, and can be deposited at relatively low temperatures of 200-500°C versus ~800-1450°C for silicon processing.⁷ Thinner material may also allow for new applications. For example, companies are using CIGS in lightweight products with potential for flexible applications or replacement of roofing material.¹⁰

CdTe and CIGS are the highest efficiency inorganic thin film cells and have reached certified cell efficiencies of 21.0% (CdTe) and 21.7% (CIGS), almost meeting that of multicrystalline Si (22.3%).¹¹ By comparison, the record cell efficiency of a-Si is 10.2 %, that of monocrystalline Si is 25.8%, and that of a monocrystalline Si/a-Si heterojunction is 26.7%.¹¹ These values are for cells with an area greater than 1 cm². CIGS and CdTe cells with area less than 1 cm² have reached even higher efficiencies of 22.6% and 22.1%, respectively.¹¹

Module efficiencies are typically lower than cell efficiencies. The record CdTe module efficiency is 18.6% (First Solar) and that of CIGS is 19.2% (Solar Frontier).¹¹ Record module efficiencies of Si-based cells are 24.4% (crystalline Si), 19.9% (multicrystalline Si), and 12.3% (stabilized amorphous Si/nanocrystalline tandem).¹¹

Solar energy capacity is estimated to reach at least 3 TW of cumulative installations by 2030, with the potential to reach 5-10 TW if costs and photovoltaic performance are sufficiently improved.¹⁰ It has been suggested that the scale up of photovoltaic technologies may face material limitations.¹² The toxicity of Cd¹³ and the scarcity of In and Te^{13, 14} have motivated a search for low-toxic, earth-abundant, inexpensive absorber materials. Some of the alternative materials include Cu₂S, Cu₂O, FeS₂, Zn₃P₂, and CuO.^{15, 16} Particularly of note is copper zinc tin sulfide-selenide (CZTSSe), which has surpassed 10% efficiency. In 2013, CZTSSe deposited by a hydrazine-based solution method at IBM reached a record efficiency of 12.6%. These inorganic, thin film-based cells are much less impacted by instability and degradation than other third generation technologies such as perovskites, dye-sensitized solar cells, quantum dot solar cells, and organic photovoltaics.

SnS, a component of the CZTSSe system, is also an earth-abundant compound with low toxicity. It possesses promising properties for use as an absorber layer in photovoltaics, such as band gaps of ~1.1 eV (indirect) and ~1.3 eV (direct) in bulk form and an absorption coefficient greater than 10^5 cm^{-1} in the visible range (Figure 5.1).^{17, 18} With only two elements, it is potentially a simpler system to control than CZTSSe, which is negatively impacted by a low formation energy of Cu/Zn antisite defects ($[\text{Cu}_{\text{Zn}}^- + \text{Zn}_{\text{Cu}}^+]$) that are believed to produce tail states near the band gap, reducing V_{OC} .¹⁹⁻²¹ Additionally, SnS evaporates congruently,²² such that sublimation of SnS could provide a simple method to deposit cells. (Note that sublimation is used to deposit CdTe.⁶) SnS has potential to reach 24% efficiencies based on Loferski's diagrams^{17, 23} or ~32% based on the Shockley-Queessier limit for single-junction cells.²⁴ While efficiencies have improved since the reported value of 0.29% in 1994,²⁵ the current highest performing SnS cell has an efficiency of only 4.36%, as certified by NREL.²⁶

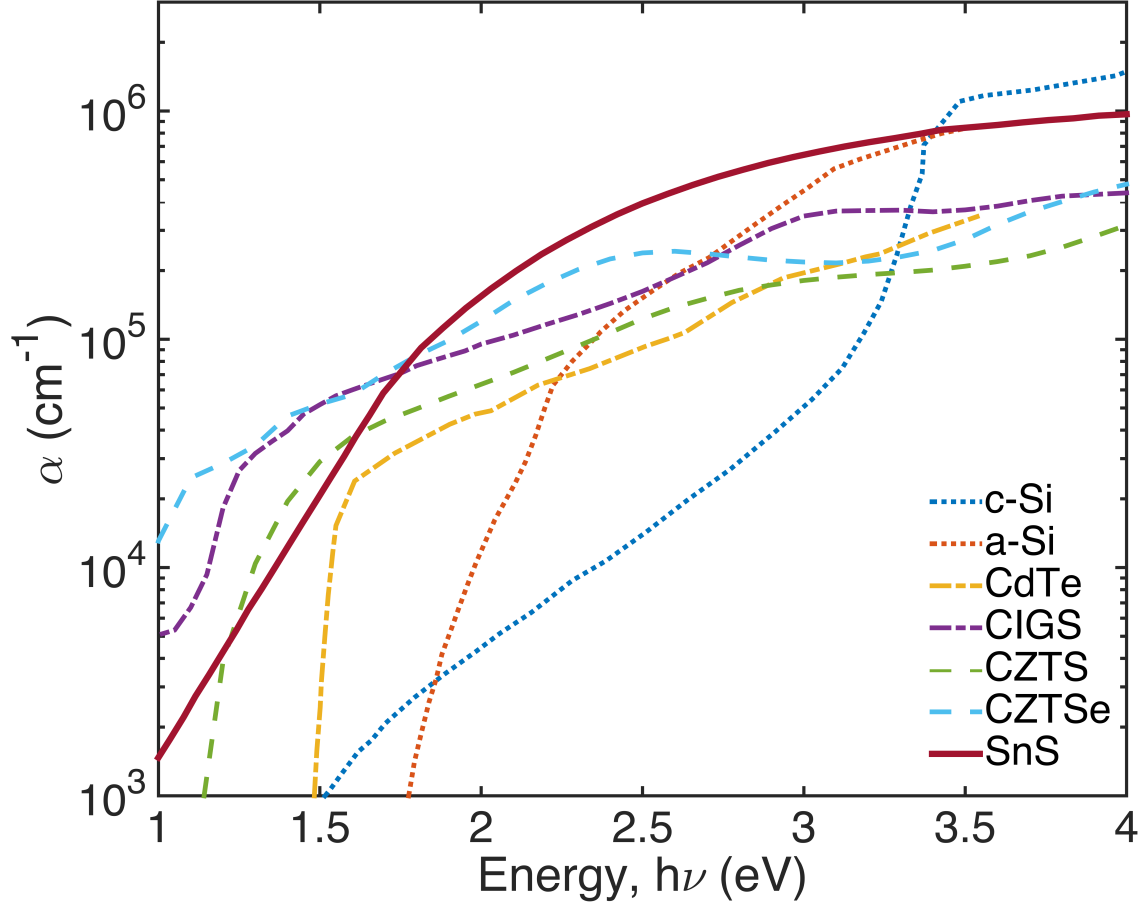


Figure 5.1: Absorption coefficients of different photovoltaic materials from literature. Data for SnS, a-Si, and CdTe are from Banai *et al.*¹⁷ Data for CIGS is from Paulson, *et al.*,²⁷ data for c-Si is from Sze and Ng,²⁸ and data for CZTS and CZTSe are from Adachi.²⁹

Possible limitations to the efficiency are poor band alignment and defect states at SnS/buffer interfaces, improper selection of the back contact, defects in the SnS film, secondary phases, and poor crystalline quality and morphological properties.³⁰ Many SnS solar cell device stacks are based on those developed for CdTe and CIGS and employ CdS as an n-type buffer layer and/or use a Mo back contact,^{25, 26, 31-39} but these may not be ideal for SnS-based solar cells. For example, CdS forms a negative conduction band offset with SnS, which increases recombination at the interface.^{40, 41 42}

The highest efficiency SnS solar cell consisted of a stack of glass/Mo (450 nm)/SnS (400 nm)/SnO₂ (<1 nm)/Zn(O,S):N (30 nm)/ZnO (10 nm)/ITO (300 nm)/Ni (5 nm)/Al (500 nm).²⁶ This device utilized a Mo back contact. However, it has been suggested that Mo should be replaced because it could react with SnS to form MoS₂ and increase resistance.³⁰ MoS₂ forms at Mo/CZTS interfaces after annealing and leads to poor interface morphology, formation of secondary phases at the interface, S diffusion into the contact, and Mo diffusion into CZTS.^{43, 44} ⁴⁵ A similar reaction at the Mo/SnS interface would be detrimental. Mo diffusion into SnS and sulfur vacancies in the SnS layer would be undesirable, as studies found that Mo_{Sn} defects⁴⁶ and sulfur vacancies⁴⁷ form mid gaps states in SnS and are detrimental to minority carrier lifetime.⁴⁸ Impedance spectroscopy measurements by Patel *et. al.* found large inhomogeneities at the Mo/SnS interface corresponding to tunneling assisted recombination.⁴⁹ Alternatively, a recent study by Yang *et. al.* hypothesized that the formation of MoS_x at the Mo/SnS interface may be beneficial, as they found Mo had a lower specific contact resistance than the high work function metal Au.⁵⁰ The contact resistance of Mo after annealing in a substrate configuration measured under AM 1.5 illumination was 0.1 Ω-cm², which may not significantly impact the low efficiencies currently achievable, but will become limiting if efficiencies improve.⁵⁰ Therefore, it is of interest to investigate alternative back contact metals to Mo.

The SnS layer in the record efficiency solar cell was deposited by ALD at T_{sub} = 200°C, then annealed in H₂/S ambient to promote grain growth while suppressing sulfur vacancy formation.²⁶ ALD can produce high quality films but is a slow process and is not economical or compatible with large-scale manufacturing.

5.1.2 Contribution of This Work

This study concerns the challenges of SnS back contact selection and processing-property relationships of SnS thin films deposited by electron-beam (e-beam) evaporation. E-beam evaporation is a less explored method for deposition of SnS thin films that can allow for higher deposition rates than ALD. In this study, the impact of film thickness, substrate temperature, and post annealing on electrical and optical properties, morphology, and presence of secondary phases of SnS films deposited by e-beam evaporation are determined. It is found that at substrate temperatures of 100°C and 200°C, a mixture of α -SnS and π -SnS phases form, while at room temperature and 300°C, α -SnS is deposited. These phases have different electrical, structural and optical properties, and understanding conditions at which they form would be beneficial. Additionally, different metal contacts are explored as replacements to the Mo back contact. The specific contact resistances of metals with a range of work functions (Ti/Au, Ru/Au, Ni/Au, and Au) on SnS thin films were compared before and after annealing.

5.1.3 Sn-S System

An atmospheric pressure phase diagram of the Sn-S system based on work by Sharma and Chang^{51, 52} is displayed in Figure 5.2. Three stable intermediate tin sulfide phases exist: tin monosulfide (SnS) known as the mineral herzenbergite, tin sesquisulfide (Sn₂S₃) or ottemannite, and tin disulfide (SnS₂) or berndtite, which exist naturally as rare minerals.⁵³ Sn₃S₄ and Sn₄S₅ have also been reported, but their existences have been questioned more recently.^{22, 54, 55}

Tin monosulfide is most stable in the α -SnS phase at standard conditions. α -SnS is orthorhombic (space group *Pnma*, lattice constants $a = 1.1180$ nm, $b = 0.3982$ nm, and $c = 0.4329$ nm⁵⁶) and can be thought of as a distorted rocksalt structure, where Sn(5s) electron lone pairs

polymorphs have not been determined.⁵⁹ α - Sn_2S_3 phase is orthorhombic (space group $Pnma$).⁶⁰ δ - Sn_2S_3 melts peritectically at 760°C to form β - SnS_2 and a liquid phase.⁵¹ α - Sn_2S_3 has the narrowest band gap of the tin sulfides (~ 0.82 eV, indirect, ~ 0.95 eV, direct),⁶¹ and is reported to be intrinsically n-type,⁶² although it has been suggested that the mixture of Sn^{2+} and Sn^{4+} may allow n-type or p-type behavior.⁶³ Despite its narrower band gap, the onset of strong optical absorption does not occur until ~ 1.75 eV, making Sn_2S_3 less desirable for solar cell applications.⁶¹

α - SnS_2 , or 2H- SnS , (trigonal, space group $P\bar{3}m1$) has a hexagonal unit cell and is stable at room temperature.⁶⁴ It undergoes a transition at 691°C to β - SnS_2 . The crystal structure of β - SnS_2 in the reported phase diagram is unclear.^{51, 54} β - SnS_2 melts congruently at 865°C.⁵¹ Over 70 polytypes of SnS_2 have been established, which share the same hexagonal, close packed structure but possess different layer stacking and interlayer lattice parameters.⁶⁵ SnS_2 has generated interest as a 2D material because of its layered structure. 2H- SnS and 4H- SnS are n-type semiconductors.^{66 62} A reported calculated band gap of bulk 2H- SnS is 2.24 eV and is indirect.⁶² The band gap of bulk 4H- SnS is reported to be similar, and remains indirect in a monolayer without significantly increasing or decreasing.⁶⁷ A multilayer SnS_2 transistor with a top, solution-gate was reported to have a mobility of $230 \text{ cm}^2/(\text{V}\cdot\text{s})$. In addition, SnS_2 has been demonstrated as a buffer layer for SnS thin film solar cells.⁶⁸ However, it may not be ideal, as calculations indicate SnS_2 forms a negative conduction band offset with SnS ,⁶² which would likely increase recombination rates at the interface.

The phase diagram indicates that there is a eutectic transformation at 738°C from a liquid to β - SnS and γ - Sn_2S_3 , a monotectic transformation from a liquid to β - SnS_2 and liquid S at 841°C, and a monotectic transformation from a liquid to β - SnS and liquid Sn at 860 °C.⁵¹ These

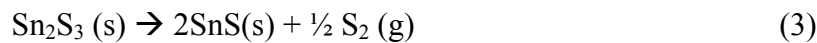
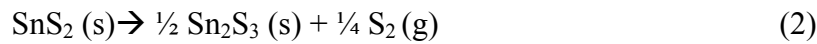
temperatures are greater than the post-deposition processing temperatures used in this study. The films in this study are deposited and annealed in vacuum; therefore it is of interest to know the phase diagram at lower pressures. Low-pressure phase diagrams of the S-Sn system were calculated by Lindwall, *et. al.*⁵⁴ for pressures as low as 10^{-3} mbar ($\sim 7.5 \times 10^{-4}$ Torr). As pressure decreased, there were fewer phases present in the phase diagrams. For example, at 10^{-3} mbar, α -SnS sublimates at a temperature lower than its transition temperature to β -SnS, therefore β -SnS does not form.⁵⁴ The results indicate that at certain temperatures and pressures, α -SnS can exist over a wider range of stoichiometry than α -SnS at atmospheric pressure.⁵⁴ This is beneficial to vacuum processing.

5.1.3 Congruent Evaporation of SnS

SnS is reported to evaporate congruently, lending itself well to evaporation deposition methods.⁶⁹ A sublimation study by Piacente *et. al.*²² using a torsion-Knudsen effusion method found that SnS predominately vaporizes by the reaction



A mass spectrometry study found a small amount of Sn_2S_2 vapor.⁷⁰ The sulfur rich sulfides were found to vaporize by first forming sulfur gas and solid SnS as residue according to the reactions²²



The vaporization of SnS_2 occurs by the consecutive reactions (2) (3), (1) and that of Sn_2S_3 by reactions (3), (1). This suggests that SnS_2 and Sn_2S_3 thin films can be annealed in vacuum to form pure SnS, which has been reported.^{69, 71} The SnS(g) vapor pressure over SnS(s) , p , as a function of temperature, T , was determined to be $\log p \text{ (kPa)} = (9.40 \pm 0.10) - (10.7 \pm 0.1) \times 10^3 / T$,²² and is plotted in Figure 5.3 This relation is in good agreement with those determined in

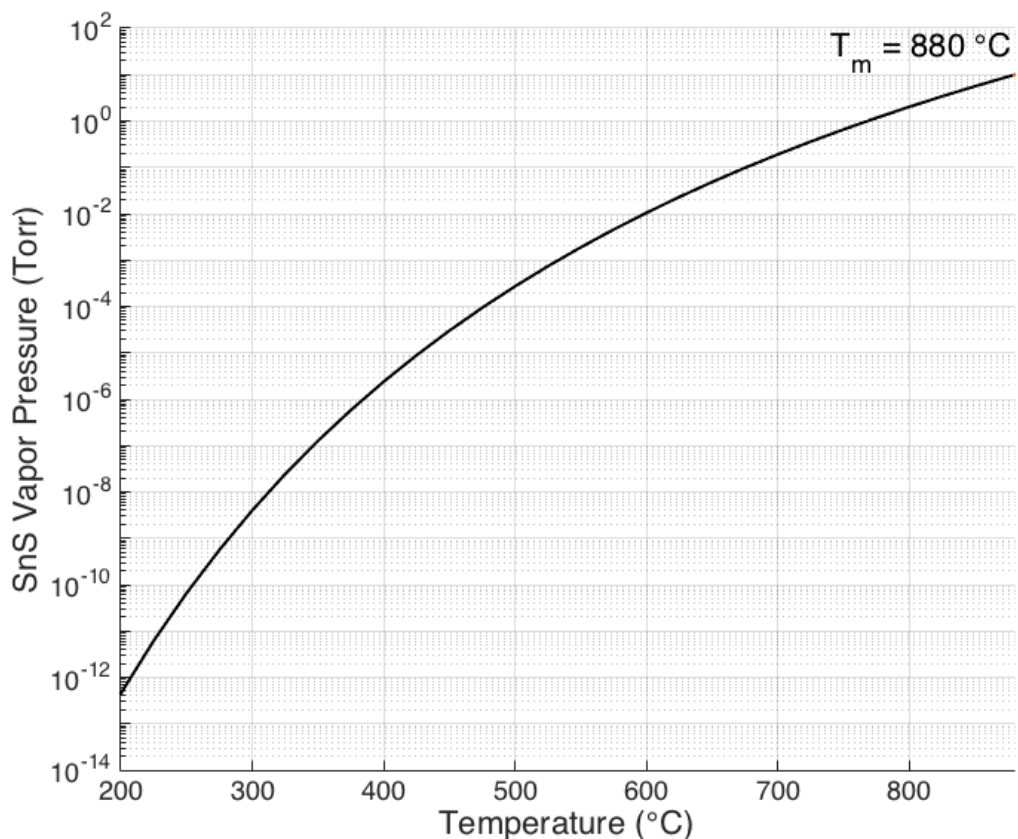


Figure 5.3: Vapor pressure of SnS (g) over SnS (s) as a function of temperature. Equation parameters determined by Piacente et al.²² were used. The melting temperature of SnS is 880 °C.

other tin sulfide sublimation studies.^{70, 72, 73} It can be seen in Figure 5.3 that the vapor pressure of SnS reaches 10^{-3} mbar at a temperature lower than the α - to beta phase transition of SnS, in agreement with the low temperature phase diagrams calculated by Lindwall, *et. al.*⁵⁴ The deposition and vacuum annealing pressures utilized in this thesis chapter are in the 10^{-7} to 10^{-9} Torr range. Processing temperatures must be low enough to prevent re-evaporation of SnS films at these pressures.

5.1.4 SnS Polymorphs

In addition to the equilibrium α -SnS and β -SnS phases, three cubic polymorphs of SnS have been reported: the rocksalt (space group $Fm\bar{3}m$),⁷⁴ zincblende (space group $F\bar{4}3m$),⁷⁵ and the recently discovered π -SnS phase (space group $P2_13$).⁷⁶⁻⁷⁹ Crystal structures of the tin sulfide phases are displayed in Figure 5.4.

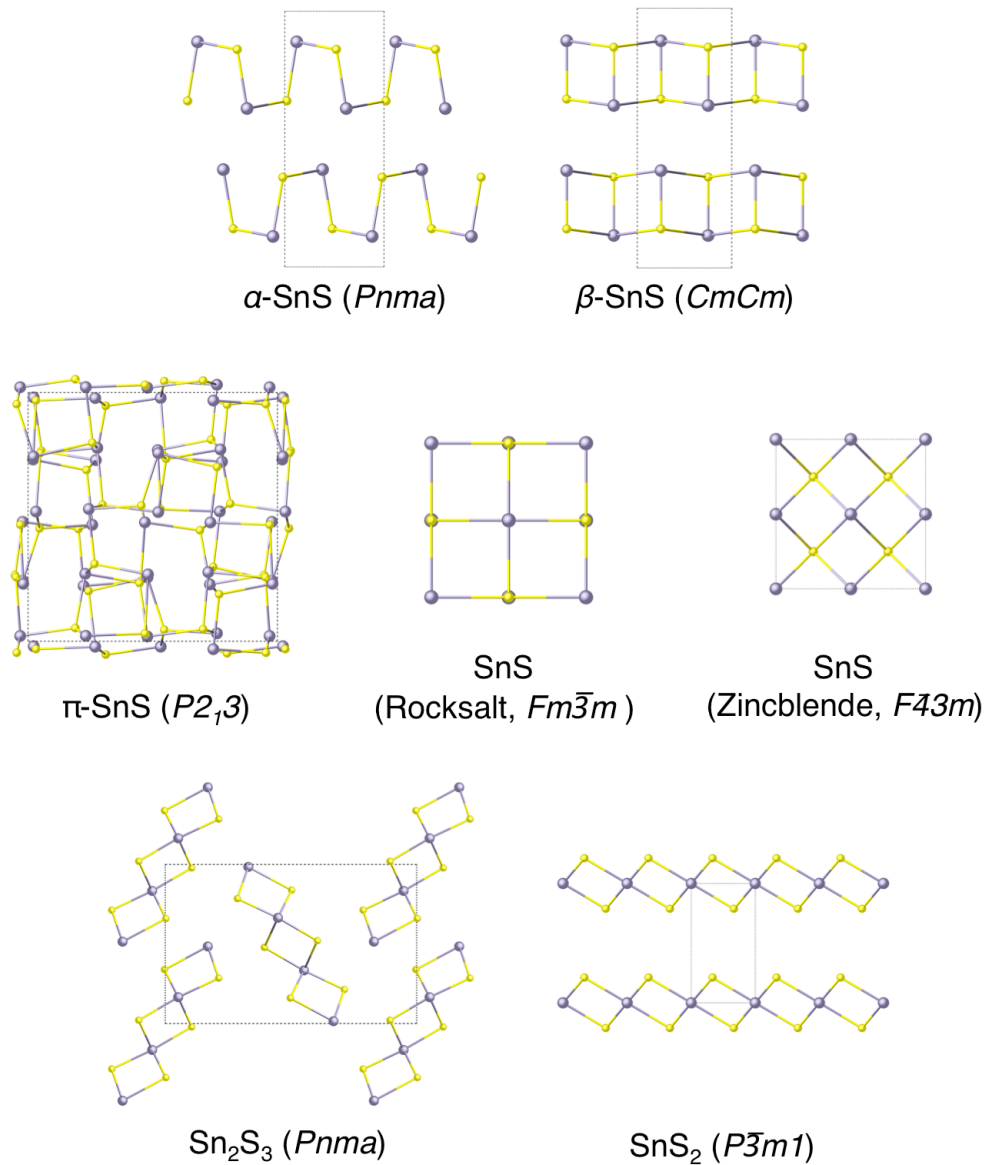


Figure 5.4: Crystal structures of tin sulfide phases and SnS polymorphs. Lattice parameters and atomic positions are from Villars⁵⁶ (α -SnS, rocksalt SnS, Sn_2S_3), Abutbul *et al.*⁷⁸ (π -SnS), Chattopadhyay *et al.*⁵⁸ (β -SnS), and materialsproject.org⁸⁰ (zincblende SnS, SnS_2).

Orthorhombic, α -SnS can be described as having a distorted rocksalt structure. It was found that depositing SnS thin films onto a NaCl substrate at 150 °C could “undistort” the lattice, and an epitaxial rocksalt phase of SnS was observed.⁷⁴ Rocksalt SnS has also been stabilized by alloying SnS with CaS.⁸¹ Phonon dispersion calculations indicate that rocksalt SnS is dynamically unstable in ambient conditions but can be stabilized under moderate compression or pressure.⁸²

The zincblende structure has been reported in literature for thin films^{34, 83, 84} and nanocrystals,⁸⁵⁻⁸⁷ including an α -SnS/zincblende SnS heterojunction solar cell.³⁸ However, more recent studies indicate that zincblende SnS is not a stable phase and was likely misidentified.^{88, 89} Enthalpies of formation calculated by Skelton, *et. al.*⁸² indicate the zincblende structure is unlikely to form at typical synthesis conditions.^{82, 88} Molecular dynamic simulations and phonon calculations have additionally found the zincblende phase to be dynamically unstable.⁸⁸ The first report of zincblende SnS was a thin film evaporated onto NaCl.⁷⁵ The XRD spectra of the rocksalt and zincblende phases are very similar, possibly leading to misidentification.⁸⁸ It has been noted that reported experimental XRD patterns of the zincblende phase exclusively consist of a mixture of zincblende and α -SnS reflections.⁸⁹ It was shown that modifying the α -SnS unit cell by expanding the intralayer lattice parameters and contracting the interlayer lattice parameter could account for all of the observed reflections as a single pseudotetragonal phase.⁸⁹

More recently, a cubic π -SnS phase has been discovered,⁷⁶ which can fully account for previously reported zincblende XRD patterns for SnS nanocrystals and films. It has a 64 atom unit cell with lattice parameter $a = 1.159 \text{ nm} - 1.17 \text{ nm}$.^{76, 78} This is approximately twice that of the rocksalt phase ($a = 0.58 \text{ nm}$) and it has been suggested that π -SnS is a “defect ordered variant” of rocksalt SnS.⁷⁶ Its space group, $P2_13$, and atomic model were determined from

precession electron diffraction and precession electron diffraction tomography data.⁷⁶ Atomic positions solved by analysis of an XRD spectrum of a SnS thin film deposited by chemical bath deposition were in agreement with this π -SnS structure.⁷⁸ The π -SnS phase is metastable with higher formation energy than α -SnS and β -SnS, but lower formation energy than the rocksalt phase.⁸² π -SnS was also determined to be dynamically stable from phonon dispersion calculations. It has been suggested that cubic SnS is more likely to exist in the π -SnS phase than the rocksalt phase under typical conditions.⁸²

The optical band gaps of π -SnS are reported to be 1.52 eV (indirect),⁷⁷ and ~ 1.66 -1.75 eV (direct),⁹⁰⁻⁹² from UV-vis measurements, which generally agree with calculated band gaps of 1.72 eV (indirect) and 1.74 eV (direct).⁷⁹ π -SnS is p-type^{79, 91} and a mobility of 77.7 cm²/Vs was reported for a π -SnS thin film synthesized by chemical bath deposition.⁹¹ Electron and hole effective masses of π -SnS were calculated to be 0.76 m_0 and 1.22 m_0 , respectively.⁴⁷ In addition to chemical bath deposition,⁹⁰⁻⁹³ π -SnS has been synthesized by thermal evaporation,⁹⁴ ALD,^{95, 96} aerosol assisted CVD,⁹⁷ and solution synthesis methods.⁷⁶

It has been suggested that thin films with a cubic structure may perform better in solar cells than the highly anisotropic α -SnS phase.⁹⁸ A solar cell with a π -SnS absorber layer reached 1.28% efficiency in 2015.⁹⁴ Its open circuit voltage ($V_{OC} = 470$ mV) was higher than that of the record efficiency α -SnS cell ($V_{OC} = 372$ mV).^{26, 92} The stack consisted of stainless steel/ π -SnS/CdS/ZnO/ZnO:Al. XPS studies have indicated that, similar the α -SnS phase, Zn(O:S) has a favorable band alignment with π -SnS for certain O:S ratios.⁹⁹

5.1.5 SnS Thin Film Deposition Methods and Processing

Film properties such as S:Sn ratio, grain size, morphology, structure, and resistivity can vary with deposition method, deposition conditions and post-processing such as annealing. SnS thin films have been deposited by a variety of methods including thermal evaporation,¹⁰⁰⁻¹⁰⁶ sputtering,¹⁰⁷ chemical vapor deposition (CVD),¹⁰⁸⁻¹¹⁰ electron beam evaporation,¹¹¹⁻¹¹³ electrochemical deposition,¹¹⁴⁻¹¹⁷ spray pyrolysis,¹¹⁸⁻¹²¹ vapor transport,¹²² chemical bath deposition,^{38, 123-126} sulfurization of Sn films,^{39, 127} atomic layer deposition,¹²⁸ molecular beam epitaxy,¹²⁹ and close spaced sublimation.¹³⁰

5.1.6 Review of Electron-Beam Evaporated SnS Films

Although less commonly used than other methods to deposit SnS, e-beam evaporation was employed in this study, due to its simplicity and the presence of an ultra-high vacuum e-beam system in our laboratory. A review of previous studies on e-beam evaporated SnS films is described in this section.

In 2003, Tanusevski *et. al.*¹¹¹ e-beam evaporated SnS films from a 96% pure powder SnS source onto glass substrates at 300°C. The depositions occurred at $\sim 6 \times 10^{-6}$ Torr and a rate of 3 nm/s. The films were characterized using XRD, AFM, UV-vis spectroscopy, photoconductivity measurements, and resistance measurements. XRD spectra displayed peaks corresponding to α -SnS. The indirect and direct optical band gaps were 1.23 eV and 1.38 eV, respectively.

Henry *et. al.*¹¹² e-beam evaporated SnS thin films from a pellet source made from solution-synthesized nanoparticles at a pressure of 4×10^{-4} Torr at room temperature. Films were post-annealed at 100°C, 200°C, and 300°C for 1 hr in an unspecified ambient and were characterized with XRD and UV-vis optical spectroscopy. As-deposited films did not exhibit XRD peaks and were believed to be amorphous. After annealing, a single XRD peak at 31.6°

was present, which was attributed to the α -SnS (111) reflection. The intensity of the peak increased with annealing temperature. Absorbance and transmittance spectra were measured and an optical direct band gap of 1.57-1.77 eV was extracted.

Gedi *et. al.*¹³¹ performed short, high temperature (587 °C) anneals on e-beam evaporated SnS films evaporated from 99.999% SnS flakes. Films were deposited on Mo-coated glass at room temperature at 10^{-6} Torr. Short (1-5 min) anneals were performed in an evacuated tube furnace that was back-filled with N₂, which also served as a carrier gas. XRD, reflectance measurements, SEM, EDX, Raman spectroscopy and TEM were performed on the films. XRD and Raman spectroscopy indicated the films were α -SnS. The as-deposited films were crystalline, (in contrast to those deposited by Henry, *et. al.*), and exhibited a vertically aligned platelet morphology. After high temperature annealing, α -SnS single crystals with lengths on the orders of microns formed on the surface of the nanocrystalline films. The annealed films were non-uniform with rough surface morphology.

Park *et. al.*¹¹³ e-beam evaporated SnS films at different substrate temperatures (T_{sub}) of 25°C, 100°C, 200°C, 250°C, and 280°C. Films were deposited from a 99.99% pure SnS powder source at a rate of 0.1-0.7 nm/s onto Si, SiO₂, or soda-lime glass substrates. Measured resistivities of the films were 430 Ω -cm, 51 Ω -cm, and 350 Ω -cm for T_{sub} = 25 °C, 100 °C, and 200 °C, respectively. The resistance of film deposited at 250 °C was out of range of the instrument. XRD spectra of films deposited at substrate temperatures of 200 °C and 250 °C contained a peak at $2\theta \approx 26.6^\circ$, which does not correspond to α -SnS. This peak, along with an observed shift of the (101) and (111) α -SnS peaks for the film deposited at 250 °C were attributed to the presence of the Sn₂S₃ phase. The direct band gaps of films deposited at 200 °C and 250 °C were larger than those deposited at 25 °C and 100 °C, which was attributed the

presence of Sn_2S_3 in the films at higher deposition temperatures. The S/Sn ratio of the film deposited at 250 °C was found to be sulfur rich (S/Sn \sim 1.2) consistent with a mixture of Sn_2S_3 and SnS. The film deposited at 200 °C had an S/Sn ratio of \sim 1.0. It was believed that there was a phase evolution from SnS at low substrate temperatures to Sn_2S_3 at high substrate temperatures.

It is possible that the recently reported π -SnS is present in the 200 °C film instead of Sn_2S_3 . The reported peak positions of 26.60°, 30.80°, and 31.77° in the films deposited at 200 °C and 250 °C closely match the reported π -SnS Bragg reflections. π -SnS also has a larger optical direct band gap than α -SnS, and a mixture of α -SnS and π -SnS could alternatively explain the reported increase in band gap at this temperature.

θ - 2θ XRD characterization alone is not necessarily sufficient to unambiguously determine the phase of tin sulfide films because the different phases have similar d-spacings and observed Bragg reflections may in some cases be indexed to multiple phases. Additionally, there is a lack of information on the impact of annealing on electrical properties of e-beam evaporated films. Further characterization of e-beam evaporated films at different substrate temperatures and after annealing would be beneficial.

5.1.7 Review of Contacts to SnS

At the beginning of this study, few contact studies had been performed on SnS thin films.^{132,115,133,134} The findings of these studies are summarized in Table 5.1. With the exception of Au, the metals studied have a small range of work functions (4.12-4.42 eV). SnS is typically p-type; therefore metals with higher work functions should be investigated as well. Contacts had poor thermal stability. In, Sn, and Zn have melting points lower than the temperatures at which they were annealed. Somewhat conflicting results were reported. For example Sato *et. al.*¹¹⁵ found that resistance increased from In (ϕ_m = 4.12 eV) , Au (5.1 eV), Ag (4.26 eV) to Al (4.28

eV), while Devika *et. al.*¹³² found that resistance increased from Zn (4.33 eV), In (4.12 eV), Sn (4.42 eV), Al (4.28 eV), to Ag (4.26 eV). Ag was found to form a Schottky contact with a barrier height of 0.649 eV on sheets cleaved from SnS single crystals.¹³⁵ Devika *et. al.*¹³² observed ohmic behavior for Al, while Mathews *et. al.*¹³⁴ and Ghosh *et. al.*¹³⁶ observed rectifying behavior.

Table 5.1: Summary of contacts to SnS thin films in literature. R refers to resistance measured between two contacts.

Metal	WF (eV)	Melting Point (°C)	Properties
Zn	4.33	419.5	Ohmic as deposited, lower R than Ag, In, Sn, Al ¹³³ Rectifying/semi-ohmic, annealing up to 300°C decreased R. Higher R than Ag, Au, In ¹¹⁵
Al	4.28	660	Ohmic as deposited. Higher R than In, Sn, lower R than Ag. Annealing up to 400°C decreased R ¹³² Schottky barrier as deposited. $n=1.45$ ¹³⁴
Ag	4.26	961.8	Poor reproducibility. Contact became darker, possibly forming Ag ₂ S. High R than In, Au. Lower R than Al. ¹¹⁵ Ohmic as deposited from -6V to +6V, but not for entire -10V to +10V range. As deposited R higher than In, Sn, Al. Annealing at 300°C-500°C decreases R and contact becomes ohmic from -8V to +8V. After annealing at 500 °C, R was lowest of metals tested. ¹³²
Au	5.1-5.2	1064	Ohmic as deposited. R close to that of In, but slightly higher. Lower R than Ag, Al ¹¹⁵
In	4.12	156.6	Ohmic as deposited. Lower R than Au, Ag, Al. Annealing from 100-300°C increased R. Annealing at 400°C slightly decreased R. Metal evaporated upon annealing. ¹¹⁵ Ohmic as deposited. Lower R than Sn, Al, Ag. R decreases after 300°C anneal, then greatly increases after 400°C and 500°C anneal. Metal evaporated upon annealing. ¹³²
Sn	4.42	231.9	Ohmic as deposited. Higher R than In. Lower R than Al, Ag. R steadily increases after annealing at 300, 400, 500°C, but remains ohmic. Can evaporate during annealing. ¹³²

Resistance did not follow a trend with metal work function, and many metals (Au, In, Sn, Zn) formed ohmic contacts as deposited. Interfacial reactions are expected for many metals used in these studies, which could alter the work function at the interface.

More recently, two papers have been published on contacts to SnS thin films. Gurunathan, *et. al.*,¹³⁷ measured contact resistances of the high work function metals Pd and Au using CTLM structures. The ~200 nm thick SnS films were deposited by sputtering SnS₂ followed by a vacuum anneal to form to SnS. They found that Au had a lower specific contact resistance than Pd as-deposited. The contact resistance of Pd decreased upon annealing at 300 °C and 400 °C, and the Pd contact degraded at 500 °C. Mixing of Pd and SnS at the interface was observed through cross sectional SEM and Auger electron spectroscopy. Au contacts were found to be stable upon annealing, with a minimum contact resistance at 400°C.

Yang, *et. al.*,⁵⁰ measured specific contact resistances of Mo, Au, and Ti with CTLM and TLM patterns in the superstrate configuration and in a TLM pattern with large contact dimensions in a substrate configuration. As-deposited contact resistance decreased with work function from Ti to Mo to Au. They found strong Fermi level pinning based on temperature-dependent specific contact resistance measurements and the thermionic emission model. After annealing, the specific contact resistance of Mo became lower than Au. The contact resistance of Mo after annealing under AM 1.5 illumination was 0.1 $\Omega\text{-cm}^2$, which may not significantly impact the low efficiencies currently achievable, but is believed to become limiting if efficiencies improve.⁵⁰ Therefore, it remains of interest to identify lower resistivity contact metals to SnS.

5.2 Deposition and Characterization of Electron-Beam Evaporated SnS Thin Films

5.2.1 Experimental Methods: Deposition of SnS Thin Films

SnS thin films were deposited by e-beam evaporation from a granular SnS source (Sigma Aldrich, 99.99%) in a glassy coated graphite crucible liner (Thermionics). The base pressure of the deposition chamber was in the 10^{-9} Torr range. Films were deposited at a rate of 0.3-0.4 Å/s, as monitored by a QCM, with the exception of the 515 nm thick film in Section 6.2.3, which was deposited at a rate of 0.3-1 Å/s. SnS sublimed and high deposition rates could be achieved at low e-beam currents of ~25 mA. Pressures during depositions were in the $10^{-7} - 10^{-8}$ Torr range.

SnS films were deposited onto silicon, soda lime glass (Corning), or borosilicate glass (Lab Safety Supply) slides. SnS films deposited onto silicon substrates were used for SEM and EDX characterization. Films on soda lime glass substrates were used for XRD, SEM, Raman spectroscopy, transmittance and reflectance measurements, Hall and resistivity measurements, and AFM. Films on borosilicate glass were used for CTLM measurements, as well as initial studies in Section 5.2.3 for XRD, Hall measurements, AFM, transmittance, and reflectance measurements. Prior to deposition, all substrates were sonicated for 15 minutes sequentially in acetone, isopropanol, and deionized water, then blown dry with N₂. Substrate temperatures, T_{sub} , during depositions were room temperature (RT), 100°C, 200°C or 300°C. Select samples were post-annealed in the vacuum deposition chamber at 300°C. Pressure during vacuum annealing was in the 10^{-7} Torr range.

5.2.2 Results: Characterization of SnS Source

As received commercial SnS powders have been reported to contain Sn_2S_3 ,⁶⁹ therefore, the SnS source used in this study was first characterized to determine if secondary phases were present. Figure 5.5 a is an SEM image of the granular SnS source showing layered particles of varying size. XRD $\theta/2\theta$ scans were performed on the SnS source as received and after e-beam evaporations and results are displayed in Figure 5.5 b. The as received powder can be indexed to orthorhombic α -SnS. No Sn_2S_3 or SnS_2 peaks were observed, indicating these phases are not present within the detection limit of XRD. The small peak at $\sim 34^\circ$ can be indexed to the SnO_2 (101) reflection (JCPDS 41-1445). SnS is known to form an oxide.¹³⁸

The XRD spectrum after depositions is similar with some difference in peak intensities, which may be due to the large crystallite size of the SnS powder source. EDX indicated that the source becomes sulfur deficient after evaporations with 41.45 (± 4.11) atomic % S and 58.55 (± 4.11) at. % Sn.

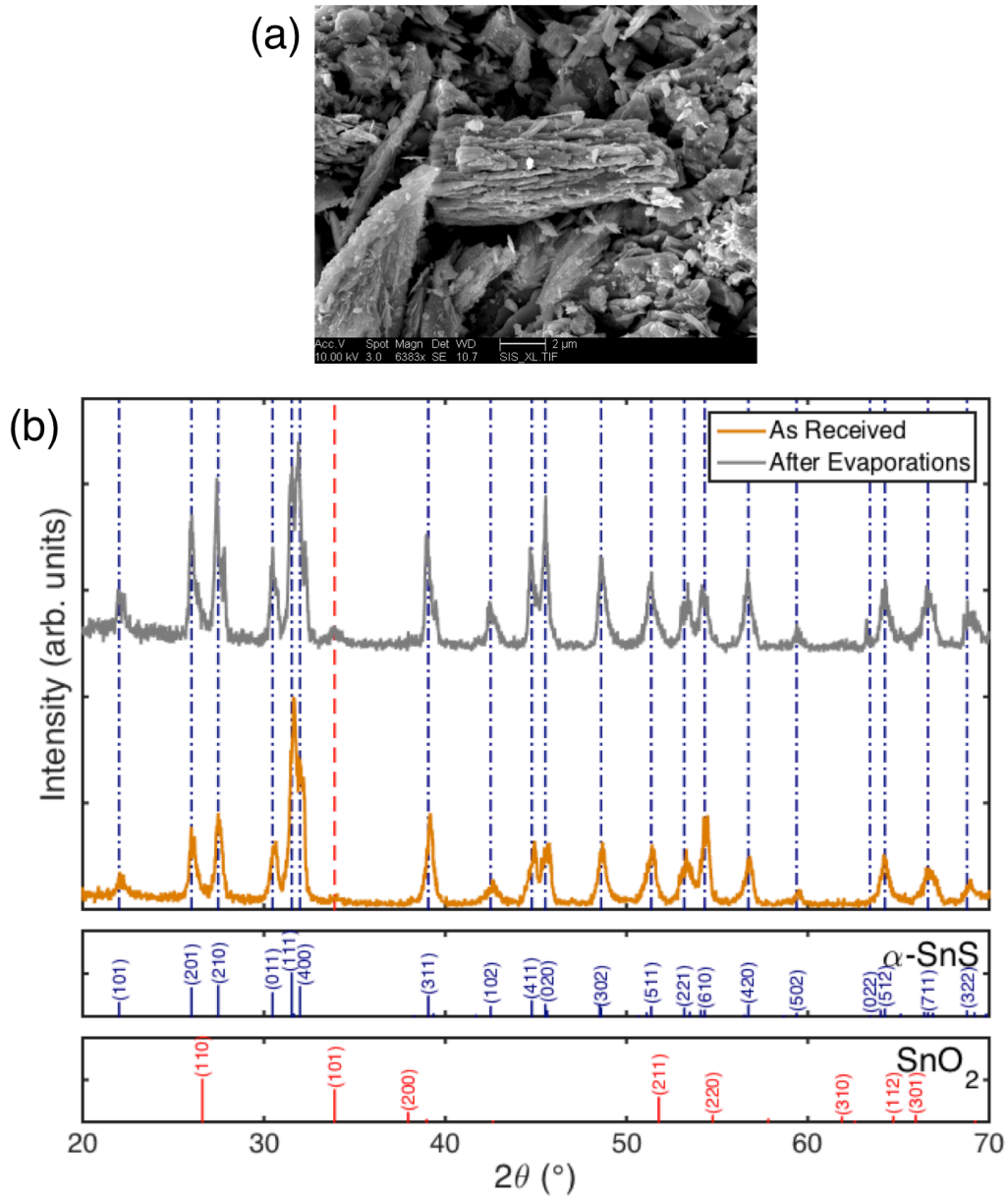


Figure 5.5: (a) SEM image of SnS granular source. (b) XRD scan of SnS source as received and after performing e-beam evaporations.

5.2.3 Results: Deposition and Characterization of 50 nm and 515 nm Thick SnS Films

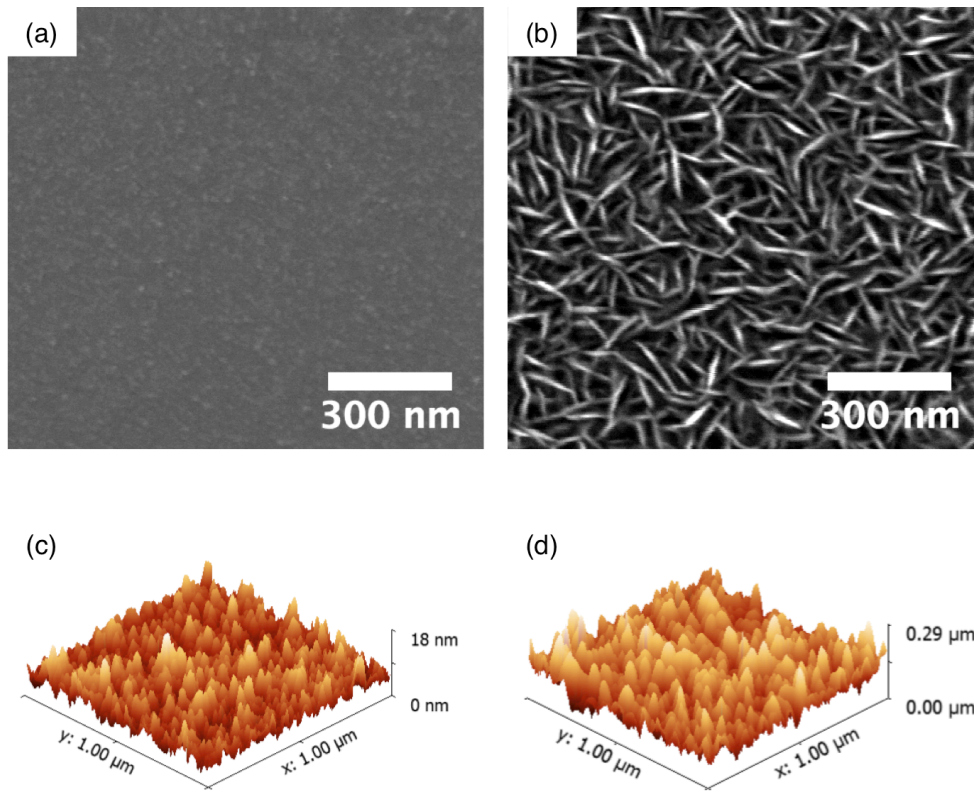


Figure 5.6: SEM (a,b) and AFM topography (c,d) images of (a,c) 50 nm and (b,d) 515 nm thick SnS films deposited on borosilicate glass at room temperature.

Impact of thickness on morphology

SEM images of SnS films deposited at room temperature in Figure 5.6 a, b indicate a 50 nm thick film is relatively planar with bumps that are tens of nanometers in size (RMS roughness = 2.08 nm), whereas a 515 nm thick film has larger, non-equiaxed grains and appears porous (RMS roughness = 36.9 nm). Thicknesses were determined by AFM. In literature, cross sectional SEM images of 370 nm – 1.5 μm thick SnS films grown by ALD, thermal evaporation, and e-beam evaporation at low substrate temperatures (room temperature or 120°C) show initially denser grains for the first ~50-90 nm followed by the formation of a vertically aligned platelet

morphology, consistent with what is seen here.^{113, 139, 140} Vertical nanosheet morphology has also been observed for SnSe films grown by physical vapor transport.¹⁴¹ The vertically aligned platelet morphology may be a result of the anisotropic surface energies of SnS and a difference between interlayer and intralayer bonding. Calculated surface energies increase from 0.26 J/m² for the [100], 0.38 J/m² for the [011], 0.57 J/m² for [010], 0.58 J/m² for [001] and [110], and 0.63 J/m² for [101] surfaces of SnS (for a unit cell with $a = 1.112$ nm, $b = 0.395$ nm, and $c = 0.424$ nm).¹⁴² Atoms may preferentially attach to the dangling covalent bonds at edge plane surfaces, resulting in faster growth rates along these planes at low substrate temperatures.

For applications such as contact resistance measurements, the thinner, more planar film is desired. The high surface area of the thicker films could be useful for applications such as anode materials for lithium ion batteries¹⁴³ or for photoelectrochemical water splitting.¹⁴⁴

Impact of annealing on electrical properties and composition of 50 nm thick films

Vacuum annealing the 50 nm thick film was explored with the intent of lowering its sheet resistance for specific contact resistance studies. The film was annealed at 300°C in the vacuum chamber for 1 hr. Hall measurements were performed using an MMR Technologies Hall and van der Pauw measurement system at room temperature. Ti/Au (50/50 nm) contacts were deposited on the unannealed sample and Ni/Au (50/50 nm) contacts were deposited on the annealed sample by e-beam evaporation in a van der Pauw configuration. All contacts were determined to be ohmic by performing I - V sweeps with a Signatone probe station. Silver paste was applied on top of the evaporated contacts to protect the films from the Hall measurement system probes. Ag paste solvents were evaporated at 100°C on a hot plate in ambient.

The MMR technologies system has a capability of measuring carrier mobilities from 1 cm²/(V-s) to 10⁷ cm²/(V-s), resistivities of 10⁻⁴ Ω-cm to 10¹³ Ω-cm, and carrier concentrations of

10^3 cm^{-3} to 10^{19} cm^{-3} with an accuracy of $\pm 2\%$ mid-range and $\pm 5\%$ end-range. For these films, the mobility is near the end-range of the measurement system; therefore an accuracy of $\pm 5\%$ is expected for the mobility. In the van der Pauw configuration, the four contacts should be deposited at the very edges of the sample. In this case there was an approximately 1 mm space between the edge of the SnS film and the contacts, which could result in an $\sim 10\%$ error in the measurement. Measurements were repeated 10 times for each sample.

The results of van der Pauw Hall measurements on the 50 nm thick films on borosilicate glass are displayed in Table 5.2. The mobilities of the as deposited and annealed films were similar and within the error, while the annealed film had a lower resistivity and higher carrier concentration. Both films were measured to be p-type, as expected.

The elemental composition of the as deposited and annealed films was measured with a Phillips XL30 SEM with Oxford Inca EDX software. 515 nm thick SnS films were used for EDX measurements to allow sufficient x-ray signal generation from the film, since the penetration depth of the electron beam during EDX is on the order of microns. 10 kV accelerating voltage was used for data acquisition and the as received 99.99% pure SnS powder was used as a standard for quantification at 10 kV. Films on silicon substrates, instead of glass

Table 5.2: Van der Pauw resistivity and Hall measurement results for as-deposited and annealed (300 °C / 1 hr) 50 nm thick SnS films on borosilicate glass. Error listed is the standard deviation.

	As Dep	Annealed
Resistivity ($\Omega\text{-cm}$)	750 ± 13	100 ± 1.1
Mobility ($\text{cm}^2/\text{V-s}$)	5.4 ± 0.5	4.7 ± 0.2
Density (cm^{-3})	$1.6 (\pm 0.1) \times 10^{15}$	$1.3 (\pm 0.08) \times 10^{16}$
Hall Coeff. (cm^3/C)	$4.1 (\pm 0.3) \times 10^3$	$4.8 (\pm 0.3) \times 10^2$
Type of Carriers	holes	holes

substrates, were measured to reduce sample charging and to simplify quantification with fewer elements present than in glass.

Spectra were taken at nine different areas ($\sim 44,000 \mu\text{m}^2$) of the sample, resulting in average S/Sn ratios and standard deviations of 1.06 ± 0.01 and 1.01 ± 0.01 for the as deposited and annealed films, respectively. These values are very close to the expected S/Sn ratio of 1.00 and are within the systematic error of the instrument.

Impact of film thickness and annealing on XRD spectra

θ - 2θ XRD spectra of the films were obtained with a Rigaku MiniFlex XRD with Cu K α radiation and are displayed in Figure 5.7. Films were indexed to the following JCPDS cards: PDF 39-0354 for SnS (space group #62, $a = 0.43291 \text{ nm}$, $b = 1.11923 \text{ nm}$, $c = 0.39838 \text{ nm}$), PDF 14-0619 for Sn₂S₃ (space group #62, $a = 0.88640 \text{ nm}$, $b = 1.420200 \text{ nm}$, $c = 0.37470$) and PDF 23-0677 for SnS₂ (space group #164, $a = b = 0.3686 \text{ nm}$, $c = 0.59822 \text{ nm}$). The π -SnS spectrum was simulated in CrystalDiffract based on the crystal structure and atomic positions listed in Abutbul, *et. al*⁷⁸ and the lattice parameter $a = 1.16 \text{ nm}$. The broad peak at ~ 20 - 30° present in most scans is attributed to the amorphous glass substrate, as it was observed in the spectrum of a bare glass slide.

The 50 nm thick as-deposited film exhibited a single peak at $2\theta = 31.68^\circ$. This peak lies between the (111) and (040) Bragg reflections of α -SnS, which are at $2\theta = 31.532^\circ$ and 31.972° , respectively. Figure 5.8 shows a higher resolution scan in the region of this peak. In addition to the α -SnS peaks, the Sn₂S₃ (211) and π -SnS (041) reflections also lie within the region. It is possible that the peak observed is a sum of multiple reflections. For this reason, XRD may not conclusively determine the film is pure α -SnS. Upon annealing the 50 nm thick film, this peak

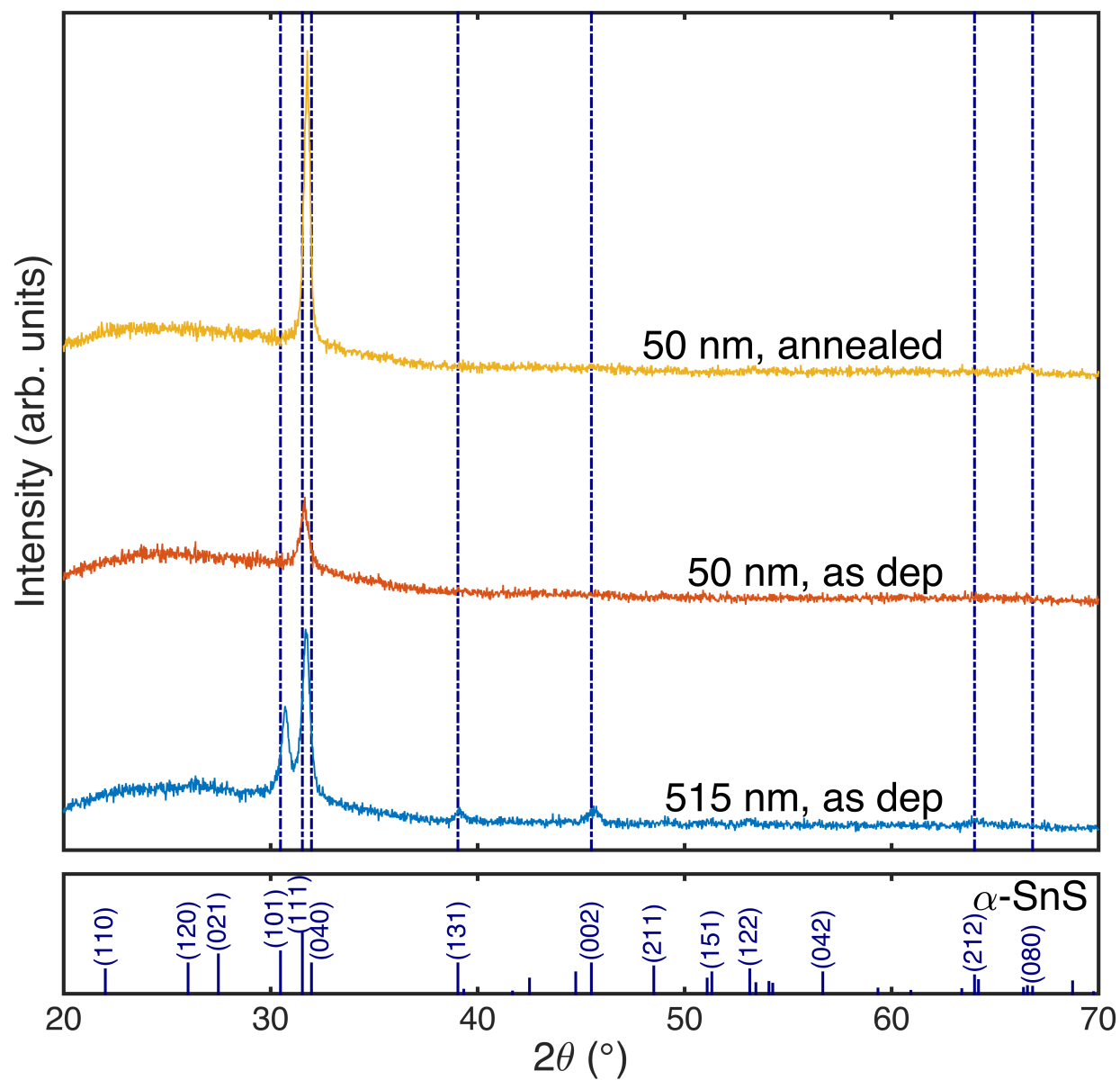


Figure 5.7: XRD spectra of 50 nm and 515 nm thick as deposited films and an annealed 50 nm thick film from $2\theta = 20^\circ$ to 70° .

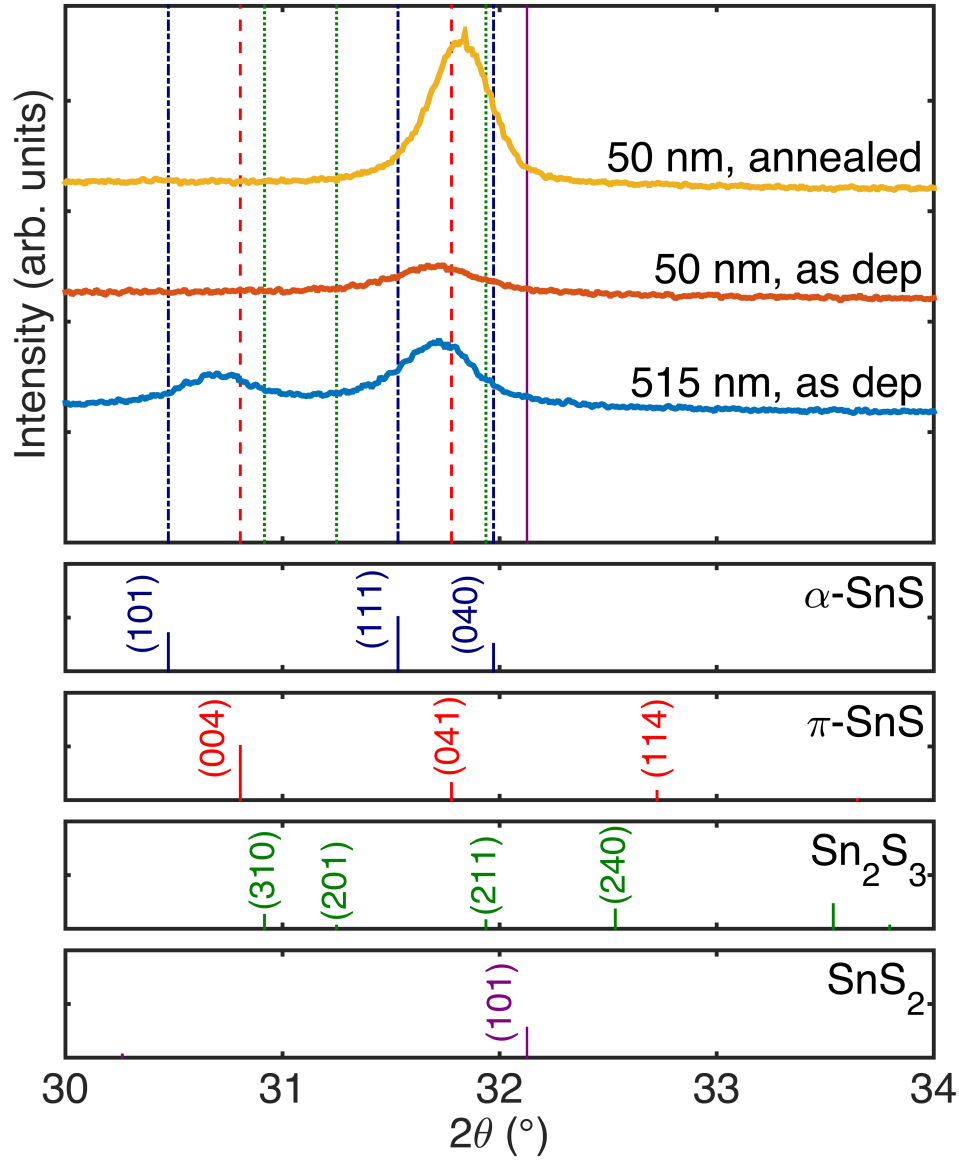


Figure 5.8: XRD spectra of 50 nm and 515 nm thick as deposited films and an annealed 50 nm thick film from $2\theta = 30^\circ$ to 34° showing locations of α -SnS, π -SnS and secondary phase peaks.

shifted towards the (040) peak to $2\theta = 31.79^\circ$ and its intensity increased. The appearance of the (080) reflection after annealing suggests the film is predominately α -SnS oriented in the [010] direction, with SnS layers parallel to the substrate. The FWHM of the $\sim 31.7^\circ$ - 31.8° peak, decreased from 0.45° to 0.31° after annealing. This corresponds to an increase in Scherrer

crystallite size from 18 nm to 26 nm, calculated from $\tau = \frac{\kappa \lambda}{\omega \cos \theta_B}$, where τ is the mean size of crystalline domains, κ is a shape factor (0.9 was used), λ the incident x-ray wavelength, θ_B the Bragg angle, and ω the FWHM.¹⁴⁵

The highest intensity peak of the 515 nm thick film was between the (111) and (040) reflections at $2\theta = 31.67^\circ$. In addition to this peak, new peaks were present that index to the (101), (131), (002), and (212) α -SnS reflections. These peaks correspond well with the observed microstructural change for thicker films in SEM, where layer growth appears to be perpendicular to the substrate. The (002) and (101) reflections correspond to crystallographic planes that are perpendicular to the SnS layers. The other new planes are also at large angles to the (010) plane, with the (212) plane at an angle of 82.5° , the (111) plane at an angle of 75.3° , and the (131) plane at an angle of 51.8° . Similar to the 50 nm films, Figure 5.8 indicates the 31.67° peak near the α -SnS (101) and (111) reflections could be indexed to multiple phases. The 31.67° peak FWHM is 0.41° , corresponding to a Scherrer crystallite size of 20 nm.

Impact of film thickness and annealing on transmittance and reflectance spectra

Transmittance and reflectance of the films (Figure 5.9) were measured using an Optronics OL770 spectrometer with 6 inch diameter integrating sphere attachment. Figure 5.9 b shows that the 515 nm as-deposited film has a lower reflectance than the 50 nm films, likely due to its textured morphology.

Absorption coefficients were calculated using the equation $\alpha \approx -\frac{1}{d} \ln \left(\frac{T}{1-R} \right)$, where d is film thickness, T is transmittance, and R is reflectance. This equation is frequently used to report absorption coefficients of SnS films and assumes a negligible reflection at the glass/film interface.

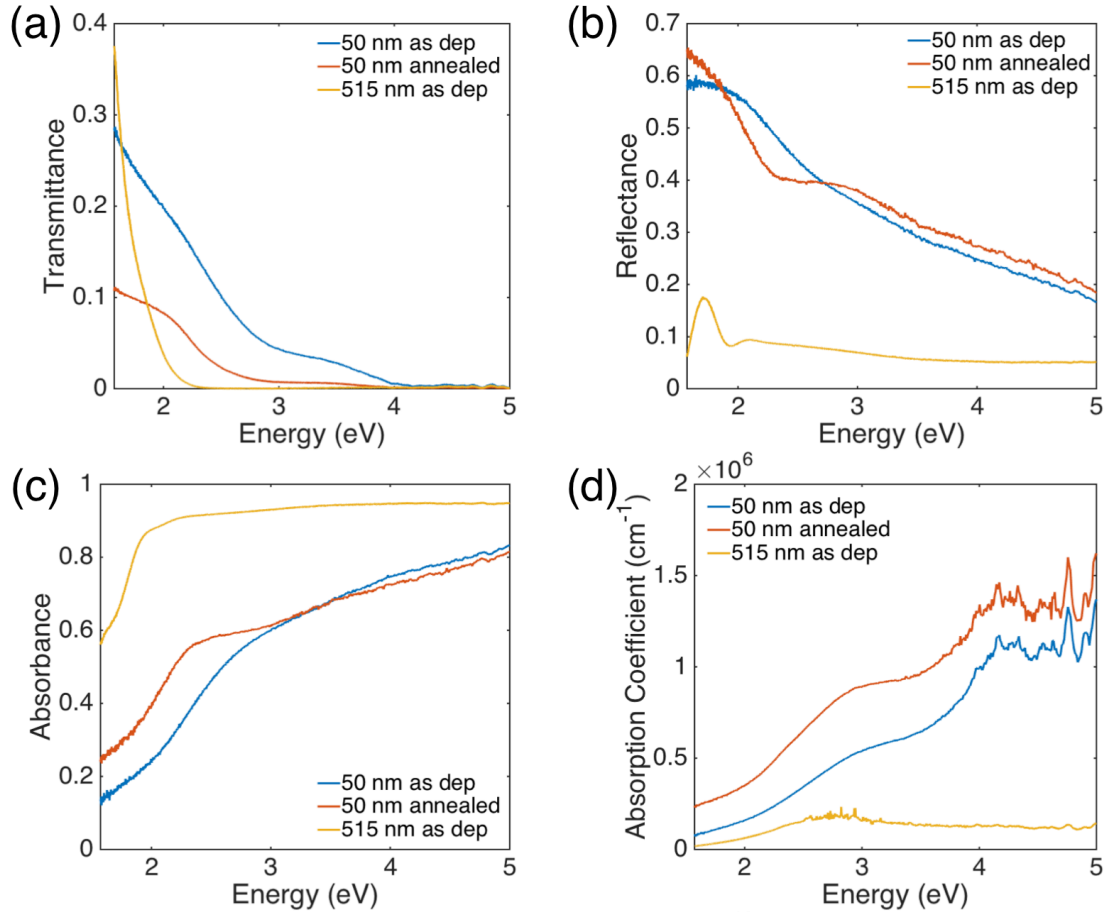


Figure 5.9: Optical properties of 50 nm and 515 nm thick, as-deposited films and 50 nm thick annealed films. (a) Transmittance spectra, (b) Reflectance spectra, (c) absorbance spectra, (d) absorption coefficient.

Comparison of films on borosilicate glass and soda lime glass substrates

50 nm thick films were deposited onto soda lime glass, annealed at 300°C for 1 hr, and characterized with XRD and Hall measurements. Hall measurement results shown in Table 5.3 indicate 50 nm thick SnS films on soda lime glass substrates exhibit p-type behavior. There is a small increase in hole concentration and decrease in mobility in the film on a soda lime glass

Table 5.3: Comparison of Hall measurement results of 50 nm thick SnS films deposited at $T_{\text{sub}} = \text{RT}$ and post annealed at 300°C for 1 hr on borosilicate glass and soda lime glass substrates. Error listed is the standard deviation of 10 measurements.

	Borosilicate Glass	Soda Lime Glass
Resistivity ($\Omega\text{-cm}$)	100 ± 1.1	90 ± 3.6
Mobility ($\text{cm}^2/\text{V-s}$)	4.7 ± 0.2	2.7 ± 0.4
Carrier Density (cm^{-3})	$1.3 (\pm 0.1) \times 10^{16}$	$2.6 (\pm 0.3) \times 10^{16}$
Hall Coeff. (cm^3/C)	$4.8 (\pm 0.3) \times 10^2$	$2.4 (\pm 0.3) \times 10^2$
Type of Carriers	holes	holes

substrate relative to that on a borosilicate substrate. This is consistent with Steinmann *et. al.*,¹⁴⁶ who reported a decrease in mobility and increase in carrier concentration for SnS films thermally evaporated onto an NaCl layer, and with DFT-based calculations indicating that in sulfur-rich conditions, Na_{Sn} defects are acceptors with a low formation energy in SnS and could serve as a p-type dopant.⁴⁶

The XRD spectrum of the SnS film on soda lime glass showed the peak between the α -SnS (111) and (040) peaks shifted to $2\theta = 31.94^\circ$, which is very close to the reported α -SnS (040) peak position. The Scherrer crystallite size of 25 nm is comparable to that of the annealed film on borosilicate glass. Table 5.4 summarizes information regarding the XRD peak between the α -SnS (111) and (040) reflections for SnS films deposited at different conditions.

Table 5.4: Characteristics of the XRD peak between α -SnS (111) and (040) for different deposition conditions. SLG refers to soda lime glass. “Annealed” refers to a post-deposition anneal at 300°C for 1 hr in vacuum.

Thickness (nm)	Post Treatment	Substrate	$T_{\text{sub}} (^\circ\text{C})$	$2\theta (^\circ)$	FWHM($^\circ$)	Crystallite Size (nm)
50	As dep	Borosilicate	RT	31.68	0.451	18
50	Annealed	Borosilicate	RT	31.79	0.31	26
50	Annealed	SLG	RT	31.94	0.33	25
515	As dep	Borosilicate	RT	31.67	0.408	20

5.2.4 Results: Impact of Substrate Temperature on Properties of SnS Films

While the resistivity of the 50 nm thick SnS film decreased through post-deposition annealing, its sheet resistance remained higher than desired for specific contact resistance studies. Sheet resistance should decrease if a thicker film is deposited. Thicker films may additionally be of greater interest for solar cell applications because $\sim 1 \mu\text{m}$ is necessary to allow for sufficient absorption of sunlight. As discussed in the previous section, the first 50-90 nm of SnS films are reported to have denser, more planar microstructures than those at greater thicknesses, therefore a SnS film with a thickness greater than $\sim 100 \text{ nm}$ is expected to be more comparable to that used in a solar cell.

In this section, the impact of substrate temperature and post-deposition annealing on $\sim 200 \text{ nm}$ to $\sim 300 \text{ nm}$ thick films is determined. SnS films were evaporated onto Si and soda lime glass substrates at substrate temperatures from room temperature (RT) to 300°C . Half of the films were post-annealed in the vacuum chamber at 300°C for 1 hr. The thicknesses, measured with AFM, for each condition are given in Table 5.5.

Table 5.5. Thicknesses of as-deposited and annealed SnS films deposited at different substrate temperatures. The post treatment “anneal” refers to an anneal at 300°C for 1 hr in vacuum ($\sim 10^{-7}$ Torr). Target thicknesses monitored by the QCM in the deposition chamber are listed in addition to film thicknesses measured with AFM.

$T_{\text{sub}} (^\circ\text{C})$	Post Treatment	Thickness, QCM (nm)	Thickness, AFM (nm)
RT	As dep	200	291 ± 6
RT	Anneal	200	316 ± 13
100	As dep	141	188 ± 13
100	Anneal	141	203 ± 19
200	As dep	200	224 ± 15
200	Anneal	200	229 ± 4
300	As dep	200	225 ± 5
300	Anneal	200	226 ± 8

SEM microstructure

SEM images of SnS films deposited on Si at different substrate temperatures, before and after annealing at 300 °C in vacuum, are shown in in Figure 5.10. Differences in morphology are apparent. At RT, a vertically aligned platelet morphology is present. The platelets become thicker and shorter as substrate temperature increases from 100°C to 200°C. Additionally, at 200°C, circular grains are present in the background. This change in morphology is consistent with that reported by Park *et.al.*¹¹³ for e-beam evaporated films at substrate temperatures from RT to 200°C. Additionally, the circular grains in the film deposited at 200°C are similar to a morphology reported for π -SnS films deposited by ALD.⁹⁵ At 300°C, the morphology changes to larger grains. Annealing appeared to widen the platelets of films deposited at lower temperatures, and did not promote grain growth for the film deposited at 300°C.

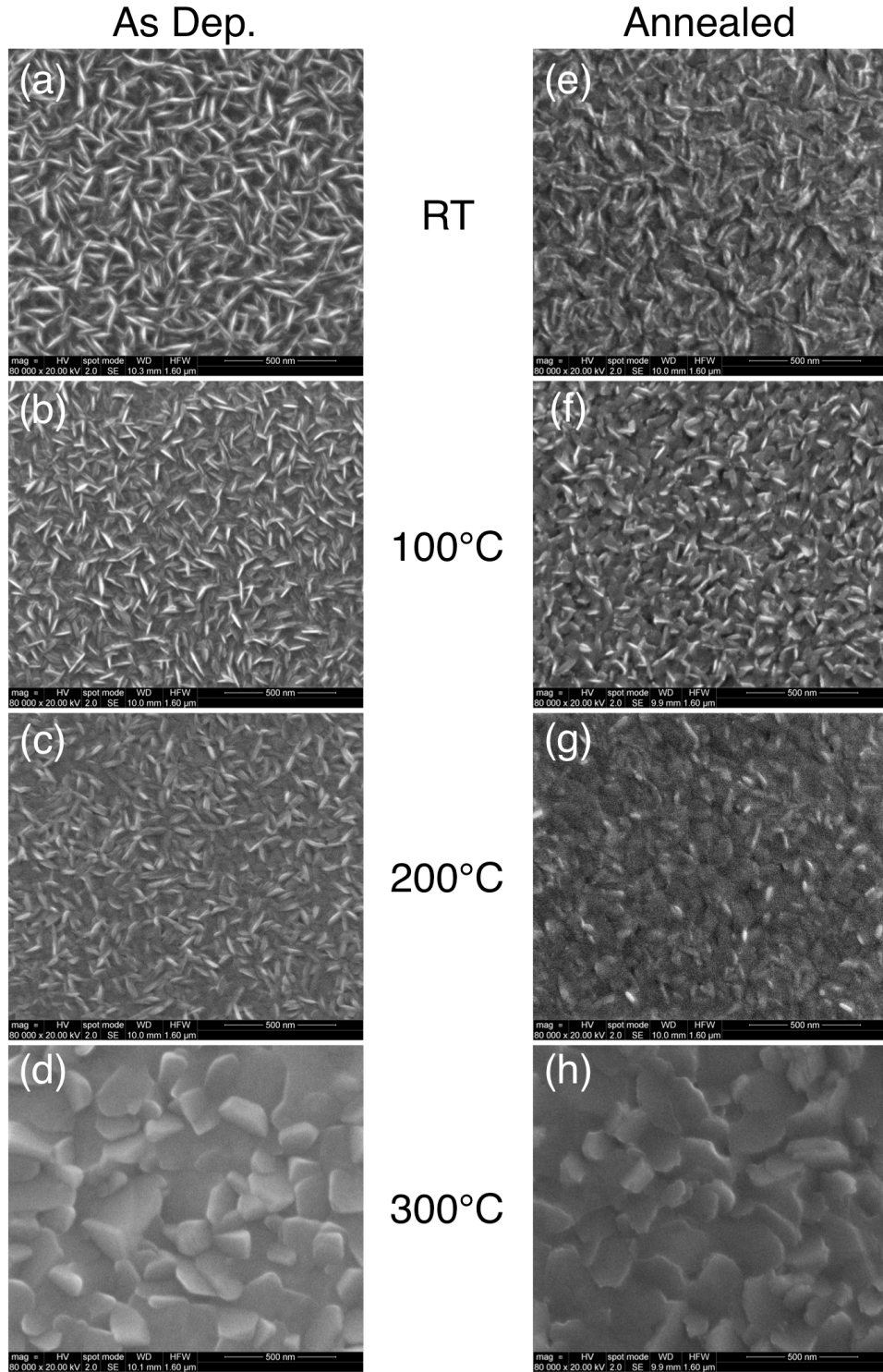


Figure 5.10: SEM images of SnS films on Si substrates deposited at $T_{\text{sub}} = \text{RT}$, 100°C, 200°C, and 300°C, as indicated by the temperatures listed in the center of the image. Films in the left column are as-deposited. Films in the right column were post-annealed at 300°C for 1 hr in vacuum.

Re-evaporation of SnS on Si

For some depositions at $T_{\text{sub}} = 300\text{ }^{\circ}\text{C}$, SnS films were not present on the Si substrates after removal from the vacuum chamber, but films that were deposited during the same batch on glass substrates remained. This may be due to re-evaporation of SnS from the Si substrate. It is hypothesized that the surface of the Si substrate may be at a higher temperature than that of the thicker glass substrate, allowing for re-evaporation.

Pressures during depositions varied between the 10^{-7} to 10^{-8} Torr range. According to Figure 5.3, SnS vapor pressures of $\sim 1 \times 10^{-8}$ to $\sim 1 \times 10^{-7}$ Torr correspond to temperatures of $\sim 312^{\circ}\text{C}$ $\sim 347^{\circ}\text{C}$, suggesting that if the surface of the Si substrate was greater than glass by only tens of degrees, re-evaporation could occur during some depositions and not others, depending upon the deposition chamber pressure.

The films shown in Figure 5.10 d, h, and Figure 5.11 a were deposited onto Si without a glass slide underneath, but were difficult to repeat without re-evaporation. The morphology of the films on Si in Figure 5.10 d, h and Figure 5.11 a differed from that of films deposited onto glass during the same deposition batch (Figure 5.11 b). The morphology of the former films were similar to that of a reported thermally evaporated film deposited at 350°C with base pressure $< 7.5 \times 10^{-6}$ Torr.⁹⁴

When a glass slide was inserted underneath the Si substrate during deposition, the SnS film on Si repeatedly remained intact (Figure 5.11 c). The morphology of such films (Figure 5.11 c) matched more closely to that of films on glass at substrates deposited at 300°C (Figure 5.11 b, d, e). The morphologies of films on glass were consistent regardless if SnS re-evaporated from Si substrates during the same deposition batch (Figure 5.11 d) or if the film on Si remained (Figure

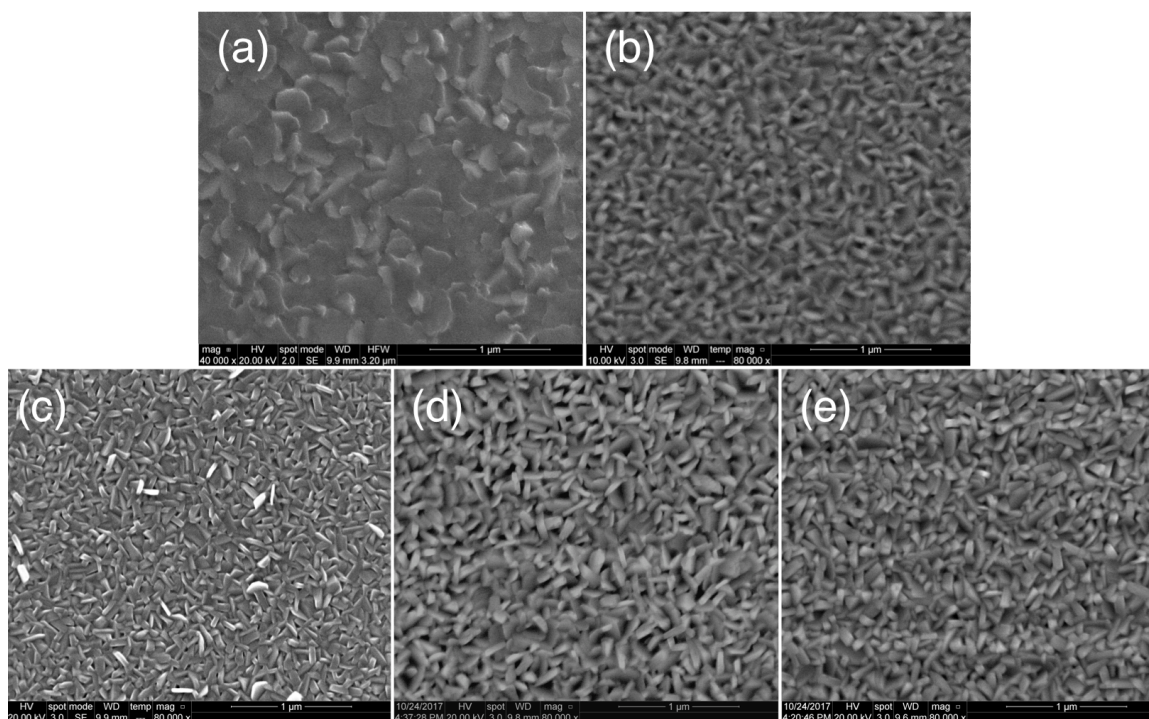


Figure 5.11: SEM images of SnS thin films deposited at 300°C and annealed in vacuum at 300°C for 1 hr. (a) Film deposited onto Si, showing unique morphology. (b) Film deposited onto soda lime glass during the same deposition batch as the film in (a). (c) Film deposited onto Si with glass slide underneath Si substrate. Film morphology more closely matches that of (b) than (a). (d) Film deposited onto soda lime glass during deposition in which there was no film adherence to Si. (e) Film deposited onto borosilicate glass during the same deposition batch as (d). SEM was in low vacuum mode during image acquisition of (d) and (e).

5.11 b). Morphologies were also consistent between soda lime substrates (Figure 5.11 b, d) and borosilicate glass substrates (Figure 5.11 e).

XRD spectra

XRD spectra were acquired for films on soda lime glass. The spectra in Figure 5.12 show that the as-deposited films are polycrystalline. Peaks corresponding to α -SnS are present in all films. However, the film deposited at 200°C also displays peaks that correspond to the π -SnS (222), (114), (143), (044), and (226) reflections (at 26.60°, 32.69°, 39.60°, 44.16° and 52.30°,

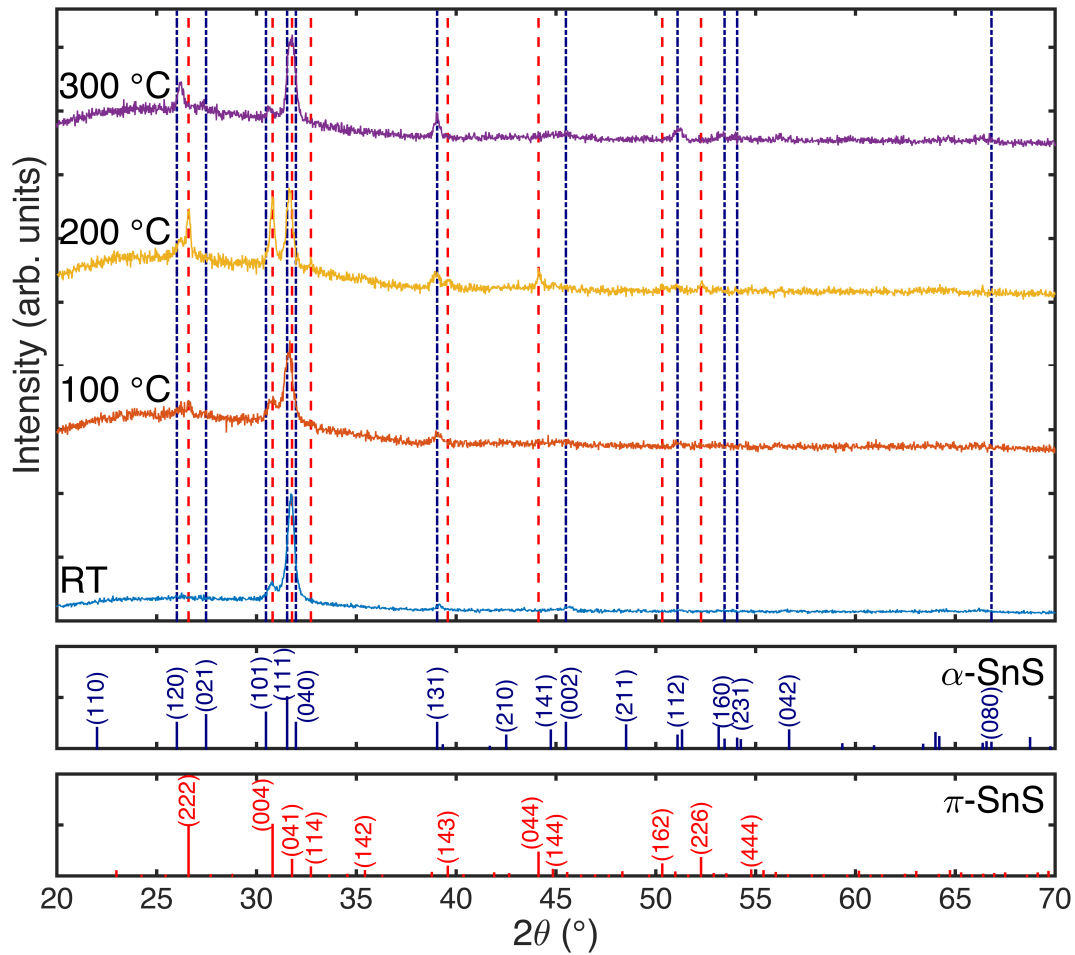


Figure 5.12: XRD spectra of SnS thin films deposited on soda lime glass at different substrate temperatures in the as-deposited condition. The temperature labels indicate substrate temperature during depositions. Spectra are normalized to their maximum intensity value.

respectively). The α -SnS (131) peak is additionally present in this film, indicating the film is a mixture of the α -SnS and π -SnS phases. A low intensity π -SnS (222) peak is present in the film deposited at 100°C, suggesting it contains a small amount of π -SnS. No distinctive π -SnS peaks are present in the spectra for films deposited at RT or 300°C. However the peaks between 30.4°–31° and 31.5°–32° cannot clearly be indexed to a certain phase (Figure 5.14).

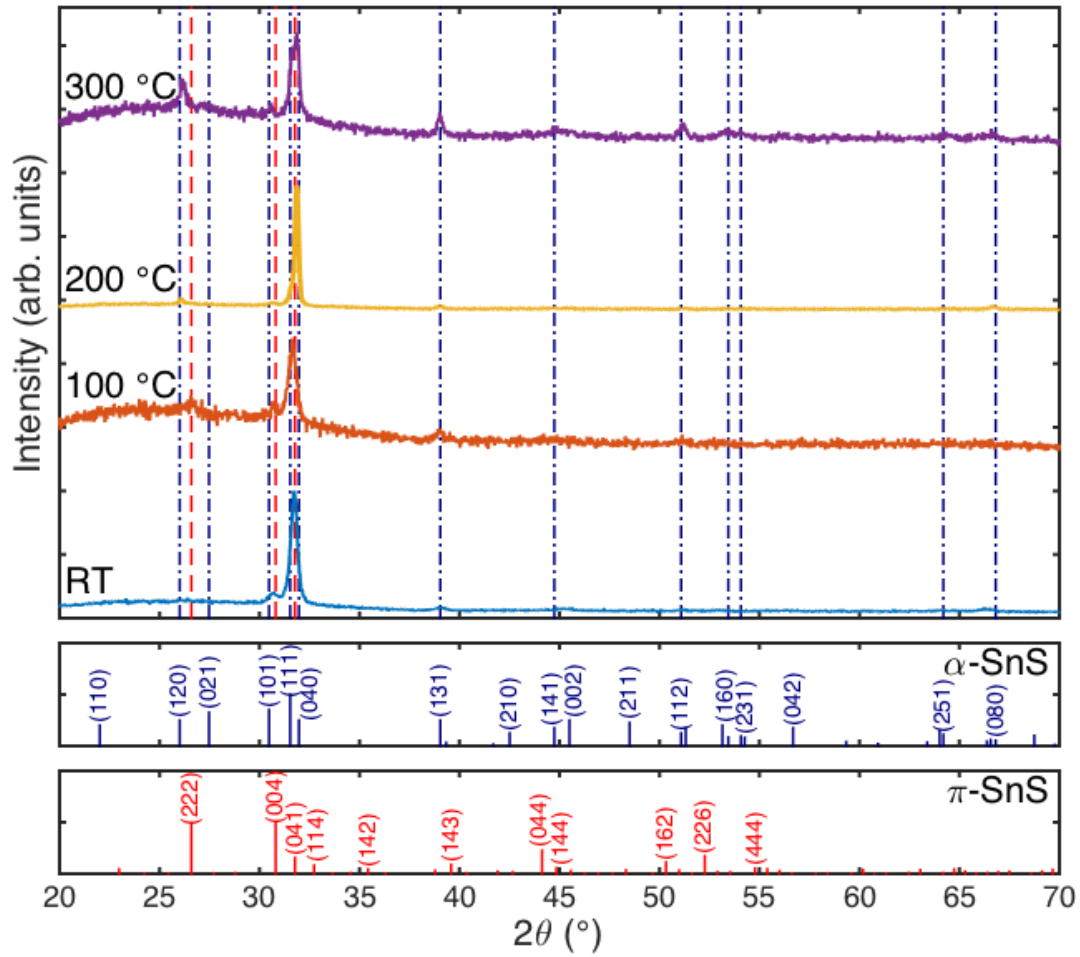


Figure 5.13: XRD spectra of SnS thin films deposited on soda lime glass at different substrate temperatures that were annealed at 300 °C for 1 hr. The temperature labels indicate substrate temperature during depositions. Spectra are normalized to their maximum intensity value.

After annealing (Figure 5.13), the distinctive π -SnS peaks in the 200°C film spectrum are no longer present, and the α -SnS peaks became sharper, suggesting that annealing allowed the film to transform to the more stable α -SnS phase. A small π -SnS (222) peak remains in the $T_{\text{sub}} = 100^\circ\text{C}$ film after annealing.

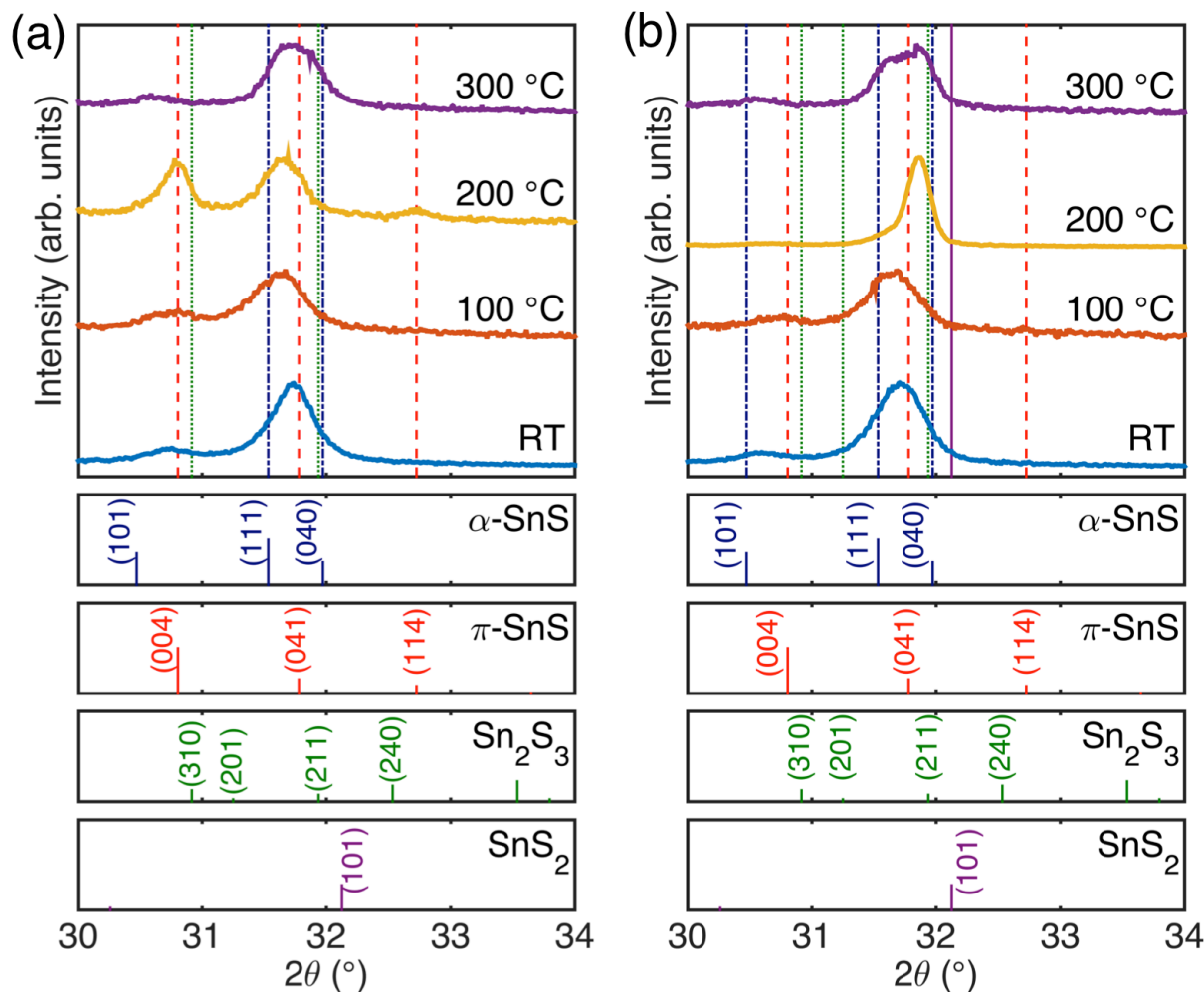


Figure 5.14: XRD spectra in 30° - 34° range for SnS thin films deposited at different substrate temperatures: (a) as deposited and (b) post-annealed films. The temperature labels indicate substrate temperature during depositions. All films represented in (b) were annealed at 300°C for 1 hr in vacuum.

As apparent in the higher resolution scans shown in Figure 5.14, the positions of the peaks between $\sim 30.4^\circ$ - 31° and $\sim 31.5^\circ$ - 32° often lie between Bragg reflections of two different phases, making them difficult to index. X'Pert HighScore Plus software was used to fit the peaks in this region, and results are displayed in Figures 5.15-5.21.

Figures 5.15 and 5.16 display fits to the XRD spectrum of an annealed film deposited at 300°C . In Figure 5.15, positions of the peaks are constrained to the reported peak positions of

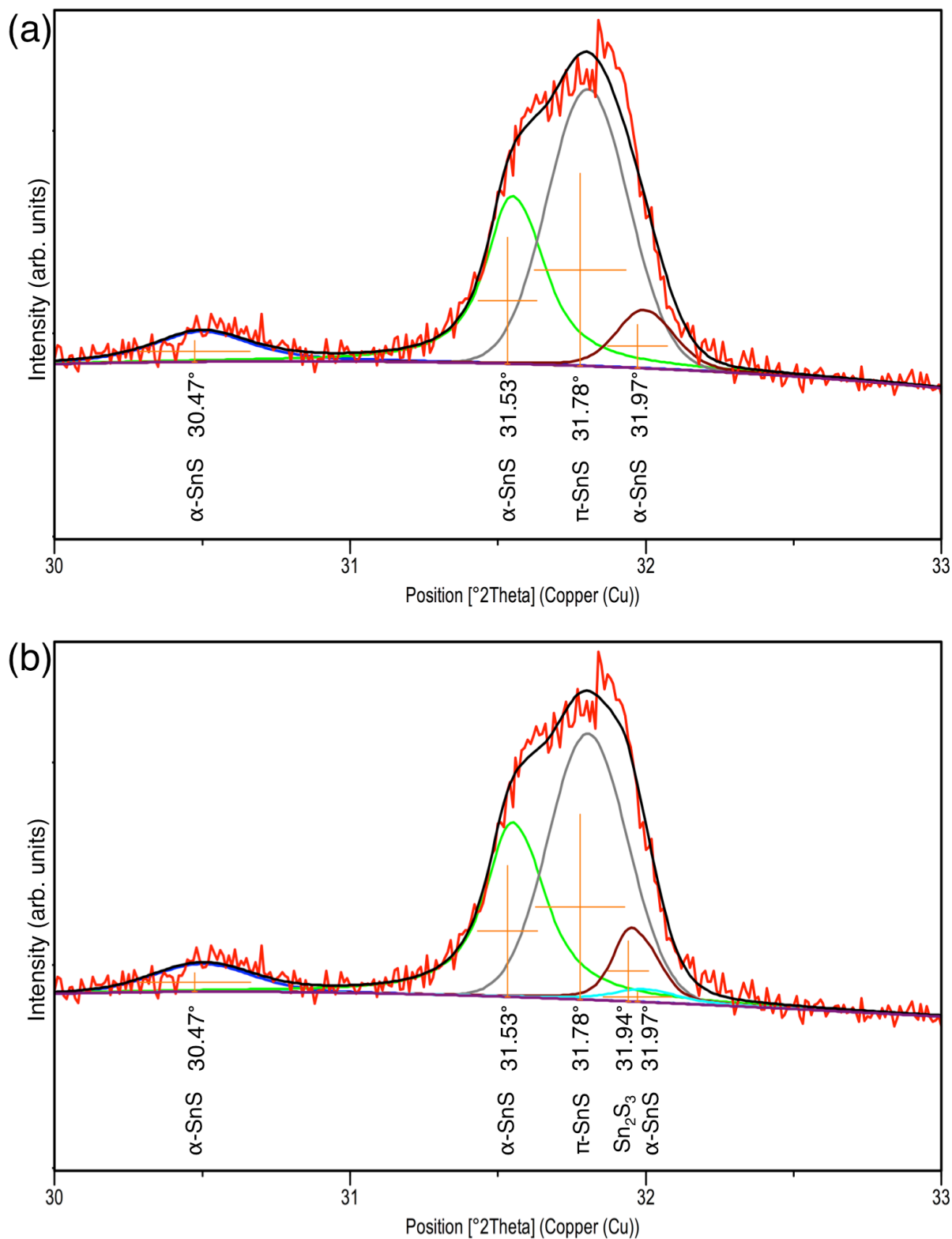


Figure 5.15: Fit of the XRD spectra of an annealed SnS film deposited at 300 $^{\circ}\text{C}$. Peak positions were constrained to reported positions. (a) Fit containing a mixture of α -SnS and π -SnS peaks. (b) Fit containing a mixture of α -SnS, π -SnS, and Sn_2S_3 peaks.

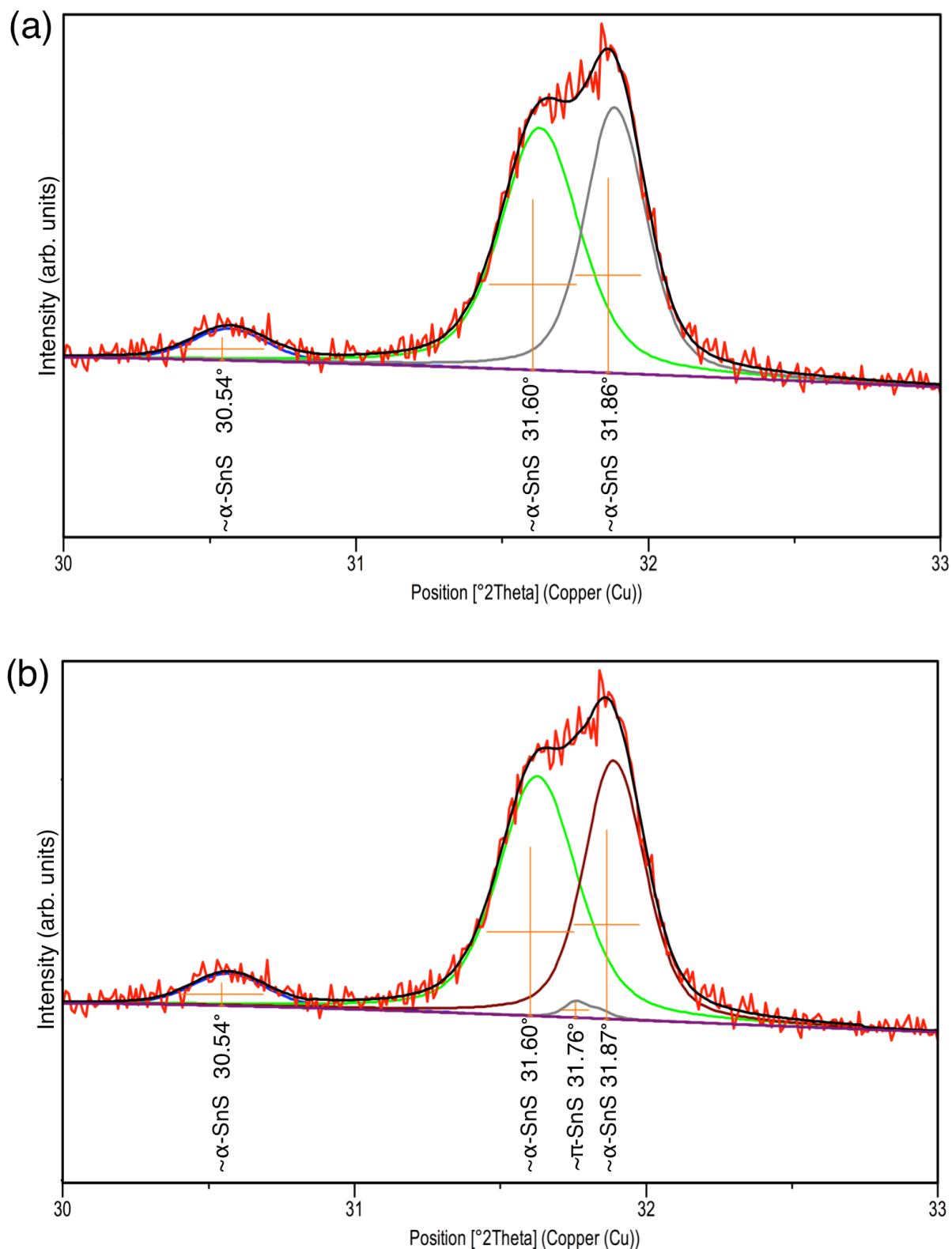


Figure 5.16: Fit of the XRD spectra of an annealed SnS film deposited at 300 °C. Peak positions were allowed to shift from reported values. The tin sulfide phase listed next to the 2θ value is the phase to which the peak is attributed. (a) Fit using three peaks. (b) Fit with an additional peak near the π -SnS Bragg reflection.

the tin sulfide phases (PDF 39-0354 (α -SnS), PDF 14-0619 (Sn_2S_3), and Abutbul, *et. al*⁷⁸ (π -SnS)). Figure 5.15 a includes α -SnS and π -SnS peaks only, whereas Figure 5.15 b includes an additional Sn_2S_3 peak that provided a small improvement to the fit. In Figure 5.16, positions of the peaks were not constrained to reported values, which further improved the fit.

In Figure 5.16 a, three unconstrained peaks are present. The peak at 31.86° lies between reported peak positions of the π -SnS (041) reflection and the α -SnS (040) reflection. The peaks at 30.54° and 31.60° are shifted from the reported α -SnS (101) and (111) peak positions, respectively. The shift in peak positions could be explained by compressive strain in the nanocrystalline film resulting in a reduction of the α -SnS a and c lattice parameters accompanied by an increase in the b lattice parameter. An expansion of the b lattice parameter would shift the (040) peak of α -SnS to lower 2θ . For example an increase from $b = 11.1923$ angstrom to $b = 11.225$ angstrom would shift the α -SnS (040) peak to $\sim 31.86^\circ$. A decrease of the a and c lattice parameters would shift the α -SnS (101) and (111) peak positions to higher 2θ values. For example, a reduction of the a and c lattice parameters by 0.25% would shift the (101) and (111) peaks to 30.55° and 31.59° , respectively, which are close to the observed positions in Figure 5.16 a. In Figure 5.16 b, an additional peak near the π -SnS (041) reflection is included in the fit. The intensity of this peak is small, suggesting that if π -SnS is present in the film, it is a small amount.

Figure 5.17 displays fits to the XRD spectrum of an unannealed film deposited at 300°C . The α -SnS (040) peak in the film is similarly shifted to lower 2θ , corresponding to an increase in the α -SnS b lattice parameter. The peaks at 30.59° and 31.63° could correspond to shifted α -SnS (101) and (111) peaks, respectively. The peaks are shifted to higher 2θ values than in the annealed film deposited at 300°C , which would correspond to a larger reduction in the a and c

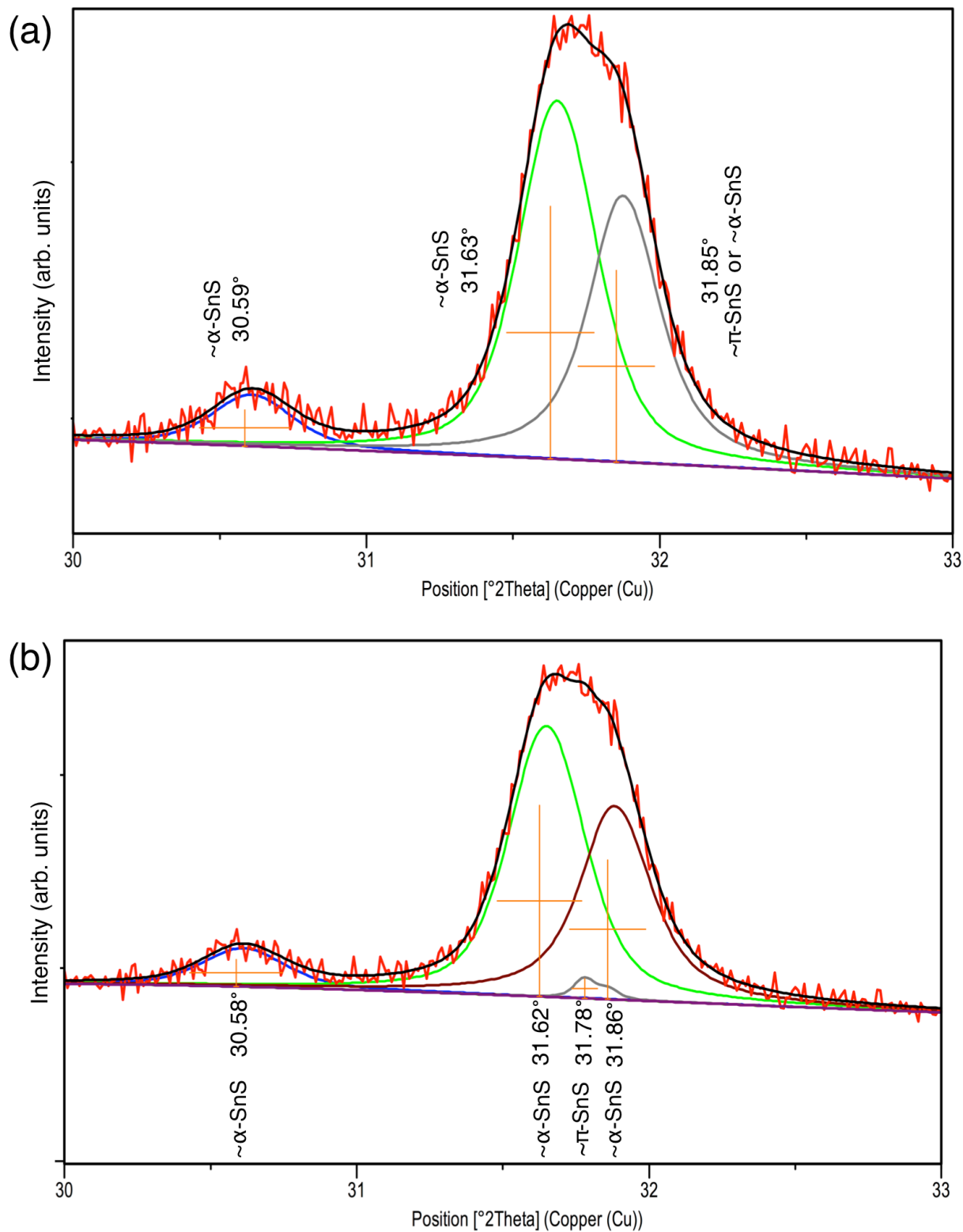


Figure 3.17: Fit of the XRD spectra of an as-deposited SnS film deposited at 300 °C. Peak positions were allowed to shift from reported values. The tin sulfide phase listed next to the 2θ value is the phase to which the peak is attributed. (a) Fit using three peaks. (b) Fit using an additional peak near the $\pi\text{-SnS}$ Bragg reflection.

lattice parameters in the as-deposited film. This suggests that annealing allowed the film deposited at 300°C to partially relax.

Figure 5.18 displays fits of the XRD spectra of an annealed SnS film deposited at 200 °C. In Figure 5.18 a, two peaks are present, which are centered at 30.63° and 31.82°. These peaks lie between α -SnS and π -SnS peaks. The peak at 30.63° is closest to the reported α -SnS (101) reflection, and the peak at 31.82° is closest to the π -SnS (041) reflection. The fit was improved by including an additional peak (Figure 5.18 b). The three peaks in Figure 5.18 b are positioned at 30.59°, 31.77°, and 31.86° are attributed to a shifted α -SnS (101) reflection, a π -SnS (041) reflection, and a shifted α -SnS (040) reflection. These fits indicate the annealed film deposited at 200 °C contains a mixture of the α -SnS and π -SnS phases.

The unannealed film deposited at 200 °C contains additional peaks corresponding to π -SnS (Figure 5.19). The peak at 30.76° is indexed to the π -SnS (004) reflection, and the peak at 32.70° is indexed to the π -SnS (114) reflection. In Figure 5.19 a, a third peak is positioned at 31.62°, which lies between the π -SnS (041) and α -SnS (111) reflections. Further analysis is required to determine if this peak is a sum of the π -SnS (041) and α -SnS (111) reflections.

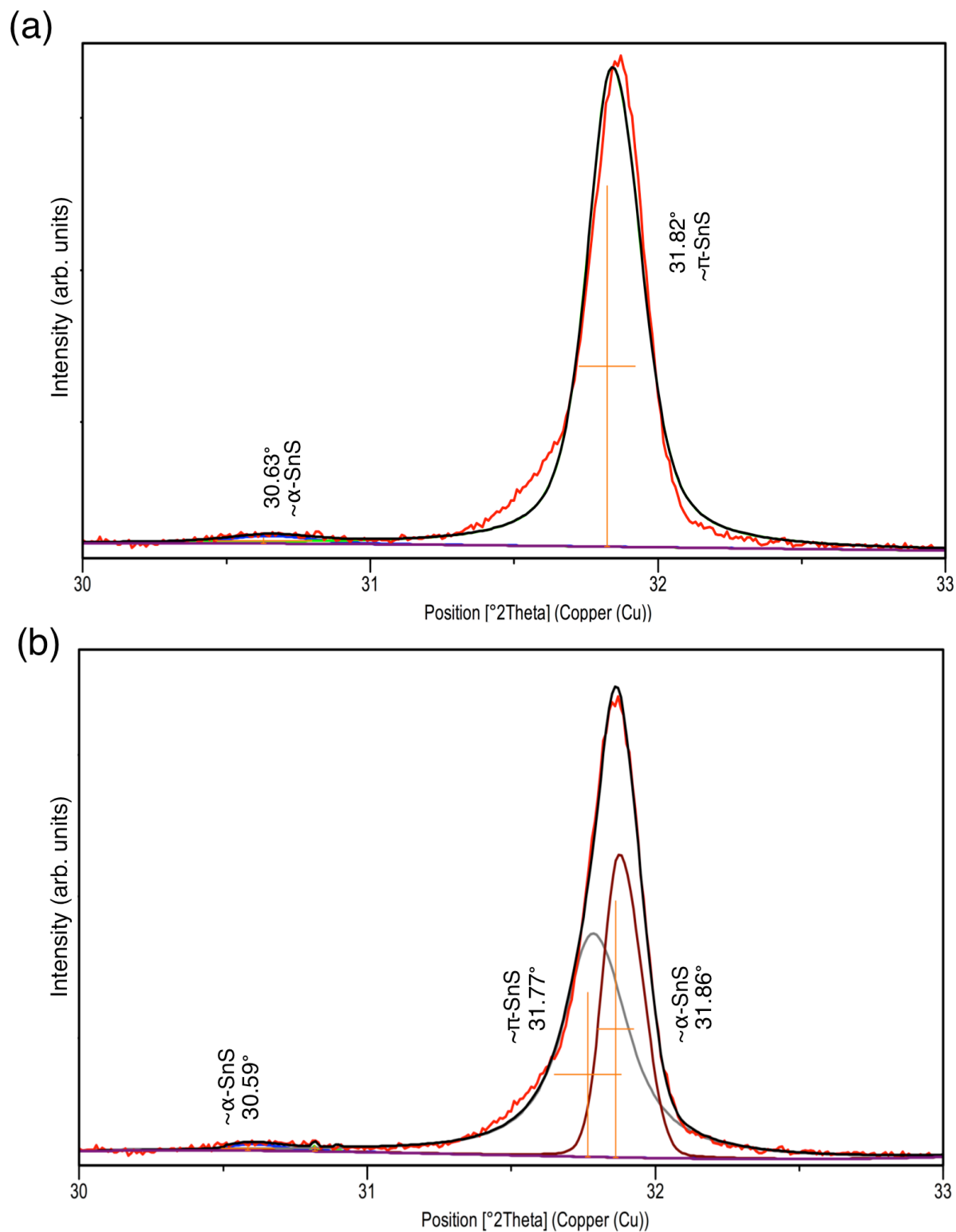


Figure 5.18: Fit of the XRD spectra of an annealed SnS film deposited at 200 $^{\circ}\text{C}$. Peak positions were allowed to shift from reported values. The tin sulfide phase listed next to the 2θ value is the phase to which the peak is attributed. (a) Fit including two peaks. (b) Fit including an additional peak.

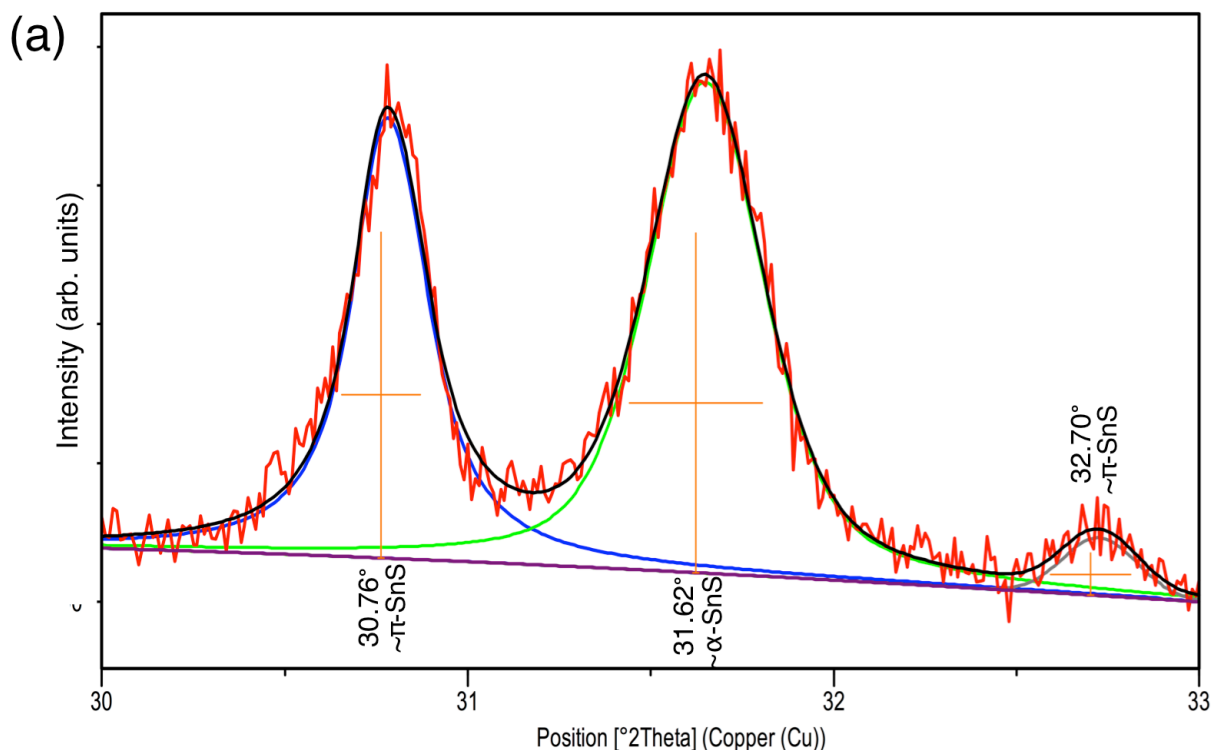


Figure 5.19: Fit of the XRD spectra of an as-deposited SnS film deposited at 200 °C. Peak positions were allowed to shift from reported values. The tin sulfide phase listed next to the 2θ value is the phase to which the peak is attributed.

Figure 5.20 displays fits of the XRD spectra of SnS films deposited at 100 °C that were annealed (Figure 5.20 a) and not annealed (Figure 5.20 b). The positions of the peaks cannot be attributed to a single phase. Fits of the XRD spectra of SnS films deposited at RT are shown in Figure 5.21. Similarly, these peaks cannot be attributed to a single phase. The position of the peak between 31°-32° does not shift upon annealing for the films deposited at RT.

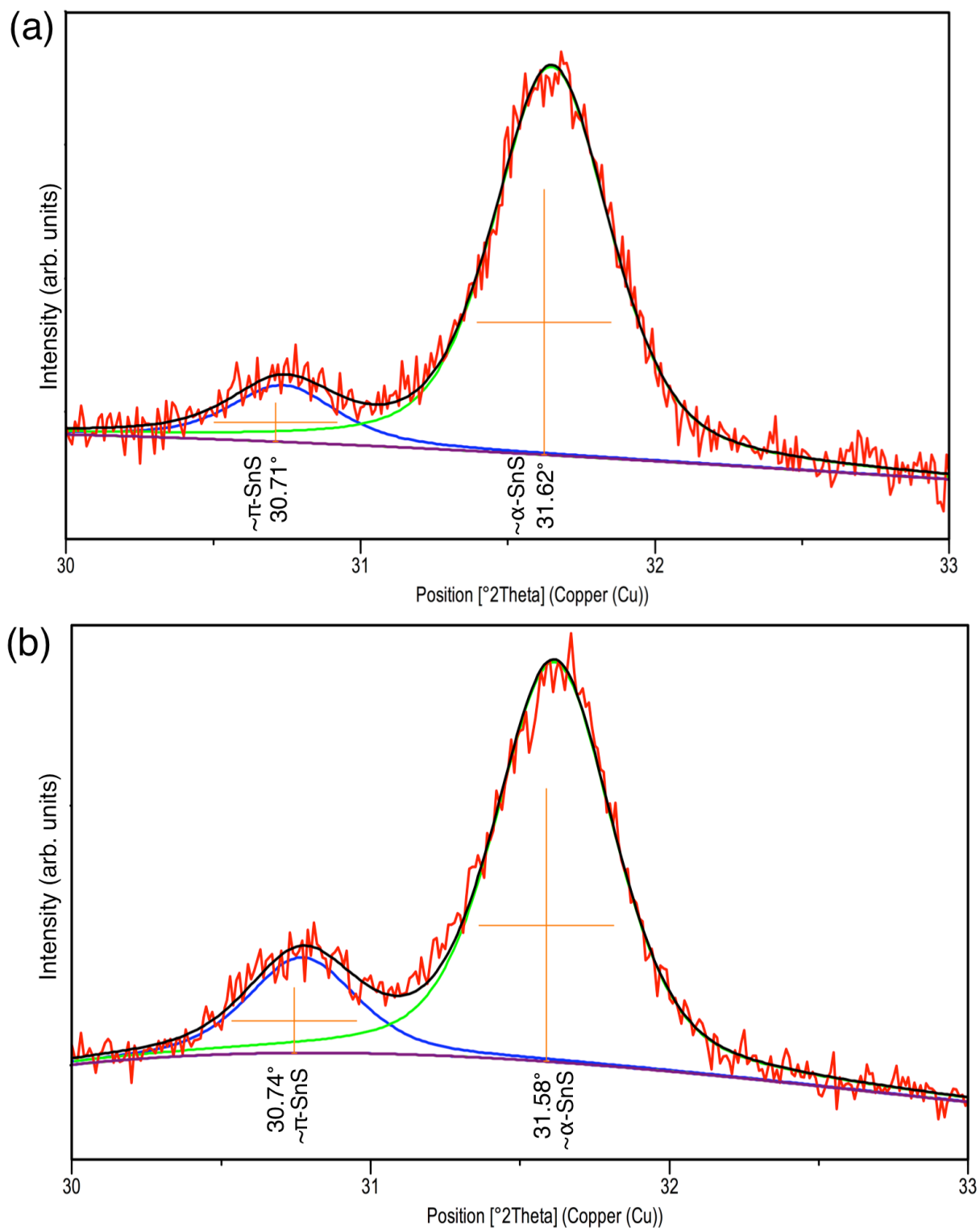


Figure 5.20: Fit of the XRD spectra of an (a) annealed and (b) unannealed SnS film deposited at 100 °C. Peak positions were allowed to shift from reported values. The tin sulfide phase listed next to the 2θ value is the phase to which the peak is attributed.

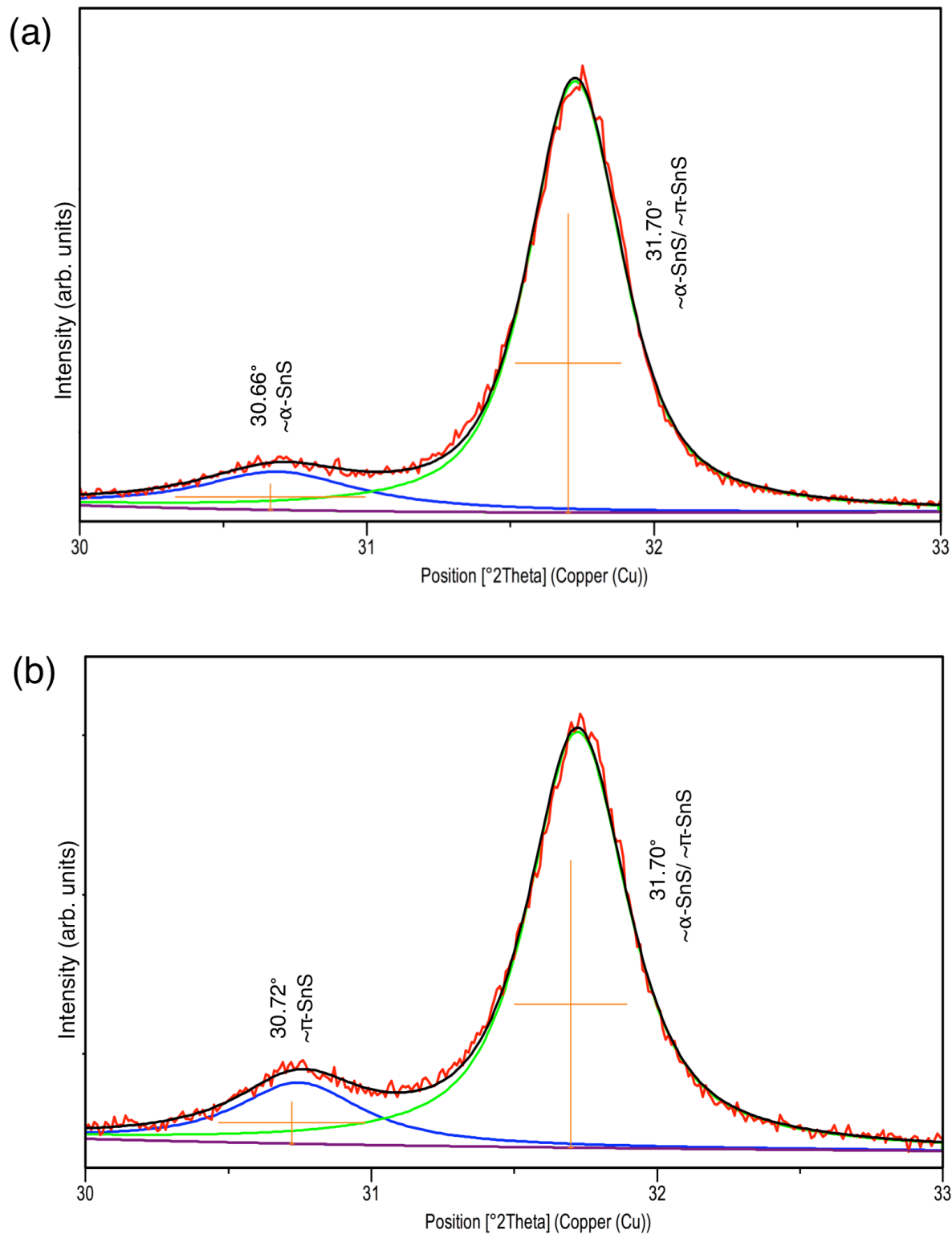


Figure 5.21: Fit of the XRD spectra of an (a) annealed and (b) unannealed SnS film deposited at RT. Peak positions were allowed to shift from reported values. The tin sulfide phase listed next to the 2θ value is the phase to which the peak is attributed.

Scherrer crystallite size, SEM grain size measurements, EDX, and resistivity

The position of the peak between $2\theta = 31^\circ$ - 32° is plotted in Figure 5.22 a for films deposited at temperatures from RT to 200°C . Figure 5.22 b shows the corresponding Scherrer crystallite size of the $2\theta = 31^\circ$ - 32° peak. The films are nanocrystalline. Grain sizes were additionally measured from SEM images using ImageJ. The short and long dimensions of the grains were measured. The measured grain size of the short dimension in SEM images (Figure 5.22 c) and the Scherrer crystallite sizes are similar. The ratio of long to short dimension of the grains are plotted in Figure 5.22 d. The long and short dimensions became more equal as substrate temperature increased as well as after annealing.

EDX was performed to determine composition of the films, and results are plotted in Figure 5.22 e. All of the films were close to stoichiometric SnS. Sulfur loss was evident after annealing the films that were deposited at RT and 100°C . Resistivities of the films (Figure 5.22 f) were calculated from van der Pauw measurements using Ni/Au contacts. The resistivities of the films deposited at RT and 100°C increased after annealing, possibly due to the observed sulfur loss. Resistivity of the films deposited at 200°C and 300°C decreased after annealing. The lowest resistivity was observed for the $T_{\text{sub}} = 300^\circ\text{C}$, post annealed film.

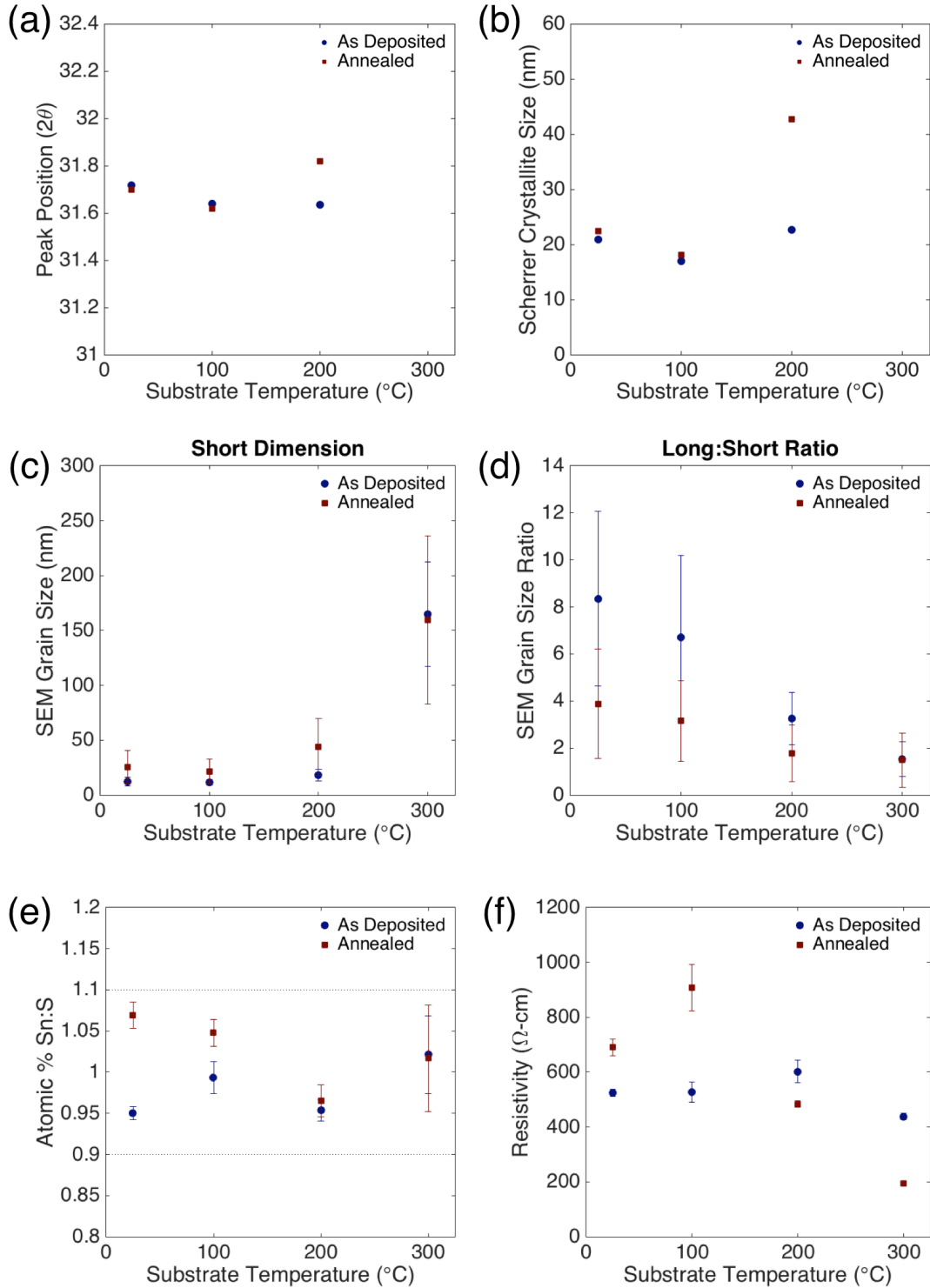


Figure 5.22: (a) Position of XRD peak between 31.5° - 32° (b) Scherrer crystallite size determined from 31.5° - 32° XRD peak (c) SEM measurement of the short dimension of grain size (d) Ratio of long dimension grain size to short dimension determined from SEM images. All anneals were conducted at 300°C for 1 hr in vacuum. (e) Ratio of atomic % Sn:S for different film conditions, as determined by EDS analysis. (f) Resistivities of SnS films deposited at different conditions, as calculated from van der Pauw measurements.

Raman spectroscopy

As mentioned in the previous section, in some cases the d-spacings of different phases were very close and difficult to distinguish with XRD. Therefore, Raman spectroscopy was used as a complementary tool to identify film composition.

Figures 5.23 and 5.24 show Raman spectra of annealed and unannealed films obtained with excitation wavelengths of 532 nm and 633 nm, respectively. α -SnS has 12 active Raman modes. The locations of experimentally determined Raman peaks of a reported bulk α -SnS crystal (70, 95, 164, 192, 218, 290 cm^{-1}) are indicated by solid vertical red lines in Figures 5.23 and 5.24.¹⁴⁷ The positions of these peaks deviate slightly in literature.¹⁴⁸ For example, a recent first-principles lattice dynamic study by Skelton *et al.*¹⁴⁹ calculated the positions of main α -SnS peaks to be 92, 161, 189, and 220 cm^{-1} .

Experimentally reported Raman shifts of π -SnS are indicated in Figures 5.23 and 5.24 by dashed green lines and correspond to 59, 71, 90, 112, 123, 176, 192, 202, and 224 cm^{-1} , as reported by Abutbul *et al.*⁷⁷ These experimental peaks generally agree with those calculated by Skelton *et al.*¹⁴⁹ (59, 66, 83, 109, 119, 175, 187, 203, and 221 cm^{-1}).

An experimental study¹⁵⁰ on 2H-SnS₂ crystals reports the highest intensity peak corresponds to the A_{1g} mode at 315 cm^{-1} ,¹⁵⁰ which is indicated by the dotted grey line. There is an additional lower intensity peak at 205 cm^{-1} corresponding to the E_g mode. Bulk Sn₂S₃ has experimentally determined Raman active modes at frequencies of 54, 63, 73, ~90 (weak), 154, 192, 209, 236, 252, and 308 cm^{-1} .

1 151

Figures 5.23 and 5.24 show that α -SnS Raman peaks are present in all samples, and peaks corresponding to α -SnS were sharper for the 300°C substrate temperature condition. Figure 5.23 (a) shows a low intensity peak corresponding to the A_{1g} mode of SnS₂ was present in unannealed films

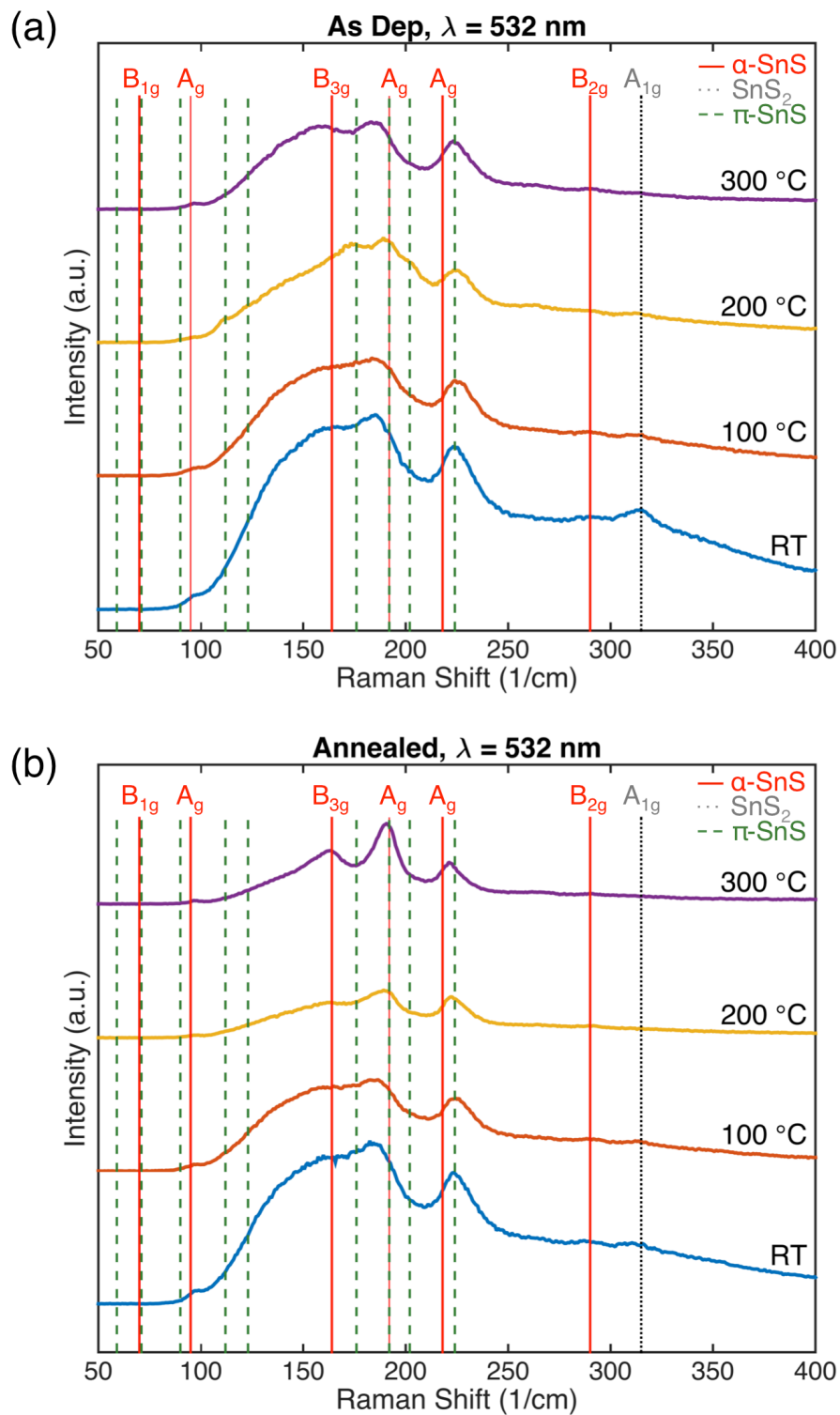


Figure 5.23: Raman spectra of as-deposited (a) and annealed (b) SnS films deposited at different substrate temperatures, as indicated. Incident laser wavelength was 532 nm. The anneals were conducted at 300 °C for 1 hr in vacuum.

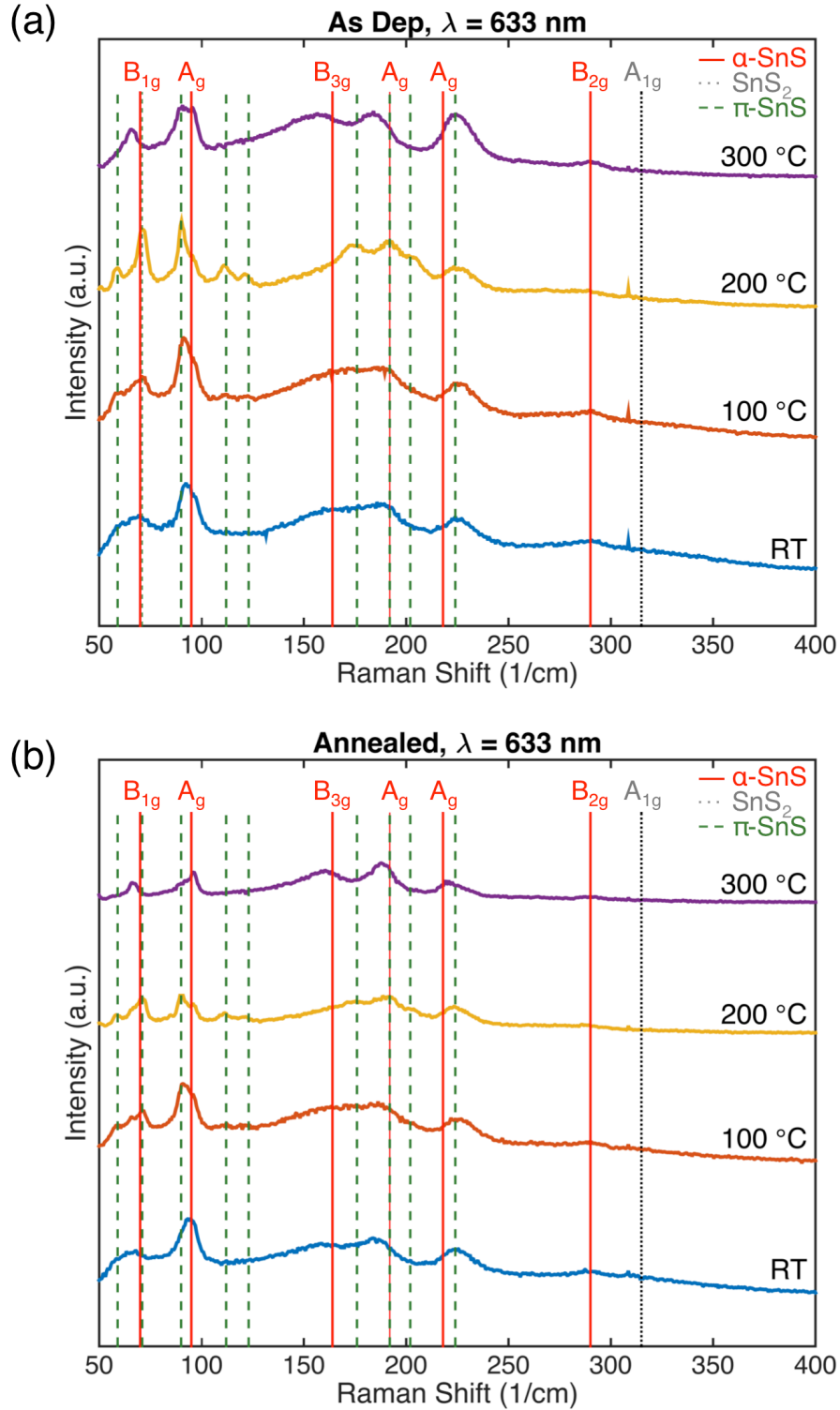


Figure 5.24: Raman spectra of as-deposited (a) and annealed (b) SnS films deposited at different substrate temperatures, as indicated. Incident laser wavelength was 633 nm. The anneals were conducted at 300 °C for 1 hr in vacuum.

deposited at RT, 100 °C, and 200 °C. After annealing, the SnS₂ peak decreased in intensity for films deposited at RT and 100°C and was removed for the 200°C substrate temperature condition (Figure 5.23 (b)).

Due to the hardware and filters present in our Raman system, low frequency Raman shifts could not be measured with a 532 nm excitation wavelength. Therefore, a 633 nm excitation wavelength was additionally used to detect the lower frequency Raman shifts (Figure 5.24). Although lower frequency shifts were measureable when a $\lambda = 633$ nm laser was used, the SnS₂ peak could no longer be detected. This may be because the $\lambda = 633$ nm laser has an energy (1.96 eV) that is smaller than the bandgap of SnS₂. The energy of the $\lambda = 532$ nm laser (2.33 eV) is near the bandgap of SnS₂, 2.18–2.44 eV,⁶⁶ and may enhance the SnS₂ peaks. Because different peaks were visible with different incident wavelengths, spectra from both wavelengths are reported here.

It is evident in Figure 2.24 that the unannealed film deposited at 200 °C is not pure α -SnS, and many of its Raman peaks match well with the spectra of π -SnS reported by Abutbul et. al.⁷⁷ The presence of the B_{2g} α -SnS peak at ~ 290 cm⁻¹ suggests the film is comprised of a mixture of α -SnS and π -SnS. This is the first identification of π -SnS deposited by e-beam evaporation, to the author's knowledge.

Mixtures of α -SnS and π -SnS have been reported in SnS thin films deposited by atomic layer deposition.^{95, 96} In these studies, the substrate temperature was varied between 80-200°C or 90-240°C. Similar to what was observed here, π -SnS was detected at moderate substrate temperatures, and α -SnS was favored at higher temperatures. In these studies, HRTEM was used in addition to Raman and XRD, which identified regions of α -SnS and regions of π -SnS on the same film for films deposited at 120°C⁹⁵ and 90°C.⁹⁶

To better determine if the films contain a mixture of α -SnS and π -SnS, deconvolutions of the spectra in Figure 5.24 were performed. Fluorescence can cause a large background in Raman spectra, which can impact peak fitting. Ideally, source of fluorescence would be removed during the experiment to prevent loss of peaks by being obscured by the background. However, there are also methods of subtracting background. Here, an open source R package by Zhang, et. al.¹⁵² was used which incorporates peak detection, a continuous wavelet transform, and a penalized least squares algorithm to simulate manual background subtraction. An example of background subtraction using this method on the unannealed SnS film deposited at 200°C is shown in Figure 5.25.

After background subtraction, Fityk,¹⁵³ a free curve fitting software was used to fit and sum the peaks. The experimental peaks most closely matched Lorentzian functions.

Figure 5.26 shows the deconvoluted Raman spectra of unannealed SnS films at different T_{sub} . Figures 5.26 a,b show Raman spectra of films deposited at room temperature using α -SnS

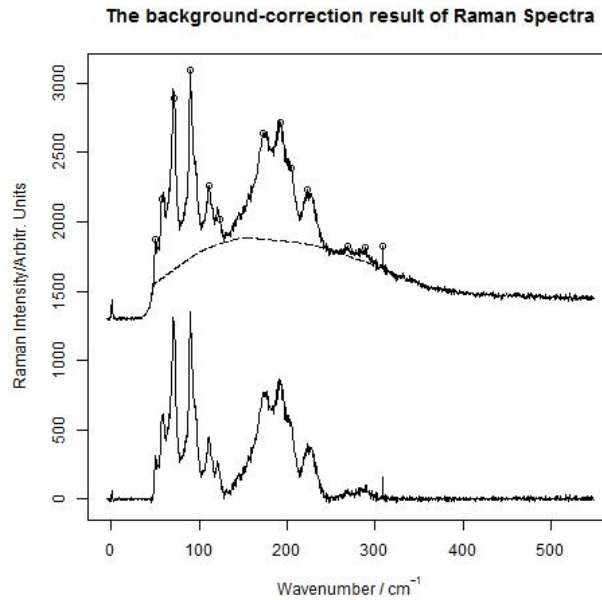


Figure 5.25: Example background subtraction of Raman spectrum of $T_{\text{sub}}=200\text{ }^{\circ}\text{C}$, annealed film.

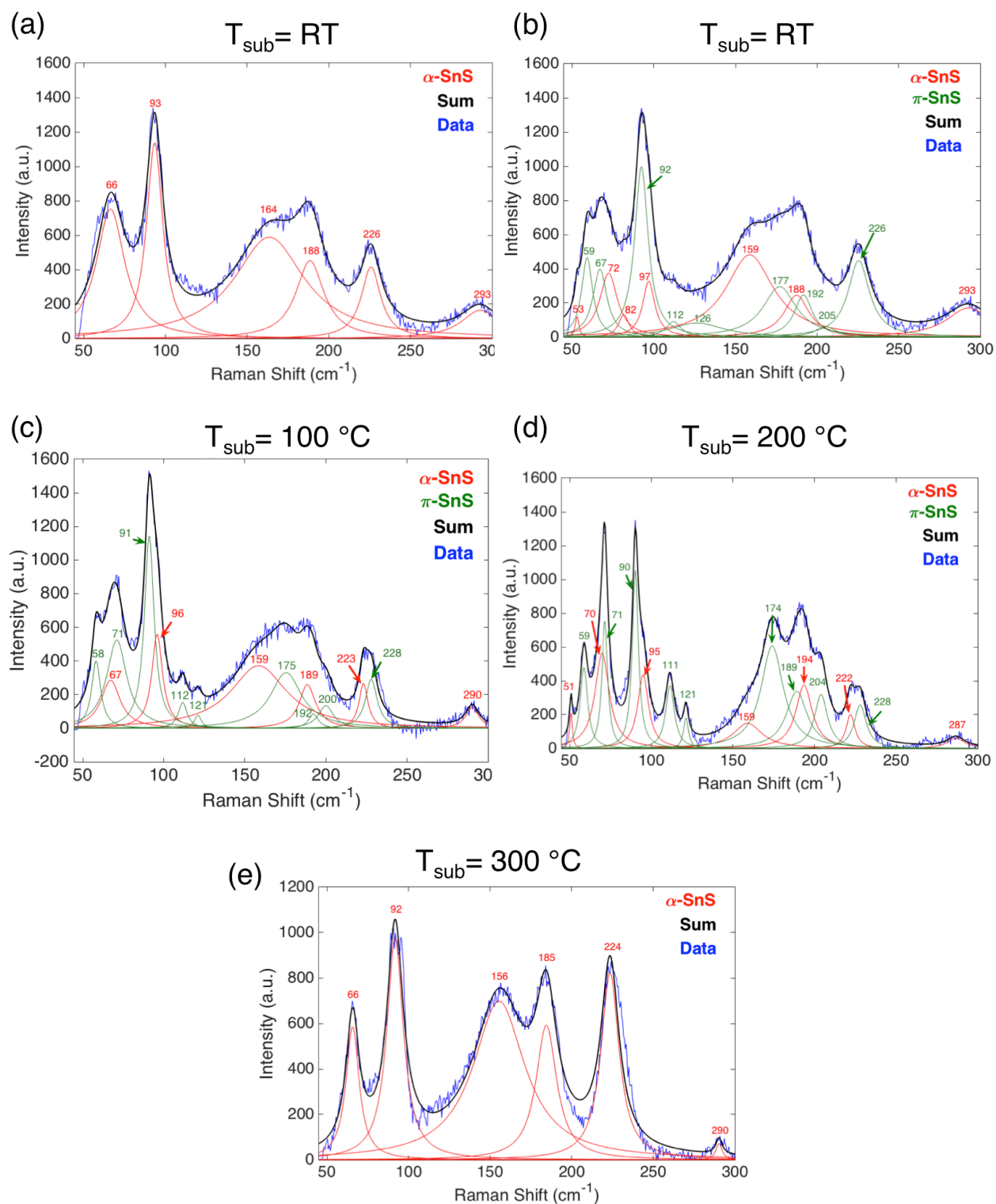


Figure 5.26: Deconvolution of Raman spectra of as-deposited films with 633 nm excitation wavelength after background subtraction. Deposition temperature is indicated by the T_{sub} value.

peaks only for deconvolution (Figure 5.26 a) and a mixture of α -SnS and π -SnS peaks (Figure 5.26 b). Deconvolution comprised of only α -SnS peaks (Figure 5.26 a) provided a good fit. The Raman spectrum of the film deposited at 100°C however, has distinct peaks at 112 cm⁻¹, 121 cm⁻¹ and 175 cm⁻¹ corresponding to π -SnS, indicating a mixture of α -SnS and π -SnS are present (Figure 5.26 c). The Raman spectrum of the film deposited at 200°C has clear peaks at 59, 71, 111, 121, 174, 189, 204 cm⁻¹ that correspond to π -SnS as well as peaks at 51 cm⁻¹ and 287 cm⁻¹ that distinctively correspond to α -SnS, suggesting this film is also a mixture of the α - and π -phases (Figure 5.26 d). The T_{sub} = 300°C condition was indexed to pure α -SnS (Figure 5.26 e).

The deconvoluted spectra of the annealed films are displayed in Figure 5.27. Figure 5.27 a, b indicates the room temperature deposition condition yielded pure α -SnS. The inclusion of π -SnS peaks during deconvolution (Figure 5.27b) does not provide significant improvement to the fit.

The intensity of π -SnS Raman peaks was lower for the film deposited at 100°C after annealing (Figure 5.27 c). Although the presence of π -SnS peaks at 110 cm⁻¹ and 120 cm⁻¹ may be debatable, the more distinctive π -SnS peak at 58 cm⁻¹ suggests π -SnS is present in this film.

The 200°C annealed film also shows a mixture of α -SnS and π -SnS phases (Figure 5.27 d). The intensity of the π -SnS peaks is lower than in the unannealed film, indicating annealing the film allowed the more stable α -phase to form.

The Raman spectra of a film deposited at 300°C and annealed at 300°C for 1 hr shows α -SnS peaks only (Figure 5.27 e). This result agrees with the analysis from XRD characterization (Figure 5.12, 5.13).

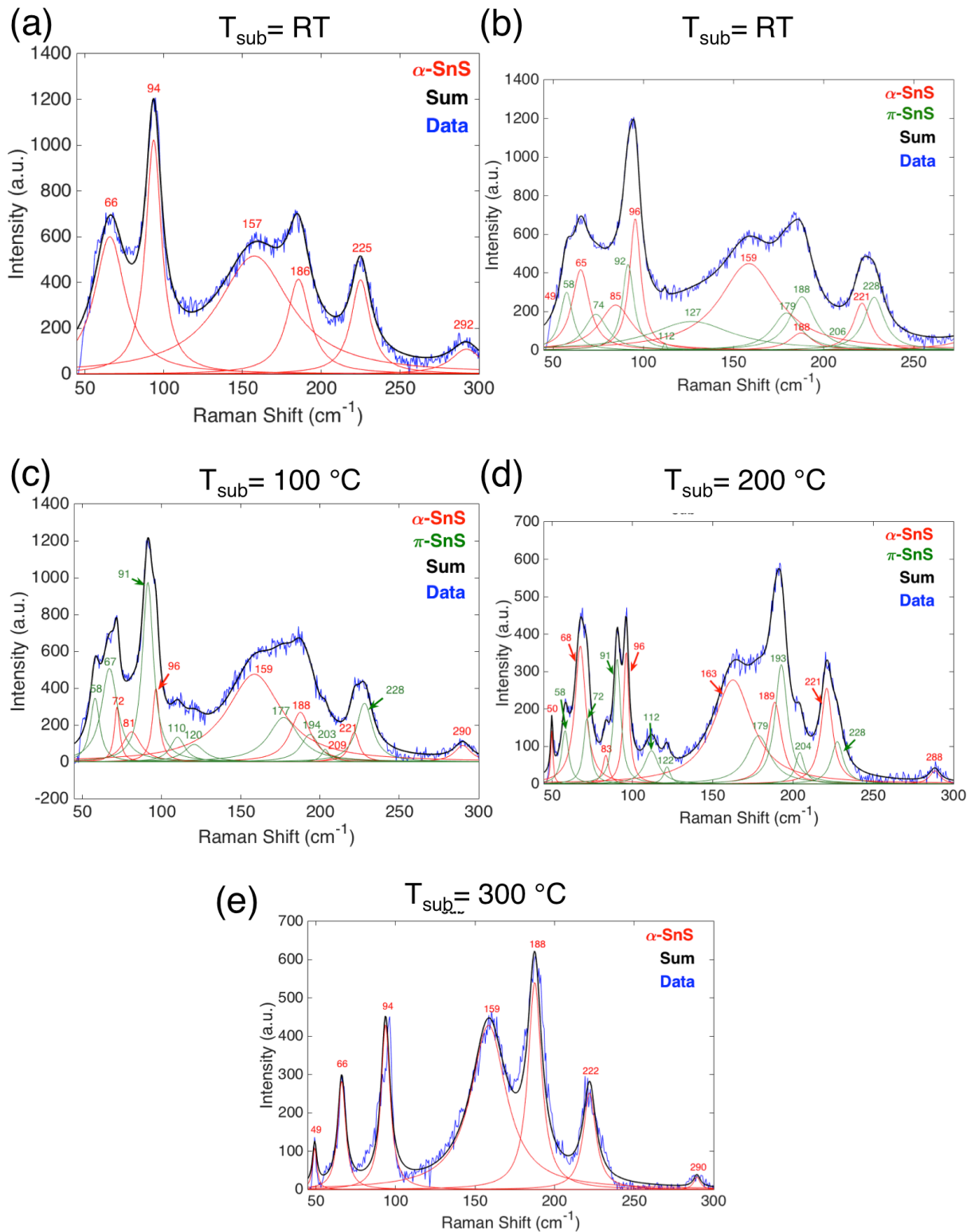


Figure 5.27: Deconvolution of Raman spectra of annealed films with 633 nm excitation wavelength. Deposition temperature is indicated by the T_{sub} value. Films were annealed at 300 $^{\circ}\text{C}$ for 1 hr).

Table 5.6 Summary of phases present determined by XRD and Raman spectroscopy.

	α SnS	π SnS	Sn ₂ S ₃	SnS ₂
RT	XRD, Raman			Raman
RT annealed	XRD, Raman			Raman
100°C	XRD, Raman	XRD, Raman		Raman
100°C annealed	XRD, Raman	XRD, Raman		Raman
200°C	XRD, Raman	XRD, Raman		
200°C annealed	XRD, Raman	XRD, Raman		
300°C	XRD, Raman			
300°C annealed	XRD, Raman			

Table 5.6 summarizes phases that were detected by XRD and Raman spectroscopy for each deposition condition. It is noted that Raman spectroscopy is more sensitive for detecting tin sulfide phases than XRD. Additionally, there is less ambiguity in phase identification than in XRD. The results indicate that deposition at $T_{\text{sub}} = 300\text{C}$ produced pure α -SnS. At intermediate deposition temperatures, π -SnS was present in the films.

Hall measurements were performed on an annealed α -SnS film that was deposited at 300°C and an unannealed α -SnS/ π -SnS mixed film that was deposited at 200°C. The former measurement was performed on a film that was deposited during the same batch as SnS films used for CTLM measurements in the next section. Ni/Au contacts were deposited for Hall measurements. The results are displayed in Table 5.7. Both films were p-type, which is expected of α -SnS and π -SnS.^{79, 91} The α -SnS film displayed a lower resistivity (and higher charge carrier mobility) than the mixed π -SnS/ α -SnS film.

Table 5.7: Hall measurement results of a mixed π -SnS and α -SnS film, which was deposited at 200 °C, and of an α -SnS film, which was deposited at 300 °C then post annealed at 300 °C. Error is the standard deviation, of 10 measurements.

	$T_{\text{sub}} = 200^\circ\text{C}$, As Dep	$T_{\text{sub}} = 300^\circ\text{C}$, Annealed
Resistivity ($\Omega\text{-cm}$)	600 ± 2.1	207 ± 14
Mobility ($\text{cm}^2/\text{V-s}$)	3.9 ± 1.3	5.8 ± 0.8
Density (cm^{-3})	$2.9 (\pm 0.9) \times 10^{15}$	$5.3 (\pm 0.8) \times 10^{15}$
Hall Coeff. (cm^3/C)	$2.4 (\pm 0.8) \times 10^2$	$1.2 (\pm 0.2) \times 10^2$
Type of Carriers	holes	holes

Transmittance and reflectance spectra of the films are plotted in Figure 5.28 a and 5.28 b, respectively. The films exhibit very low transmittance above 2.5 eV. The reflectance of the room temperature films was lower, which is attributed to their rougher surface morphology. Absorbance spectra of the films are plotted in Figure 5.28 (c). Absorption coefficients were calculated using the equation $\alpha \approx -\frac{1}{d} \ln \left(\frac{T}{1-R} \right)$ and are plotted in Figure 5.28 (d). The absorption coefficient of the α -SnS films are $> 10^{-5} \text{ cm}^{-1}$ in the visible range. Tauc plots for extracting indirect and direct band gaps are plotted in Figure 5.28 (e,f). The indirect band gap curves for the as-deposited and annealed films deposited at 200 °C appear to have two linear regions (Figure 5.28 e). The extracted indirect band gaps are listed in Table 5.8 for a linear fit to the 1.75 eV -2 eV range. The band gap of the films containing π -SnS appear to be higher, and the highest band gap occurred for the unannealed film deposited at 200 °C, which had the highest intensity π -SnS peaks in XRD and Raman spectroscopy. A larger band gap for π -SnS agrees with reported literature: The indirect band gap of α -SnS was reported to be $\sim 1.08 \text{ eV}$,¹⁵⁴ whereas a reported indirect band gap of π -SnS extracted from UV-vis measurements is 1.52 eV (indirect).⁷⁷

Table 5.8: Indirect band gaps extracted from 1.75 eV -2 eV region of Tauc plot in Figure 5.28 (e) for SnS films deposited at different substrate temperatures and with different post-deposition treatments. Composition was determined from XRD and Raman spectroscopy.

$T_{\text{sub}} (\text{°C})$	Post Treatment	E_g Indirect (eV)	Composition
25	As dep	1.21	α -SnS, SnS ₂
25	Anneal	1.19	α -SnS, SnS ₂
100	As dep	1.26	α -SnS, π -SnS, SnS ₂
100	Anneal	1.27	α -SnS, π -SnS, SnS ₂
200	As dep	1.37	α -SnS, π -SnS, SnS ₂
200	Anneal	1.35	α -SnS, π -SnS
300	As dep	1.18	α -SnS
300	Anneal	1.17	α -SnS

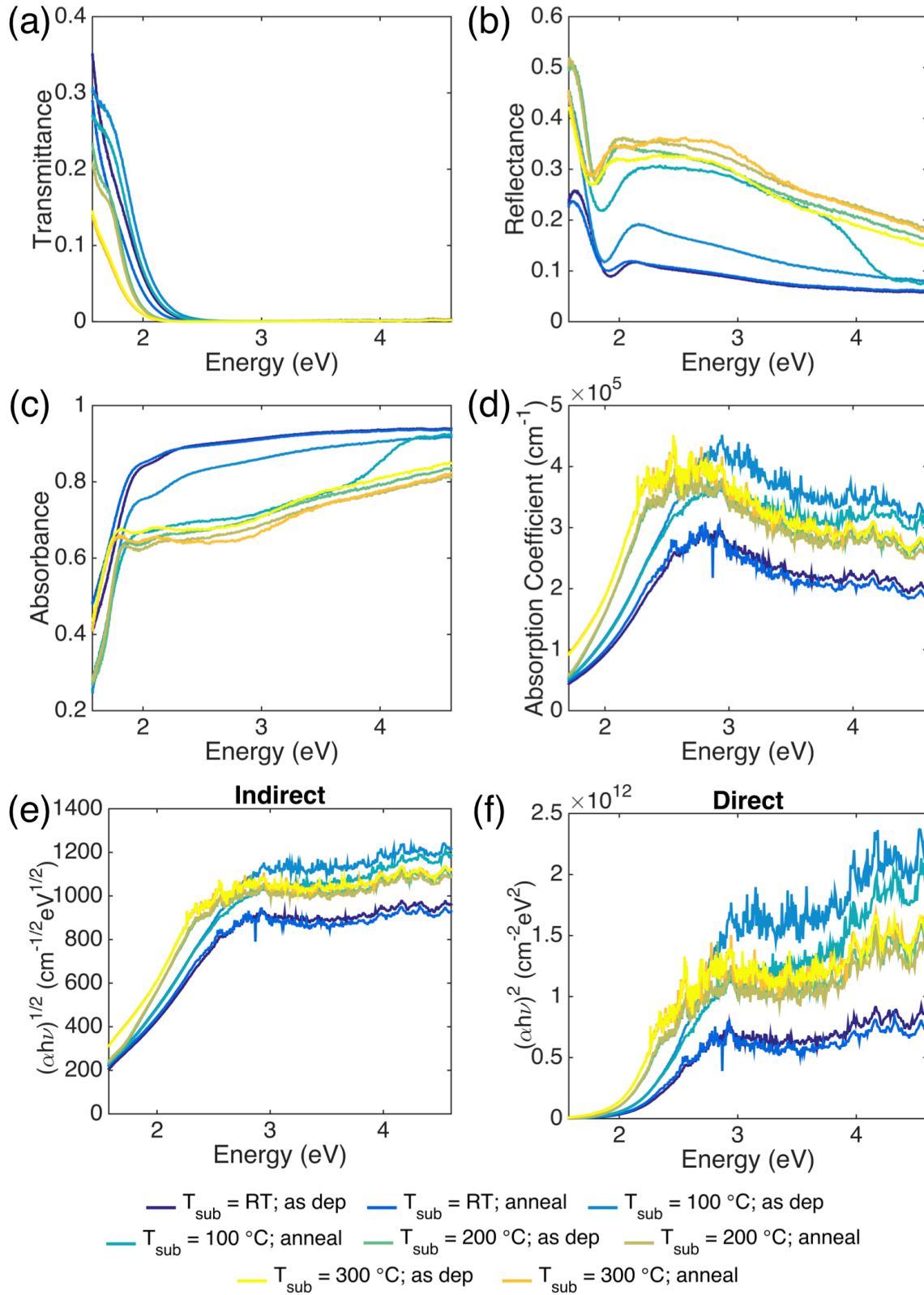


Figure 5.28 Optical spectra of SnS films. (a) Transmittance, (b) reflectance, (c) absorbance (d) absorption coefficient (e) Tauc plot for determining indirect band gap (f) Tauc plot for determining direct band gap.

5.3 Contacts to Electron-Beam Evaporated SnS Thin Films

5.3.1 Experimental Methods: Specific Contact Resistance Test Structure

Fabrication and Measurement

Circular Transfer Length Method (CTLM) pattern fabrication

The SnS films for CTLM contact resistance measurements were deposited on borosilicate glass substrates, which were cleaned immediately before the SnS depositions. The substrate cleaning process consisted of sonication in acetone, isopropanol, and DI water for 15 min each, followed drying with N₂. SnS films with three different processing conditions were employed: (1) 50 nm thick SnS films deposited at $T_{\text{sub}} = \text{RT}$, no post-deposition anneal (a.k.a. “as-deposited”); (2) 50 nm thick SnS films deposited at $T_{\text{sub}} = \text{RT}$, then annealed at 300°C for 1 hr; and (3) 226 nm thick SnS films deposited at $T_{\text{sub}} = 300^\circ\text{C}$, and annealed at 300°C for 1 hr.

CTLM patterns with dimensions of channel spacings indicated in Figure 5.29 a were fabricated using photolithography, as described in Section 3.4.2. Prior to contact deposition, SnS films with processing conditions (2) and (3) were treated with a 1 min, 100 W O₂ plasma clean (March Plasmod) followed by a 1% HF dip for 30s, a dip in DI water for 30s, and a N₂ drying step. Samples were loaded immediately (within 5-10 minutes) into the UHV chamber for e-beam evaporation. Ti/Au (50/50 nm), Ru/Au (50/50 nm), Ni/Au (50/50 nm), or Au (100 nm) contacts were deposited, followed by liftoff in acetone, to create the contact patterns shown in Figure 5.29 b.

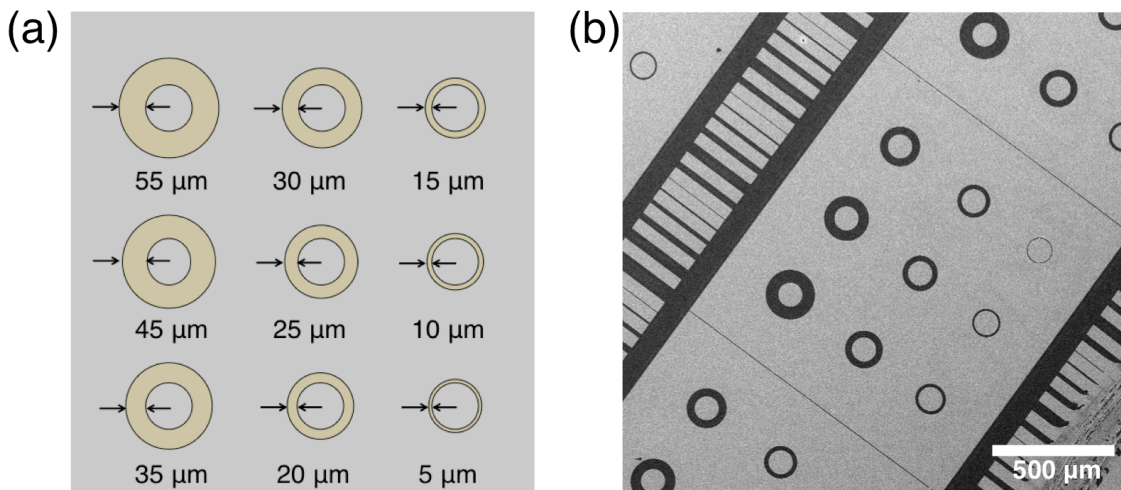


Figure 5.29: (a) Schematic of CTLM pattern indicating spacings. (b) Secondary electron SEM image of CTLM pattern.

Specific contact resistance measurements

I-V measurements were performed in the dark across each spacing with a Signatone probe station. Contact spacings were determined from SEM images and an ImageJ macro. A non-linear least-squares fit of the total resistance and spacings data to Equation 3.5 was performed in MATLAB.

5.3.2 Results: Initial Study of Contacts on 50 nm Thick Films

Initial contact resistance studies were performed on 50 nm thick SnS films. Ti/Au, Ru/Au, Ni/Au, and Au all formed ohmic contacts as deposited (Figure 5.30 a). An example CTLM fit to a plot of total resistance vs. contact outer radius is shown in Figure 5.30 b.

The red, filled circles in Figure 5.30 c indicate specific contact resistance values on unannealed SnS films with no surface treatment prior to contact deposition. Ti/Au contacts had the highest contact resistance; however, there is also significant uncertainty in the values corresponding with considerable standard deviations. For some contacts, it was difficult to

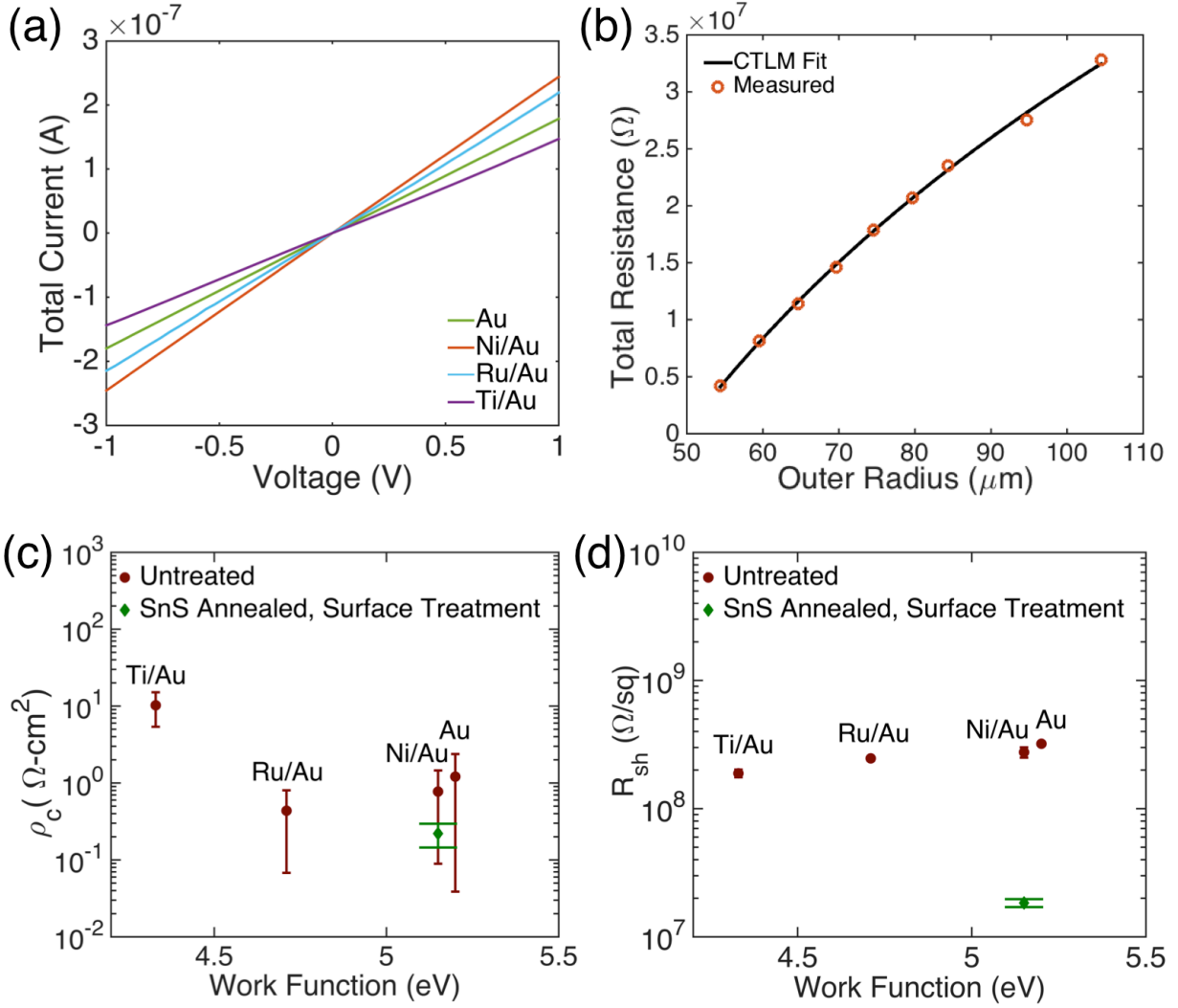


Figure 5.30: Results of CTLM measurements on 50 nm thick SnS films deposited at $T_{\text{sub}} = \text{RT}$. (a) I-V characteristics of metals deposited with a 5 μm CTLM spacing (b) Example least squares fit of total resistance versus outer radius to Equation 3.5 for Ni/Au contacts. (c) Extracted specific contact resistances for contacts on 50 nm thick SnS films: both as-deposited films with no surface treatment (red circles) and SnS films annealed at 300°C for 1 hr followed by a surface treatment of O_2 plasma followed by a 30s dip in 1% HF (green diamond). Annealing was performed prior to contact deposition.

extract a specific contact resistance due to short transfer lengths, indicating the contact resistance may be lower than what was measurable at these sheet resistances.

SnS films having low sheet resistance are needed to accurately extract low specific contact resistances values. In specific contact resistance measurements, a sufficient amount of

the total resistance should be comprised of the contact resistance and not obscured by a high semiconductor channel resistance. For high R_{sh}/ρ_c ratios, the transfer length becomes small ($L_T = \sqrt{\frac{\rho_c}{R_{sh}}}$) and the K_0 and K_1 terms in the Equation 3.5 become so small that they are at the computational limit (2.2251×10^{-308}) of the program. If an approximation for the Bessel functions is used for these cases, slight changes in the shape of the fit to the experimental curve result in a large change in the extracted transfer length, making the values unreliable. Therefore, it is of interest to decrease the resistivity of the SnS films for the contact resistance measurements in this study. For this reason, contacts were also deposited on annealed 50 nm thick SnS films, which had a lower measured resistivity than the as-deposited 50 nm thick SnS films (Section 5.2.3).

An additional consideration is the cleanliness of the semiconductor surface, as the properties of metal-semiconductor contacts are often sensitive to the surface preparation and cleaning method of the semiconductor. Therefore, prior to contact deposition a surface treatment consisting of a 100 W O_2 plasma exposure was performed to remove residual photoresist. Subsequently the samples were submersed for 30 s each in an aqueous solution of 1% HF and then DI water; these steps were intended to remove the surface oxide.

The green diamond in Figure 5.30 c corresponds to the contact resistance of Ni/Au on an annealed, 50 nm thick film that received the above surface treatment. Ru/Au and Au contacts were also deposited on SnS films at these conditions; however, they faced challenges with short transfer lengths, making contact resistance extraction difficult; there were large variations in the values. Therefore contact resistance values for the Ru/Au and Au contacts on surface treated films are not plotted.

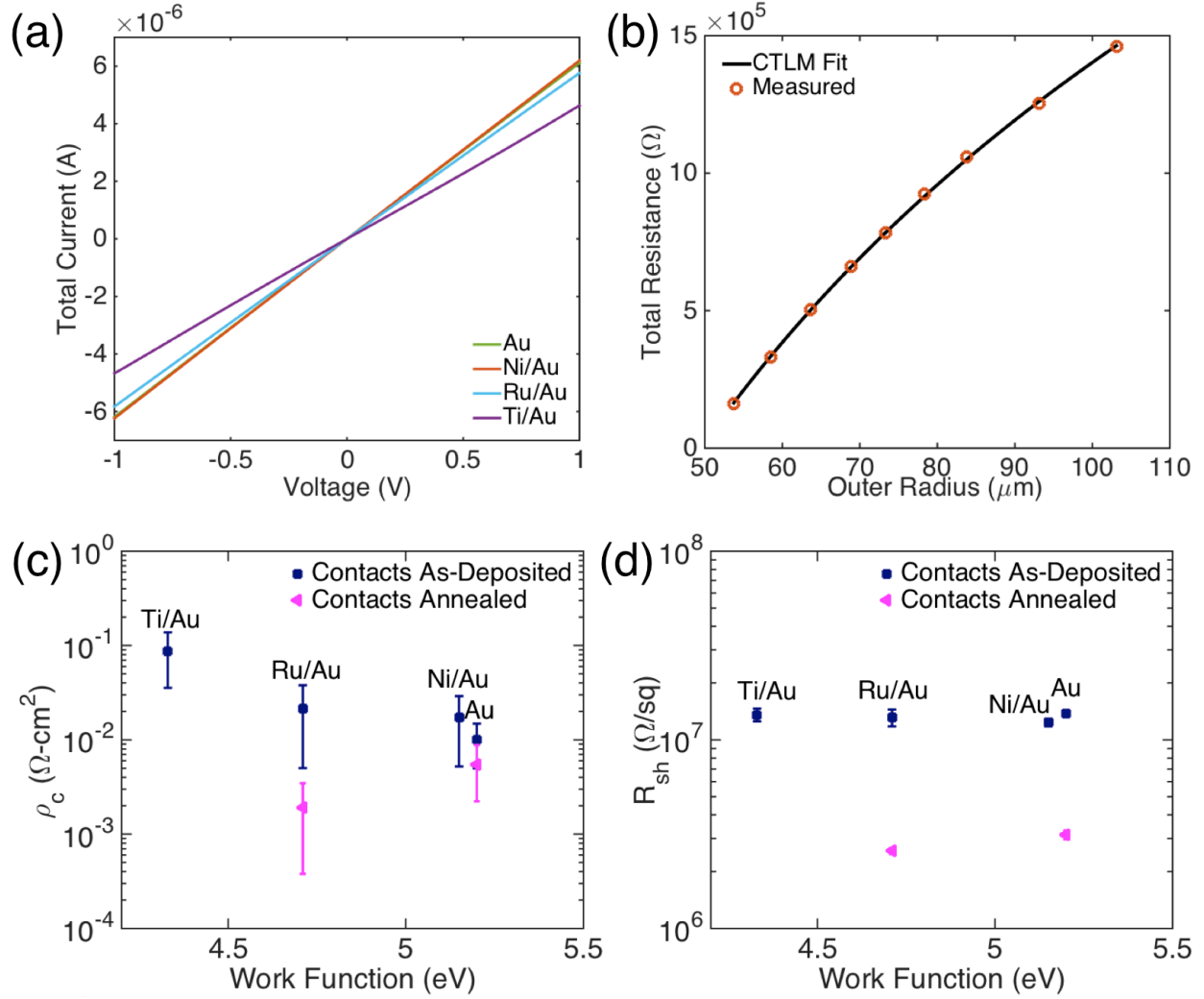


Figure 5.31: Results of CTLM measurements on 226 nm thick SnS films deposited at $T_{\text{sub}} = 300^\circ\text{C}$, then post annealed in vacuum at 300°C for 1hr. A surface treatment of O_2 plasma followed by a 1% HF dip was performed. (a) I-V characteristics of metals deposited with a 5 μm CTLM spacing (b) Example least squares fit of total resistance versus outer radius to Equation 3.5 for Ni/Au contacts. Extracted specific contact resistances (c) and sheet resistances (d) of metals deposited on SnS. Blue squares correspond to as-deposited contacts, whereas the magenta triangles correspond to contacts that were annealed at 350°C in Ar for 5 min.

5.3.3 Results: Contacts on $T_{\text{sub}} = 300^\circ\text{C}$, Post Annealed Films

Contacts were deposited onto ~ 226 nm thick, $T_{\text{sub}} = 300^\circ\text{C}$, post annealed, α -SnS films.

All contacts were ohmic as deposited (Figure 5.31 a). An example of a fit to a plot of total resistance vs. outer contact radius for Ni/Au contacts is shown in Figure 5.31 b. Standard deviations are smaller for contacts deposited on these SnS films compared to those the previous

section. Average specific contact resistance decreases with metal work function, from Ti/Au. Ru/Au, Ni/Au to Au. However, in contrast to the observed Schottky and ohmic behavior on SnS nanoribbons (Chapter 4), all contacts are ohmic on the SnS thin films, suggesting at least partial Fermi level pinning.

Contacts were additionally annealed at 350°C in Ar for 5 min. Specific contact resistances of the Ru/Au contacts decreased after annealing to an average value of $\rho_c = 1.9 \times 10^{-3} \Omega\text{-cm}^2$. The specific contact resistance of the Au contacts remained almost the same after annealing. Both calculations using FactSage® thermochemical software¹⁵⁵ and a reported calculated phase diagram¹³⁷ indicate that Au does not react with SnS at this temperature, which may explain the relative stability in the Au/SnS contact resistance before and after annealing. The sheet resistance of SnS was found to decrease for Ru/Au and Au contacts after annealing. (Figure 5.31 d).

Both Ni and Ti metals are expected to be reactive with bulk SnS, according to FactSage® thermochemical software.¹⁵⁵ The electrical characteristics also suggest that reactions and/or interdiffusion may have occurred at the Ni/SnS and Ti/SnS interfaces after annealing. For example, Figure 5.32 a shows that, contrary to the overall trend, the total resistance for the smallest Ni/Au contact spacing was larger than that for the next smallest spacing; this behavior was consistent in all annealed Ni/Au contact sets. Figure 5.32 b is a plot of a fit of the data without the smallest spacing. The extracted parameters (Table 5.9) from either fit (Figure 5.32 a, b) indicate that the contact resistance of the Ni/Au films increased after annealing. Additionally, the extracted SnS sheet resistance value and its standard deviation were both larger for the annealed Ni/Au contact compared to the annealed Ru/Au and Au contacts (Figure 5.31). Annealing the Ti/Au contacts resulted in inconsistent electrical behavior, suggesting an

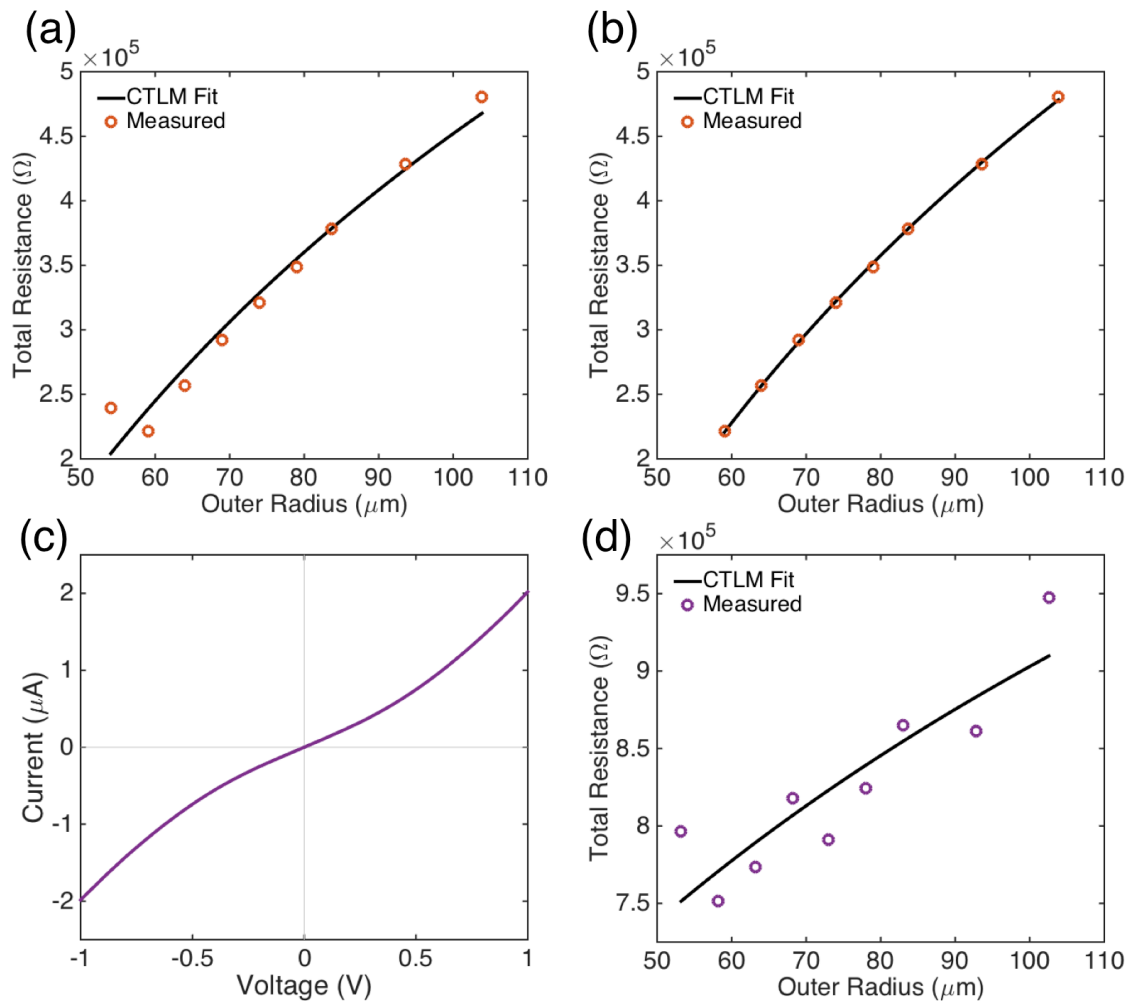


Figure 5.32: (a) Plot of outer radius versus total resistance of Ni/Au contacts on SnS after annealing the contacts, showing a deviation from the expected trend of decreasing total resistance with contact spacing. (b) Fit performed to Ni/Au contact data after annealing without small spacing included. The parameters extracted from both fits are included in Table 5.9. (c) Current-voltage characteristics of Ti/Au contacts after annealing. (d) Inconsistent electrical behavior after annealing Ti/Au contacts. The SnS film in (a-d) was deposited at the same conditions as in Figure 5.31.

unfavorable reaction occurred (Figure 5.32 d). Further study is needed to confirm any reaction or interdiffusion at the Ni/SnS and Ti/SnS interfaces

Table 5.9: Extracted contact resistance parameters for Ni/Au contacts after annealing: with smallest contact spacing included in fit, and without.

	ρ_c	R_{sh}	L_T	R^2
With Small Spacing	2.44 ± 0.4	$4.7 (\pm 1.6) \times 10^6$	7.4 ± 1.2	0.9704 ± 0.0097
Without Small Spacing	1.67 ± 0.36	$4.9 (\pm 1.7) \times 10^6$	6.0 ± 1.2	0.9965 ± 0.0022

Comparison to literature

A comparison of specific contact resistances and sheet resistances measured in this study to those reported in literature is shown in Figure 5.33 (a, b). The average specific contact resistance of as-deposited Au contacts in the present study is similar to that reported by Gurunathan, *et. al.*,¹³⁷ but lower than that reported by Yang *et. al.*. Au was found to be unreactive after annealing (Gurunathan, *et. al.*), which is consistent with ρ_c remaining generally constant in the present study. On the contrary, Yang *et. al.* observed a decrease in ρ_c after annealing in H₂S in a substrate configuration for Au and Ti, which was not observed here for anneal in Ar in a superstrate configuration. In general, specific contact resistance of as-deposited metals decreases with increasing work function for these studies. However, in contrast to our results on contacts to the SnS nanoribbons (Chapter 4) all contacts to the SnS thin films were found to be ohmic.

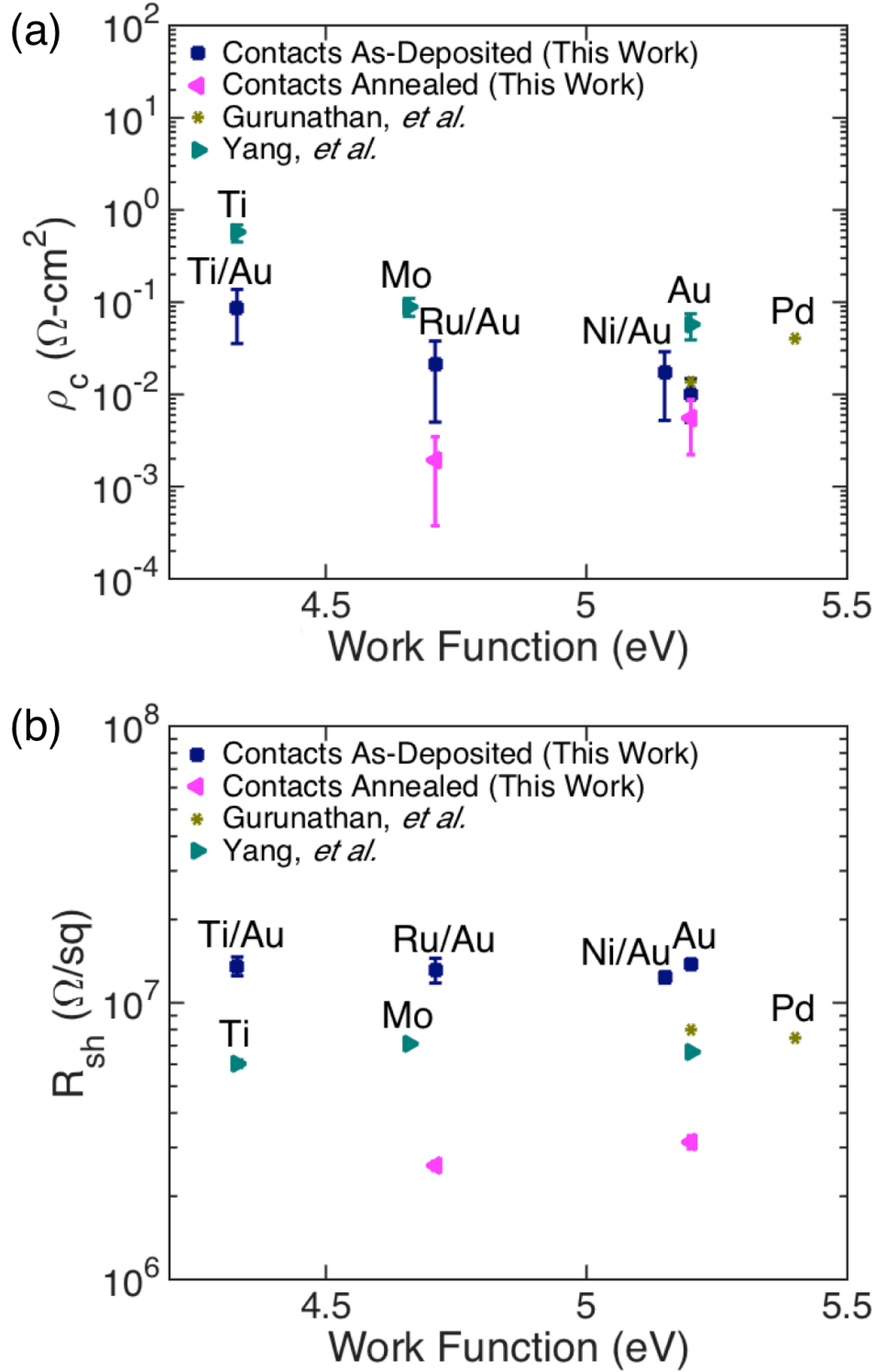


Figure 5.33: Comparison of specific contact resistances and sheet resistances determined in this study to those in Gurunathan, *et. al.* and Yang, *et. al.*⁵⁰

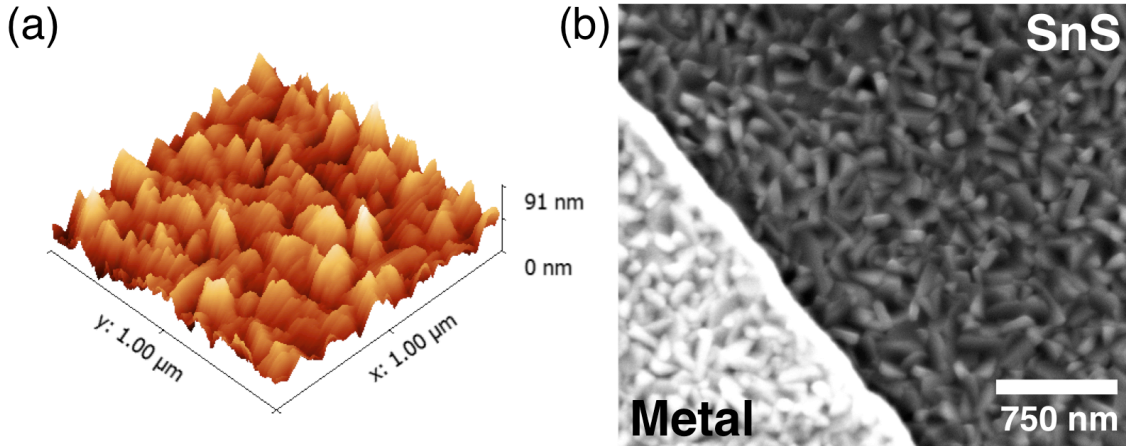


Figure 5.34: (a) Topology of an SnS film obtained with AFM. The SnS film was deposited onto a soda lime glass substrate at $T_{\text{sub}} = 300^{\circ}\text{C}$ and post annealed at 300°C for 1 hr. RMS roughness = 12 nm. (b) Plan view secondary electron SEM image of an as-deposited Ni/Au contact on an SnS film on borosilicate glass showing conformation of the contact to the morphology of the SnS film.

Figure 5.34 a displays the surface topography of the $T_{\text{sub}} = 300^{\circ}\text{C}$, post-annealed SnS film condition used in the CTLM measurements. The RMS roughness of the surface was 12 nm, and films are polycrystalline. Figure 5.34 b indicates the deposited metal conformed to the surface of the SnS film. SnS is an anisotropic material, and the metal appears to be in contact with different SnS grain facets. DFT-based calculations in literature have found the electron affinity of SnS can vary by up to 0.9 eV for different orientations.⁹⁸ It has been calculated that there are no surface states for the pristine SnS(100) surface, however other surface orientations exhibit states below the conduction band and above the valence band associated with dangling bonds.¹⁴² Contact with surfaces (or facets) containing high densities of surface states could contribute to Fermi level pinning in these films.

5.4 Conclusion

SnS films were electron-beam evaporated at different substrate temperatures and vacuum annealed. Chemical, electrical, and optical properties of the films were characterized. A substrate temperature of 300°C with 300°C post anneal resulted in an α -SnS film, whereas Raman spectroscopy and XRD indicated a mixture of π -SnS and α -SnS was present in films deposited at substrate temperatures of 100°C and 200°C. All films were p-type, with a minimum resistivity occurring for the films deposited at $T_{\text{sub}} = 300^\circ\text{C}$ and annealed at 300°C for 1 hr. Contacts with a range of work functions were deposited on the nanocrystalline α -SnS films, and specific contact resistances were measured before and after annealing the contacts at 350°C in flowing Ar. As-deposited contact resistances exhibit a weak dependence on metal work function, indicating partial Fermi level pinning. Ru/Au contacts annealed at 350 °C yielded the lowest contact resistance, whereas Ni/Au and Ti/Au contacts were found to be unstable after annealing.

5.5 References

1. *Fraunhofer ISE: Photovoltaics Report*, Fraunhofer Institute for Solar Energy Systems, ISE with support of PSE Conferences & Consulting GmbH, Freiburg, 2018.
2. A. Luque, *Handbook of Photovoltaic Science and Engineering*, Wiley, 2003.
3. S. M. Sze and K. K. Ng, in *Physics of Semiconductor Devices*, J. Wiley & Sons, Hoboken, NJ, 3rd edn., 2007, ch. Appendix G, p. 790.
4. W. Shockley and H. J. Queisser, *J. Appl. Phys.*, 1961, **32**, 510-519.
5. W. N. Shafarman, S. Siebentritt and L. Stolt, in *Handbook of Photovoltaic Science and Engineering*, eds. A. Luque and S. Hegedus, John Wiley & Sons, Ltd, West Sussex, United Kingdom, 2 edn., 2011, ch. 13, pp. 546-599.
6. B. E. McCandless and J. R. Sites, in *Handbook of Photovoltaic Science and Engineering*, eds. A. Luque and S. Hegedus, John Wiley & Sons, Ltd, West Sussex, United Kingdom, 2 edn., 2011, ch. 14, pp. 600-641.
7. A. Luque and S. Hegedus, in *Handbook of Photovoltaic Science and Engineering*, eds. A. Luque and S. Hegedus, John Wiley & Sons, Ltd, West Sussex, United Kingdom, 2 edn., 2011, ch. 1, pp. 1-36.

8. K. Yoshikawa, H. Kawasaki, W. Yoshida, T. Irie, K. Konishi, K. Nakano, T. Uto, D. Adachi, M. Kanematsu, H. Uzu and K. Yamamoto, *Nature Energy*, 2017, **2**, 17032.
9. J. D. Major, *Semiconductor Science and Technology*, 2016, **31**, 093001.
10. N. M. Haegel, R. Margolis, T. Buonassisi, D. Feldman, A. Froitzheim, R. Garabedian, M. Green, S. Glunz, H. M. Henning, B. Holder, I. Kaizuka, B. Kroposki, K. Matsubara, S. Niki, K. Sakurai, R. A. Schindler, W. Tumas, E. R. Weber, G. Wilson, M. Woodhouse and S. Kurtz, *Science*, 2017, **356**, 141-143.
11. M. A. Green, Y. Hishikawa, E. D. Dunlop, D. H. Levi, J. Hohl-Ebinger and A. W. Y. Ho-Baillie, *Progress in Photovoltaics*, 2018, **26**, 3-12.
12. S. Davidsson and M. Hook, *Energy Policy*, 2017, **108**, 574-582.
13. M. A. Green, *J. Mater. Sci.: Mater. Electron.*, 2007, **18**, S15-S19.
14. A. Feltrin and A. Freundlich, *Renewable Energy*, 2008, **33**, 180-185.
15. V. Steinmann, R. E. Brandt and T. Buonassisi, *Nature Photonics*, 2015, **9**, 355-357.
16. C. Wadia, A. P. Alivisatos and D. M. Kammen, *Environmental Science & Technology*, 2009, **43**, 2072-2077.
17. R. E. Banai, M. W. Horn and J. R. S. Brownson, *Sol. Energy Mater. Sol. Cells*, 2016, **150**, 112-129.
18. G. A. Tritsarlis, B. D. Malone and E. Kaxiras, *J. Appl. Phys.*, 2013, **113**, 233507.
19. T. Gokmen, O. Gunawan, T. K. Todorov and D. B. Mitzi, *Appl. Phys. Lett.*, 2013, **103**, 103506.
20. E. Chagarov, K. Sardashti, A. C. Kummel, Y. S. Lee, R. Haight and T. S. Gershon, *J. Chem. Phys.*, 2016, **144**, 104704.
21. S. K. Wallace, D. B. Mitzi and A. Walsh, *Acs Energy Letters*, 2017, **2**, 776-779.
22. V. Piacente, S. Foglia and P. Scardala, *Journal of Alloys and Compounds*, 1991, **177**, 17-30.
23. J. J. Loferski, *J. Appl. Phys.*, 1956, **27**, 777-784.
24. S. Ruhle, *Solar Energy*, 2016, **130**, 139-147.
25. H. Noguchi, A. Setiyadi, H. Tanamura, T. Nagatomo and O. Omoto, *Sol. Energy Mater. Sol. Cells*, 1994, **35**, 325-331.
26. P. Sinsermsuksakul, L. Z. Sun, S. W. Lee, H. H. Park, S. B. Kim, C. X. Yang and R. G. Gordon, *Adv. Energy Mater.*, 2014, **4**, 1400496.
27. P. D. Paulson, R. W. Birkmire and W. N. Shafarman, *J. Appl. Phys.*, 2003, **94**, 879-888.
28. S. M. Sze and K. K. Ng, in *Physics of Semiconductor Devices*, J. Wiley & Sons, Hoboken, NJ, 3rd edn., 2007, ch. 1, p. 53.
29. S. Adachi, in *Copper Zinc Tin Sulfide-Based Thin-Film Solar Cells*, ed. K. Ito, John Wiley & Sons, Ltd, Chichester, West Sussex, UK, 2015, ch. 7, pp. 171-173.
30. J. A. Andrade-Arvizu, M. Courel-Piedrahita and O. Vigil-Galan, *J. Mater. Sci.: Mater. Electron.*, 2015, **26**, 4541-4556.
31. S. A. Bashkurov, V. F. Gremenok, V. A. Ivanov, V. V. Lazenka and K. Bente, *Thin Solid Films*, 2012, **520**, 5807-5810.
32. H. H. Park, R. Heasley, L. Z. Sun, V. Steinmann, R. Jaramillo, K. Hartman, R. Chakraborty, P. Sinsermsuksakul, D. Chua, T. Buonassisi and R. G. Gordon, *Progress in Photovoltaics*, 2015, **23**, 901-908.
33. A. Schneikart, H. J. Schimper, A. Klein and W. Jaegermann, *Journal of Physics D-Applied Physics*, 2013, **46**, 305109.

34. D. Avellaneda, M. T. S. Nair and P. K. Nair, *Journal of the Electrochemical Society*, 2008, **155**, D517-D525.
35. K. T. R. Reddy, N. K. Reddy and R. W. Miles, *Sol. Energy Mater. Sol. Cells*, 2006, **90**, 3041-3046.
36. B. Ghosh, M. Das, R. Banerjee and S. Das, *Sol. Energy Mater. Sol. Cells*, 2008, **92**, 1099-1104.
37. A. Wangperawong, P. C. Hsu, Y. Yee, S. M. Herron, B. M. Clemens, Y. Cui and S. F. Bent, *Appl. Phys. Lett.*, 2014, **105**, 173904.
38. D. Avellaneda, M. T. S. Nair and P. K. Nair, *Thin Solid Films*, 2009, **517**, 2500-2502.
39. J. Malaquias, P. A. Fernandes, P. M. P. Salome and A. F. da Cunha, *Thin Solid Films*, 2011, **519**, 7416-7420.
40. A. M. Haleem and M. Ichimura, *J. Appl. Phys.*, 2010, **107**, 034507.
41. M. Sugiyama, K. T. R. Reddy, N. Revathi, Y. Shimamoto and Y. Murata, *Thin Solid Films*, 2011, **519**, 7429-7431.
42. L. A. Burton and A. Walsh, *Appl. Phys. Lett.*, 2013, **102**, 132111.
43. J. J. Scragg, J. T. Watjen, M. Edoff, T. Ericson, T. Kubart and C. Platzter-Bjorkman, *J. Am. Chem. Soc.*, 2012, **134**, 19330-19333.
44. S. Lopez-Marino, M. Placidi, A. Perez-Tomas, J. Llobet, V. Izquierdo-Roca, X. Fontane, A. Fairbrother, M. Espindola-Rodriguez, D. Sylla, A. Perez-Rodriguez and E. Saucedo, *Journal of Materials Chemistry A*, 2013, **1**, 8338-8343.
45. G. K. Dalapati, S. Zhuk, S. Masudy-Panah, A. Kushwaha, H. L. Seng, V. Chellappan, V. Suresh, Z. H. Su, S. K. Batabyal, C. C. Tan, A. Guchhait, L. H. Wong, T. K. S. Wong and S. Tripathy, *Scientific Reports*, 2017, **7**, 1350.
46. B. D. Malone, A. Gali and E. Kaxiras, *Phys. Chem. Chem. Phys.*, 2014, **16**, 26176-26183.
47. J. Vidal, S. Lany, M. d'Avezac, A. Zunger, A. Zakutayev, J. Francis and J. Tate, *Appl. Phys. Lett.*, 2012, **100**, 032104.
48. A. Polizzotti, A. Faghaninia, J. R. Poindexter, L. Nienhaus, V. Steinmann, R. L. Z. Hoye, A. Felten, A. Deyine, N. M. Mangan, J. P. Correa-Baena, S. S. Shin, S. Jaffer, M. G. Bawendi, C. Lo and T. Buonassisi, *Journal of Physical Chemistry Letters*, 2017, **8**, 3661-3667.
49. M. Patel and A. Ray, *ACS Appl. Mater. Interfaces*, 2014, **6**, 10099-10106.
50. C. X. Yang, L. Z. Sun, R. E. Brandt, S. B. Kim, X. Z. Zhao, J. Feng, T. Buonassisi and R. G. Gordon, *J. Appl. Phys.*, 2017, **122**, 045303.
51. R. C. Sharma and Y. A. Chang, *Bulletin of Alloy Phase Diagrams*, 1986, **7**, 269-273.
52. R. C. Sharma and Y. A. Chang, *ASM Alloy Phase Diagram Database*, 2006, Diagram Number: 902053.
53. A. H. Clark, *Naturwissenschaften*, 1972, **59**, 361-361.
54. G. Lindwall, S. L. Shang, N. R. Kelly, T. Anderson and Z. K. Liu, *Solar Energy*, 2016, **125**, 314-323.
55. H. Wiedemeier and F. J. Csillag, *Zeitschrift Fur Anorganische Und Allgemeine Chemie*, 1980, **469**, 197-206.
56. P. Villars, *Pearson's Handbook Desk Edition: Crystallographic Data for Intermetallic Phases*, ASM International, Materials Park, OH, 1997.
57. A. Walsh and G. W. Watson, *Journal of Physical Chemistry B*, 2005, **109**, 18868-18875.
58. T. Chattopadhyay, J. Pannetier and H. G. Vonschnering, *Journal of Physics and Chemistry of Solids*, 1986, **47**, 879-885.

59. G. H. Moh, *Neues Jahrb Mineral, Abhdl*, 1969, **111**, 227-263.
60. R. Kniep, D. Mootz, U. Severin and H. Wunderlich, *Acta Crystallographica Section B: Structural Crystallography and Crystal Chemistry*, 1982, **38**, 2022-2023.
61. D. J. Singh, *Appl. Phys. Lett.*, 2016, **109**, 032102.
62. L. A. Burton, D. Colombara, R. D. Abellon, F. C. Grozema, L. M. Peter, T. J. Savenije, G. Dennler and A. Walsh, *Chem. Mater.*, 2013, **25**, 4908-4916.
63. A. K. Singh and R. G. Hennig, *Appl. Phys. Lett.*, 2014, **105**, 042103.
64. R. M. Hazen and L. W. Finger, *American Mineralogist*, 1978, **63**, 289-292.
65. T. Jiang and G. A. Ozin, *Journal of Materials Chemistry*, 1998, **8**, 1099-1108.
66. L. A. Burton, T. J. Whittles, D. Hesp, W. M. Linhart, J. M. Skelton, B. Hou, R. F. Webster, G. O'Dowd, C. Reece, D. Cherns, D. J. Fermin, T. D. Veal, V. R. Dhanak and A. Walsh, *Journal of Materials Chemistry A*, 2016, **4**, 1312-1318.
67. Y. Huang, E. Sutter, J. T. Sadowski, M. Cotlet, O. L. A. Monti, D. A. Racke, M. R. Neupane, D. Wickramaratne, R. K. Lake, B. A. Parkinson and P. Sutter, *ACS Nano*, 2014, **8**, 10743-10755.
68. S. Gedi, V. R. M. Reddy, B. Pejjaai, C. W. Jeon, C. Park and K. T. R. Reddy, *Applied Surface Science*, 2016, **372**, 116-124.
69. V. Steinmann, R. Jaramillo, K. Hartman, R. Chakraborty, R. E. Brandt, J. R. Poindexter, Y. S. Lee, L. Z. Sun, A. Polizzotti, H. H. Park, R. G. Gordon and T. Buonassisi, *Advanced Materials*, 2014, **26**, 7488-7492.
70. R. Colin and J. Drowart, *J. Chem. Phys.*, 1962, **37**, 1120-1125.
71. R. E. Banai, J. C. Cordell, G. Lindwall, N. J. Tanen, S. L. Shang, J. R. Nasr, Z. K. Liu, J. R. S. Brownson and M. W. Horn, *J. Electron. Mater.*, 2016, **45**, 499-508.
72. A. W. Richards, *Transactions of the Faraday Society*, 1955, **51**, 1193-1197.
73. H. Wiedemeier and F. J. Csillag, *Thermochimica Acta*, 1979, **34**, 257-265.
74. A. N. Mariano and K. L. Chopra, *Appl. Phys. Lett.*, 1967, **10**, 282-284.
75. S. B. Badachhape and A. Goswami, *Journal of the Physical Society of Japan*, 1962, **17**, 251-253.
76. A. Rabkin, S. Samuha, R. E. Abutbul, V. Ezersky, L. Meshi and Y. Golan, *Nano Lett.*, 2015, **15**, 2174-2179.
77. R. E. Abutbul, E. Segev, L. Zeiri, V. Ezersky, G. Makov and Y. Golan, *RSC Adv.*, 2016, **6**, 5848-5855.
78. R. E. Abutbul, A. R. Garcia-Angelmo, Z. Burshtein, M. T. S. Nair, P. K. Nair and Y. Golan, *Crystengcomm*, 2016, **18**, 5188-5194.
79. J. M. Skelton, L. A. Burton, F. Oba and A. Walsh, *Apl Materials*, 2017, **5**, 036101.
80. A. Jain, S. P. Ong, G. Hautier, W. Chen, W. D. Richards, S. Dacek, S. Cholia, D. Gunter, D. Skinner, G. Ceder and K. a. Persson, *APL Materials*, 2013, **1**, 011002.
81. J. Vidal, S. Lany, J. Francis, R. Kokenyesi and J. Tate, *J. Appl. Phys.*, 2014, **115**, 113507.
82. J. M. Skelton, L. A. Burton, F. Oba and A. Walsh, *J. Phys. Chem. C*, 2017, **121**, 6446-6454.
83. C. Gao, H. L. Shen and L. Sun, *Applied Surface Science*, 2011, **257**, 6750-6755.
84. C. Gao, H. L. Shen, L. Sun, H. B. Huang, L. F. Lu and H. Cai, *Materials Letters*, 2010, **64**, 2177-2179.
85. L. Ren, Z. G. Jin, W. D. Wang, H. Liu, J. Y. Lai, J. X. Yang and Z. L. Hong, *Applied Surface Science*, 2011, **258**, 1353-1358.
86. Z. T. Deng, D. R. Han and Y. Liu, *Nanoscale*, 2011, **3**, 4346-4351.

87. E. C. Greyson, J. E. Barton and T. W. Odom, *Small*, 2006, **2**, 368-371.
88. L. A. Burton and A. Walsh, *J. Phys. Chem. C*, 2012, **116**, 24262-24267.
89. A. J. Biacchi, D. D. Vaughn and R. E. Schaak, *J. Am. Chem. Soc.*, 2013, **135**, 11634-11644.
90. P. K. Nair, A. R. Garcia-Angelmo and M. T. S. Nair, *Phys. Status Solidi A*, 2016, **213**, 170-177.
91. U. Chalapathi, B. Poornaprakash and S. H. Park, *Superlattices and Microstructures*, 2017, **103**, 221-229.
92. A. R. Garcia-Angelmo, R. Romano-Trujillo, J. Campos-Alvarez, O. Gomez-Daza, M. T. S. Nair and P. K. Nair, *Phys. Status Solidi A*, 2015, **212**, 2332-2340.
93. U. Chalapathi, B. Poornaprakash and S. H. Park, *Solar Energy*, 2016, **139**, 238-248.
94. K. O. Hara, S. Suzuki and N. Usami, *Thin Solid Films*, 2017, **639**, 7-11.
95. O. V. Bilousov, Y. Ren, T. Torndahl, O. Donzel-Gargand, T. Ericson, C. Platzer-Bjorkman, M. Edoff and C. Hagglund, *Chem. Mater.*, 2017, **29**, 2969-2978.
96. I. H. Baek, J. J. Pyeon, Y. G. Song, T. M. Chung, H. R. Kim, S. H. Baek, J. S. Kim, C. Y. Kang, J. W. Choi, C. S. Hwang, J. H. Han and S. K. Kim, *Chem. Mater.*, 2017, **29**, 8100-8110.
97. I. Y. Ahmet, M. S. Hill, A. L. Johnson and L. M. Peter, *Chem. Mater.*, 2015, **27**, 7680-7688.
98. V. Stevanovic, K. Hartman, R. Jaramillo, S. Ramanathan, T. Buonassisi and P. Graf, *Appl. Phys. Lett.*, 2014, **104**, 211603.
99. K. C. Sanal, P. K. Nair and M. T. S. Nair, *Applied Surface Science*, 2017, **396**, 1092-1097.
100. Y. Gupta and P. Aruna, *Journal*, Submitted February 19, 2015.
101. M. Devika, K. T. R. Reddy, N. K. Reddy, K. Ramesh, R. Ganesan, E. S. R. Gopal and K. R. Gunasekhar, *J. Appl. Phys.*, 2006, **100**, 023518.
102. M. Devika, N. K. Reddy, D. S. Reddy, Q. Ahsanulhaq, K. Ramesh, E. S. R. Gopal, K. R. Gunasekhar and Y. B. Hahn, *Journal of the Electrochemical Society*, 2008, **155**, H130-H135.
103. M. Devika, N. K. Reddy, K. Ramesh, R. Ganesan, K. R. Gunasekhar, E. S. R. Gopal and K. T. R. Reddy, *Journal of the Electrochemical Society*, 2007, **154**, H67-H73.
104. A. Abou Shama and H. M. Zeyada, *Optical Materials*, 2003, **24**, 555-561.
105. M. M. El-Nahass, H. M. Zeyada, M. S. Aziz and N. A. El-Ghamaz, *Optical Materials*, 2002, **20**, 159-170.
106. N. K. Reddy, K. Ramesh, R. Ganesan, K. T. R. Reddy, K. R. Gunasekhar and E. S. R. Gopal, *Applied Physics a-Materials Science & Processing*, 2006, **83**, 133-138.
107. K. Hartman, J. L. Johnson, M. I. Bertoni, D. Recht, M. J. Aziz, M. A. Scarpulla and T. Buonassisi, *Thin Solid Films*, 2011, **519**, 7421-7424.
108. A. T. Kana, T. G. Hibbert, M. F. Mahon, K. C. Molloy, I. P. Parkin and L. S. Price, *Polyhedron*, 2001, **20**, 2989-2995.
109. I. P. Parkin, L. S. Price, T. G. Hibbert and K. C. Molloy, *Journal of Materials Chemistry*, 2001, **11**, 1486-1490.
110. A. Ortiz, J. C. Alonso, M. Garcia and J. Toriz, *Semiconductor Science and Technology*, 1996, **11**, 243-247.
111. A. Tanusevski and D. Poelman, *Sol. Energy Mater. Sol. Cells*, 2003, **80**, 297-303.

112. J. Henry, K. Mohanraj, S. Kannan, S. Barathan and G. Sivakumar, *Journal of Experimental Nanoscience*, 2015, **10**, 78-85.
113. H. K. Park, J. Jo, H. K. Hong, G. Y. Song and J. Heo, *Current Applied Physics*, 2015, **15**, 964-969.
114. B. Subramanian, C. Sanjeeviraja and M. Jayachandran, *Materials Chemistry and Physics*, 2001, **71**, 40-46.
115. N. Sato, M. Ichimura, E. Arai and Y. Yamazaki, *Sol. Energy Mater. Sol. Cells*, 2005, **85**, 153-165.
116. M. Ichimura, K. Takeuchi, Y. Ono and E. Arai, *Thin Solid Films*, 2000, **361**, 98-101.
117. K. Takeuchi, M. Ichimura, E. Arai and Y. Yamazaki, *Sol. Energy Mater. Sol. Cells*, 2003, **75**, 427-432.
118. K. S. Kumar, C. Manoharan, S. Dhanapandian, A. G. Manohari and T. Mahalingam, *Optik*, 2014, **125**, 3996-4000.
119. K. S. Kumar, C. Manoharan, S. Dhanapandian and A. G. Manohari, *Spectrochimica Acta Part a-Molecular and Biomolecular Spectroscopy*, 2013, **115**, 840-844.
120. K. S. Kumar, A. G. Manohari, S. Dhanapandian and T. Mahalingam, *Materials Letters*, 2014, **131**, 167-170.
121. M. Calixto-Rodriguez, H. Martinez, A. Sanchez-Juarez, J. Campos-Alvarez, A. Tiburcio-Silver and M. E. Calixto, *Thin Solid Films*, 2009, **517**, 2497-2499.
122. Yanuar, F. Guastavino, C. Llinares, K. Djessas and G. Masse, *Journal of Materials Science Letters*, 2000, **19**, 2135-2137.
123. M. Ristov, G. Sinadinovski, I. Grozdanov and M. Mitreski, *Journal*, 1989, **173**, 53-58.
124. A. Tanusevski, *Semiconductor Science and Technology*, 2003, **18**, 501-505.
125. P. Pramanik, P. K. Basu and S. Biswas, *Journal*, 1987, **150**, 269-276.
126. M. T. S. Nair and P. K. Nair, *Semiconductor Science and Technology*, 1991, **6**, 132-134.
127. R. Caballero, V. Conde and M. Leon, *Thin Solid Films*, 2016, **612**, 202-207.
128. J. Y. Kim and S. M. George, *J. Phys. Chem. C*, 2010, **114**, 17597-17603.
129. H. Nozaki, M. Onoda, M. Sekita, K. Kosuda and T. Wada, *Journal of Solid State Chemistry*, 2005, **178**, 245-252.
130. X. P. Zhan, C. W. Shi, X. J. Shen, M. Yao and Y. R. Zhang, *Advanced Materials Research*, 2012, **590**, 148-152.
131. S. Gedi, V. R. M. Reddy, J. Y. Kang and C. W. Jeon, *Applied Surface Science*, 2017, **402**, 463-468.
132. M. Devika, N. K. Reddy, F. Patolsky and K. R. Gunasekhar, *J. Appl. Phys.*, 2008, **104**, 124503.
133. N. K. Reddy, M. Devika and K. Gunasekhar, *Thin Solid Films*, 2014, **558**, 326-329.
134. N. R. Mathews, *Semiconductor Science and Technology*, 2010, **25**, 105010.
135. S. Karadeniz, M. Sahin, N. Tugluoglu and H. Safak, *Semiconductor Science and Technology*, 2004, **19**, 1098-1103.
136. B. Ghosh, M. Das, P. Banerjee and S. Das, *Solid State Sciences*, 2009, **11**, 461-466.
137. R. L. Gurunathan, J. Nasr, J. J. Cordell, R. A. Banai, M. Abraham, K. A. Cooley, M. Horn and S. E. Mohny, *J. Electron. Mater.*, 2016, **45**, 6300-6304.
138. A. de Kergommeaux, J. Faure-Vincent, A. Pron, R. de Bettignies, B. Malaman and P. Reiss, *J. Am. Chem. Soc.*, 2012, **134**, 11659-11666.
139. M. R. Sazideh, H. R. Dizaji, M. H. Ehsani and R. Z. Moghadam, *Applied Surface Science*, 2017, **405**, 514-520.

140. P. Sinsermsuksakul, J. Heo, W. Noh, A. S. Hock and R. G. Gordon, *Adv. Energy Mater.*, 2011, **1**, 1116-1125.
141. X. H. Ma, K. H. Cho and Y. M. Sung, *Crystengcomm*, 2014, **16**, 5080-5086.
142. G. A. Tritsarlis, B. D. Malone and E. Kaxiras, *J. Appl. Phys.*, 2014, **115**, 173702.
143. J. G. Kang, J. G. Park and D. W. Kim, *Electrochemistry Communications*, 2010, **12**, 307-310.
144. W. S. Gao, C. S. Wu, M. Cao, J. Huang, L. J. Wang and Y. Shen, *Journal of Alloys and Compounds*, 2016, **688**, 668-674.
145. M. De Graef and M. E. McHenry, *Structure of Materials: An Introduction to Crystallography, Diffraction, and Symmetry*, Cambridge University Press, New York, 2007.
146. V. Steinmann, R. E. Brandt, R. Chakraborty, R. Jaramillo, M. Young, B. K. Ofori-Okai, C. X. Yang, A. Polizzotti, K. A. Nelson, R. G. Gordon and T. Buonassisi, *Apl Materials*, 2016, **4**, 026103.
147. H. R. Chandrasekhar, R. G. Humphreys, U. Zwick and M. Cardona, *Phys. Rev. B*, 1977, **15**, 2177-2183.
148. Y. B. Yang, J. K. Dash, Y. Xiang, Y. Wang, J. Shi, P. H. Dinolfo, T. M. Lu and G. C. Wang, *J. Phys. Chem. C*, 2016, **120**, 13199-13214.
149. J. M. Skelton, L. A. Burton, A. J. Jackson, F. Oba, S. C. Parker and A. Walsh, *Phys. Chem. Chem. Phys.*, 2017, **19**, 12452-12465.
150. A. J. Smith, P. E. Meek and W. Y. Liang, *Journal of Physics C-Solid State Physics*, 1977, **10**, 1321-1333.
151. H. R. Chandrasekhar and D. G. Mead, *Phys. Rev. B*, 1979, **19**, 932-937.
152. Z. M. Zhang, S. Chen, Y. Z. Liang, Z. X. Liu, Q. M. Zhang, L. X. Ding, F. Ye and H. Zhou, *Journal of Raman Spectroscopy*, 2010, **41**, 659-669.
153. M. Wojdyr, *Journal of Applied Crystallography*, 2010, **43**, 1126-1128.
154. W. Albers, H. J. Vink, C. Haas and J. D. Wasscher, *J. Appl. Phys.*, 1961, **32**, 2220-2225.
155. C. W. Bale, E. Belisle, P. Chartrand, S. A. Decterov, G. Eriksson, A. E. Gheribi, K. Hack, I. H. Jung, Y. B. Kang, J. Melancon, A. D. Pelton, S. Petersen, C. Robelin, J. Sangster, P. Spencer and M. A. Van Ende, *CALPHAD: Comput. Coupling Phase Diagrams Thermochem.*, 2016, **54**, 35-53.

Chapter 6: Transparent Conducting Electrodes Based on Ag NWs and Ag NW/Polymer composites

6.1 Introduction

6.1.1 Transparent Electrodes

The use of transparent electrodes has seen a dramatic increase in recent years. Resistive and capacitive touch displays, LCDs, OLEDs, solar cells, smart windows, electronic books, and smart phones all require the transmission of light through a conductive electrode.^{1,2} The need for low cost transparent electrodes is increasing.³

Degenerately doped oxides such as indium tin oxide (ITO)¹ are the traditional transparent, conductive materials used for these applications, allowing for resistivities less than 10^{-4} Ω -cm and transmittances greater than 95%.⁴ However, there are a number of important limitations of ITO. ITO is incompatible with flexible applications, as it cracks at strains of 2-3%, increasing its resistivity¹. In addition, indium is fairly rare, with its supply dominated by China and Canada. At approximately 75% indium by mass, ITO is particularly affected by price fluctuations of indium. Furthermore, ITO is often deposited using costly vacuum methods and requires high temperature processing steps that are incompatible with flexible substrates¹.

For these reasons, alternatives to doped transparent conducting metal oxides (TCOs) have emerged. These include carbon nanotube (CNT) networks, graphene sheets or films of graphene flakes, thin metal films, metal gratings, random metal nanowire networks of gold, silver, or copper, conductive polymers, and composites of these materials.^{5,2,1,6}

Each of these materials has advantages and disadvantages, for example, graphene, while theoretically able to achieve sheet resistances less than $10 \Omega/\square$ at transmittances greater than 97%, faces challenges of large resistances at grain boundaries and processing challenges such as wrinkles during substrate transfer, which can raise its sheet resistance. Large resistances at carbon nanotube junctions necessitate thick films to overcome high sheet resistances, lowering transmittance.⁵

Most applications of interest require low sheet resistances, R_s , and high transmittances, T . For example, for resistive touch panel applications, $T \geq 86\text{-}90\%$ and $R \leq 200\text{-}500 \Omega/\square$ is required. For capacitive touch panels, $T \geq 88\text{-}92\%$ and $R_s \leq 100\text{-}300 \Omega/\square$; for LCDs, $T \geq 87\text{-}90\%$ and $R_s \leq 30\text{-}300 \Omega/\square$; and for solar cell applications, $T \geq 90\%$ and $R_s \leq 10 \Omega/\square$.^{1,2} Of the emerging materials, silver nanowires (Ag NWs) currently have the best combination of optical and electrical properties, as summarized in Table 6.1.^{1,5}

Table 6.1: Properties of transparent conductive materials from literature.

	Ag NW ⁷	CNT ⁸	Graphene (CVD) ¹	Graphene (solution processed) ¹	Cu NW ⁹	Au NW ⁶	ITO ¹⁰
$R_s (\Omega/\square)$	13	60	700	2000	30	49	<5
$T (\%)$	91	90	90	85	85	83	90

6.1.2 Silver Nanowire-Based Transparent Conducting Electrodes

Silver nanowire synthesis and properties

A low-cost, high throughput method for producing Ag NWs is by solution-phase synthesis using the polyol process. In this method, silver nitrate is reduced by ethylene glycol in

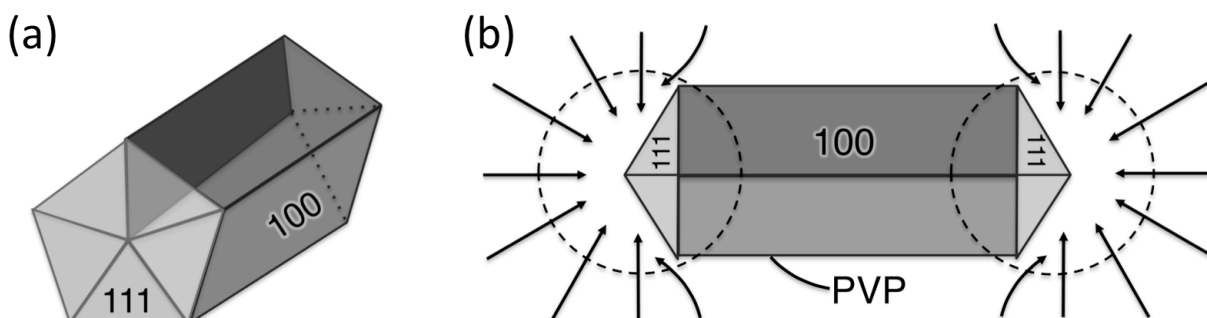


Figure 6.1: (a) Five-fold twinned structure of Ag NW illustrating the location of $\{100\}$ and $\{111\}$ planes. (b) Depiction of NW growth mechanism involving PVP adsorption to $\{100\}$ planes and diffusion of Ag atoms towards $\{111\}$ planes. After Ref [11].

the presence of poly(vinyl pyrrolidone) (PVP) and Ag (or Pt) nanoparticle seeds.¹² The Ag NWs, depicted in Figure 6.1, are known to have a five-fold twinned structure with five $\{100\}$ facets along their lengths and ten $\{111\}$ facets at their ends. It is believed that PVP interacts strongly with the $\{100\}$ planes, stabilizing them, but interacts weakly with the $\{111\}$ planes. This allows Ag to grow along the $\{111\}$ end planes by Ostwald ripening while preventing growth at the $\{100\}$ faces, forming the rod-like structure illustrated in Figure 6.1 b. In addition, silver atoms are drawn to the high energy twin boundaries, furthering growth along the NW axis.¹¹

After synthesis, the NWs are re-dispersed in a solvent such as isopropanol and formed into a networked film by spin coating, drop casting, or other methods. It has been found that the overall sheet resistance of the film is limited by very high NW-NW junction resistances, estimated to be seven orders of magnitude greater than resistances across single nanowires.¹³ Some PVP remains on the NWs, which is believed to act as an insulating barrier that contributes to the high junction resistance.¹⁴

Figure 6.2 a shows a TEM image of AgNWs used in this study. It can be seen that the end of the nanowire has a pointed shape, consistent with the expected five-fold twinned

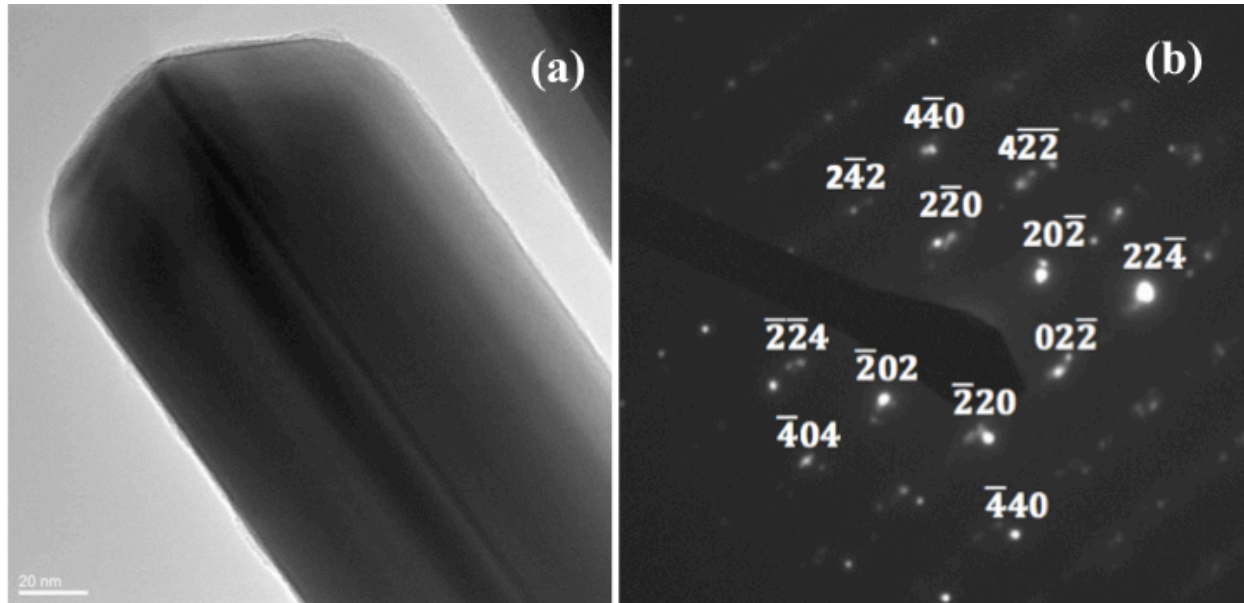


Figure 6.2: (a) TEM image of Ag NWs (purchased from Blue Nano, Inc.) drop cast onto a copper grid (SPI supplies) obtained with a JEM 2000EX II microscope. The average NW diameter in suspension was 90 nm. (b) Selected area electron diffraction (SAED) pattern of a 90 nm NW along the [111] zone axis showing crystalline material.

structure depicted in Figure 6.1 b. In addition, there is a straight line running parallel to the NW longitudinal axis, suggesting the presence of a twin boundary. Figure 6.2 b shows a SAED pattern obtained from a ~90 nm Ag NW at a location away from the nanowire end. The pattern indicates the nanowires have a crystalline structure, with additional reflections present due to twin planes.

Silver nanowire-based transparent conductors

Indicated in Table 6.1, solution-processed silver nanowire films have a favorable combination of optical and electrical properties and show promise as a potential alternative to degenerately doped transparent conducting oxides.⁵ Ag NWs are cast into randomly networked-films by methods such as spin coating,^{15,16} drop casting,¹⁷ Meyer rod coating,³ vacuum

filtration,¹⁸ and spray casting.^{19,20} Although silver is optically absorbent, the porous nature of the networked films allows for high transmittance. Intuitively, depositing higher concentrations of nanowires can increase electrical conductivity of the film, but this comes at the cost of less porosity and therefore decreased transmittance. A figure of merit (FoM) relates transmittance to sheet resistance of the film.²¹ Films will be conductive if there is connectivity of the NW network, and the areal density of nanowires at which this first occurs is referred to as the percolation threshold.²¹ A low percolation threshold will increase the FoM.²¹

6.1.3 Silver Nanowire Contacts to Silicon

Contacts to Silicon

Current issues for low resistance ohmic contacts to silicon in microelectronics arise from the ever-decreasing size of devices. Schottky barrier heights of metals to silicon show a weak dependence on the metal work function. Consequently, Ohmic contacts to silicon are largely made by heavily doping the silicon to allow transport by field emission.²² From experimental results, the barrier height of metals to n-type silicon can be predicted by the equation²³:

$$q\phi_B = 0.27q\phi_m - 0.52 \text{ eV} \quad (6.1).$$

The choice of contact metallization is often made to meet processing, stability, and economic requirements rather than to provide optimal electrical performance. When certain metals are annealed on silicon, they form metal silicides. Silicides can be beneficial because the reacted metal-silicide interface is deeper than the surface of the silicon. The metal should be able to withstand a subsequent anneals and remain stable during further metallization. Metals with

Schottky barrier heights of around half the band gap are preferred to form ohmic contacts to n- and p-type silicon.²²

ITO/Silicon Contacts

ITO/Si contact characteristics are dependent upon the deposition method of ITO. For spray coated or vacuum evaporated ITO, a rectifying contact will form to n-type Si and an ohmic contact will form to p-type.²⁴ In contrast, ion-beam sputtered ITO results in an ohmic contact to n-Si and a rectifying barrier to p-Si.²⁴ This is due to damage of the surface layers introduced by the ion beam, which causes the silicon band edges to bend downwards.²⁴ For rf-sputtered ITO on 1 Ω -cm resistivity, <100> p-Si, the specific contact resistivity evaluated by a TLM measurement was $7.143 \times 10^{-2} \Omega\text{-cm}^2$.²⁵

Silver Thin Film/Silicon Contacts

There are many reports for C-V and I-V measurements of Schottky barrier heights for thin film Ag/Si interfaces. Results vary due to crystallographic direction of Si, Si surface preparation, Si doping concentration, and Ag deposition method. For n-type Si, barrier heights range from 0.56 eV (oxidized and etched Si surface) - 0.79 eV (vacuum cleaved Si) and 0.30eV (epitaxial Ag)-0.54 eV (evaporated Ag) for n- and p-type Si, respectively.^{26, 27, 28, 29}

Silver Paste/Silicon Contacts

Screen-printed thick silver paste contact grids are commonly used as front contacts to the n-type emitter of silicon solar cells. Silver pastes typically contain silver powder, glass frit and organic binder, solvent, and additives to facilitate printing. The glass frit, usually lead

borosilicate, allows for etching through an antireflective material, typically SiN_x for solar cells.³⁰ For fritless Ag paste, the optimal annealing temperature is around 1000 °C.³¹ The addition of phosphorous to silver pastes can reduce the specific contact resistance to silicon by about two orders of magnitude due to self-doping of the underlying silicon.³¹ The specific contact resistance of silver paste to <111> n-type, dendritic web Si was found to be 1.90 $\Omega\text{-cm}^2$ without phosphorous and less than 0.04 $\Omega\text{-cm}^2$ with phosphorous.³¹

6.1.4 Contribution of This Work

Despite their favorable optical and electronic properties, a limitation of solution processed random networked nanowire structures is aggregation of nanowires during deposition of films. Electrical conduction in the nanowire network is dependent upon a connected nanowire path through which current can flow. Regions with high nanowire aggregation combined with regions of sparse nanowire coverage can negatively affect the sheet resistance and transmittance properties of a Ag NW network, as well as its reproducibility.

In this work, the morphology, electrical and optical properties of Ag NW-polymer composite films spin cast from polymer dispersions are compared to pristine Ag NW films cast from dispersions in isopropanol. It is found that a composite of Ag NWs and a transparent polymer can improve uniformity and electrical conductivity while maintaining favorable optical properties, resulting in a higher figure of merit than pristine nanowires.

In addition to low sheet resistance and high transmittance, a low contact resistance between the transparent electrode and underlying semiconducting material is often necessary. For example, as calculated by Meier and Schroder,^{32,33} for an inorganic solar cell with a

semiconductor sheet resistance of $100 \Omega/\square$, the specific contact resistivity must be less than $2 \times 10^{-3} \Omega\text{-cm}^2$ to maintain power loss $< 5\%$.

There are many reports of Ag NW electrodes used in organic-based solar cell devices.^{34,15,35,36,37} However, silicon-based solar cells additionally remain relevant since they currently account for more than 90% of the photovoltaic market. Xie et al. created a crystalline silicon solar cell using a Ag NW network as the transparent electrode.³⁸ After annealing, a 19% enhancement in energy conversion efficiency to 5.32% was achieved. A contact resistance of 0.3Ω was extracted with a simulation program, but the specific contact resistivity was not directly measured. Despite the importance of low specific contact resistance in devices, to our knowledge, no specific contact resistance measurements of metal nanowire networks to semiconductors have been performed.

In the second part of this chapter, the feasibility of Ag NW networks as transparent contacts to Si is investigated. The impact of annealing conditions and Ag NW diameter on ohmic contact formation and morphology of the nanowire network is observed. It is found that nanowire diameters must be large enough to allow sufficient annealing at standard temperatures before degradation of the film. Temperature stability is therefore another variable that one should consider when selecting the diameter of NWs. It is found that Ohmic contact formation is achievable for 90 nm-diameter nanowires that were annealed at 650°C for short durations.

6.2 Ag NW and Ag NW/Polymer Composite Films

6.2.1 Experimental Methods

Preparation of Ag NW Thin Films

Ag NWs dispersed in isopropanol (IPA) with average diameters of 90 ± 20 nm and lengths of 10-30 μm were purchased from BlueNano, Inc. The as-received dispersion of Ag NWs in IPA had a concentration of 10 mg/mL and was diluted to a range of lower concentrations, allowing films with a variety of Ag NW areal densities to be fabricated. Approximately 1 cm x 1 cm x 0.175 mm cover glass substrates from Corning, Inc were ultrasonically cleaned with acetone, deionized water, and isopropanol, sequentially. The various concentrations of Ag NWs were spin coated onto the glass substrates at 3000 rpm for 30 seconds. The samples were then heated for 30 minutes in low vacuum at 180-200°C. This temperature is above the glass transition point of polyvinyl pyrrolidone (PVP), which remains coated on the nanowires after synthesis. This heat treatment reduces the NW-NW junction resistance, a limiting factor of the total sheet resistance.³

Preparation of Ag NW/Polymer Composite Thin Films

To fabricate composite films, various concentrations of the Ag NW dispersions were centrifuged at 5000 rpm for 30 minutes in a VWR Clinical 200 centrifuge followed by removal of the IPA by pipetting. The nanowires were then re-dispersed in a polymer. The two polymers used in these experiments were poly(3,4-ethylenedioxythiophene) (PEDOT:PSS) and poly(styrenesulfonate)) (PSS) purchased from Heraeus and Alfa Aesar, respectively. PEDOT:PSS with specific conductivities of 300 S/cm (Clevios PH 500) and 850 S/cm (Clevios PH 1000) were used. 5% v/v dimethyl sulfoxide (DMSO) from Fisher Scientific was added to

the PEDOT:PSS to improve conductivity, as well as 10 % v/v isopropanol and 0.1-0.5 % v/v Dynol-604 surfactant from Air Products, Inc. to improve film wettability on the glass substrate. The Ag NW-PEDOT:PSS dispersion was spin coated at either 2000 rpm for one coat or 3000 rpm for two coats for 1 minute to achieve a polymer thickness of approximately 90 nm, as determined with a Filmetrics F50-200 spectroscopic reflectometer. 5 wt. % PSS solutions in water were prepared from a sodium salt of polystyrene sulfonate with a molecular weight of 70,000 g/mol. Hexamethyldisilazane (HMDS) was used as an adhesion promoter for the Ag NW/PSS films. The Ag NW/PSS dispersion was spin coated at 4000 rpm to result in a thickness of approximately 90 nm. The Ag NW/polymer composites were then annealed at 180-200 °C for 30 minutes in low vacuum to reduce NW-NW junction resistances.

6.2.2 Results

Transmittance and Sheet Resistance

Ag NW films, being random networked structures, are limited by percolation.²¹ Below a certain areal density of nanowires, connectivity of a conductive path will not be present and the film will become non-conductive. The conductivity of such a system is related by $\sigma_{DC} \propto (N_A - N_{A,C})^\alpha$ where N_A is number of rods per unit area, $N_{A,C}$ is the percolation threshold, and α is a critical exponent, near the percolation threshold²¹. One method to lower the percolation threshold is to combine a conductive polymer, such as PEDOT:PSS, with the nanowires to provide an alternative path for current to flow.^{3,39,17} However, PEDOT:PSS is optically absorbent in the visual spectrum. Therefore Ag NW-PEDOT:PSS composites have lower transmittance than pristine Ag NW films (Figure 6.3 a). Another limitation of PEDOT:PSS is its

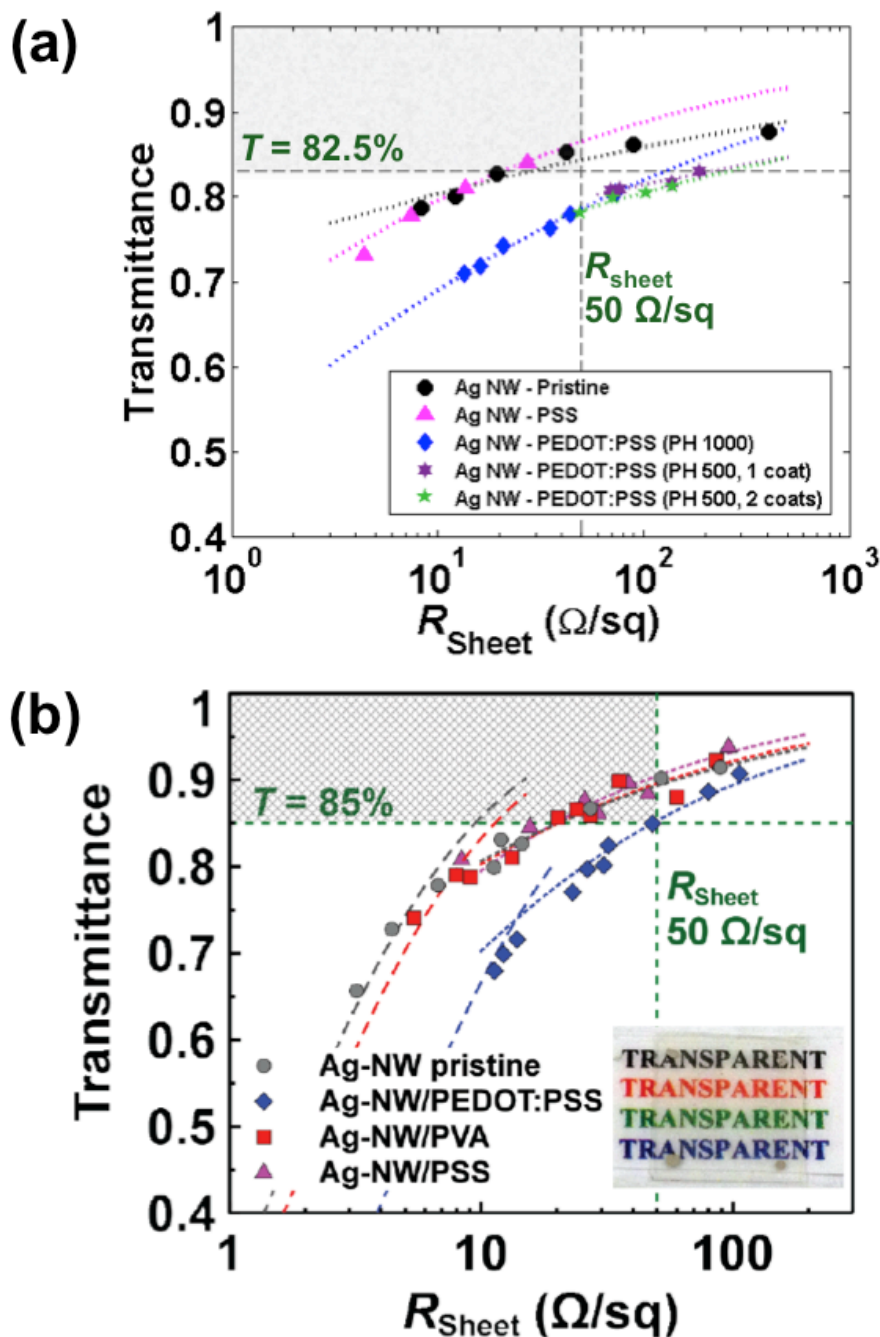


Figure 6.3: Plots of sheet resistance versus transmittance for Ag NW and Ag NW-polymer films. (a) Data collected by the author. (b) More complete dataset from paper by Narayanan, Hajzus, *et al.*¹⁶ Dotted lines show fit to data in the percolative-like regime and dashed lines show fit to data in the bulk-like regime. Area of technological interest is shaded in grey. Transmittances in (a) are 2-3% lower than in (b) due to inclusion of the glass substrate during measurements. The shaded region in (a) is adjusted to account for this. (b) Reproduced with permission from ECS Journal of Solid State Science and Technology, 3 (11) P363-P369 (2014). Copyright 2014, The Electrochemical Society.

acidity and hygroscopic nature, which can corrode the Ag NWs leading to poor stability of the electrodes.^{40,41} This is an issue for PEDOT:PSS in other applications as well, as it is known to etch ITO. Furthermore, indium can diffuse into PEDOT:PSS and through it to the active layer of devices, damaging these interfaces.^{42,43,44} Therefore, an alternative, more transparent and less acidic polymer is of interest.

For this reason, Ag NW-PSS composites were additionally investigated. PSS is a non-conductive polymer, but less optically absorbent in the wavelength range of interest. Additionally, its pH in 5 % aqueous solution was measured to be 7.9, compared to PEDOT:PSS with a pH of 2.5. As shown in Figure 6.3 a, the Ag NW-PSS films have greater transmittance than the Ag NW-PEDOT:PSS films, and conductivity is comparable to Ag NW films. Our group also investigated Ag NW – polyvinyl alcohol (PVA) composites. A more complete data set including the pristine nanowires and three different Ag-NW-polymer systems is shown in Figure 6.3 b, which is from the publication, Narayanan, Hajzus, *et al.*¹⁶ It should be noted that the transmittance values of the samples in Figure 6.3 b are slightly higher than those in Figure 6.3 a, which is because they were measured using a Cary-5000 UV-Vis spectrometer that subtracted the effect of the substrate, while the transmittances in Figure 6.3 a include absorbance and reflectance from the glass substrate, leading to a transmittance difference of around 2-3 %.

To compare the performance of different transparent conductor materials, a figure of merit (FoM) relating optical and electrical properties is used. Traditionally, the FoM is derived from the Lambert-Beer law and the definition of sheet resistance⁴⁵ and is based on $\sigma_{DC,B}/\alpha$, where $\sigma_{DC,B}$ is the bulk DC conductivity of the film and α the absorption coefficient.²¹ For nanostructured materials, the relation $\alpha \approx \sigma_{Op} Z_0$ is applied to obtain a dimensionless FoM, $\frac{\sigma_{Op}}{\sigma_{DC,B}}$,

where Z_0 is the impedance of free space (377 Ω), and σ_{op} is the optical conductivity. T , R_s and the FoM are then related by Equation 6.2²¹:

$$T_{bulk} = \left(1 + \frac{Z_0}{2R_s} \frac{\sigma_{op}}{\sigma_{DC,B}}\right)^{-2} \quad (6.2)$$

For networked structures such as Ag NW films, this equation is found to only be relevant for highly conductive films with high NW areal densities. For low densities, which are typically necessary for technologically relevant transmittances $> 90\%$, the electrical conductivity is limited by percolation of the network. A new figure of merit, as described by De *et al.*²¹, is required to encompass optical and electrical properties in this regime, shown in Equation 6.3²¹:

$$T_{percolation} = \left[1 + \frac{1}{\Pi} \left(\frac{Z_0}{R_s}\right)^{\frac{1}{n+1}}\right]^{-2} \quad (6.3a)$$

$$\text{where } \Pi = 2 \left[\frac{\sigma_{DC,B}/\sigma_{op}}{(Z_0 t_{min} \sigma_{op})^n} \right]^{1/(n+1)} \quad (6.3b)$$

Here, Π is the percolative FoM and n relates to the percolation exponent. n is affected by the dimensionality of the system ($n = 1.3$ and $n = 2$ for 2D and 3D systems, respectively) but can deviate from these values due to large junction resistances. Using these relations, dashed lines and dotted lines are fit to the data, representing the bulk-like and percolative-like regimes, respectively (Figures 6.3 a,b), and FoM are obtained.

Figures of merit extracted from Figure 6.3 b from Narayanan, Hajzus, *et al.*¹⁶ are shown in Table 6.2. It can be seen that the Ag NW-PEDOT:PSS films have lower bulk and percolative-like FoMs, which corresponds to the decrease in transmittance with the incorporation of PEDOT:PSS. The dashed horizontal and vertical lines in Figures 6.3 a, b represent the minimum or maximum technologically relevant values for transmittance, and sheet resistance, respectively. The shaded area formed by these lines then represents the region with properties of practical interest. It is evident that the performance of the transparent conductors in the percolative-like

regime is important. Ag NW-PVA and Ag NW-PSS films have higher percolative-like FoMs, suggesting that these would have improved properties for practical purposes. The higher percolative FoM for these films is attributed to higher uniformity of the films with the incorporation of a polymer.

Table 6.2: Bulk-like and percolative-like figure of merit parameters extracted from the sheet resistance versus transmittance plot in Figure 6.3 b, from Narayanan, Hajzus, et. al.¹⁶ Reproduced with permission from ECS Journal of Solid State Science and Technology, 3 (11) P363-P369 (2014). Copyright 2014, The Electrochemical Society.

Sample	Bulk-like $\sigma_{DC,B}/\sigma_{op}$	Percolation-like	
		Π	n
Ag NW pristine (literature) ²¹	415	31.7	1.9
Ag NW pristine	245	40	1.4
Ag NW-PEDOT:PSS	84	35	0.9
Ag NW-PVA	197	43.6	1.24
Ag NW-PSS	228	57.7	0.86

Film Morphology

The uniformity of the films was observed with SEM. For Ag NW-pristine films (Figure 6.4 a), many areas of NW aggregation are present. For Ag NW-PEDOT:PSS and Ag NW-PSS films (Figure 6.4 b, c), the distribution of NWs appear more uniform. The increase in uniformity is attributed to improved stability of the NW dispersions with the use of a polymer. The effect of polymer additives on the stability of the NWs was determined by Narayanan¹⁶ by measuring absorbance of NW dispersions over time at the plasma wavelength of Ag (~320 nm). The absorbance by Ag NWs dispersed in IPA and DI water decreased at a faster rate than those dispersed in polymer solutions, meaning the NWs remained dispersed in polymer solutions for a

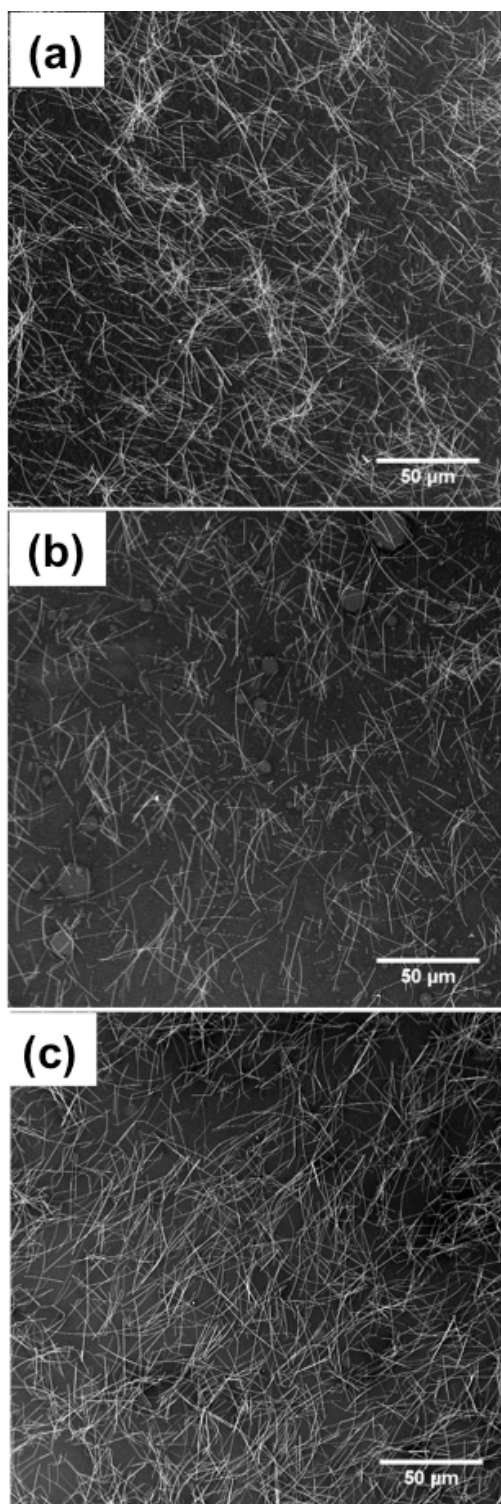


Figure 6.4: SEM micrographs of (a) pristine Ag NW, (b) Ag NW-PEDOT:PSS, and (c) Ag NW-PSS films. Areas of NW aggregation can be seen in the pristine NW film, while the Ag NW-PEDOT:PSS and Ag NW-PSS films appear more uniform.

longer period of time and NWs dispersed in IPA or DI water underwent sedimentation more rapidly.¹⁶

Areal densities of the pristine Ag NW and Ag NW-polymer films were extracted from image analysis of SEM micrographs. It can be seen in Figure 6.5 that for a given areal density of nanowires, the conductance of the films is higher for Ag NW-polymer composites, indicative of lowered percolation thresholds.

Ag NW-PSS composites and Ag NW-PVA composites, in addition to Ag NW-PEDOT:PSS composites, exhibit a lowered percolation threshold. The decrease in percolation threshold is attributed to higher uniformity in NW distribution when combined with the polymers. The higher uniformity of NWs in the deposited composite films would be expected from the higher dispersion stability observed for NWs in the polymer dispersions. The presence of an alternative conductive path is ruled out as a potential cause of lower percolation threshold, since both PSS and PVA are non-conductive.

To quantify differences in film uniformity, an image analysis technique previously utilized for analysis of carbon nanotube networked films⁴⁶ was applied to these films, as described in the manuscript¹⁶ and dissertation by S. Narayanan.⁴⁷ Briefly, the image analysis involves the calculation of the areal fraction of binarised SEM images before and after performing an image dilation, or Minkowski addition, with a disk of radius r . As r increases, the areal fraction increases until eventually saturating the image. The rate at which the image reaches saturation is an indication of the spatial uniformity of the film. The areal fraction as a function of disc radius can be related to a spherical distribution function, $H_s(r)$.⁴⁶

$$1 - H_s(r) = \frac{1 - A_f(r)}{1 - p} \quad (6.4)$$

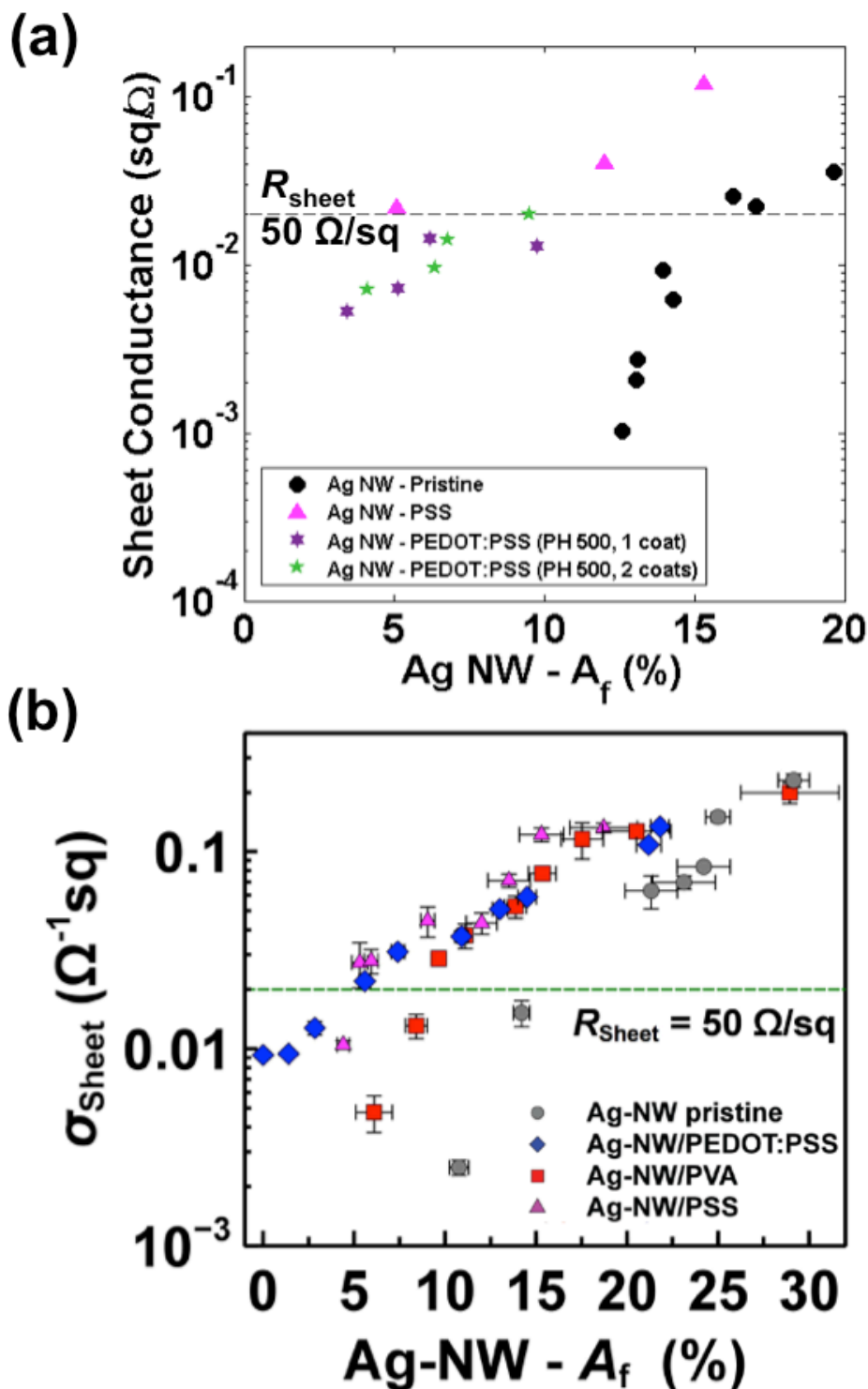


Figure 6.5: Plots of sheet conductance vs nanowire areal fraction for Ag NW and Ag NW-polymer films. (a) Data collected by the author. (b) More complete set of data from the author's co-authored publication.¹⁶ It can be seen that the composite films have lower NW areal fractions at a given sheet conductance, suggesting a lower percolation threshold with the addition of a polymer. (b) Reproduced with permission from ECS Journal of Solid State Science and Technology, 3 (11) P363-P369 (2014). Copyright 2014, The Electrochemical Society.

where p is the areal fraction of the undilated image, and $A_f(r)$ is the areal fraction after dilation with disc radius r . $H_s(r)$ can be described by the equation⁴⁶

$$H_s(r) = 1 - e^{-\gamma r(2m+\pi r)} \quad (6.5)$$

where γ is the number of segments per unit area and m is the mean length of the segments.

Spherical contact distribution functions were calculated for the polymer composites and pristine NW films. To quantify uniformity, the quantity $2\gamma m$ is used, which corresponds to the slope of $H_s(r)$ at small disc radii, i.e. the rate at which the areal fraction saturates. The image dilation process is depicted in Figure 6.6,¹⁶ as well as the parameter $2\gamma m$ at different initial areal fractions for pristine Ag NW and Ag NW/polymer films. The Ag NW-PEDOT:PSS films have high values of $2\gamma m$, and are comparable to simulated NW networks. The Ag NW-PVA films show a higher value of $2\gamma m$ than pristine Ag NW films, indicating these films were more uniform. The Ag NW/PSS films have the highest values of $2\gamma m$.

6.3 The Ag NW/Si Interface

6.3.1 Introduction

As mentioned in Section 6.1, interfacial resistances between transparent conductors and other device layers should be low. Additionally, the NWs must be able to withstand any high temperature processing steps during device fabrication. In this section, the electrical properties at the interface between Ag NWs and Si are investigated, as well as the affect of heat treatment.

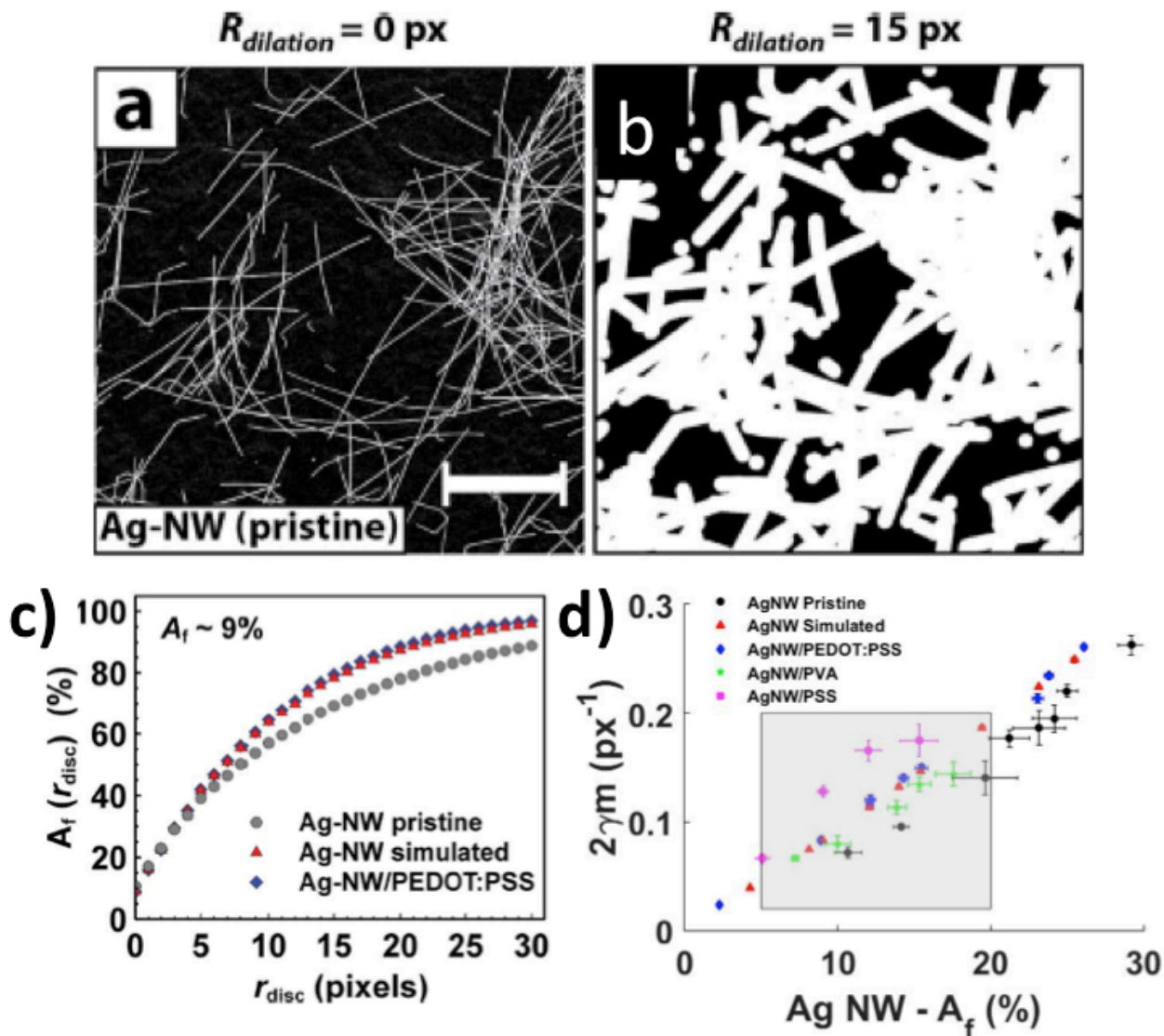


Figure 6.6: (a) Binarized SEM image of pristine Ag NW film. (b) Pristine Ag NW film after performing image dilation of $r = 15$ pixels. (c) Areal fraction of Ag NW-based films as a function of disc radii. (d) Variation of fit parameters as a function of initial areal fractions. Higher values of $2\gamma_m$ indicate faster convergence of $H_s(r)$ to unity and therefore higher uniformity of the film. (a-c) Are from Narayanan et. al.¹⁶ Reproduced with permission from ECS Journal of Solid State Science and Technology, 3 (11) P363-P369 (2014). Copyright 2014, The Electrochemical Society.

6.3.2 Experimental Methods

Sample Fabrication

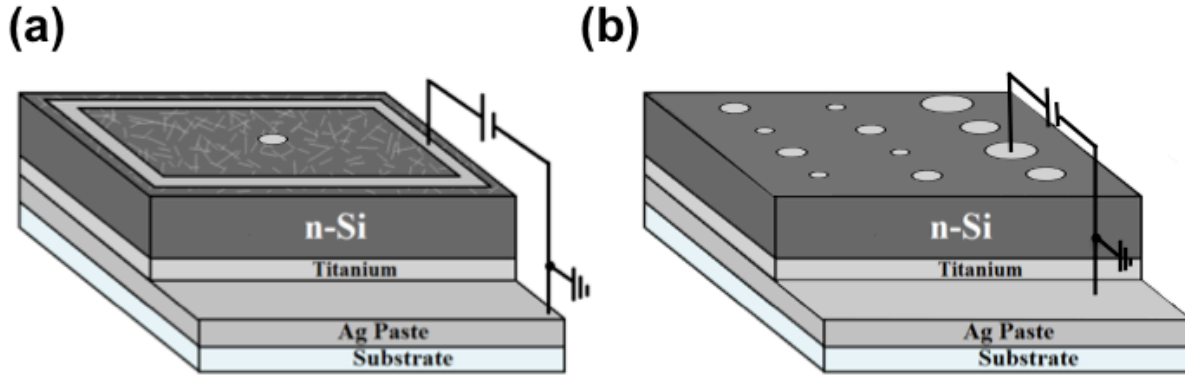


Figure 6.7: (a) Schematic of samples fabricated to measure electrical properties of the Ag NW/n-Si interface. Ti back ohmic contact was e-beam evaporated, followed by spin coating of a NW top contact and application of Ag paste square. For some samples a Ag paste center contact was applied to compare NW film resistance before and after annealing. (b) Similar structure fabricated with circular Ag thin film contacts evaporated through a shadow mask. Contact diameters are 2.5 mm, 1.3 mm, 800 μm , and 530 μm . Both kinds of samples were mounted in Ag paste on a cover glass substrate.

Single-crystal (100) n-type Si (from University Wafer) with a resistivity of 0.01-0.02 $\Omega\text{-cm}$ was ultrasonically cleaned with acetone, isopropanol, and deionized water followed by a 1 minute dip in 10% hydrofluoric acid for native oxide removal. Samples were immediately loaded into an ultra-high vacuum (UHV) deposition chamber and a 150 nm Ti back contact was deposited via electron beam evaporation at a base pressure of 5×10^{-9} Torr at 1.5 $\text{\AA}/\text{s}$. Current-voltage characteristics of the Ti/Si interface were measured with a probe station and were found to be ohmic as deposited. Ag NWs (from Blue Nano, Inc.) dispersed in isopropanol were spin coated to form a front contact. NWs of two different average dimensions were used: 35 nm diameter x 10 μm length, and 90 nm diameter x 25 μm length. Ferro FX33-130 silver paste was applied to the top Ag NW contact to ensure contact of nanowires by probe tips. Samples were

mounted in silver paste to allow for vertical probe station measurements (Figure 6.7 a). Silver paste solvents were evaporated at 100°C for 1 hr in a low vacuum oven.

Samples with Ag thin film front contacts were additionally fabricated. Circular Ag contacts of four different diameters were deposited by electron beam evaporation in a UHV chamber with a base pressure of 2×10^{-9} Torr at a rate of 1.5 Å/s through a shadow mask (Figure 6.7 b).

Annealing

Ag NW and Ag thin film samples were annealed in N₂ ambient with an AG Associates MiniPulse rapid thermal annealer (RTA) at 200°C-700°C for various times. In addition, the Ag thin film contacts were annealed in a tube furnace at 900°C for 5 min in N₂ ambient.

Characterization

I-V sweeps were performed using a Signatone S-1160 probe station and Agilent 4155C Semiconductor Parameter Analyzer. Nanowire morphology was observed using an XL30 field emission scanning electron microscope (SEM). Approximate NW areal densities were determined by analysis of SEM images with ImageJ public domain image analysis software.

6.3.3 Results

Ag Thin Film

Figure 6.8 shows current-voltage characteristics of Ag thin film contacts on Si. As-deposited Ag films exhibited rectifying I-V characteristics, which is expected based on Equation 6.1. Additionally, experimental results in literature report a Schottky barrier height for Ag thin films on n-type Si ranging from 0.56eV - 0.79eV.^{26,27,28,29} Because of this barrier, an annealing

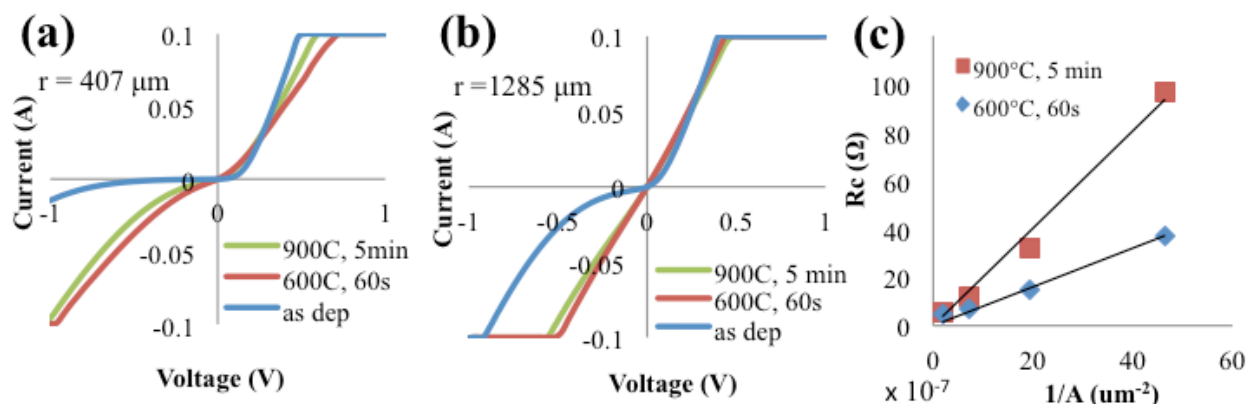


Figure 6.8: Current-voltage characteristics for Ag thin films on n-Si after annealing sequence for (a) 814 μm -diameter circular contact and (b) 2580 μm -diameter circular contact. Measurements were performed as indicated in Fig. 6.7 b. A transition to ohmic behavior is observed after annealing at 600°C. Specific contact resistances were estimated from a plot of inverse contact diameter versus contact resistance (c). Contact resistances after 600°C and 900°C anneals were $2 \times 10^{-1} \Omega\text{-cm}^2$ and $7 \times 10^{-2} \Omega\text{-cm}^2$, respectively.

step is typically required to form an ohmic contact. The annealing step can produce a reacted interface with graded composition.⁴⁸

After annealing at 600°C for 60s in N_2 ambient, the Ag thin film contacts became semi-ohmic. As expected, there was no evidence of a eutectic transformation after annealing at this temperature (Figure 6.9 a). Note that the Si-Ag binary system has a eutectic at 830-835°C at 89 atomic % Ag, and forms no equilibrium secondary phases.⁴⁹ Weber⁵⁰ calculated equilibrium solid state solubility of Si in Ag beginning at 450°C, reaching a maximum of 0.93 at.% Si at the eutectic temperature. Solid solubility of Ag in Si is known to occur at high temperatures from 1200°C to 1400°C, peaking at 4×10^{-4} at.% Ag at 1350°C.⁴⁹ Etch pits indicative of diffusion of thin film Ag in (111) Si have also been observed to begin as low as 450°C.⁵¹

After annealing above the eutectic at 900°C (5 min in N_2 ambient in a tube furnace), the contacts remained semi-ohmic (Figure 6.8 a), consistent with results for fritless Ag paste on Si.³¹ However, the resistance increased. This increase is attributed to oxidation of the contacts, which was detected from EDX analysis (Figure 6.9).

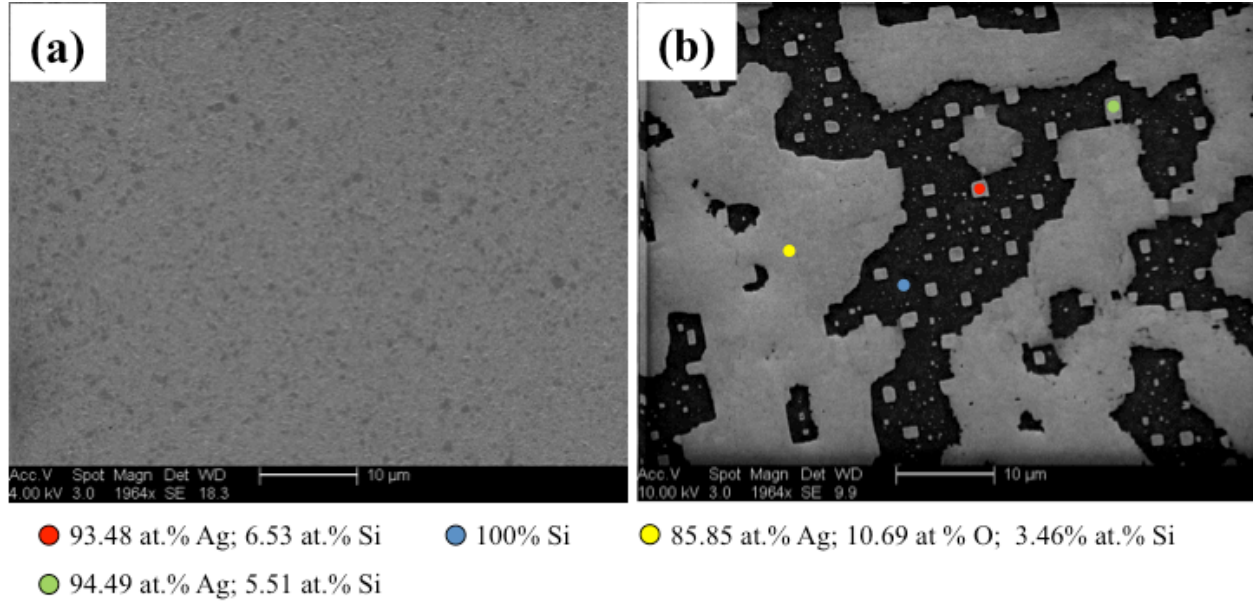


Figure 6.9: SEM micrographs of thin Ag film after annealing at (a) 600°C for 60 s in N₂ and (b) 900°C for 5 min in N₂. Colored circles show locations where EDX was performed. Oxygen is present.

A specific contact resistivity of the thin film after annealing at 600°C and 900°C was estimated from a plot of inverse contact area versus contact resistance (Figure 6.8 c). The contact resistance, R_C , was calculated from the following equation⁵²:

$$R_T = R_C + R_{sp} + R_{cb} + R_p \quad (6.6)$$

where R_T is the total resistance through the structure, R_{cb} is the contact resistance of the bottom contact, R_p is the probe resistance, and R_{sp} is the spreading resistance. The spreading resistance for a circular contact and infinitely large back contact is approximated as⁵²:

$$R_{sp} = \frac{\rho}{2\pi r} \arctan\left(\frac{2t}{r}\right) \quad (6.7)$$

where t is the thickness of the semiconductor and ρ is the resistivity of the semiconductor. R_{cb} and R_p were assumed to be negligible. The specific contact resistance is then extracted from the

slope of a linear fit to the data ($R_c = \frac{\rho_c}{A_c}$). The contact resistances of the films after annealing at 600°C and 900°C were calculated to be $2 \times 10^{-1} \Omega\text{-cm}^2$ and $7 \times 10^{-2} \Omega\text{-cm}^2$, respectively.

90nm-diameter Ag NWs

The work function of (100) Ag is 4.64 eV.⁵³ It has been reported that the expected work function decrease due to PVP on the nanowire surface is 0.1-0.2eV.⁵⁴ No work function lowering due to nanowire size should occur.⁵⁵ Equation 6.1 then predicts a barrier height of silver nanowires to n-type Si to be 0.69 eV, similar to barrier heights reported for silver thin films.^{26,28,29} Therefore, at room temperature, an ohmic contact is not expected to form unless the silicon is very highly doped to an extent that electron transport by field emission can occur.

As shown in Figure 6.10, the as-deposited 90-nm diameter Ag NWs formed rectifying contacts to Si. A summary of I-V characteristics after annealing treatments is presented in Table 6.3. The contact with lowest resistance was formed after annealing at 650 °C for 15s and was ohmic in the -1 V to 0.5 V range. Annealing for longer times at 650 °C resulted in degradation of the nanowires at the junctions, suggested by an increase in resistance (Figure 6.10) and confirmed by SEM images (Figure 6.11). It is noted that the impact of PVP on the Ag NW/Si interface during high temperature anneals requires further investigation.

Table 6.3: Summary of I-V characteristics of 90nm diameter Ag NW films after heat treatments. “R” refers to a rectifying contact. “S-O” refers to a semi-ohmic contact.

Temp. (°C), Time (s)	200, 60	300, 60	400, 75	500, 60	550, 15	600, 10	650, 15	700, 5
I-V Curve	R	R	R	R	R	S-O	S-O	S-O

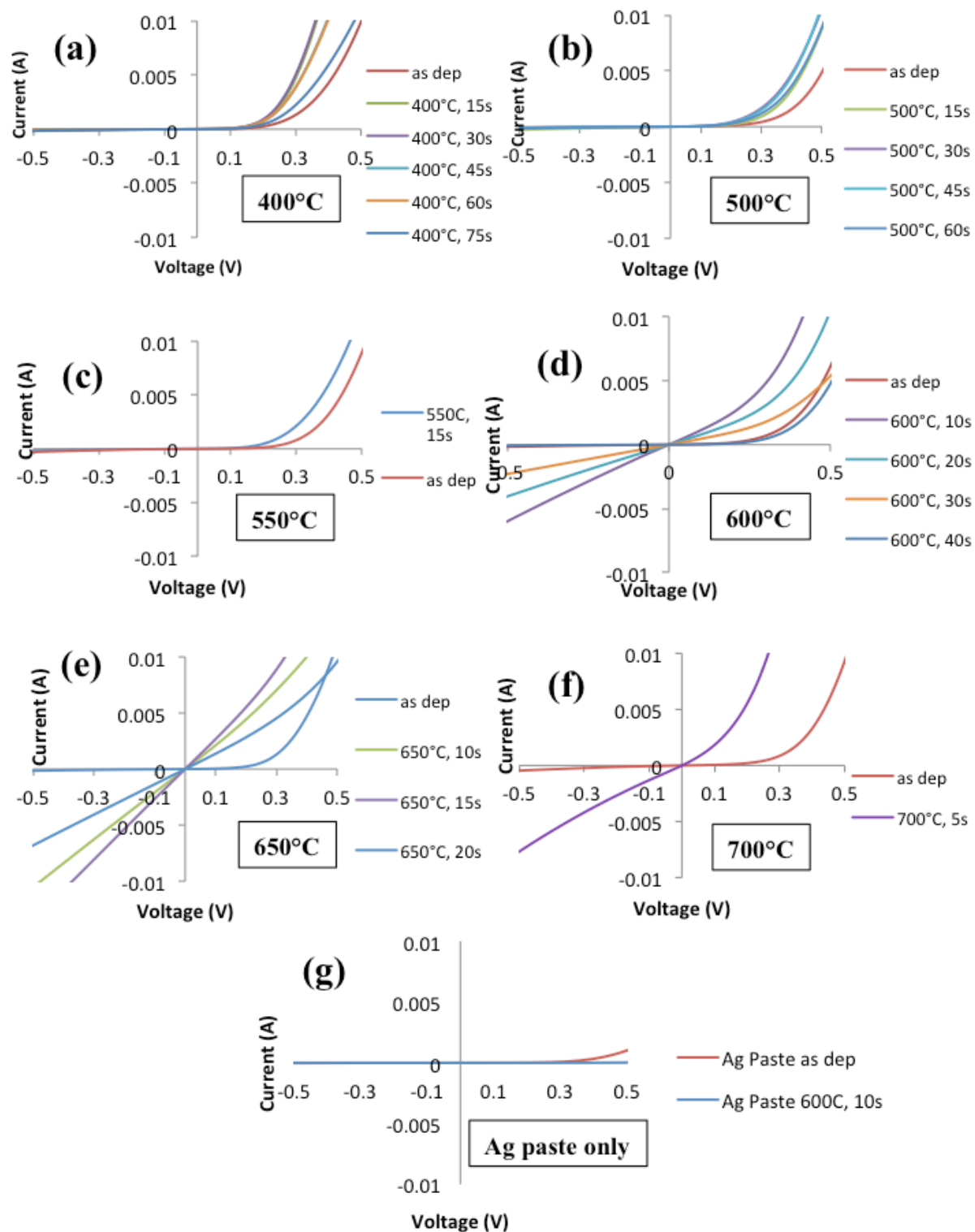


Figure 6.10: Current-voltage characteristics measured as indicated in Fig. 6.7 a for 90 nm-diameter Ag NW films on n-Si after annealing sequence. Samples annealed at 600 °C or higher exhibited a transition towards ohmic behavior. A decrease in current is observed for longer annealing times.

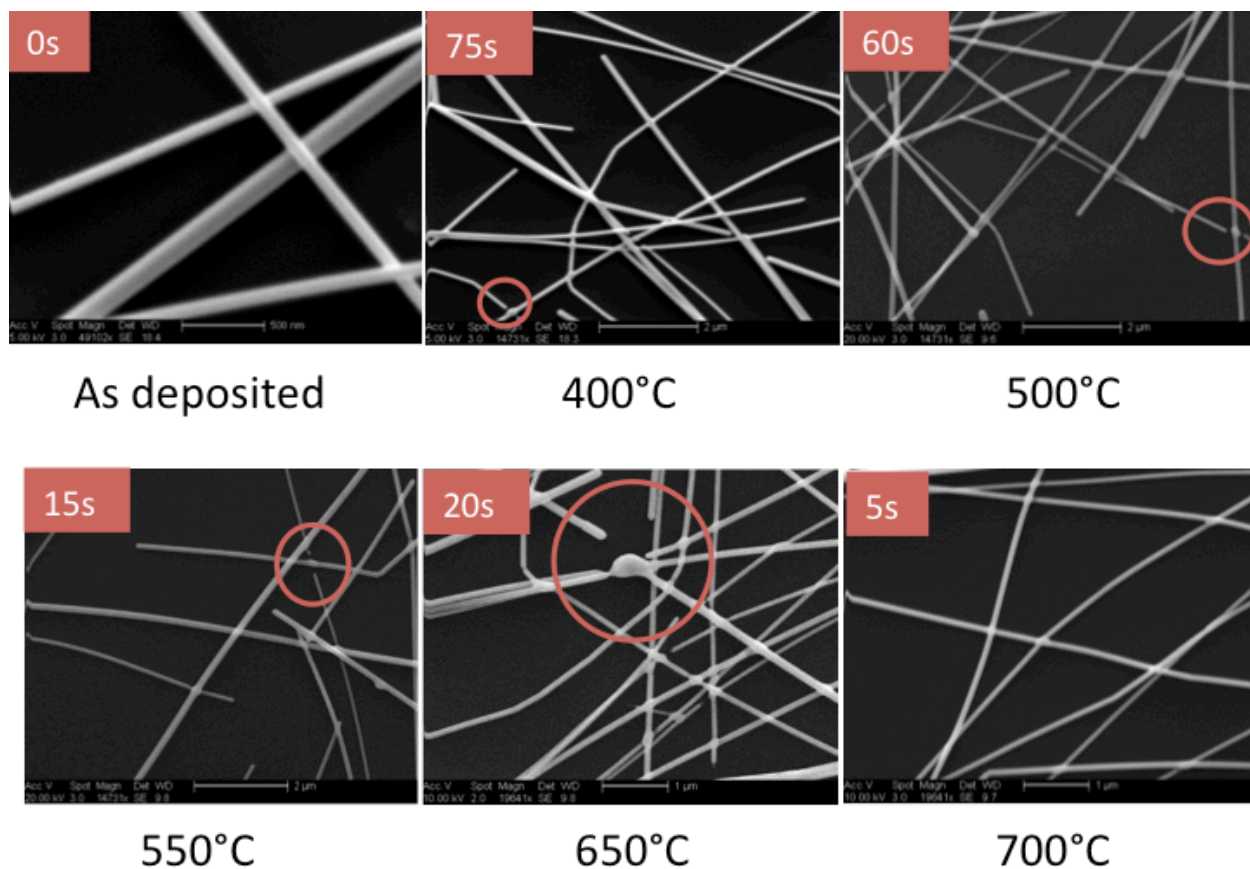


Figure 6.11: SEM micrographs of 90 nm-diameter Ag NW films after annealing at the indicated temperatures for the specified times. Circled areas show separation of NWs at the junctions after heat treatment.

Contrary to reports made by Xie et al³⁸ of improved 100 nm-diameter Ag NW contacts on Si after annealing at 400 °C, we observed no change in contact resistance after annealing the 90nm Ag NWs at 400 °C. This is consistent with the thermodynamics of thin film Ag/Si interfaces in the literature, where no solid solubility of Si in Ag occurred at 400 °C⁵⁰ and no indications of Ag diffusion into Si were observed until 450 °C.⁵¹

It is possible that annealing at higher temperatures and for a longer duration could improve the Ag NW/Si interface, due to more diffusion at the interface. However, Figure 6.11

indicates that the nanowires have poor stability at high temperatures and long periods of time. While a significant decrease in melting temperature is not anticipated until dimensions are ~ 10 nm or less,⁵⁶ Rayleigh instabilities⁵⁷ are known to cause metallic nanowires to break into spheres.^{58,59,60,61,62} Nichols and Mullins found that the morphology of a solid rod is unstable under perturbations with wavelengths greater than its circumference.⁶³ For a sinusoidal perturbation with wavelength λ and rod with radius, r , the greatest instability will occur for wavelengths $\lambda_m = 8.89 r$ (assuming surface diffusion is the dominant mechanism), and the rod will break into a line of spheres with diameter $3.78 r$, spaced λ_m apart. Rayleigh instability is not observed microscopically in solids due to kinetic limitations. However, due to the large surface to volume ratio, this phenomenon, which is facilitated by diffusion, has been observed in metallic nanowires. For example, Morales, *et al.*⁵⁸ studied 30-50 nm-diameter Cu NWs and observed fragmentation of the NWs at 500 °C and the formation of spheres at 600 °C. Larger diameter wires required higher temperatures for fragmentation to occur. Similar effects have been observed for PMMA fibers,⁶⁴ Pt NWs,⁶² Au NWs,⁵⁹ Ni NWs,⁶⁵ and Co NWs.⁶⁶ The effect of annealing on Ag NWs has also recently been investigated, and Rayleigh instabilities leading to fragmentation were observed, where morphology changes began at as low as 250 °C for 105 nm-diameter wires.^{67,61,20} Xie *et al.*³⁸ observed that annealing 100 nm-diameter NWs for 5 min caused NW breakage. Thinning was observed after only 2 minutes.

There has additionally been a report of self-limiting plasmonic welding of Ag NW junctions by exposure to tungsten-halogen lamps,²⁰ similar to the tungsten halogen lamps used in the RTA. Due to the nanoscale gap at the NW-NW junctions, there is a large field enhancement at the junction leading to localized heating. The heating is maximized when the lamp wavelength

is the localized surface plasmon resonance of the NW. Localized heating causes the junction to fuse, and once the nanoscale gap has been eliminated, the effect ends.

35nm Ag NWs

The dimensions of Ag NWs have an effect on the properties of NW films. The percolation threshold is reduced when longer nanowires are used.⁶⁸ Additionally, longer nanowire films exhibit better electrical properties after stretching.⁶⁹ The diameters of the nanowires can affect the transmittance of the film at low densities. For example, at the percolation threshold, the transmittance of NW films with smaller diameters will have a higher transmittance.⁶⁸ The use of NWs with smaller diameters can also reduce haze effects.⁷⁰

As the diameter of the nanowires decrease, the surface to volume ratio increases, making surface effects more prominent. Below ~10 nm, significant change in thermodynamic behavior of the materials may be exhibited, such as depressed eutectic⁷¹ and melting temperatures,⁷² which we hypothesize could facilitate ohmic contact formation at lower temperatures. However, at 35 nm, an increase in surface diffusion and therefore greater effects due to Rayleigh instabilities are also expected.

Figure 6.12 shows the current –voltage characteristics of the 35 nm-diameter Ag NW films. Plots (a, c, e, g) are of the vertical measurement depicted in Figure 6.7 a, including the Ag NW/Si interface. Plots (b, d, f, h) are the results of a measurement between the center Ag paste contact in Figure 6.7 a and the Ag paste square, measuring mostly the resistance of the Ag NW film. A transition to ohmic behavior does not appear to occur after annealing at 200 °C to 400 °C. On the contrary, the interfacial and film resistances appear to increase after annealing. Due to the increase in NW film sheet resistance, the vertical I-V characteristics may not be accurate.

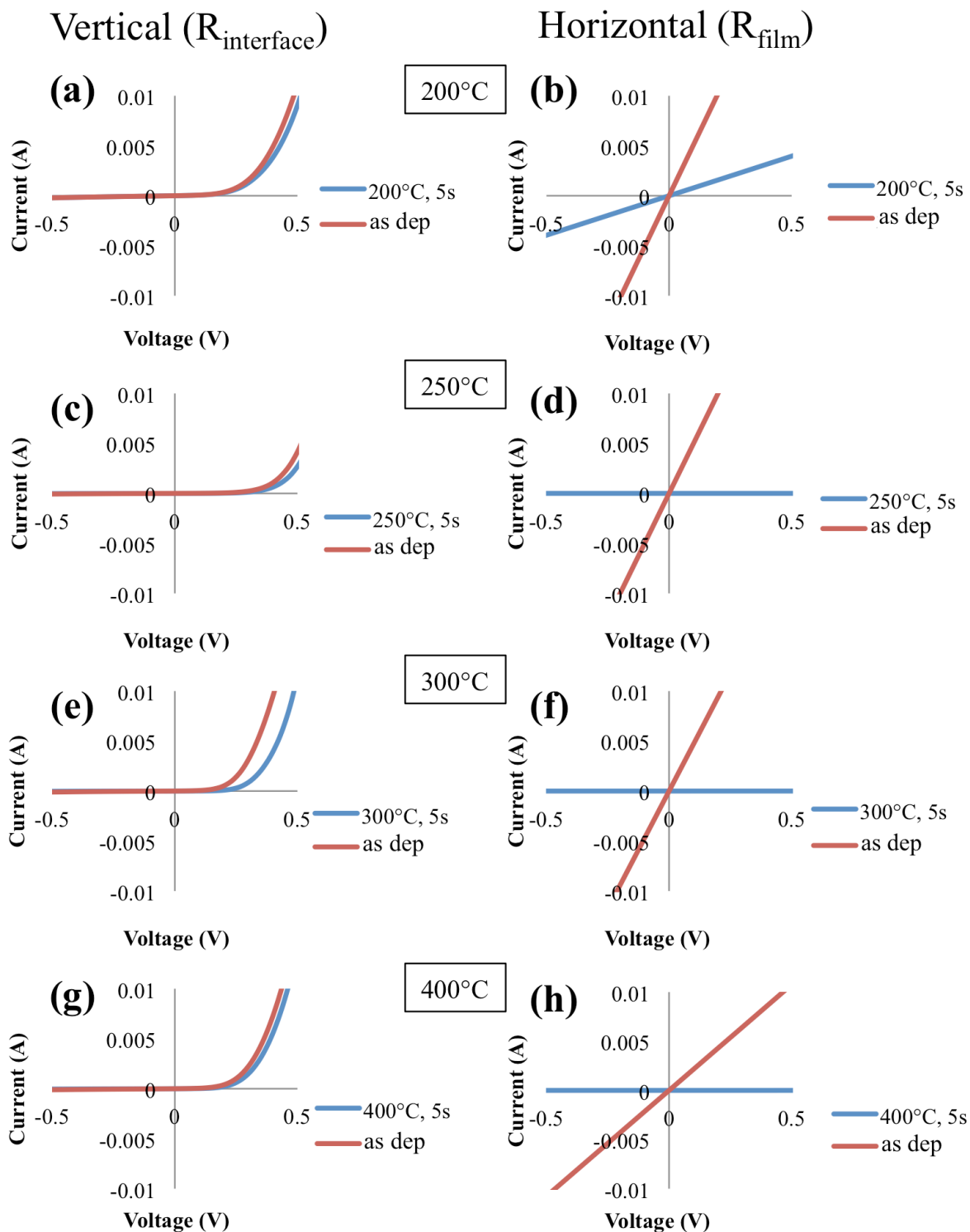


Figure 6.12: Current-voltage characteristics of 35 nm-diameter NWs after annealing at indicated temperatures. (a, c, e, g) Vertical measurement depicted in Fig. 6.7 a, where probes are placed on Ag paste square and Ag paste back contact. (b, d, f, h) Lateral measurement of Ag NW film, where probes are places on Ag paste square and Ag paste center contact (Fig. 6.7 a).

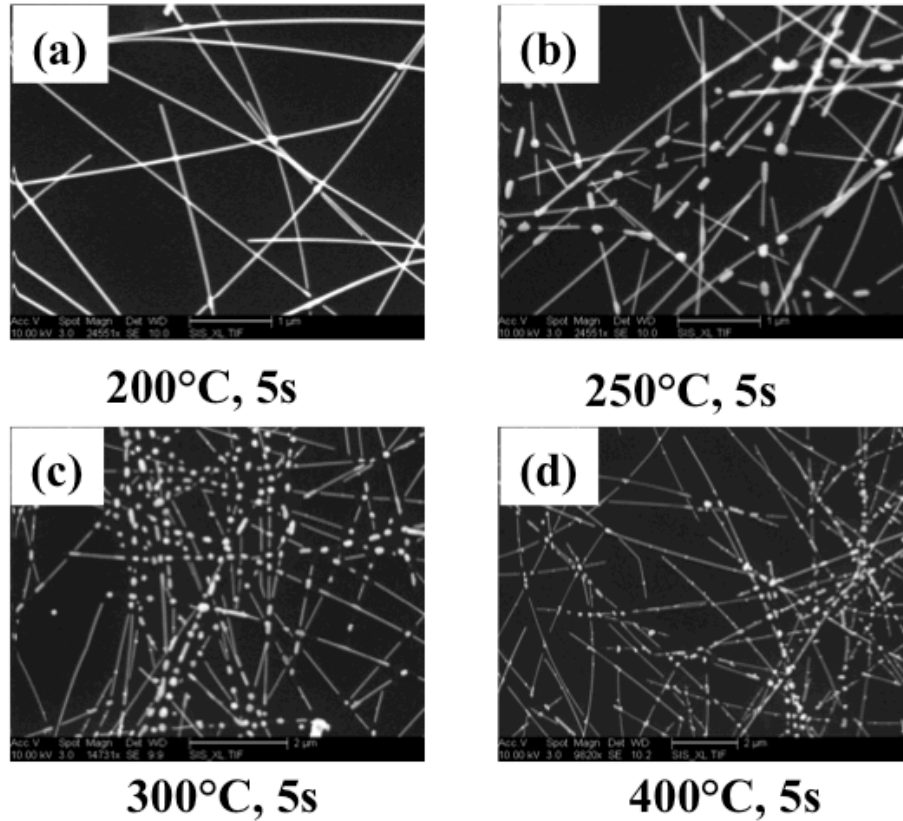


Figure 6.13: SEM micrographs of 35 nm-diameter Ag NW films on n-Si after annealing at various temperatures for 5 s in an RTA. Significant melting at NW-NW junctions is exhibited for all temperatures above 200 °C, and slight melting is seen for the sample annealed at 200 °C.

Figure 6.13 shows the SEM micrographs of the 35 nm-diameter Ag NW films after annealing. The nanowires become discontinuous after annealing for as short as 5 s and at temperatures lower than that for 90 nm-diameter NWs. This is consistent with diameter-dependent Rayleigh instability behavior.

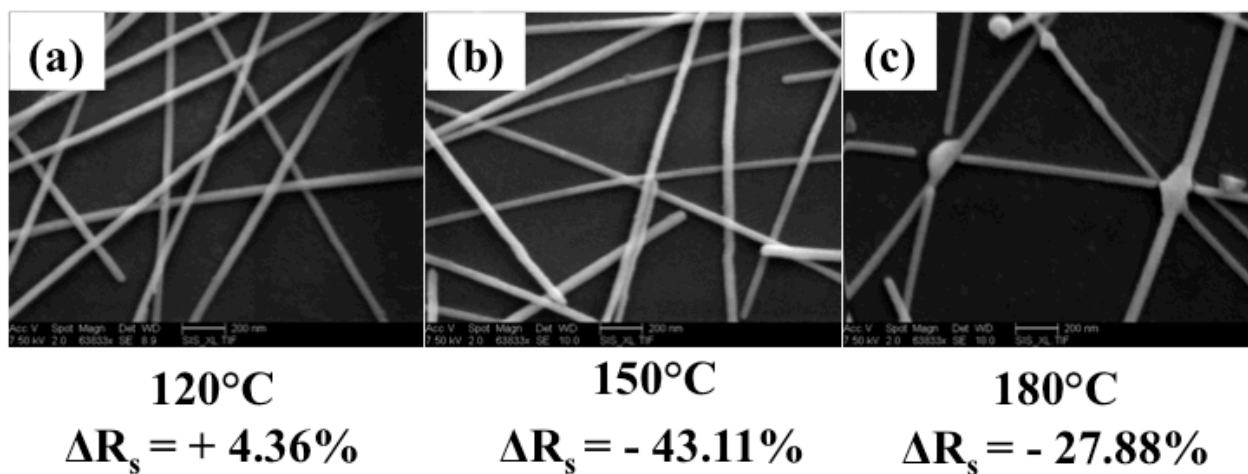


Figure 6.14: SEM micrographs of 35 nm-diameter Ag NW films on glass substrates after annealing for 20 min at the specified temperatures in low vacuum. Changes in sheet resistance, ΔR_s , are indicated. The decrease in sheet resistance after annealing at 150°C and 180°C is attributed to a decrease in NW-NW junction resistance. The smaller decrease in sheet resistance at 180°C is attributed to breakage at some of the junctions.

Breaking at the junctions was observed at temperatures as low as 200 °C. This is close to the temperature at which the 90 nm-diameter NWs are annealed to reduce junction resistance during sample fabrication. It is therefore evident that a different annealing temperature should be used in this step for smaller diameter NWs. Figure 6.14 shows SEM micrographs of 35 nm – diameter Ag NWs on glass substrates after annealing at 120 °C, 150 °C, and 180 °C for 20 minutes in a low vacuum oven. The corresponding percent increase or decrease in sheet resistance is also indicated. A small increase in sheet resistance was observed at 120 °C. This temperature is lower than the glass transition temperature of PVP,^{61,73,74} suggesting that the PVP coating is not able to flow away from the junction. On the other hand, 150 °C and 180 °C are above the PVP glass transition temperature; at these temperatures the PVP coating could therefore flow away from the NW-NW junctions, resulting in a reduction in sheet resistance. The smaller decrease in sheet resistance at 180 °C, relative to that at 120 °C, appears to be due to degradation of the nanowires at this temperature.

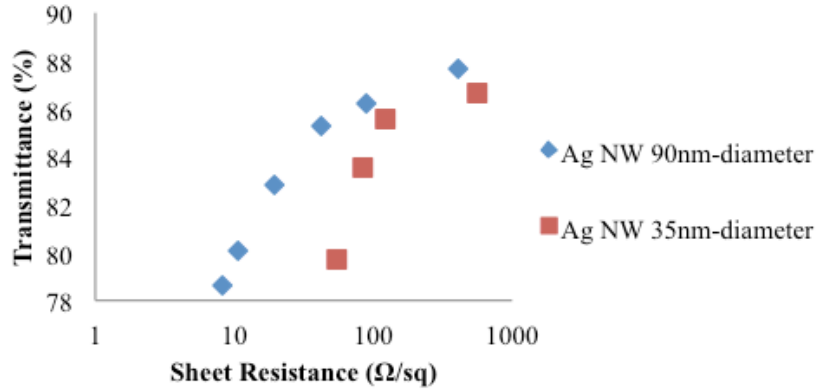


Figure 6.15: Sheet resistance versus transmittance for pristine Ag NW films with 90 nm-diameters and 35 nm diameters. Films were annealed at 180°C.

Sheet resistance and transmittance of pristine 35 nm-diameter and 90 nm-diameter Ag NW films are shown in Figure 6.15. The expected decrease in percolation threshold due to increased aspect ratio for 35 nm-diameter wires ($l/d = 286$ for 35 nm and $l/d = 277$ for 90 nm) is not observed. This could in part be due to degradation of the 35 nm diameter films after heat treatment at 180°C.

6.4 Conclusions

It has been demonstrated that Ag NWs form rectifying contacts to Si prior to annealing. The conditions for ohmic contact formation for 90 nm Ag NWs are similar to those of Ag thin films, where a change towards ohmic behavior began at 600 °C. Lowest interfacial resistance for the 90 nm-diameter wires on Si was observed after annealing at 650 °C for 15 sec. An ohmic contact for 35 nm NWs on Si was not observed due to breaking of the nanowire junctions at temperatures as low as 200 °C. The effect of heat treatment on the morphology of the nanowires was dependent upon the NW diameter, consistent with Rayleigh instability predictions. To form

an ohmic contact, the nanowire diameters must be large enough to allow sufficient annealing at standard temperatures before degradation of the film. This work indicates that the annealing temperature for 35 nm Ag NWs should remain below 180°C, which is insufficient to produce ohmic contacts to silicon. Thermal stability is therefore another property that one should consider when selecting the diameter of NWs.

It has been shown that solution processed Ag NWs dispersed in polymers have improved film uniformity and FoMs relative to those dispersed in isopropanol. PEDOT:PSS, despite its conductivity, significantly reduces the transmittance of the films, resulting in lower FoMs overall. Non-conductive, transparent polymers such as PSS and PVA have the benefit of improving NW film morphology while maintaining high transmittance, regardless of their insulating properties. These Ag NW-polymer composites also displayed reduced percolation thresholds relative to pristine nanowires.

6.5 References

1. D. S. Hecht, L. B. Hu and G. Irvin, *Advanced Materials*, 2011, **23**, 1482-1513.
2. L. B. Hu, H. Wu and Y. Cui, *Mrs Bulletin*, 2011, **36**, 760-765.
3. L. Hu, H. S. Kim, J.-Y. Lee, P. Peumans and Y. Cui, *ACS Nano*, 2010, **4**, 2955-2963.
4. A. Suzuki, T. Matsushita, T. Aoki, Y. Yoneyama and M. Okuda, *Japanese Journal of Applied Physics Part 2-Letters*, 2001, **40**, L401-L403.
5. A. Kumar and C. W. Zhou, *ACS Nano*, 2010, **4**, 11-14.
6. P. E. Lyons, S. De, J. Elias, M. Schamel, L. Philippe, A. T. Bellew, J. J. Boand and J. N. Coleman, *Journal of Physical Chemistry Letters*, 2011, **2**, 3058-3062.
7. S. W. Zhu, Y. Gao, B. Hu, J. Li, J. Su, Z. Y. Fan and J. Zhou, *Nanotechnology*, 2013, **24**, 335202.
8. D. S. Hecht, A. M. Heintz, R. Lee, L. B. Hu, B. Moore, C. Cucksey and S. Risser, *Nanotechnology*, 2011, **22**, 075201.
9. A. R. Rathmell and B. J. Wiley, *Advanced Materials*, 2011, **23**, 4798-4803.
10. S. Ray, R. Banerjee, N. Basu, A. K. Batabyal and A. K. Barua, *J. Appl. Phys.*, 1983, **54**, 3497-3501.
11. Y. G. Sun, B. Mayers, T. Herricks and Y. N. Xia, *Nano Lett.*, 2003, **3**, 955-960.
12. Y. G. Sun, Y. D. Yin, B. T. Mayers, T. Herricks and Y. N. Xia, *Chem. Mater.*, 2002, **14**, 4736-4745.
13. L. B. Hu, H. S. Kim, J. Y. Lee, P. Peumans and Y. Cui, *ACS Nano*, 2010, **4**, 2955-2963.
14. L. Bachenheimer, P. Elliott, S. Stagon and H. Huang, *Appl. Phys. Lett.*, 2014, **105**, 213104.
15. D.-S. Leem, A. Edwards, M. Faist, J. Nelson, D. D. C. Bradley and J. C. de Mello, *Advanced Materials*, 2011, **23**, 4371-4375.
16. S. Narayanan, J. R. Hajzus, C. E. Treacy, M. R. Bockstaller and L. M. Porter, *ECS Journal of Solid State Science and Technology*, 2014, **3**, 363-369.
17. J. Y. Lee, S. T. Connor, Y. Cui and P. Peumans, *Nano Lett.*, 2008, **8**, 689-692.
18. S. De, T. M. Higgins, P. E. Lyons, E. M. Doherty, P. N. Nirmalraj, W. J. Blau, J. J. Boland and J. N. Coleman, *ACS Nano*, 2009, **3**, 1767-1774.
19. Y. C. Lu and K. S. Chou, *Nanotechnology*, 2010, **21**, 215707.
20. E. C. Garnett, W. S. Cai, J. J. Cha, F. Mahmood, S. T. Connor, M. G. Christoforo, Y. Cui, M. D. McGehee and M. L. Brongersma, *Nature Materials*, 2012, **11**, 241-249.
21. S. De, P. J. King, P. E. Lyons, U. Khan and J. N. Coleman, *ACS Nano*, 2010, **4**, 7064-7072.
22. L. J. Brillson, *Contacts to Semiconductors: Fundamentals and Technology*, Noyes Publications, Park Ridge, NJ, 1993.
23. S. M. Sze and K. K. Ng, in *Physics of Semiconductor Devices*, J. Wiley & Sons, Hoboken, NJ, 3rd edn., 2007, ch. 3, pp. 134-196.
24. S. Ashok, S. J. Fonash, R. Singh and P. Wiley, *IEEE Electron Device Lett.*, 1981, **2**, 184-186.
25. G. de Cesare, D. Caputo and M. Tucci, *Ieee Electron Device Letters*, 2012, **33**, 327-329.
26. M. J. Turner and E. H. Rhoderick, *Solid-State Electron.*, 1968, **11**, 291-300.
27. B. L. Smith and E. H. Rhoderick, *Solid-State Electron.*, 1971, **14**, 71-75.
28. J. D. Vanotterloo, *Surface Science*, 1981, **104**, L205-L209.

29. H. H. Weitering, J. P. Sullivan, R. J. Carolissen, R. PerezSandoz, W. R. Graham and R. T. Tung, *J. Appl. Phys.*, 1996, **79**, 7820-7829.
30. G. Schubert, F. Huster and P. Fath, *Sol. Energy Mater. Sol. Cells*, 2006, **90**, 3399-3406.
31. L. M. Porter, A. Teicher and D. L. Meier, *Sol. Energy Mater. Sol. Cells*, 2002, **73**, 209-219.
32. D. K. Schroder and D. L. Meier, *IEEE Trans. Electron Devices*, 1984, **31**, 637-647.
33. H. Y. Chang, W. N. Zhu and D. Akinwande, *Appl. Phys. Lett.*, 2014, **104**, 5, 113504.
34. M.-G. Kang, T. Xu, H. J. Park, X. Luo and L. J. Guo, *Advanced Materials*, 2010, **22**, 4378-4383.
35. W. Gaynor, J.-Y. Lee and P. Peumans, *ACS Nano*, 2010, **4**, 30-34.
36. Z. Yu, L. Li, Q. Zhang, W. Hu and Q. Pei, *Advanced Materials*, 2011, **23**, 4453-4457.
37. J.-Y. Lee, S. T. Connor, Y. Cui and P. Peumans, *Nano Lett.*, 2010, **10**, 1276-1279.
38. S. Y. Xie, Z. Ouyang, B. H. Jia and M. Gu, *Optics Express*, 2013, **21**, A355-A362.
39. W. Gaynor, G. F. Burkhard, M. D. McGehee and P. Peumans, *Advanced Materials*, 2011, **23**, 2905-2910.
40. S. Chen, L. Song, Z. Tao, X. Shao, Y. Huang, Q. Cui and X. Guo, *Organic Electronics*, 2014, **15**, 3654-3659.
41. Y. Suh, N. Lu, S. H. Lee, W. S. Chung, K. Kim, B. Kim, M. J. Ko and M. J. Kim, *ACS Appl. Mater. Interfaces*, 2012, **4**, 5118-5124.
42. M. P. de Jong, L. J. van Ijzendoorn and M. J. A. de Voigt, *Appl. Phys. Lett.*, 2000, **77**, 2255-2257.
43. M. Jorgensen, K. Norrman, S. A. Gevorgyan, T. Tromholt, B. Andreasen and F. C. Krebs, *Advanced Materials*, 2012, **24**, 580-612.
44. Y. H. Meng, Z. H. Hu, N. Ai, Z. X. Jiang, J. Wang, J. B. Peng and Y. Cao, *ACS Appl. Mater. Interfaces*, 2014, **6**, 5122-5129.
45. G. Haacke, *J. Appl. Phys.*, 1976, **47**, 4086-4089.
46. S. Pegel, P. Potschke, T. Villmow, D. Stoyan and G. Heinrich, *Polymer*, 2009, **50**, 2123-2132.
47. S. Narayanan, PhD Thesis, Carnegie Mellon University, 2014.
48. T. Sebestyen, *Solid-State Electron.*, 1982, **25**, 543-550.
49. R. W. Olesinski, A. B. Gokhale and G. J. Abbaschian, *Bulletin of Alloy Phase Diagram*, 1989, **10**, 635-640.
50. L. Weber, *Metallurgical and Materials Transactions a-Physical Metallurgy and Materials Science*, 2002, **33**, 1145-1150.
51. L. H. Chen, Y. X. Zeng, P. Nyugen and T. L. Alford, *Materials Chemistry and Physics*, 2002, **76**, 224-227.
52. D. K. Schroder, J. Wiley & Sons, Hoboken, NJ, 3rd edn., 2006, ch. 3, pp. 127-184.
53. A. W. Dweydari and C. H. B. Mee, *Phys. Status Solidi A*, 1975, **27**, 223-230.
54. P. Andrew and A. Ilie, presented in part at the Journal of Physics: Conference Series, 2007.
55. Y. Han and D.-J. Liu, *Phys. Rev. B*, 2010, **82**, 125420.
56. W. Luo, W. Hu and S. Xiao, *J. Phys. Chem. C*, 2008, **112**, 2359-2369.
57. L. Rayleigh, *Proceedings of the London Mathematical Society*, 1878, **10**, 4-13.
58. M. E. Toimil-Molares, A. G. Balogh, T. W. Cornelius, R. Neumann and C. Trautmann, *Appl. Phys. Lett.*, 2004, **85**, 5337-5339.

59. S. Karim, M. E. Toimil-Molares, A. G. Balogh, W. Ensinger, T. W. Cornelius, E. U. Khan and R. Neumann, *Nanotechnology*, 2006, **17**, 5954-5959.
60. A. Dutta, S. Chatterjee, A. K. Raychaudhuri, A. Moitra and T. Saha-Dasgupta, *J. Appl. Phys.*, 2014, **115**, 244303.
61. D. P. Langley, M. Lagrange, G. Giusti, C. Jimenez, Y. Brechet, N. D. Nguyen and D. Bellet, *Nanoscale*, 2014, **6**, 13535-13543.
62. M. Rauber, F. Muench, M. E. Toimil-Molares and W. Ensinger, *Nanotechnology*, 2012, **23**, 475710.
63. F. A. Nichols and W. W. Mullins, *Transactions of the Metallurgical Society of Aime*, 1965, **233**, 1840-1848.
64. P.-W. Fan, W.-L. Chen, T.-H. Lee and J.-T. Chen, *Macromolecular Rapid Communications*, 2012, **33**, 343-349.
65. Z. F. Zhou, Y. Pan, Y. C. Zhou and L. Yang, *Applied Surface Science*, 2011, **257**, 9991-9995.
66. K. A. Atmane, F. Zighem, Y. Soumare, M. Ibrahim, R. Boubekri, T. Maurer, J. Margueritat, J.-Y. Piquemal, F. Ott, G. Chaboussant, F. Schoenstein, N. Jouini and G. Viau, *Journal of Solid State Chemistry*, 2013, **197**, 297-303.
67. G. Giusti, D. P. Langley, M. Lagrange, R. Collins, C. Jimenez, Y. Brechet and D. Bellet, *International Journal of Nanotechnology*, 2014, **11**, 785-795.
68. S. M. Bergin, Y. H. Chen, A. R. Rathmell, P. Charbonneau, Z. Y. Li and B. J. Wiley, *Nanoscale*, 2012, **4**, 1996-2004.
69. P. Lee, J. Lee, H. Lee, J. Yeo, S. Hong, K. H. Nam, D. Lee, S. S. Lee and S. H. Ko, *Advanced Materials*, 2012, **24**, 3326-3332.
70. C. Preston, Y. Xu, X. Han, J. N. Munday and L. Hu, *Nano Research*, 2013, **6**, 461-468.
71. J. M. Howe, H. Mori and Z. L. Wang, *Mrs Bulletin*, 2008, **33**, 115-121.
72. O. Gulseren, F. Ercolessi and E. Tosatti, *Phys. Rev. B*, 1995, **51**, 7377-7380.
73. N. Weiss, L. Mueller-Meskamp, F. Selzer, L. Bormann, A. Eychmueller, K. Leo and N. Gaponik, *RSC Adv.*, 2015, **5**, 19659-19665.
74. M. D. Buera, G. Levi and M. Karel, *Biotechnology Progress*, 1992, **8**, 144-148.

Chapter 7: Summary and Future Directions

In first part of this work, Ni, Pd, Cr, and Ti contact test structures were fabricated onto individual, solution-synthesized, p-type SnS nanoribbons. High work function metals (Ni and Pd) formed ohmic or semi-ohmic contacts to SnS nanoribbons, while the lower work function metals (Cr and Ti) formed Schottky contacts. The Schottky barrier heights calculated for Cr and Ti agree well with the band alignment predicted by Schottky-Mott theory, whereas the ohmic behavior of Ni and Pd also agree with the expectations from this model. Of the two ohmic metals, a lower specific contact resistance (on the order of $10^{-4} \Omega\text{-cm}^2$ or lower) was consistently calculated for Ni. The results of this study indicate a lack of Fermi level pinning in metal-SnS nanoribbon structures. Further investigations to determine the nature of the interface, such as if diffusion or reactions are occurring or if an interfacial layer is present, would be beneficial to elucidate the mechanisms underlying the observed lack of Fermi level pinning.

In the second portion of this thesis, contacts to electron-beam evaporated SnS thin films were investigated. Deposition and processing conditions were shown to impact phase composition, morphology, and electrical properties of SnS films. Films deposited at a substrate temperature of 300°C were identified to be α -SnS, whereas films deposited at substrate temperatures of 100°C and 200°C resulted in a mixture of π -SnS and α -SnS phases. The resistivity of films deposited at 300°C was reduced by annealing in vacuum. Ti/Au, Ru/Au, Ni/Au, and Au as-deposited metallizations formed ohmic contacts to α -SnS thin films. Average specific contact resistances were found to decrease with increasing metal work function from Ti/Au, Ru/Au, Ni/Au, to Au. After annealing the contacts at 350°C in argon, Ru/Au had the lowest average specific contact resistance of $1.9 \times 10^{-3} \Omega\text{-cm}^2$. Ni/Au and Ti/Au contacts were found to be unstable after annealing. Further investigations to identify the physical nature of the

interface, such as if diffusion of Ni into SnS is occurring, would be beneficial. Ru/Au demonstrated a low specific contact resistance; however, Ru is rare, and faces high fluctuations in supply and price. Alternative high work function metals, or incorporation of diffusion barriers in the contact structure, should be investigated.

The third portion of this thesis concerns the use of silver nanowire (Ag NW) networked films as transparent conductors. Ag NW-polymer composites demonstrated improved film uniformity from pristine Ag NWs; however, the incorporation of PEDOT:PSS reduced transmittance, resulting in a lower figure of merit. PSS and PVA were found to improve NW film morphology while maintaining high transmittance. Ag NWs formed rectifying contacts to Si prior to annealing. The lowest interfacial resistance of 90 nm-diameter Ag NWs on Si was observed after annealing at 650°C for 15 sec. Thermal stability of these contacts must be considered, as anneals can cause fragmentation of the nanowires and disrupt connectivity of the conductive NW network.